Effect of anti-site disorder and film thickness on the structural, magnetic, electrical- and magneto-transport properties of Co₂FeAl_{0.5}Si_{0.5} Heusler alloy thin films

A thesis submitted in partial fulfillment of the award of the degree of

Doctor Of Philosophy

By Lanuakum A Longchar Reg. No.: 17PHPH18



School of Physics University of Hyderabad Hyderabad – 500 046 Telangana, INDIA

February, 2024

DECLARATION

I, Lanuakum A Longchar, hereby declare that the matter embodied in the thesis entitled, "Effect of anti-site disorder and film thickness on the structural, magnetic, electrical- and magnetotransport properties of Co₂FeAl_{0.5}Si_{0.5} Heusler alloy thin films", is the result of the investigations carried out by me in the School of Physics, University of Hyderabad, Hyderabad, India, under the supervision of Prof. S. Srinath. This thesis is free from plagiarism. I hereby declare that it has not been submitted previously in part or in full to this or any other University or Institution for award of any degree or diploma.

Date: 3) ol 29
Place: Hyderabad

Lanuakum A Longchar Reg. No.: 17PHPH18



CERTIFICATE

This is to certify that the thesis entitled "Effect of anti-site disorder and film thickness on the structural, magnetic, electrical- and magneto-transport properties of Co₂FeAl_{0.5}Si_{0.5} Heusler alloy thin films", submitted by Mr. Lanuakum A Longchar, bearing registration number 17PHPH18, in partial fulfilment of the requirements for award of Doctor of Philosophy in the School of Physics is a bonafide work carried out by him under my direct supervision.

This thesis is free from plagiarism and has not been submitted previously in part or in full to this or any other University or Institution for award of any degree or diploma.

Further, the student has the following publications and conference proceedings before the submission of the thesis for adjudication.

- Resistivity minima in disordered Co₂FeAl_{0.5}Si_{0.5} Heusler alloy thin films.
 Lanuakum A Longchar, Mainur Rahaman, Binoy Krishna Hazra, R. Rawat, M. Manivel Raja, S.N. Kaul, S. Srinath. Journal of Magnetism and Magnetic Materials 569, 170439 (2023).
- Effect of film thickness on the electrical transport in Co₂FeAl_{0.5}Si_{0.5} thin films.
 Lanuakum A. Longchar, Mainur Rahaman, Binoy Krishna Hazra, M. Manivel Raja, R. Rawat, S. N. Kaul and S. Srinath. AIP Advances 13, 025106 (2023).

- 3. Effect Of Film Thickness On The Structural and Magnetic Properties of Co₂FeAl_{0.5}Si_{0.5} Heusler Alloy Thin Film"
 - Lanuakum A Longchar, Mainur Rahaman, Lalita, G A Basheed, M. Manivel Raja, S. N. Kaul, and S. Srinath. AIP conference proceedings (2023).
- Magnetization reversal and damping in Co₂FeAl_{0.5}Si_{0.5} quaternary Heusler alloy".
 Lanuakum A Longchar, Mainur Rahaman, M. Manivel Raja, V. Raghavendra Reddy, S.
 N. Kaul and S. Srinath Conference: 2023 IEEE International Magnetic Conference Short Papers (INTERMAG Short Papers)

Further, the student has passed the following courses towards the fulfilment of course required for PhD.

Course code	Name	Credits	Pass/Fail	
PY801	Research Methodology	4	Pass	
PY802	Advanced Quantum Mechanics	4	Pass	
PY803	Advanced Experimental Techniques	4	Pass	
PY804	Advanced Condensed Matter Physics	4	Pass	

Dean

School of Physics

University of Hyderabad.

DEMN

School of Physics
University of Hyderabad
HYDERABAD - 500 946.

Prof. S. Srinath

Thesis Supervisor

School of Physics

Dr. S. Srinath
Professor
School of Physics
UNIVERSITY OF HYDERABAD
Central University P.O.
Hyderabad-500 046

Acknowledgement

I wish to express my sincere respect and gratitude to my supervisor, Professor S. Srinath, for his exceptional mentorship, continuous support, and kindness throughout my research period. Learning the art of research from him has been a privilege. Words cannot adequately convey how Prof. Srinath has instilled belief in myself. Sir, I appreciate your generosity in providing me the space to fail, make mistakes, and learn from them. A special acknowledgment goes to Professor S. N. Kaul for guiding me in my work and teaching me the importance of passion and patience in research. His unwavering support and valuable suggestions were instrumental in overcoming challenges and achieving success. I am aware that these words fall short in expressing the depth of my gratitude to him.

I want to express my gratitude to my Ph.D. review committee members Dr. Venkataiah Gorige and Prof. Nageswara Rao S. V. S. for their suggestions during doctoral review presentations. I also extend my gratitude to my former Ph.D. review committee member Prof. V. Seshu Bai. I would also like to thank the present dean Prof. K. C. James Raju and the former deans Prof. Bindu A Bambah, Prof. V. Seshu Bai, Prof. Ashok Chatterjee for providing the necessary facilities.

I am grateful to Dr. M. Manivel Raja, DMRL, Hyderabad for providing facility to grow the thin films. He has also help me to make bulk samples and to carry out other measurements. I would also like to thank Dr. Arout Chelvane J and Dr. Himalay Basumatary for their help during my DMRL visit. I would like to thank the UGC-DAE Consortium for Scientific Research, Indore for providing the facility and accommodation during my visit to UGC-DAE for different measurements. I thank Dr. Rajeev Rawat and Dr. V. R. Reddy from UGC-DAE CSR, Indore, for providing facility to carry out magnetic, resistivity and MOKE measurements. I also thank Dr. Mukul Gupta for allowing me to use the multi-target sputtering system to grow thin films. My sincere gratitude goes to Dr. A. Haldar, IIT, Hyderabad for providing CPW-FMR facility and to carry out measurements. I would like to express my gratitude to Dr. G. A Basheed, CSIR-NPL Delhi, for the low-temperature FMR measurements.

I am thankful to the School of Physics office staffs Mr. Sudarshan, Mrs. Shashikala, Mr. Narasimha Rao, Mr. Prasad, Mrs. Deepika, Mr. Abraham, Mrs. Vijayalakshmi, for their help in administrative matters. I would also like to thank the operators Ms. Sunitha, Mr. Laxmi Narayan and Mrs. Jyothi from school of physics for helping me carry out the experiments.

I would like to acknowledge the UGC-NET JRF/SRF fellowship for providing financial support.

I am delighted to express my gratitude to Prof. Y. Sundarayya for his encouragements and motivations. I also extend my gratitude to Dr. Vijaya Laxmi for her caring nature and for the occasional treats towards all of us in the lab. I thank all my seniors Dr. Binoy Krishna Hazra, Dr. Leelashree S, Dr. Suresh Pittala, Dr. Pavan Venu Prakash Madduri, Dr. B Ravi Kumar for their encouragement and support. I also would like to thank my lab mates, Dr. Anshu Gaur, Saarthak Dulgaj, Mainur Rahaman, Jyotiranjan and Shivangi for creating a lively lab atmosphere, their continuous co-operation and stimulating discussions. I couldn't have asked for better lab mates.

I would also like to thank my batch mates and friends Pawan Kumar Verma, Dr. Najirul Islam, Sushmita, Arki and Aishwarya Bhatta for their support and love, making stay in the university memorable. I will forever cherish our time together.

To my friends who have been a tremendous support system and I am immensely grateful to them for their love and encouragement. In particular, I would like to thank Mr. Nyanthanglo Woch, Dr. Boniface Kamei, Mr. Saptarshi Dey, Dr. Limakumba Walling, Dr. Rhelo Kenye, Mr. Jongpongyanger Jamir, Mr. Thano Rengma, Mr. Chenithung L Ngullie, Dr. Amihe Swu, Mr. Imliakum Pongen, Dr. Injangbuanang Pamei, Dr. Ali, Dr. Venusa Tinyi, Ms. Thejasenuo Belho, Mr. Nagahoto Chophy, Dr. Vekhepu, Dr. Neikesonuo Rame, Ms. Senchumbeni Odyuo, Mr. Akaito Chophy, Mr. Kaikho Hrüzhünio, Ms. Sensonaro Longchar, Ms. Yinge Wangnao, Ms. Neito-ü Mero, Ms. Nekhotsolu Chuzho, Mr. Chothazo Nienu, Ms. Wapanginla Aier, Ms. Shanngam Kasom, Ms. Sari Luikham, Ms. Lungmila Woleng. Thank you for your support and friendship. I also thank my friend Lipokrenla Longkumer for her encouragement and support throughout my research life.

To my mother, Mrs. Amongla, my father, Mr. Atsung Longchar and sister, Moajungla A Longchar, thank you for your unconditional support and prayers, endless patience, love and encouragement throughout, without which I would not have reach this far.

To My Family and teachers

List of figures

- 1. **Fig. 1.1:** Electronic band structure near ε_f of a (a) paramagnet, (b) ferromagnet and (c) ferromagnetic half-metal. P is the electron spin polarization.
- 2. **Fig. 1.2:** (a) Heusler alloy with the perfectly ordered L2₁ structure (b) B2 disorder with Y and Z atom interchanging their sites and (c) A2 disorder with all the atoms occupying random sites. [28, 29,30]
- 3. **Fig. 1.3:** Proposed (a) Co Co hybridization and (b) Co₂ M' hybridization. [35, 36]
- 4. **Fig. 1.4** (a) DOS of CFAS system with the ε_f at the middle of the gap. (b) shows the gap in the minority states with respect to the ε_f . The positions of the valence band maximum (VBM) and the conduction band minimum (CBM) are compared. [39, 40]
- 5. **Fig. 2.1:** Schematic diagram of sputtering process [2].
- 6. **Fig. 2.2:** (a) Image of the Ultra-high vacuum DC magnetron sputtering used for depositing CFAS films (b) Target holder with the shutter, inside the main chamber.
- 7. Fig. 2.3: (a) FESEM attached with EDS (b) Schematic diagram of FESEM [3].
- 8. **Fig. 2.4:** (a) Grazing incident X-ray diffractometer used for structural characterizing of CFAS films, (b) Schematic diagram of an X-ray diffractometer [5,6].
- 9. Fig. 2.5: (a) Picture of the PPMS setup (b) Sample puck mounted on a user bridge.
- 10. Fig. 2.6: (a) Cavity FMR setup, (b) A typical FMR spectra on an interface.
- 11. **Fig. 2.7:** (a) Half-cut quartz rod sample holder, (b) CFAS film placed on the sample holder for measurement, (c) resonance cavity of the FMR setup.
- 12. **Fig. 2.8:** (a) Image of the CPW strip placed between the magnet poles, (b) a schematic diagram of CPW with sample film placed on top of the signal line [10].
- 13. **Fig. 2.9:** (a) Photograph of MOKE setup used for CFAS films under study, (b) Schematic diagram of MOKE experimental setup [11].
- 14. **Fig. 3.1:** (a) Surface of the CFAS thin film where the sample has been scanned over a rectangular area for EDS, and (b)the intensity or count of the Co, Fe, Si and Al elements from the CFAS thin film with their corresponding energy (in keV).
- 15. Fig. 3.2: (a) and (b): Schematic sketch of the film with and without the SiO₂ buffer layer in between the Si(100) substrate and the film. (c) EDS image of the as-deposited films indicating their chemical composition. (d) Cross- sectional FESEM image facilitating the visualization of the film thickness and the film-substrate interface.

- 16. **Fig. 3.3:** Grazing incidence X-ray diffraction patterns of 50 nm thick Co₂FeAl_{0.5}Si_{0.5} thin films deposited at substrate temperatures 27 °C, 350 °C, 450 °C, 500 °C and 550 °C on (a) SiO₂/Si(100)and (b) Si(100) substrates.
- 17. **Fig. 3.4:** The degree of atomic site order in B2 structure in the CFAS thin films, deposited on SiO₂/Si(100) and Si(100) substrates, at different substrate temperatures.
- 18. Fig. 3.5: GIXRD diffraction pattern for 12 nm, 25 nm, 50 nm and 75 nm CFAS films.
- 19. **Fig. 4.1:** Schematic diagram for the electrical resistivity measurement in the (a) Longitudinal configuration (b) Transverse configuration
- 20. **Fig. 4.2:** Longitudinal resistivity (ρ||): (a) data and fits for the RT films, based on Eq. (4.14) with the electron-phonon contribution given by the modified diffraction model. (b) (e): Zero-field and in-field resistivity (black and red open circles) in the temperature range 5 300 K with theoretical fits (black and red continuous curves), based on Eq. (4.14) for TS350, TS450, TS500 and TS550 films deposited on SiO₂/Si(100). Insets (a-e) give the enlarged view of the zero-field and in-field resistivity (open circles) in the range 5-70 K with theoretical fits (continuous lines), based on Eq. (4.14) for the, TS350, TS450, TS500 and TS550 films.
- 21. **Fig. 4.3:** Transverse resistivity (ρ^⊥): (a) data and fits for the RT films, based on Eq. (4.14) with the electron-phonon contribution given by the modified diffraction model. (b) − (e): Zero-field and in-field resistivity (black and red open circles) in the temperature range 5-300 K with theoretical fits (black and red continuous curves), based on Eq. (4.14), for TS350, TS450, TS500 and TS550 films deposited on SiO2/Si(100). Insets (a-e) give the enlarged view of the zero-field and in-field resistivity (open circles) in the range 5-70 K with theoretical fits (continuous lines), based on Eq. (4.14), for the TS350, TS450, TS500 and TS550 films.
- 22. **Fig. 4.4:** (a) Residual resistivity (ρ 5K), (b) Tmin and (c) residual resistivity ratio, as functions of substrate temperature in the CFAS thin films, obtained from longitudinal resistivity data. (d) Residual resistivity (ρ 5K), (e) Tmin and (f) residual resistivity ratio, as functions of substrate temperature in the CFAS thin films, obtained from transverse resistivity data.
- 23. Fig. 4.5: Longitudinal resistivity (ρ||): (a) data and fits for the RT films, based on Eq. (4.14) with the electron-phonon contribution given by the modified diffraction model.
 (b) (e): Zero-field and in-field resistivity (black and red open circles) in the temperature range 5 300 K with theoretical fits (black and red continuous curves),

- based on Eq. (4.14) for TS350, TS450, TS500 and TS550 films deposited on Si(100). Insets (a-e) give the enlarged view of the zero-field and in-field resistivity (open circles) in the range 5-70 K with theoretical fits (continuous lines), based on Eq. (4.14) for the, TS350, TS450, TS500 and TS550 films.
- 24. **Fig. 4.6:** Residual resistivity (ρ_{5K}) and T_{min} as functions of substrate temperature in the CFAS thin films deposited on the (a), (b): SiO2/Si(100) substrate, (c), (d): Si(100) substrate.
- 25. **Fig. 4.7:** Linear variation of $\Delta \rho$ with lnT at T < T_{min} for (a), (c): RT and TS350, and (b), (d): TS450, TS500, and TS550 CFAS/SiO₂/Si(100) and CFAS/Si(100) thin films. The straight lines through the data symbols serve to highlight the linear relationship between $\Delta \rho$ and lnT. Open symbols and solid circles denote the 'zero-field' (H = 0) and 'in-field' (H = 80 kOe) $\Delta \rho$ data, respectively.
- 26. **Fig. 4.8:** (a) Zero-field, $\rho(T, H = 0)$, and in-field resistivity, $\rho(T, H = 80 \text{ kOe})$, (open circles) as functions of temperature with theoretical fits (continuous lines), based on Eq. (4.14), and the temperature variations of the contributions from the e-d scattering (ρ_{e-d}) , WL (ρ_{WL}) , e-m (ρ_{e-m}) and e-p (ρ_{e-p}) scattering for the RT film. Magnetic field of strength H=80 kOe leaves ρ_{e-d} and ρ_{e-p} unaltered in the entire temperature range but tends to suppress ρ_{WL} and ρ_{e-m} . (b) (d) Zero-field resistivity, $\rho(T, H=0)$, (open circles) as a function of temperature, with theoretical fits (continuous lines), based on Eq. (4.14), and the temperature variations of ρ_{e-d} , ρ_{WL} , ρ_{e-m} and ρ_{e-p} for TS350, TS500 and TS550.
- 27. **Fig. 4.9:** (a) Comparison of the percentage deviations from the DW + T^2 and DW + $[T / D_{SW}(T)]^2$ fits (b)-(e) Comparison of the percentage deviations from the BW + T^2 and BW + $[T / D_{SW}(T)]^2$ fits (based on Eq. (14)) in RT, TS350, TS450 TS500 and TS550 CFAS thin films. For all the figures, inset (i) Displays the percentage deviations from the BG + T^2 and BW + T^2 fits, inset (ii) Compares the percentage deviations from the BG + T^2 and BG + $[T / D_{SW}(T)]^2$ fits. See the text for details about different types of theoretical fits.
- 28. **Fig. 4.10:** TS500 CFAS thin film as an example; (a) displays the percentage deviations from the BG + T^2 and BW + T^2 fits. (b) Compares the percentage deviations from the BG + T^2 and BG + $[T/D_{SW}(T)]^2$ fits. (c) Comparison of the percentage deviations from the BW + T^2 and BW + $[T/D_{SW}(T)]^2$ fits (based on Eq. (4.14)). See the text for details about different types of theoretical fits.

- 29. **Fig. 4.11:** (a) (T \lesssim T_{min}) Variation with the substrate temperature of ρ_{e-d} and ρ_{WL} at 5 K and T_{min} for CFAS thin films (b) (T \gtrsim T_{min}) Variation with substrate temperature of ρ_{e-m} , ρ_{e-p} at T_{min} and 300 K. The open black and filled red dots indicate the zero-field and in-field data, respectively.
- 30. **Fig. 4.12:** (a) (d) Comparison of the observed $\rho_{e-m}^{||}$ (T, H = 80 kOe) (open circles) with the $\rho_{e-m}^{||}$ (T, H = 80 kOe) computed (red curves) from $\rho_{e-m}^{||}$ (T, H = 0 kOe)) using the theoretical expression, Eq. (4.16). Inset (b) clearly bears out the suppression of ρ_{e-m} (T) at H = 80 kOe.
- 31. **Fig. 4.13:** (a) (e) Comparison of the observed ρ_{e-m}^{\perp} (T, H = 80 kOe) (open circles) with the ρ_{e-m}^{\perp} (T, H = 80 kOe) computed (red curves) from ρ_{e-m}^{\perp} (T, H = 0 kOe) using the theoretical expression, Eq. (4.16).
- 32. **Fig. 4.14:** Temperature dependence of AMR % for the RT, TS350, TS450, TS500 and TS550 CFAS films.
- 33. **Fig. 4.15:** Variations of the residual resistivity ρ_{5K} , T_{min} , and the residual resistivity ratio (RRR) with the thickness, t, for the CFAS thin films.
- 34. **Fig. 4.16:** (a) (d) Longitudinal resistivity, $\rho(T, H = 0)$ (open circles), as a function of temperature along with theoretical fits (red solid lines), based on Eq. (4.14). Insets of sub-figures (b) (d) show enlarged view of $\rho(T, H = 0)$ data (open circles) and the theoretical fits over the temperature range 5 K 70 K to highlight the minimum in resistivity.
- 35. **Fig. 4.17:** Variation of (a) ρ_{e-d} , (b) ρ_{wl} , (c) ρ_{e-m} and (d) ρ_{e-p} with the film thickness.
- 36. **Fig. 5.1:** In-plane configuration geometry.
- 37. **Fig. 5.2:** Out-of-plane configuration geometry.
- 38. **Fig. 5.3:** (a) FMR spectra recorded from 4 to 18 GHz for TS500 CFAS film and (b)Asymmetric Lorentzian fit showing the symmetric (absorptive) and anti-symmetric (dispersive) terms.
- 39. **Fig. 5.4:** Variation of (a) Landé g factor and (b) M_s, with substrate temperature.
- 40. **Fig. 5.5:** The value of $H_{res}^{||}$ obtained from the fit using Eq. (5.62) is plotted against the frequency ($\omega = 2\pi f$). The red solid curves represent the kittel fit.
- 41. Fig. 5.6: ΔH^{\parallel} obtained from the Kittel fit using Eq. (5.62), plotted against the frequency ($\omega = 2\pi f$). The solid red curves represent the fits using Eq. (5.64).

- 42. **Fig. 5.7:** α obtained from the fit using Eq. (5.64) plotted as a function of deposition temperature
- 43. **Fig. 5.8:** In-plane magnetization and anisotropy field as a function of deposition temperature.
- 44. **Fig. 5.9:** Variation of the $H_{res}(\phi_H)$ along with fits for RT, TS350, TS450, TS500 and TS550 CFAS thin films.
- 45. **Fig. 5.10:** (a) Variation of M_s and H_k with deposition temperature, (b) Variation of the φ_M with φ_H for RT, TS350, TS450, TS500 and TS550 CFAS thin films
- 46. **Fig. 5.11:** Variation of the $\Delta H^{||}(\phi_H)$ along with fits for RT, TS350, TS450, TS500 and TS550 CFAS thin films.
- 47. **Fig. 5.12:** Variation of the $H_{res}^{\perp}(\theta_H)$ along with fits for RT, TS350, TS450, TS500 and TS550 CFAS thin films.
- 48. **Fig. 5.13:** Variation of the $\Delta H^{\parallel}(\theta_H)$ along with fits for RT, TS350, TS450, TS500 and TS550 CFAS thin films.
- 49. **Fig. 5.14:** Variation of (a) M_s with TS, (b) θ_M vs θ_H
- 50. **Fig. 5.15:** Saturation magnetization (M_S) as a function of temperature. $M_S(T)$ is fitted using the spin wave expression.
- 51. **Fig. 5.16:** $H_{res}^{||}$ variation with frequency. Open circles denote the raw data and red continuous line denote the fit.
- 52. **Fig. 5.17:** Thickness variation of M_s and H_k
- 53. **Fig. 5.18:** Frequency dependence of ΔH^{\parallel} . Open circles denote the raw data and red continuous line denote the fit.
- 54. **Fig. 5.19:** Gilbert damping constant (α) plotted for different thickness.
- 55. **Fig 5.20:** Angular variation of $H_{res}^{||}$ for 12 nm and 7 nm CFAS films along with the fits
- 56. Fig. 5.21: Angular variation of ΔH^{\parallel} for the thickness series along with the fits.
- 57. Fig. 5.22: Variation of the φ_M with φ_H 25 nm, 50 nm and 75 nm CFAS thin films
- 58. **Fig. 5.23:** Variation of the $H_r^{||}(\theta_H)$ along with fits for 12 nm, 50 nm and 75 nm CFAS thin films.
- 59. Fig. 5.24: Variation of the θ_M with θ_H for 25 nm, 50 nm and 75 nm CFAS thin films
- 60. **Fig. 5.25:** Variation of ΔH^{\perp} with θ_H for the thickness series along with the fits showing contribution of ΔH^{LLG} , ΔH^{TMS} and ΔH^{θ_H} .

- 61. **Fig. 6.1:** Considering a single domain system with the easy axis of magnetic anisotropy axis, external magnetic field and magnetization directions.
- 62. Fig. 6.2: Kerr hysteresis loops recorded at $\phi_H = 0^\circ, 40^\circ, 50^\circ, 90^\circ$ for the TS series CFAS thin films.
- 63. **Fig. 6.3:** $\frac{M_r}{M_S}$ (ϕ_H) plot for the (a) RT, (b) TS350, (c)TS450, (d) TS500 and (e) TS550 CFAS thin films. The red continuous lines represent the fit and open circles represent the raw data.
- 64. **Fig. 6.4:** $H_C(\phi_H)$ plot for (a)RT, (b) TS350, (c) TS450, (d) TS500 and (e) TS550, CFAS film along with the fit, red lines, obtained from Eq. (6.13) and (6.17) and (6.20) as illustrated in the text.
- 65. **Fig. 6.5:** Domain images taken at various points along the hysteresis curve at $\phi_H = 0^\circ$ for (a) RT, (b) TS350, (c) TS450, (d) TS500 and (e) TS550, CFAS films
- 66. **Fig. 6.6:** Domain images taken at various points along the hysteresis curve at $\phi_H = 45^\circ$ for (a) RT, (b) TS350, (c) TS450, (d) TS500 and (e) TS550, CFAS films
- 67. **Fig. 6.7:** Domain images taken at various points along the hysteresis curve at $\phi_H = 90^\circ$ for (a) RT, (b) TS350, (c) TS450, (d) TS500 and (e) TS550, CFAS films.
- 68. **Fig. 6.8:** Kerr hysteresis loops recorded at $\phi_H = 0^\circ$, 40° , 50° , 90° for (a) 12 nm, (b) 25 nm, (c) 50 nm and (d) 75 nm, CFAS thin films.
- 69. **Fig. 6.9:** Angular variation of $\frac{M_r}{M_S}$ for (a) 12 nm, (b) 25 nm, (c) 50 nm and (d) 75 nm, CFAS thin films. The red continuous lines represent the fit and open circles represent the raw data.
- 70. **Fig. 6.10:** $H_c(\phi_H)$ plot for (a) 12 nm, (b) 25 nm, (c) 50 nm and (d) 75 nm, CFAS thin films along with the fit, red lines, obtained from Eq. (6.13) and (6.17) and (6.20) as illustrated in the text.
- 71. **Fig. 6.11:** Domain images taken at various points along the hysteresis curve for the (a) 12 nm (b) 25 nm and (c) 75 nm, CFAS film, captured with L-MOKE, at $\phi_H = 0^\circ$.
- 72. **Fig. 6.12:** Domain images taken at various points along the hysteresis curve for the (a) 12 nm (b) 25 nm and (c) 75 nm, CFAS film, captured with L-MOKE, at $\phi_H = 45^\circ$.
- 73. **Fig. 6.13:** Domain images taken at various points along the hysteresis curve for the (a) 12 nm (b) 25 nm and (c) 75 nm, CFAS film, captured with L-MOKE, at $\phi_H = 90^\circ$.

List of Tables

- 1. **Table 3.1:** Lists out the deposition parameter optimization process by varying DC power, Ar pressure and the corresponding atomic percentage for different depositions.
- Table 4.1: AMR ratios of various ferromagnets reported in the literature. WI FM, SI FM and FM stand for Weak itinerant-electron ferromagnet, Strong itinerant-electron ferromagnet and ferromagnet, respectively.
- 3. **Table 5.1:** Landé g factor, M_s, ΔH_{inhomo}, α and TMS contribution obtained from the fits using Eqs. (5.63) and (5.64) along with the frequency range over which the line width is fitted.
- 4. **Table 5.2:** H_{res}^{\parallel} at $(\phi_H = 0^\circ)$ and $(\phi_H = 90^\circ)$, M_s , and H_k obtained from the fits, based on equations (5.42) and (5.43), for the RT, TS350, TS450,TS500 and TS550 CFAS thin films .
- 5. **Table 5.3:** H_{res}^{\perp} , M_s , and H_k obtained from the fits, based on equations (5.44) and (5.45), for the RT, TS350, TS450, TS500 and TS550 CFAS thin films.
- Table 5.4: Lande-g factor, M_s, ΔH_{inhomo}, α and TMS contribution obtained from the
 best fits along with the frequency range over which the line width is fitted and the
 corresponding values are obtained.
- 7. **Table 5.5:** H_{res}^{\parallel} at $(\phi_H = 0^\circ)$ and $(\phi_H = 90^\circ)$, M_s , and H_k obtained from the fits, based on equations (5.42) and (5.43), for the 25 nm, 50 nm and 75 nm CFAS thin films.
- 8. **Table 5.6:** H_{res}^{\perp} , M_s^{\perp} , and H_k^{\perp} obtained based on equations (5.44) and (5.45) for 25 nm, 50 nm and 75 nm CFAS films.
- 9. **Table 6.1:** H_C and H_k obtained from the Kerr loops at $\phi_H = 0^\circ$ and $\phi_H = 90^\circ$ field angle respectively, along with the obtained values of y_1 and y_2 , from the fit for TS series CFAS films.
- 10. **Table 6.2:** The values of H_C, H_k, and the corresponding free-fitting parameters, derived from Equation (6.20) for the 12 nm, 25 nm, and 50 nm CFAS films, and from Equation (6.17) for the 75 nm film, are provided.

Contents

L	IST O	OF FIGURES	(i)		
L	IST O	OF TABLES	ii)		
1	Introduction				
	1.1	Literature Survey	1		
	1.2	Heusler alloys	1		
		1.2.1 Co-based half-metallic ferromagnetic Heusler alloys	2		
		1.2.2 Structure and disorder	3		
		1.2.3 Half-metallicity and origin of the minority spin gap	4		
		1.2.4 Slater–Pauling behaviour and magnetic moment	5		
	1.3	$Co_2FeAl_{0.5}Si_{0.5} \ Heusler \ alloy \qquad . \qquad $	7		
	1.4	Aims and objectives	10		
		1.4.1 Organization of the thesis	10		
2	Expe	erimental techniques	20		
	2.1	Sample preparation	20		
		2.1.1 Thin film growth using DC magnetron sputtering	20		
	2.2	Thin film characterization	25		
		2.2.1 Energy dispersive X-ray spectroscopy for composition analysis	25		
		2.2.2 Grazing incident x-ray diffraction for structural characterization	27		
	2.3	Electrical resistivity	29		
		2.3.1 Physical property measurement system	29		
	2.4	Ferromagnetic resonance	30		
		2.4.1 X-band Cavity ferromagnetic resonance	30		

		2.4.2 Temperature dependant FMR
		2.4.3 Broadband ferromagnetic resonance
	2.5	Magneto Optic Kerr Effect
3	Struc	eture and surface morphology of Co ₂ FeAl _{0.5} Si _{0.5} Heusler alloy thin films 38
	3.1	Experimental details
	3.2	Crystallographic structure of the Heusler compound
	3.3	Structural investigation
		3.3.1 Effect of deposition temperature
		3.3.2 Effect of film thickness
	3.4 C	onclusion
4	Effec	t of deposition temperature and film thickness on electrical resistivity and
	magı	netoresistance in Co2FeAl0.5Si0.5 thin films
	4.1	Experimental details
	4.2	Resistivity mechanisms at $T < T_{min}$
		4.2.1 Scattering involving Kondo spin-flip/two-level tunnelling states/diffusons. 49
		4.2.2 Enhanced electron-electron interaction (EEI)
		4.2.3 Weak localization/quantum interference effect 50
	4.3	Resistivity mechanisms at $T > T_{min}$
		4.3.1 Electron-phonon scattering
		4.3.2 Electron-magnon scattering
	4.4.	Data analysis, results, and discussion
		4.4.1 Effect of deposition temperature (CFAS-TS)
		4.4.1.1 Effect of deposition temperature on Magnetoresistance 69
		4.4.1.2 Effect of deposition temperature on Anisotropic Magnetoresistance
		(AMR)

		4.4.2 Effect of CFAS film thickness					
4	4.5. \$	Summary and conclusion					
5 1	Effect of deposition temperature and film thickness on magnetization, magnetic						
:	aniso	otropy, and Gilbert damping parameter in Co ₂ FeAl _{0.5} Si _{0.5} thin films 85					
4	5.1	Theoretical background					
4	5.2	Lineshape calculation					
4	5.3	Angular variation of the resonance field					
4	5.4	Angular variation of linewidth					
4	5.5	Data analysis, results, and discussion					
		5.5.1 Effect of deposition temperature					
		5.5.1.1 Broad band FMR					
		5.5.1.2 Angular dependent Ferromagnetic resonance					
		5.5.1.3 Temperature dependence of FMR					
		5.5.2 Effect of film thickness					
		5.5.2.1 Broadband FMR					
		5.5.2.2 Angular dependent Ferromagnetic resonance					
4	5.6	Conclusion					
6]	Effec	ct of deposition temperature and film thickness on magnetization reversal and					
1	magı	netic anisotropy					
(6.1	Experimental details					
(6.2	Theoretical Background					
		6.2.1 Introduction to magnetic domains and domain walls					
		6.2.2 Stoner and Wohlfarth model					
		6.2.3 Two-phase model					
í	6.3	Data analysis, results and discussion					

		6.3.1 Effect of deposition temperature
		6.3.2 Effect of thickness
	6.4	Conclusion
7	Conc	clusion and future scope
	7.1	Summary
		7.1.1 Effect of anti-site disorder on the structural, magnetic, electrical- and magneto
		transport properties of $Co_2FeAl_{0.5}Si_{0.5}$ Heusler alloy thin films 174
		7.1.2 Effect of thickness on the structural, magnetic, electrical- and magneto
		transport properties of Co ₂ FeAl _{0.5} Si _{0.5} Heusler alloy thin films 176
	7.2	Future scope of the thesis work
L	IST O	F PUBLICATIONS

Chapter 1

Introduction

This chapter presents a comprehensive evaluation of the existing literature on the $Co_2FeAl_{0.5}Si_{0.5}$ Heusler alloy thin films and concludes with the aim and scope of the thesis.

1.1 Literature Survey

Information storage and processing devices depend on magnetic materials and semiconductors. These devices rely on the charge and the orientation of the magnetic moment associated with the electron to operate. Significant advantage arises with the manipulation of charge flow with controlled spin orientation [1]. Spin current is a fundamental element in the field of spintronics. The adaptation of spintronic devices over conventional electronics presents several benefits, such as enhanced transfer speed, lower power consumption, compact device size and more [2].

Interest in the field has grown drastically with the discovery of the giant magnetoresistance (GMR) effect by Albert Fert [3] and Peter Grunberg [4] for which they won the Nobel prize in 2007. A large GMR of 79 % at 4 K has been achieved in Fe-Cr-Fe multilayer although spin polarization of Fe is only 46 % at Fermi level [5]. These reports have prompted renew interest for research in application as well as fundamental understanding of these systems.

1.2 Heusler alloys

The discovery of Heusler compounds dates back to 1903, the year Friedrich Heusler reported [6] the discovery of a ferromagnetic material at room temperature (RT) formed from the elements Cu, Mn, and Al, which are not ferromagnetic at room temperature. This was a remarkable discovery owing to the availability of a smaller number of elemental ferromagnets. Moreover, the concepts of anti-ferromagnetism and ferrimagnetism were introduced by Louis Néel in the 1930s—1940s after Heusler's discovery [7]. The tunability of these compounds by means of chemical

substitutions and structural order/disorder made the Heusler compound unique. At the time of the discovery of these compounds by Heusler, the crystal structure of the compound was not known until later in 1934, Otto Heusler [8] and Bradley and Rodgers [9] confirmed the crystal structure of Cu_2MnAl as four interpenetrating face-centered-cubic (fcc) sublattices. Full Heusler compounds have the general formula X_2YZ , where X and Y are d-block transition metal elements and Z is a p-block element. Alternatively, if the X site is left vacant then the *half-Heusler* compound, XYZ, is formed. In addition, the full-Heusler compounds have several variants: the *inverse Heusler* alloy, X_2YZ , in which the valence electron count of X is lower than Y and the *quaternary Heusler* compound, having XX'YZ formula with X' too a transition element [10, 13]. The Heusler name now envelopes a broad and extensive family of compounds, that include compounds with structural distortions (tetragonal or hexagonal structural distortion), chemical substitution and non-stoichiometric compounds [6, 11].

1.2.1 Co-based half-metallic ferromagnetic Heusler alloys

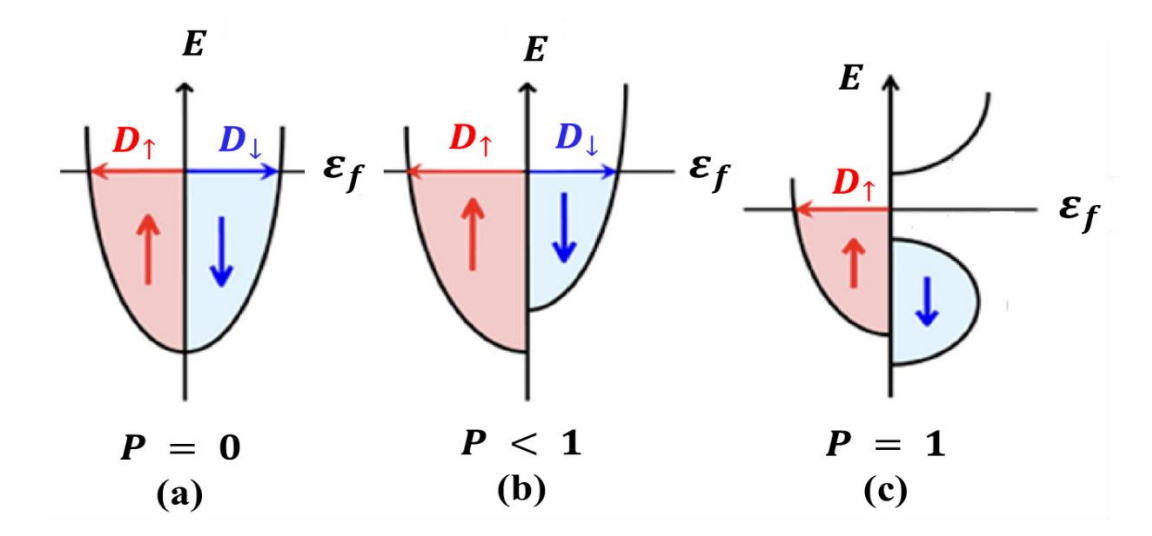


Fig. 1.1: Electronic band structure near ε_f of a (a) paramagnet, (b) ferromagnet and (c) ferromagnetic half-metal. P is the electron spin polarization.

In 1983, de Groot et al. [14], through band structure calculation, first predicted the half-metallic ferromagnetic behavior in Mn-based Heusler alloys. Half-metallic ferromagnets (HMF) exhibit unique band structure in which the majority spin channel behaves like a metal and the minority spin electrons exhibit a semiconducting or insulating behavior (e.g., NiMnSb). Fig. 1.1

shows the electronic band structure near ε_f of a (a) paramagnet, (b) ferromagnet and (c) ferromagnetic half-metal; P is the electron spin polarization. HMFs are of great interest because they are theoretically expected to intrinsically exhibit 100 % spin polarization at the Fermi energy level (ε_f) [15].

HMF Co-based Heusler alloys were first explored by *Ishida et al.* [16] in Co₂MnSn, Co₂TiAl and Co₂TiSn systems. The electronic structures of these compounds were calculated using Local Density Approximation (LDA) [17] method. Later, several other Heusler compounds were also predicted to be HMF [18-22]. The presence of band gap in the minority spin channel was reported by Kübler *et al.* [18] for the Co₂MnAl Heusler compound. In 2014, *Jourdan et al.* [23] experimentally showed the HMF nature of Co₂MnSi Heusler alloy by using spin-polarized photoemission technique.

HMFs are of great interest for spintronic applications. One example is the magnetic tunnel junction (MTJ) which comprises two ferromagnet layers as electrodes, separated by a thin insulating layer which acts as a tunnel barrier. Depending on the magnetization orientation of the two ferromagnetic electrodes, the current flow across the tunnel barrier can be controlled. When the magnetization orientation of the two electrodes is parallel, the current experiences low resistance. Conversely, if the magnetization of the electrodes aligns precisely antiparallel, the tunneling current diminishes, reaching zero in the case of HMF [24-27].

1.2.2 Structure and disorder

Full Heusler compounds with the stochiometric composition X_2YZ crystallize in the L2₁ structure ($fm\overline{3}m$ space group) which is shown in Fig. 1.2 (a). The unit cell consists of four interpenetrating fcc sublattices, in which the X atoms occupy the 8c Wyckoff position ($\frac{1}{4}$, $\frac{1}{4}$, $\frac{1}{4}$), Y atoms occupy the 4b ($\frac{1}{2}$, $\frac{1}{2}$, $\frac{1}{2}$) and the Z atoms take the 4a (0,0,0) positions [28-30].

Heusler alloy with the stoichiometric composition can have disorder which may arise due to the partial interchange of the atoms with respect to their crystallographic sites. Depending on the amount of atomic antisite disorder present, full Heusler X₂YZ alloys can exist in one of the three phases: L2₁, B2, A2 [28-30]. The most ordered phase has the L2₁ structure in which all the corner sites are occupied by X atoms while Y and Z atoms occupy alternate body centered sites.

When all the X atoms are on the corner sites and some fraction of the Y and Z atoms switch their respective body centered sites, the phase with B2 structure is formed, Fig. 1.2 (b). In the most disordered phase with A2 structure [28, 30-35], all the atomic sites are randomly occupied by X, Y and Z atoms, Fig. 1.2 (c). If X and Y or X and Z atoms are interchanged on their crystallographic positions, the DO3-type structure is obtained.

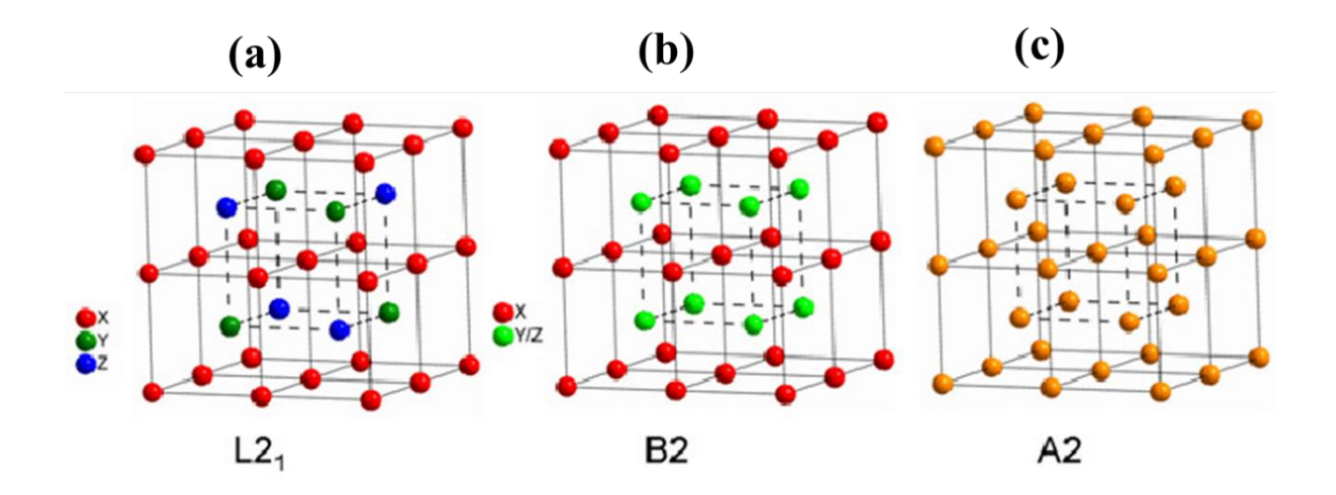


Fig. 1.2: (a) Heusler alloy with the perfectly ordered L2₁ structure (b) B2 disorder with Y and Z atom interchanging their sites and (c) A2 disorder with all the atoms occupying random sites. [28, 29,30]

1.2.3 Half-metallicity and origin of the minority spin gap

I. Galanaski et al. described the origin of the minority band gap in the minority spin channel [30]. To illustrate, consider the electronic band structure of the minority band of Co_2M 'Z Heusler system, shown in Fig. 1.3 [35]. The degenerate states of the d- orbitals d_{xy} , d_{yz} and d_{zx} form the t_{2g} states and d_{z^2} and $d_{x^2-y^2}$ form the e_g states. If the Mn sites are neglected, the two Co atoms sit in the cubic lattice with octahedral symmetry. The t_{2g} orbitals at the Co site can only couple with the t_{2g} of the other Co site (or Mn site) having the same symmetry, similarly e_g orbitals can only couple with the e_g orbital of another Co (or Mn atom). The d_{xy} , d_{yz} and d_{zx} orbitals of the two Co atoms hybridize creating a triply-degenerate t_{2g} state which are bonding states and triply-degenerate t_{1u} -antibonding state. The d_{z^2} and $d_{x^2-y^2}$ orbitals form the doubly degenerate e_g and e_u states which are bonding and antibonding, respectively, shown in Fig. 1.3 (a). Next for the Mn

atom, that sits in the tetrahedral environment and undergoes hybridization with the Co – Co resultant degenerate states. The triply degenerate t_{2g} state of the Co-Co hybridizes with the d_{xy} , d_{yz} and d_{zx} orbitals of the Mn atom to give two triply degenerate t_{2g} states. Among these, one of the triply degenerate states is bonding and occupied, while the other is antibonding and high in energy above the Fermi energy level (ϵ_f) . The doubly degenerate e_g orbitals couple with the d_{z^2} and $d_{x^2-y^2}$ of the Mn atom resulting in a doubly degenerate occupied e_g state (bonding) and another doubly degenerate e_g which is unoccupied and lies above ε_f . The remaining triply degenerate t_{1u} , which is below ε_f and occupied, and doubly degenerate e_u , which is above the ε_f , do not undergo hybridization because of the difference in symmetry, shown in Fig. 1.3 (b). Thus, eight minority d-bands are occupied and lying below ε_f whereas seven are empty which are above the ε_f and the ε_f lies in between the doubly degenerate unoccupied e_u and the triply degenerate occupied t_{1u} states.

The Z atom containing the s and p states have no direct contribution to the gap formation in the minority band. However, the Z atom significantly contributes to the positioning of the ε_f within the minority band gap as it contributes to the total number of occupied and unoccupied d-states. This is clearly seen in the case of $\text{Co}_2\text{FeAl}_{0.5}\text{Si}_{0.5}$ Heuler alloy [30, 35]. As a result, for a full Heusler alloy, there are twelve occupied minority states per unit cell; doubly degenerate e_u states, triply degenerate t_{2g} orbital, triply degenerate t_{1u} , one from s band and three from p band.

1.2.4 Slater-Pauling behavior and magnetic moment

In analogous to the Slater–Pauling behavior of the binary transition metal alloys [36], the generalized Slater–Pauling rule for Heusler [37, 38] alloys directly relate the total magnetic moment (in Bohr magnetons, μ_B per formula unit) with the total number of valence electrons.

The total magnetic moment (m_t) for a system is given by the difference between the total number of majority states (N_{\uparrow}) and the total minority states (N_{\downarrow}) :

$$m_t = N_{\uparrow} - N_{\downarrow} \tag{1.1}$$

and the total valence electrons (N_V) for a given system is expressed by:

$$N_V = N_\uparrow + N_\downarrow \tag{1.2}$$

Thus, from Eqs. (1.1) and (1.2), we have

$$m_t = N_V - 2N_{\downarrow} \tag{1.3}$$

As discussed above, for a full Heusler alloy, a total of eight occupied minority d states are created by undergoing hybridization of d-orbitals of the transition atoms. In addition, the Z atom contributes one s and three p bands, giving rise to a total of twelve occupied minority states (N_{\downarrow}) per formula unit. The total magnetic moment per formula unit, given by Eq. (1.3), is:

$$m_t = N_V - 24 \tag{1.4}$$

Thus, by knowing the total number of valence electrons, the total magnetic moment can be calculated for a given full Heusler alloy. Since, N_V is an integer number, the Slater–Pauling rule gives an integer value of the magnetic moment. The quaternary Heusler compounds are an exception, which have non-integer site occupancy.

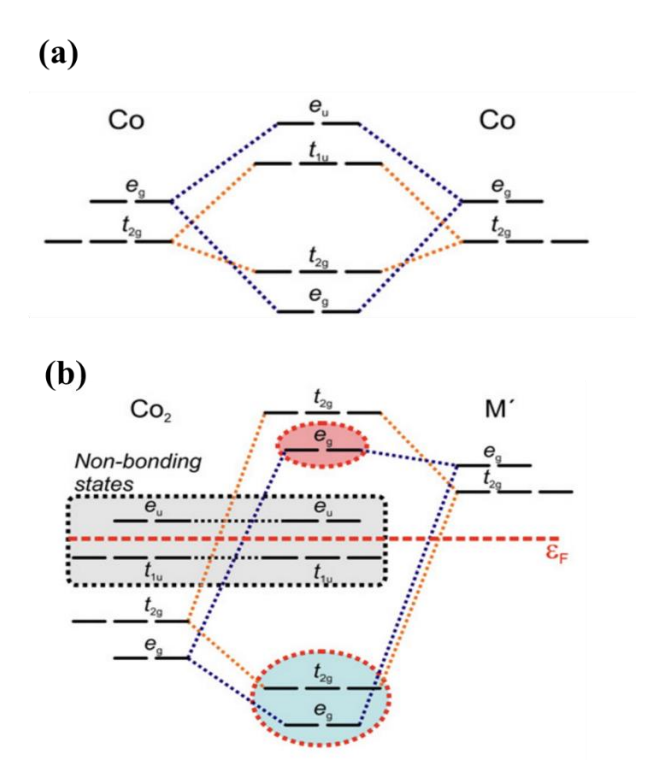


Fig. 1.3: Proposed (a) Co – Co hybridization and (b) Co₂ – M' hybridization. [35, 36]

1.3 Co₂FeAl_{0.5}Si_{0.5} Heusler alloy

Among the Co-based Heusler compounds, ab-initio band structure (DFT) calculations [39, 40] on Co₂FeAl_{1-x}Si_x alloys have revealed that the Fermi level for Co₂FeAl (Co₂FeSi) lies near the top of the valence band, E_V , (bottom of the conduction band, E_C) of minority spins. Small *effective* energy gap, ($\varepsilon_f - E_V$) or ($E_C - \varepsilon_f$), makes these compounds prone to the thermally induced degradation of half-metallicity (and hence of spin polarization). These calculations suggest that x can be used as a control parameter to tune the Fermi level so as to achieve a full band gap for the minority spins, as in a half-metal.

This situation is realized for the composition $\text{Co}_2\text{FeAl}_{0.5}\text{Si}_{0.5}$ when ε_f shifts to the middle of the band gap, resulting in robust half-metallicity, refer Fig. 1.4. In conformity with this theoretical expectation, at room temperature, L2₁ ordered $\text{Co}_2\text{FeAl}_{0.5}\text{Si}_{0.5}$ has a much higher spin polarization than that in the end compositions x = 0 and x = 1, and a reasonably large magnetization of 5.5 $\mu_B/\text{f.u}$ [40], besides a high T_c of ~1150K [39-42].

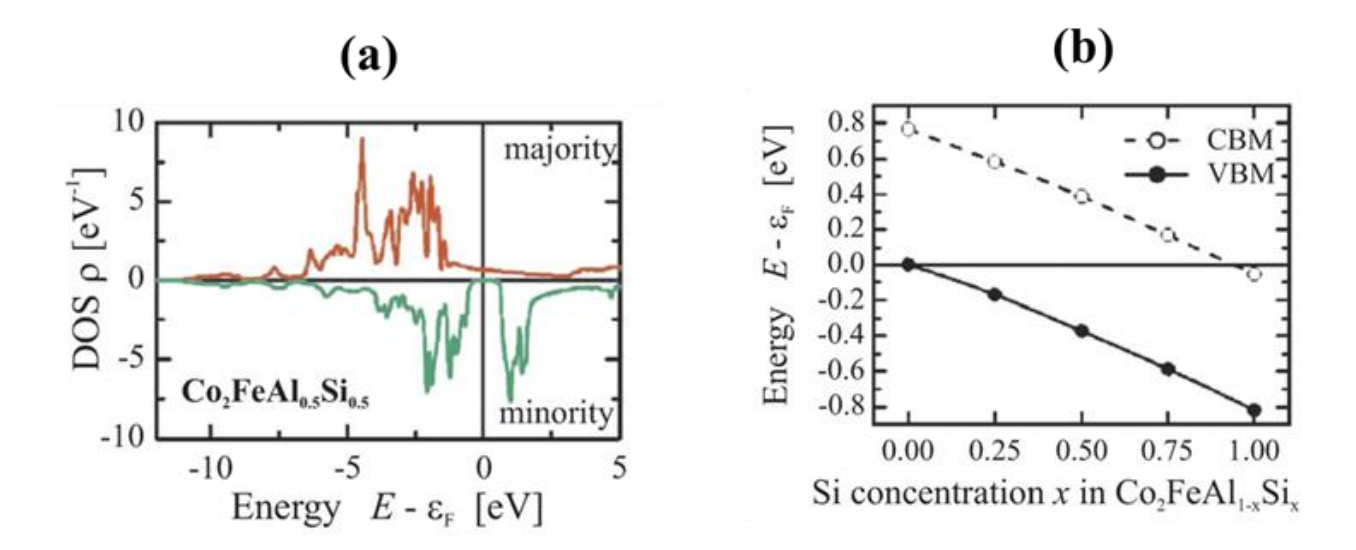


Fig. 1.4 (a) DOS of CFAS system with the ε_f at the middle of the gap. (b) shows the gap in the minority states with respect to the ε_f . The positions of the valence band maximum (VBM) and the conduction band minimum (CBM) are compared. [39, 40]

In addition, apart from the spin polarization of the system, Gilbert damping parameter (α) of a ferromagnetic material is crucial in the selection of suitable spintronic devices for applications. For instance, a low α value is essential for magnetic tunnel junction devices and for reducing power

consumption in spin-torque transfer-based devices [44, 45] while a high α value is favored to enhance thermal stability in current-perpendicular-to-plane GMR read sensors [46, 47]. Since α is directly related to the density of state (DOS) of the system at ε_f [48-51], value of α is greatly influenced by the anti-site disorder present in the system. Previously, for an L2₁ ordered Co₂FeAl_{0.5}Si_{0.5} Heusler compound, the value of α has been reported to be 0.001 [52] which lies in between the parent compounds Co₂FeAl and Co₂FeSi. In the Co-Mn based Heusler alloys, α decreases with the increase in annealing temperature. Thus, by controlling the anti-site disorder and the structure present in the system, the α can be tuned for spintronic applications. Experimentally the value of α can be determined through the frequency dependence of linewidth or the angular dependence of linewidth (at a particular frequency). This is, in turn, reflected in the broadening of the linewidth of the ferromagnetic resonance (FMR) spectra. Besides the intrinsic Gilbert damping contribution, the FMR linewidth has contributions from the system inhomogeneity and the extrinsic contributions like the two-magnon scattering [53, 54]. Thus, a systematic study is required to deduce the dependence of α on the system disorder and to estimate the intrinsic contributions.

In disordered systems, apart from the electron-phonon (e - p) and e - m scattering (ballistic transport) mechanisms contributing to resistivity $\rho(T)$ and responsible for the positive temperature coefficient of resistivity (TCR) in crystalline metallic ferromagnets, atomic site-disorder gives rise to the enhanced electron-electron interaction (EEI) and weak localization (WL) effects (diffusive transport), which account for the negative TCR at low temperatures. Thus, the negative and positive TCR contributions to $\rho(T)$ compete to produce a minimum at a certain temperature, T_{min} . In many Co-based Heusler thin film systems, at temperatures below T_{min} , the temperature variation $\rho(T) \sim -T^{1/2}$, has been attributed to either WL [55-57] or particle-particle channel EEI or particle-hole channel EEI [58], whereas $\rho(T) \sim -\ln T$ is deemed to originate from orbital two-channel Kondo effect [52, 62] or electron-diffuson scattering [58-61]. Such an approach does not yield unambiguous results because several (relevant) scattering mechanisms operate concurrently and the relative magnitudes of their contributions to $\rho(T)$ depend on the temperature range chosen for the fit. Accurate quantitative estimates for the contributions arising from the diffusive and ballistic transport mechanisms to $\rho(T)$ in disordered systems and their temperature variations can be obtained only when the theoretical fits closely reproduce the observed $\rho(T)$ over

the entire temperature range covered in the experiments. Recognizing that the energy gap Δ at ε_f in ferromagnetic half-metallic Heusler compounds gets reflected in the electrical resistivity, ρ , as the exponential suppression of the electron-magnon (e-m) scattering rate with decreasing temperature, $\rho(T,H)$ has been extensively studied [62] in several ferromagnetic Heusler compounds. Such investigations have unambiguously revealed the existence of an energy gap only in fully L2₁– ordered Co₂FeSi single crystal [62] but not in Co₂FeSi and other Co-based Heusler alloy thin films with L2₁ or B2 crystallographic order. Thus, a comprehensive study is required to understand the different scattering mechanisms contributing to $\rho(T)$ and the role of quantum corrections to the origin of T_{min} .

Anisotropy arises from the spin-orbit coupling resulting in magnetocrystalline anisotropy (MCA) [63, 64]. Apart from MCA, competition between shape and volume anisotropy can lead in a preference for magnetization alignment to be within the film plane or out of the film plane, in thin films. Heusler compounds were viewed as materials with entirely quenched orbital moments. However, recent XMCD studies on compounds like Co₂FeAl and Co₂Cr_{0.6}Fe_{0.4}Al [65, 66], Co₂MnGe [67], Co₂MnAl and Co₂MnSi [68] and Co₂FeSi [22], revealed noticeable orbital moments [38-42]. These reports have sparked renewed theoretical interest in the orbital magnetism of Co₂-based Heusler alloys. Various computational studies have attempted to determine elementspecific magnetic moments in Co₂M'Z compounds [69], but none have achieved satisfactory agreement with experimental results. Calculated orbital moments are typically 2 to 4 times smaller than experimental values. Due to the cubic structure, the Heusler alloys are expected to have cubic anisotropy but there have been several reports of Heusler alloys showing uniaxial anisotropy. Ambrose et al. [70, 71] reported a fourfold cubic anisotropy for Co₂MnGe system with a uniaxial anisotropy superimposed with the cubic anisotropy. Similarly, presence of two uniaxial anisotropies with two magnetization easy directions were also reported for Co₂FeSi system [72]. Such observations have been attributed to the growth conditions and discussed by Ambrose et al. [70, 71], Uemura et al. [73] and Wang et al. [74, 75], yet the underlying mechanisms are not explored.

1.4 Aims and objectives

The comprehensive literature review given above clearly reveals that there exists a notable gap in the exploration of the influence of anti-site disorder and film thickness on the structure, magnetization dynamics, magnetic anisotropy, monetization reversal and electrical- and magneto-transport properties in Co₂FeAl_{0.5}Si_{0.5} thin films. This particular area remains insufficiently examined and merits further investigation. Specifically, the following issues need to be addressed.

- 1. To ascertain the dominant scattering mechanisms which contribute to $\rho(T)$ and are responsible for the resistivity minimum in CFAS Heusler alloy thin films.
- 2. The relaxation mechanisms that contribute to the broadening of ferromagnetic resonance linewidth in these thin films.
- 3. What effect does the anti-site disorder and film thickness have on the Gilbert damping parameter?
- 4. What is the nature of magnetic anisotropy in CFAS thin films and how does it get affected by disorder and film thickness?
- 5. Does the disorder and film thickness have any influence on the magnetization reversal process in this system?

1.4.1 Organization of the thesis

❖ The present chapter gives a critical assessment of the existing literature on the Cobalt based Heusler alloy thin films (particularly, Co₂FeAl_{0.5}Si_{0.5} Heusler alloys) and concludes with the aim and scope of the thesis.

In **chapter 2**, the experimental techniques used to grow and characterize the Co₂FeAl_{0.5}Si_{0.5} thin films are discussed. DC magnetron sputtering has been used to grow two sets of CFAS films. The first set of films (TS series) had a thickness of 50 nm and the varying degree of disorder in them was achieved by depositing the films at different substrate temperatures, ranging from room temperature (RT) to 550°C referred to as RT, TS350, TS450, TS500 and TS550. The second set (thickness series) was grown by varying the thickness between 12 nm and 75 nm, while keeping the best deposition temperature obtained from the TS series, i.e., keeping the substrate temperature

constant at 500°C. Grazing angle x-ray diffraction study is employed to study the underlying crystalline structure prevalent in these films. The stoichiometry of the deposited films is optimized using the energy dispersive x-ray spectroscopy. The film thickness has been confirmed by using both cross-sectional FESEM imaging and x-ray reflectivity technique. Further, FMR and MOKE are employed to study the magnetization dynamics and magnetization reversal in the CFAS films, respectively.

Chapter 3

The presence of B2 crystal structure was ascertained in all the films through grazing incidence X-ray diffraction patterns. The film deposited at 500 °C displayed the highest degree of B2 structural order. Based on the substrate/deposition temperatures (TS), the CFAS films have been labelled as RT (room temperature), TS350, TS450, TS500, and TS550. Additionally, the relative atomic composition of the as-deposited films was confirmed as Co: 50, Fe: 25, Al: 12.5, and Si: 12.5, by employing Energy Dispersive X-ray Spectroscopy (EDAX) accessory of the Carl-Zeiss Field Emission Scanning Electron Microscope (FESEM).

In the thickness series, the B2 structure order is observed in 12 nm, 25 nm, and 50 nm CFAS films but not in the 75 nm films. As a function of the film thickness, the intensity of the superlattice peaks, corresponding to the B2 order, goes through a peak for the film of thickness 50 nm.

Chapter 4

In this chapter, the electrical- and magneto-transport properties of the CFAS films are discussed. A detailed analysis of the *zero-field* $\rho(T, H = 0)$ and *in-field* $\rho(T, H \neq 0)$ resistivity data, taken in two sample configurations (in which the electrical current is flowing along the length in the film plane while the external magnetic field, H, is applied either parallel or perpendicular to the film plane): $\rho^{\parallel}(T, H = 80 \text{ kOe})$ and $\rho^{\perp}(T, H = 80 \text{ kOe})$, was carried out. Further, the magnetoresistance and anisotropic-magnetoresistance (AMR) data are also discussed.

In all the TS series films, the resistivity (ρ) goes through a minimum at a temperature T_{min} when measured in *zero-field* and *in-field* configurations. T_{min} has the highest value (≈ 95 K) for the RT film and shifts to lower temperatures with increasing B2 order. The TS500 film with $T_{min} \approx 23$ K has the highest B2 order.

In the thickness series, the residual resistivity, ρ_{5K} , has a minimum value for t=50 nm. Irrespective of the film thickness, $\rho(T)$ goes through a minimum at T_{min} and T_{min} decreases from 105 K for 12 nm to 23.7 K for 50 nm. In comparison to the 50 nm films, the surface and interface contributions to $\rho(T)$ in 12 nm and 25 nm films are expected to be significantly larger than those caused by the underlying anti-site disorder (B2 structure). Thus, for t=12 nm and 25 nm, $\rho(T)$ has a large value in the range of $220-250~\mu\Omega$ cm.

The diffuson and weak-localization contributions, responsible for *negative* temperature coefficient of resistivity (TCR) compete with electron – magnon (*e-m*) and electron – phonon (*e-p*) contributions responsible for the *positive* TCR, to produce the resistivity minimum in both zero-field and in-field resistivity. In ρ^{\parallel} (T, H = 80 kOe) and ρ^{\perp} (T, H = 80 kOe), H has no influence on the diffuson and e-p contributions but suppresses weak localization (*wl*) and e-m scattering. Consequently, T_{min} shifts to lower temperatures and a negative magneto-resistance is observed. In the TS350, TS450, TS500, T550 CFAS films and the thickness series (12 nm, 25 nm, 50 nm and 75 nm), the Bloch-Wilson model correctly describes the functional dependence of ρ_{e-p} on temperature and thereby asserts that the *phonon-induced* non-spin-flip two-band ($s\uparrow\downarrow$ - $d\uparrow\downarrow$) scattering dominantly contributes to $\rho(T,H)$. RT film is an exception where the modified diffraction model adequately describes the functional dependence of ρ_{e-p} on temperature.

The temperature dependence of anisotropic resistance (AMR) for the RT film is positive over the temperature range 5K to 300 K. In contrast to the RT films, for the higher ordered TS350 and TS550 films, the AMR is -0.03 % and for the TS450 and TS500, the AMR is -2.31% and -0.84%, respectively. Negative AMR ratio for TS350, TS450, TS500, TS550 films confirms that the dominant s-d scattering is due to $s\uparrow$ to $d\uparrow$ spin sub-band, indicating that the films TS350, TS450, TS500 and TS550 are half-metallic in nature.

Chapter 5

This chapter deals with the magnetization dynamics, magnetic anisotropy and Gilbert damping constant (α) in the CFAS films, investigated by the ferromagnetic resonance (FMR) technique. A detailed analysis of the angular variations of resonance field (H_{res}) and FMR linewidth (ΔH) in both the in-plane (IP) and out-of-plane (OP) sample configurations, recorded at a fixed X- band frequency of 9.45 GHz by the cavity-based FMR reveals the following.

In the TS series, decrease in the disorder strength with increasing T_S is reflected as a systematic reduction in ΔH and H_{res} . The analysis of the broad-band FMR spectra shows that the TS500 film has the highest magnetization, $M_s \sim 1107$ G and lowest $\alpha \approx 1.35 \times 10^{-4}$. Irrespective of the degree of disorder, the two-fold variation of H_{res} with the magnetic field angle (φ_H) establishes that the CFAS films have *in-plane uniaxial anisotropy*. Gilbert damping and two-magnon scattering are the dominant mechanisms responsible for the linewidth broadening in the OP case.

 H_{res} and ΔH were also investigated over the frequency range 4 - 18 GHz using the broad-band CPW-FMR technique. The functional dependence of H_{res} on frequency, obtained from the CPW-FMR spectra, is best described by the Kittel resonance condition. The value of magnetization, obtained from the best fits, increases with thickness, and has a maximum for the 50 nm film. The in-plane resonance field as a function of 'in-plane' field angle (φ_H) shows two-fold symmetry which represents the dominant 'in-plane' uniaxial anisotropy for all the thicknesses. The anisotropy is small for the 50 nm film but increases with decrease in thickness due to surface anisotropy at lower thicknesses. For all the films, Gilbert damping and inhomogeneous broadening due to crystallite misorientation give the dominant contributions to linewidth broadening. α for 25 nm and 75 nm CFAS films is found to be 0.0057 and 0.016, respectively.

Chapter 6

This chapter presents the results of a detailed study of magnetization reversal in CFAS films by longitudinal magneto-optical Kerr effect (L-MOKE) microscopy. The hysteresis loops and domain images are captured at different 'in-plane' magnetic field angles (φ_H) with respect to the easy axis of magnetization ($\varphi_H = 0^\circ$). For all the TS films, except for TS450, rectangular hysteresis loops are observed along $\varphi_H = 0^\circ$. Such loops are characterized by the normalized squareness ratio $M_r/M_s \cong 1$ (where M_r is the remanent magnetization and M_s is the saturation magnetization). As the field angle increases from 0° , M_r/M_s decreases gradually and tends to 0 along the hard axis, i.e., $\varphi_H = 90^\circ$. This angular variation of the M_r/M_s shows a dominant two-fold variation which confirms the existence of in-plane uniaxial anisotropy in all the films. H_c decreases with T_S due to the decrease in defects, magnetic inclusions, and local magnetic inhomogeneities. The angular variation of H_c is analyzed in terms of the Stoner-Wohlfarth model, two-phase model and modified two-phase model, which considers two uniaxial anisotropies with easy axes mutually perpendicular to each other. In the RT film, a combination of Stoner-Wohlfarth

model and two-phase model describe the angular dependence of H_c whereas in the TS350 and TS500, two phase model alone describes the functional dependence of H_c on φ_H . When H points along the easy axis ($\varphi_H = 0^\circ$), irrespective of T_S and hence the strength of site-disorder, magnetization reversal takes place through the nucleation of reverse domains and their subsequent growth by 180° domain wall movement as H increases. At $\varphi_H = 45^\circ$, magnetization reversal occurs through the field-induced growth of 180° domains at the expense of ripple domains.

In the thickness series, a crossover in the angular dependence of M_r/M_s and H_c , reflecting two mutually perpendicular uniaxial anisotropy easy axes to that of a single uniaxial anisotropy easy axis, is observed as thickness increases from 12 nm to 75 nm. $H_c(\varphi_H)$ for 12 nm and 25 nm is described well by the modified two-phase model whereas a variation of H_c with φ_H , characteristic of the uniaxial anisotropy, is observed for the 75 nm film. Irrespective of the film thickness, the domain images for $\varphi_H = 0^\circ$ show the nucleation and subsequent growth of reverse domains by domain wall motion. At $\varphi_H = 45^\circ$, magnetization reversal occurs through ripple domains whereas for $\varphi_H = 90^\circ$, magnetization reversal mainly proceeds through domain rotation.

References

- 1. D. Awschalom and M. Flatté. *Nature Phys* **3**, 153–159 (2007). https://doi.org/10.1038/nphys551
- B. Dieny, I.L. Prejbeanu, K. Garello, P. Gambardella, P. Freitas, R. Lehndorff, W. Raberg, U. Ebels, S. O. Demokritov, J. Akerman, A. Deac, P. Pirro, C. Adelmann, A. Anane, A.V. Chumak, A. Hirohata, S. Mangin, Sergio O. Valenzuela, M. Cengiz Onbaşl, M. d'Aquino, G. Prenat, G. Finocchio, L. Lopez-Diaz, R. Chantrell, O. Chubykalo-Fesenko and P. Bortolotti. *Nat Electron* 3, 446–459 (2020). https://doi.org/10.1038/s41928-020-0461-5
- 3. M.N. Baibich, J.M. Broto, A. Fert, F. Nguyen van Dau, F. Petroff, P. Etienne, et al. *Phys. Rev. Lett.* **61**, 2472 (1988).
- 4. P. Grnberg, R. Schreiber, Y. Pang, M.B Brodsky, H. Sowers. *Phys. Rev. Lett.* **57**, 2442 (1986).
- 5. P. M. Tedrow and R. Meservey. *Phys. Rev. B* **7**, 318 (1973).
- 6. L. Wollmann, Ajaya K. Nayak, Stuart S.P. Parkin and Claudia Felser. *Annu. Rev. Mater. Res.* **47**, 247–70 (2017)
- 7. L. Neel. Rev. Mod. Phys. 25, 58–63 (1953)
- 8. O. Heusler O. *Adv. Phys.* **411**, 155–201 (1934)
- 9. A.J. Bradley, J.W Rodgers. *Proc. R. Soc. A* **144**, 340 59 (1934)
- 10. I. Galanakis, P.H Dederichs, N. Papanikolaou. *Phys. Rev. B* 66, 13442 (2002)
- 11. T. Graf, C. Felser, S.S.P. Parkin. *Prog. Solid State Chem.* **39**, 1–50 (2011)
- 12. P.J Webste. *Phys. Chem. Solids* **32**, 1221–31(1971)
- 13. P.J Webster, R.S Tebble. *Philos. Mag.* **16**, 347–61(1967)
- 14. R.A de Groot, F.M Mueller, P.G van Engen, K.H.J Buschow. *Phys. Rev. Lett.* **50**, 2024–27 (1983)
- 15. C. Felser, G. Fecher, B. Balke. *Angew. Chem. Int. Ed.* **46**, 668–99 (2017)
- 16. S. Ishida, S. Akazawa, Y. Kubo, J. Ishida. *J. Phys.F Met. Phys.* **12**, 1111 (1982)
- 17. Vosko SH, Wilk L, Nusair M. Can. J. Phys. **58**, 1200–11 (1980)
- 18. Kübler J, William AR, Sommers CB. *Phys. Rev. B* **28**, 1745 (1983)
- 19. H. C. Kandpal, G. H. Fecher, and C. Felser, J. Phys. D: Appl. Phys. 40, 1507 (2007)
- 20. I. Galanakis, P. H. Dederichs, and N. Papanikolaou, Phys. Rev. B 66, 174429 (2002)

- 21. E. Sasioglu, L. M. Sandratskii, P. Bruno, and I. Galanakis, Phys. Rev. B 72, 184415(2005)
- 22. S. Wurmehl, G. H. Fecher, H. C. Kandpal, V. Kseno-fontov, C. Felser, H. J. Lin, and J. Morais, *Phys. Rev. B* **72**, 184434 (2005)
- 23. Jourdan M, Minar J, Braun J, Kronenberg A, Chadov S, et al. *Nat. Commun.* **5**, 3974 (2014)
- 24. Ishikawa T, Marukame T, Kijima H, Matsuda K-i, Uemura T, Yamamoto M. *Appl. Phys. Lett.* **89**, 192505 (2006)
- 25. Tsunegi S, Sakuraba Y, Oogane M, Telling ND, Shelford LR, Arenholz E, et. al. *J. Phys. D: Appl. Phys.* **42**, 195004 (2009)
- 26. Taira T, Ishikawa T, Itabashi N, Matsuda K, Uemura T, Yamamoto M. *J. Phys. D: Appl. Phys.* **42**, 084015 (2009)
- 27. C. Herbot, E.A Jorge, M. Jordan. *Appl. Phys. Lett.* **94**, 142504 (2009)
- C. Felser and A. Hirohata. Springer Series in Materials Science 222, Springer International Publishing Switzerland (2016)
 https://doi.org/10.1007/978-3-319-21449-8
- C. Felser, L. Wollmann, S. Chadov, G.H. Fecher, and S.S. P. Parkin. *APL Mater.* 3, 041518 (2015).
 https://doi.org/10.1063/1.4917387.
- 30. I. Galanakis, P.H. Dederichs, and N. Papanikolaou. *Phys. Rev. B* **66**, 174429 (2002) https://doi.org/10.1103/PhysRevB.66.174429.
- 31. K.R.A. Ziebeck and P.J. Webster. *J. Phys. Chem. Solids* **35,** 1-7 (1974). https://doi.org/10.1016/0022-3697(74)90002-X.
- 32. T. Saito, N. Tezuka, and S. Sugimoto. *Materials Transactions* **52**, 370–373 (2011) https://doi.org/10.2320/matertrans.MBW201004.
- 33. P.J. Webster and K.R.A. Ziebeck. *J. Phys. Chem. Solids* **34**, 1647-1654 (1973) https://doi.org/10.1016/S0022-3697(73)80130-1.
- 34. Y. Takamura, R. Nakane, and S. Sugahara. J. Appl. Phys. **107**, 09B111 (2010) https://doi.org/10.1063/1.3350914.
- Simon Trudell, Oksana Gaier, Jaroslav Hamrle and Burkard Hillebrands. *J. Phys. D: Appl. Phys.* 43, 193001 (2010)
 https://doi:10.1088/0022-3727/43/19/193001

- 36. J. Kubler, "Theory of Itinerant Electron Magnetism revised edn". (New York: Oxford University Press) (2009).
- 37. J.C Slater. J. Appl. Phys. 8, 385 (1937)
- 38. L. Pauling. *Phys. Rev.* **54**, 899(1938)
- 39. G.H. Fecher and C. Felser. *J. Phys. D: Appl. Phys.* **40,** 1582 (2007) http://dx.doi.org/10.1088/0022-3727/40/6/S12
- 40. B. Balke, G.H. Fecher, and C. Felser. *Appl. Phys. Lett.* **90**, 242503 (2007) https://doi.org/10.1063/1.2748341
- 41. J.Karel, J.E. Fischer, S. Fabbrici, E. Pippel, P. Werner, M. Vinicius Castergnaro, P. Adler, S. Ouardi, B. Balke, G. H. Fecher, J. Morais, F. Albertini, S.S.P. Parkin and C. Felser. *J. Mater. Chem. C* 5, 4388 (2017). https://doi.org/10.1039/C7TC01241A.
- 42. R. Shan, H. Sukegawa, W.H. Wang, M. Kodzuka, T. Furubayashi, T. Ohkubo, S. Mitani, K. Inomata, and K. Hono. *Phys. Rev. Lett.* 102246601 (2009) https://doi.org/10.1103/PhysRevLett.102.246601
- 43. Yoshio Miura, Kazutaka Nagao, and Masafumi Shirai. Phys. Rev. B 69, 144413 (2004)
- 44. L. Berger, *Phys. Rev. B* **54**, 9353 (1996).
- 45. J. C. Slonczewski, J. Magn. Magn. Mater. 159, L1 (1996).
- 46. Smith N and Arnett P, Appl. Phys. Lett. **78**, 1448 (2001).
- 47. Liu X, Zhang W, Carter M J and Xiao G, J. Appl. Phys. 110 033910 (2011).
- 48. Takahide Kubota, Sumito Tsunegi, Mikihiko Oogane, Shigemi Mizukami, Terunobu Miyazaki, Hiroshi Naganuma, and Yasuo Ando, *Appl. Phys. Lett.* **94**, 122504 (2009).
- 49. S. Mizukami, D. Watanabe, M. Oogane, Y. Ando, Y. Miura, M. Shirai, and T. Miyazaki, *J. Appl. Phys.* **105**, 07D306 (2009).
- 50. M. Oogane, T. Kubota, Y. Kota, S. Mizukami, H. Naganuma, A. Sakuma, and Y. Ando, *Appl. Phys. Lett.* **96**, 252501 (2010).
- 51. Oogane M, Kubota T, Naganuma H and Ando Y, *J. Phys. D: Appl. Phys.* **48** 164012 (2015).
- 52. M.S. Gabor, M. Belmeguenai, T. Petrisor, C. Ulhaq-Bouillet, S. Colis, and C. Tiusan. *Phys. Rev. B* **92**, 054433 (2015) https://doi.org/10.1103/PhysRevB.92.054433
- 53. B. Heinrich, *Phys. Rev. Lett.* **59**, 15 (1987).

- 54. W. Platow, A. N. Anisimov, G. L. Dunifer, M. Farle, and K. Baberschke, *Phys. Rev. B* 58, 9 (1998).
- 55. M. Aftab, G. Hassnain Jaffari, S. K. Hasanain, Turab Ali Abbas, and S. Ismat Shah. *J. Phys. D: Appl. Phys.* **45,** 475001 (2012). http://dx.doi.org/10.1088/0022-3727/45/47/475001.
- 56. M. Aftab, G. Hassnain Jaffari, S. K. Hasanain, T. Ali Abbas, and S. Ismat Shah. *J. Appl. Phys.* **114**, 103903 (2013) . https://doi.org/10.1063/1.4821125.
- 57. M. Obaida, K. Westerholt, and H. Zabel. *Phys. Rev. B* **84**, 184416 (2011) https://doi.org/10.1103/PhysRevB.84.184416.
- 58. L.J. Zhu and J.H. Zhao. Sci. Rep. 7, 42931 (2017). https://doi.org/10.1038/srep42931.
- 59. B.K. Hazra, M.M. Raja, R. Rawat, A. Lakhani, S.N. Kaul, and S. Srinath. *J. Magn. Magn. Mater.* **448**, 371-377 (2018) https://doi.org/10.1016/j.jmmm.2017.04.010.
- 60. B.K. Hazra, S.N. Kaul, S. Srinath, M.M. Raja, R. Rawat, and A. Lakhani. *J. Magn. Magn. Mater.* **481**, 194-202 (2019). https://doi.org/10.1016/j.jmmm.2019.02.081.
- 61. B.K. Hazra, S.N. Kaul, S. Srinath, M.M. Raja, R.Rawat, and A. Lakhani. Phys. Rev. B **96**, 184434 (2017). https://doi.org/10.1103/PhysRevB.96.184434.
- 62. S. Tong, X. Zhao, D. Wei and J. Zhao. *Phys. Rev. B* **101**, 184434 (2020) https://doi.org/10.1103/PhysRevB.101.184434
- 63. D. Bombor, C.G.F. Blum, O. Volkonskiy, S. Rodan, S. Wurmehl, C. Hess, and B. Büchner. *Phys. Rev. Lett.* **110,** 066601(2013) https://doi.org/10.1103/PhysRevLett.110.066601
- 64. Hubert A and Schafer R, "Magnetic Domains—The Analysis of Magnetic Microstructures (Berlin: Springer) (1998)
- 65. Elmers H J, Wurmehl S, Fecher G H, Jakob G, Felser C and Schonhense G. *J. Magn. Magn. Mater.* **758**, 272–276 (2004)
- 66. Wurmehl S et al. *J. Phys. D: Appl. Phys.* **39**, 803 (2006)
- 67. K. Miyamoto, A. Kimura, K. Iori, K. Sakamoto, T. Xie, T. Moko, S. Qiao, M. Taniguchi and K. Tsuchiya. *J. Phys.: Condens. Matter* **16**, S5797 (2004)
- 68. N. D Telling. et al., *Phys. Rev. B* **78**, 184438 (2008)
- 69. Sargolzaei M, Richter M, Koepernik K, Opahle I, Eschrig H and Chaplygin I. *Phys. Rev. B* **74**, 224410 (2006)

- 70. Ambrose T, Krebs J J and Prinz G A. Appl. Phys. Lett. **76**, 3280 (2000)
- 71. Ambrose T, Krebs J J and Prinz G A. J. Appl. Phys. **87**, 5463 (2000)
- 72. Binoy Krishna Hazra, S. N. Kaul, S. Srinath Zaineb Hussain, V. Raghavendra Reddy, M. Manivel Raja. *AIP Advances* **10**, 065017 (2020)
- 73. Uemura T, Yano T, Matsuda K-i and Yamamoto M. Thin Solid Films 515, 8013 (2007)
- 74. Wang W H, Ren X B, Wu G H, Przybylski M, Barthel J and Kirschner J. *IEEE Trans. Magn.* **41,** 2805 (2005)
- 75. Wang W H, Przybylski M, Kuch W, Chelaru L I, Wang J, Lu Y F, Barthel J, Meyerheim H L and Kirschner J. *Phys. Rev. B* **71**, 144416 (2005)

Chapter 2

Experimental techniques

In this chapter, the experimental instruments and techniques used in this work are discussed. DC magnetron sputtering is used to grow the CFAS films. Structural characterization is carried out by X-ray diffraction technique and stoichiometry by energy dispersive X-ray study. Ferromagnetic spectra are recorded using cavity-based X-band FMR and broad band FMR. Temperature dependent FMR is carried out in the temperature range of 120 K to 300 K. Film resistivity is measured using four probe method in a Physical Property Measurement System (PPMS). Magneto optic Kerr effect in the CFAS thin films have been studied by using a L-MOKE setup.

2.1 Sample preparation

2.1.1 Thin film growth using DC magnetron sputtering

In thin films, the surface to volume ratio is large and the surface and interface characteristics become important in deciding the properties of such thin films. As a result, the conditions of the thin film growth, thickness of the film and nature of substrate used on which the films are deposited becomes very important. Thin film is generally grown by two methods, chemical vapour deposition (CVD) and physical vapour deposition (PVD) [1]. Chemical vapour deposition requires a chemical reaction for the films to be grown, while physical vapour deposition is achieved by physical etching of material by ions, lasers, etc., and subsequently deposited on to the substrate.

DC sputtering is a PVD technique which is widely utilized to grow thin films. The process involves the use of a direct current (DC) electric field to generate a plasma in a low-pressure gas environment, the target material is bombarded with high-energy ions generated by the plasma. To deposit the thin film, the target required to be deposited is

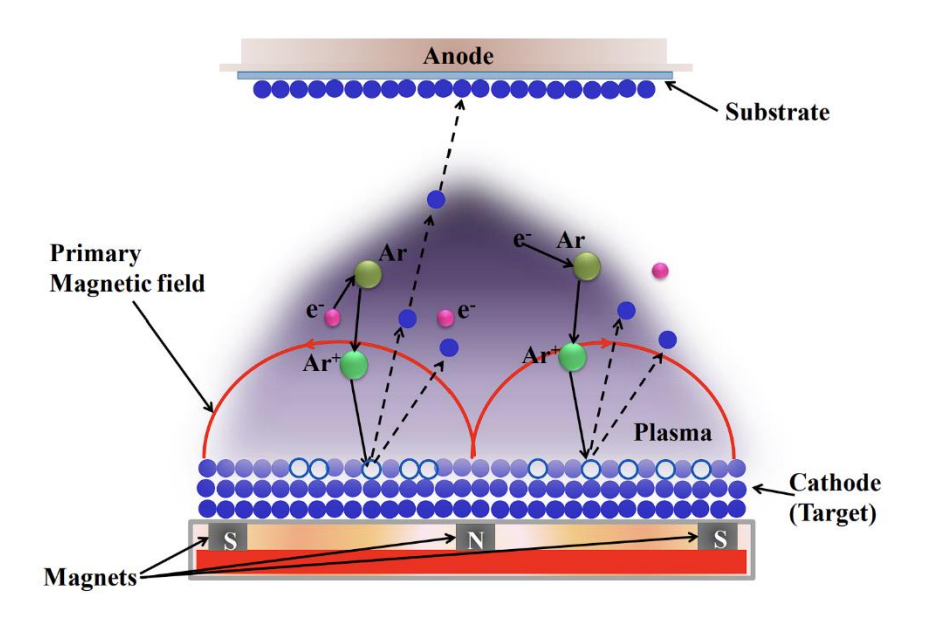


Fig. 2.1: Schematic diagram of sputtering process [2].

fitted to the target holder which acts as the cathode and the substrate is placed at the anode which is in vacuum, inside the deposition chamber. Argon (Ar) gas is introduced into the chamber and then, the voltage is applied between the cathode and the anode. Due to this, the Ar atoms which are inert gas and neutral, gets ionized (Ar⁺) and accelerate towards the cathode, target. The accelerating Ar⁺ ions bombards and sputters the target material which in turn gets deposited on the substrate. The magnetron configuration, distinguished by the incorporation of magnetic fields, enhances the efficiency and uniformity of the sputtering process. The sputtering process is depicted in Fig. 2.1. The advantage in using a magnetron sputtering is the magnetic field around the target material assures that the electrons are confined close to the target, this results in an increased ionization of Ar atoms and hence increased deposition rate can be achieved. Metallic thin films are generally deposited by a DC sputtering but to deposit a dielectric material RF sputtering is utilized. The challenge with dielectric target is the accumulation of charge on the target. The alternating voltage in RF sputtering inverts the cathode and anode periodically resulting in the removal of charge accumulation around the target.





Fig. 2.2: (a) Image of the Ultra-high vacuum DC magnetron sputtering used for depositing CFAS films (b) Target holder with the shutter, inside the main chamber.

The UHV DC magnetron sputtering used for deposition of CFAS films is presented in Fig. 2.2 (a) and (b). The Co₂FeAl_{0.5}Si_{0.5} thin films (CFAS) were grown using ultra-high vacuum (UHV) DC magnetron sputtering instrument (LJ-UHV Technology Co. Ltd.). The main components of the sputtering system include:

- 1. **Main Chamber:** The main chamber is a sealed enclosure where the sputtering process takes place. A very high vacuum environment is maintained inside the chamber. In this system, a base pressure of the order of 10⁻⁸ Torr can be achieved. The main chamber should be free from contamination and impurities. To monitor the film thickness and deposition rate at the time of film deposition, a quartz crystal is positioned inside the main chamber (between the target and the substrate).
- 2. **Load-lock chamber:** The load lock chamber serves in the efficient handling of substrates and acts as a gate-way for the introduction and removal of substrates without compromising the overall vacuum environment. The chamber is maintained at a high vacuum of the order of 10⁻⁶ Torr. The load lock chamber minimizes air exposure, preventing contamination, and ensuring a stable vacuum condition for the main vacuum chamber.
- 3. Vacuum system: Maintaining the desired high vacuum environment is essential for the deposition. A very high vacuum environment assures a stable mean free path for the atoms or particles during deposition. A pressure control system regulates the gas flow and evacuation of the chamber to achieve and sustain the optimal pressure conditions for the sputtering process. In order to achieve this required vacuum, a cryo-pump (which can

- achieve up to 10^{-9} Torr) along with a dry pump is connected to the main chamber. For the load-lock chamber, a turbo-molecular pump ($\sim 10^{-7}$) along with a mechanical pump is used. It should be taken care that a pressure of the order of 10^{-3} must be achieved first using a rotary pump before turning on the turbo-molecular pump.
- 4. **Target holder:** The target material is mounted on the target holder within the vacuum chamber at the cathode and its surface is bombarded by ions (Ar⁺) during the sputtering process. In this sputtering unit, five targets can be loaded at a time which are located at the top of the main chamber. Each target size is 2 inch in diameter. All the targets make an angle of 45° with the normal to the substrate holder ensuring oblique deposition. A shutter is placed for each target which covers the target material and prevents deposition on the substrate during the initial plasma formation process.
- 5. **Substrate holder:** A substrate is the material onto which the thin film is deposited. Depending on the application it can be amorphous or crystalline with specific orientation. The substrate is positioned within the main chamber on the substrate holder. The typical distance between target and substrate holder is 15 cm and the substrate holder can be rotated with different speeds to a maximum value of 20 rpm. The substrate holder also has the provision to heat the substate up to 700 °C.
- 6. **Gas supply system:** A controlled gas supply system introduces a low-pressure inert gas into the vacuum chamber. The gas molecules are ionized to form a plasma, which aids in the sputtering process by providing ions that will bombard the target material, causing it to eject atoms or ions for deposition on the substrate. In this system, three valves are attached to the main chamber which regulates the flow of Argon, Oxygen and Nitrogen gas.
- 7. **DC and RF Power Supply:** The DC power supply applies a voltage between the target material and the substrate. This potential difference creates an electric field that accelerates ions from the plasma towards the target, initiating the sputtering process. In this system, out of five targets, four targets are configured with DC power supply and one target is on RF power supply. The DC power can be varied up to a maximum of 300 Watts and RF up to 250 Watts.
- 8. **Magnetron Configuration:** The magnetron configuration is a distinctive feature of DC magnetron sputtering that involves the use of magnetic fields to trap electrons near the target surface, intensifying ionization and improving the efficiency of the sputtering

- process. The magnetron configuration also contributes to a uniform deposition of material on the substrate. It should be noted that the thickness of the target should be low enough (~ 3 mm) so that the magnetic field lines are present outside the target material
- 9. **Cooling System:** Sputtering generates heat, and it is crucial to maintain stable operating temperatures within the system. An external chiller system is connected to the entire system which circulates de-ionized water to dissipate the heat generated during the sputtering process, preventing overheating and ensuring the longevity of the equipment.
- 10. **Process Monitoring and Control System:** The gas flow, deposition time, voltage, etc., are fully controlled by a LabView program through computer. Modern DC magnetron sputtering systems often incorporate advanced monitoring and control systems. These systems may include sensors for measuring parameters such as deposition rate, film thickness, and other relevant factors. Real-time monitoring allows operators to adjust parameters for precise control over the thin film deposition process.

A single stoichiometric Co₂FeAl_{0.5}Si_{0.5} (CFAS) target was prepared by arc melting. Co, Fe, Al and Si are taken in the stoichiometric ratio and melted several times using arc melting to get the homogeneous ingot. The ingot is then cut into 2 mm thickness. All the CFAS thin films were deposited from a single stoichiometric CFAS target (*Co: 50; Fe: 25; Al: 12.5; Si: 12.5*). In order to optimize the deposition rate, film thickness and composition of the deposited films, sputtering power (30, 50 and 70 W) and Ar pressure (5, 8 and 10 mTorr) have been varied in a wide range.

The base pressure prior to deposition was 3.16×10^{-8} Torr. An optimum sputtering rate of 0.04 nm/sec was achieved at a power of 40 Watt and 2.8×10^{-3} Torr Ar pressure. Before mounting the substrates in the load-lock chamber, they were cleaned thoroughly with acetone and IPA in ultrasonicator for 10 min. The substrates are mounted and then, the remaining native oxide layer on the substrate was removed by etch biasing. The film thickness was measured using a surface profilometer and the deposition rate was optimized by dividing the measured thickness of the films to the total time taken for deposition. First, in order to optimize the film stoichiometry, 100 nm-thick films were deposited on a GaAs (100) substrate at room temperature. The composition of as deposited thin films was checked using energy dispersive x-ray spectroscopy (EDX) attached to a field emission scanning electron microscope (FESEM). Finally, two set of series were grown under the optimised deposition parameters. After cooling the substrate and

CFAS films to room temperature, the deposited films were capped with 2 nm of Ta to prevent oxidation.

- (i) TS series: 50 nm thick $Co_2FeAl_{0.5}Si_{0.5}$ (CFAS) thin films were grown at different substrate temperatures (TS) which can enable the deposited films to be prepared in different anti-site disorder states, TS = room temperature (27°C), 350 °C, 450 °C, 500 °C and 550 °C on two different Si(100) substrates, one with an oxidized 300 nm SiO₂ top layer (SiO₂/Si(100)) and the other without the top SiO₂ layer (only Si(100)). The TS series films constitute the RT, TS350, TS450, TS500 and TS550 CFAS films.
- (ii) *Thickness series*: In this series, 12 nm, 25 nm, 50 nm and 75 nm thick CFAS films were grown under the optimized deposition condition at 500 °C substrate temperature.

2.2 Thin film characterization

2.2.1 Energy dispersive X-ray spectroscopy for composition analysis

Energy dispersive X-ray spectroscopy (EDS) study allows for the identification and quantification of the elements present in a sample. Each element has unique X-ray energies associated with its electronic transitions, enabling the determination of the elemental composition of the material under investigation. A field emission gun is used, in which a very strong electrical field (109 V/m) assist to extract electrons from a metal filament. The high-energy electron beam is directed onto the sample with the help of magnetic lenses. The interaction of the high-energy electron gives rise to either backscattered electrons (BSEs) or secondary electrons (SEs). BSEs are the incident electrons which are scattered by the atom (~100 eV), whereas SEs are the electrons ejected from the sample (~10 eV to 50 eV). Due to higher energy, BSEs are used for the elemental composition contrast. These BSEs are detected using solid state detectors or silicon drift detector.

EDS analyses X-rays emitted from the region of the sample (typically about 1 micron in size). The energy of the emitted X-ray is characteristic of the specific element from which it originates. EDS detectors use Si crystals to detect the X-ray and their energies. The pulse processing electronics converts the charge induced in crystal to EDS spectrum. Peaks in the spectrum correspond to the energies of X-rays emitted by specific elements in the sample, the obtained spectrum is then analysed to determine the elemental composition of the sample. The

intensity of the peaks in the spectrum provides information about the relative abundance of each element [4]. EDS is often employed in conjunction with the Field emission scanning electron microscopy (FESEM) which enables for microscopic imaging of the sample.

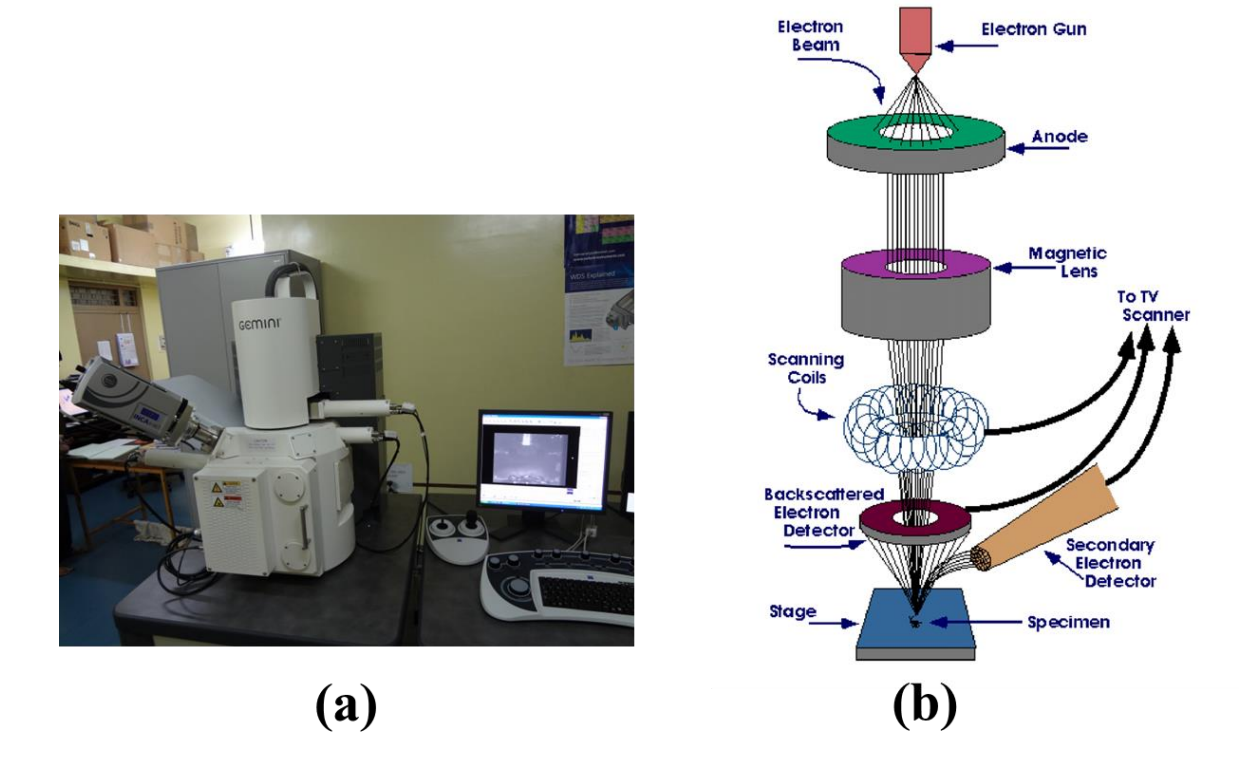


Fig. 2.3: (a) FESEM attached with EDS (b) Schematic diagram of FESEM [3].

The stoichiometry of the as-deposited CFAS films were estimated using an Oxford Instruments EDS which is an attachment to FESEM (Carl Zeiss), Fig. 2.3(a). A block diagram of FESEM is shown in Fig. 2.3(b). For the composition analysis the CFAS films were first deposited on the GaAs substrate. A 10 x 10 mm sampled is used for the measurement. These samples are held on the stabs (sample holder stage) by using a double-sided *Carbon tape*. The measurement is done with a working distance of 8 mm and 20 kV beam energy. The analysis and stoichiometric composition of different elements in the CFAS thin films is presented in chapter 3.

2.2.2 Grazing incident x-ray diffraction for structural characterization

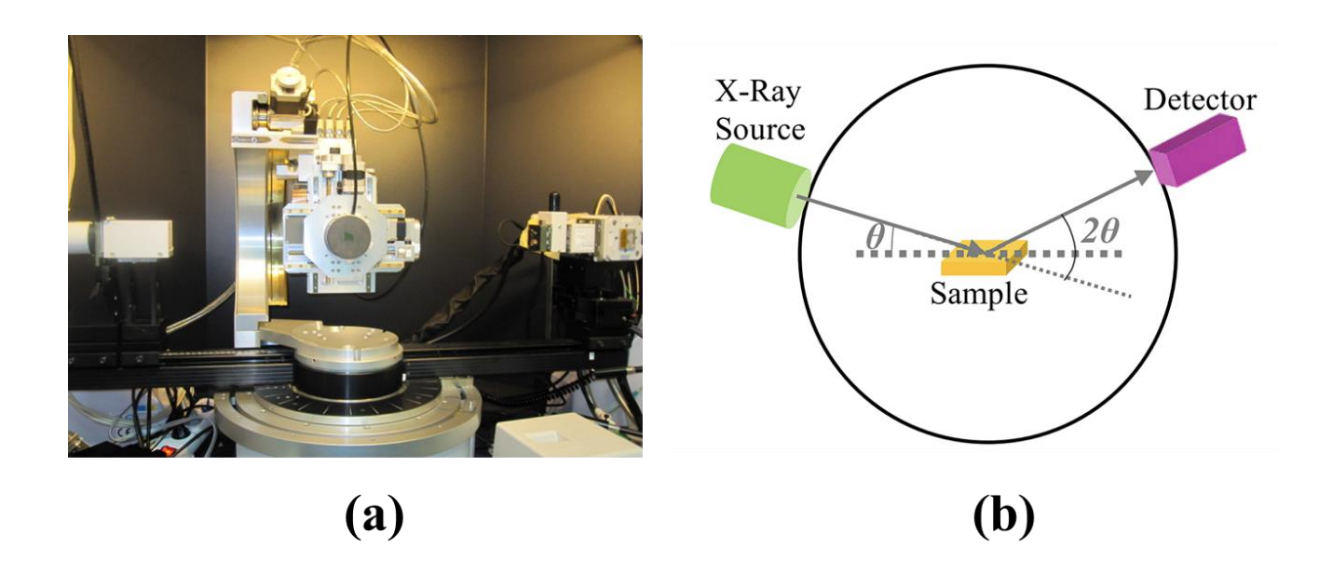


Fig. 2.4: (a) Grazing incident X-ray diffractometer used for structural characterizing of CFAS films, (b) Schematic diagram of an X-ray diffractometer [5,6].

Grazing incident X-ray Diffraction (GIXRD) technique is used to investigate the structural properties of thin films. In GIXRD, the incident X-rays strike the sample surface at an angle, typically less than the critical angle for total external reflection. This geometry maximizes the interaction of X-rays with the surface layers of the sample while minimizing penetration into the substrate. As a result, grazing incidence geometry allows to probe the surface layers of the thin film. Normal X-ray diffraction may be less effective for thin films due to the dominance of signal from the substrate. Thus, GIXRD has an advantage over the normal XRD geometry. A diffraction peak is observed when X-rays scattered by atomic planes undergo constructive interference. Bragg's law defines the condition for this constructive interference as [5, 6]:

$$n\lambda = 2 d_{hkl} \sin \theta_{hkl}$$

Here, θ_{hkl} is the incident angle with respect to the film plane, d_{hkl} is the inter planar distance, n is the order of diffraction and λ the wavelength of X-ray used. The expression for the intensity of X-rays reflected from h, k, l planes is given by,

$$I_{hkl} = K \frac{1 + \cos^2(2\theta)}{4 \sin^2\theta \cos\theta} |F_{hkl}|^2$$

here,
$$F_{hkl} = \sum f_i \exp[2\pi j (hx_i + ky_j + lz_k)]$$

The structure factor F_{hkl} is dependent on the atomic form factor, f_i . Thus, the intensity is sensitive to atomic number and also the difference in the atomic number. Since the Co₂FeAl_{0.5}Si_{0.5} (CFAS) thin films have Co (atomic number = 27) and Fe (atomic number = 26), whose f_i are close, structural characterization by GIXRD technique becomes challenging moreover the intensity observed is also low in thin films.

A Bruker X-ray diffractometer, D8 Discover model, Fig. 2.4(a), schematic diagram of X-ray diffractometer is shown in Fig. 2.4(b), is employed to investigate the structural characteristics of CFAS thin films. The instrument comprises an X-ray tube, gobel mirror, monochromator, cradle sample stage, and detectors. The X-ray tube utilizes a Cu K α source, producing X-rays with a wavelength of 1.54 Å. A dedicated gobel mirror transforms the X-rays into a parallel beam directed onto the film. The cradle sample stage can move along the X, Y, Z directions, rotate 'in-plane' (xy) with the angle (ϕ) ranging from 0° to 360°, and rotate perpendicular to the z-direction with the angle (χ) ranging from 0° to 90°. Sample size of 2 x 2 cm in dimension is used for the measurement. In the GIXRD measurement, a scintillation detector collects the diffracted beam. Throughout the measurement, the incident angle is fixed at 0.6°, and the detector moves from 20° to 90°. Prior to commencing the measurement, the film is meticulously aligned by adjusting the Z-axis, omega (ω), ϕ , and χ . The crystal structure is determined by observing the peak position and intensity from the collected diffraction pattern.

2.3 Electrical resistivity

2.3.1 Physical property measurement system

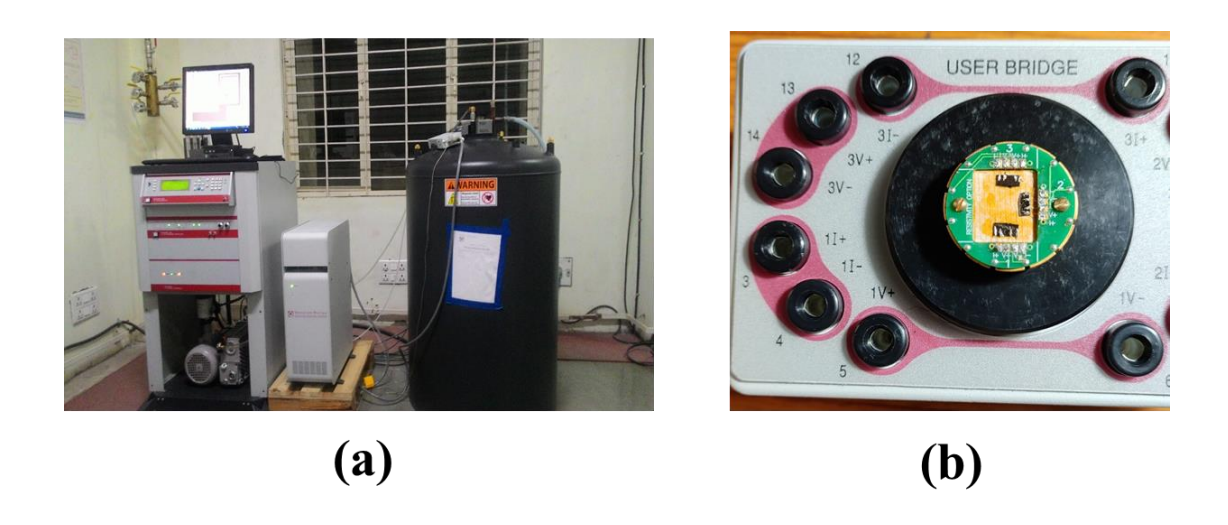


Fig. 2.5: (a) Picture of the PPMS setup (b) Sample puck mounted on a user bridge.

A Physical Property Measurement System (PPMS) provides provision to measure various physical properties of materials at high magnetic fields and with precise temperature control. PPMS systems are equipped with advanced temperature control mechanisms, using cryogenic methods like liquid helium or liquid nitrogen, to achieve temperature range of $2 K \le T \le 350 K$. The system is structured with a superconducting magnet composed of niobium titanium alloy embedded in copper, generating a magnetic field characterized by high homogeneity within the measurement region. This magnet has the capability to apply a static magnetic field during both AC and DC measurements [7]. PPMS facilitates the measurement of physical properties in materials, including magnetization, magneto-transport, specific heat, thermal transport, magnetic susceptibility and more

Electrical resistivities are measured by mounting the CFAS films on a sample puck. A 4 mm in length and 2 mm in film dimension is used on which the electrical contacts were made using Indium and very thin Copper wires are used for leads. 'Zero-field' and 'in-field' electrical resistivity in longitudinal and transverse configurations were measured using four probe setups with an 80 kOe superconducting magnet.

2.4 Ferromagnetic resonance

2.4.1 X-band Cavity ferromagnetic resonance

Ferromagnetic materials are characterized by the alignment of magnetic moments of neighboring atoms or ions, resulting in a net macroscopic spontaneous magnetization. When subjected to an external magnetic field, these magnetic moments tend to align with the field. Ferromagnetic resonance occurs when the material is exposed to both a static external magnetic field (applied DC magnetic field) and a perpendicular alternating magnetic field (AC magnetic field) at a frequency corresponding to the Larmor precession frequency of the magnetic moments.

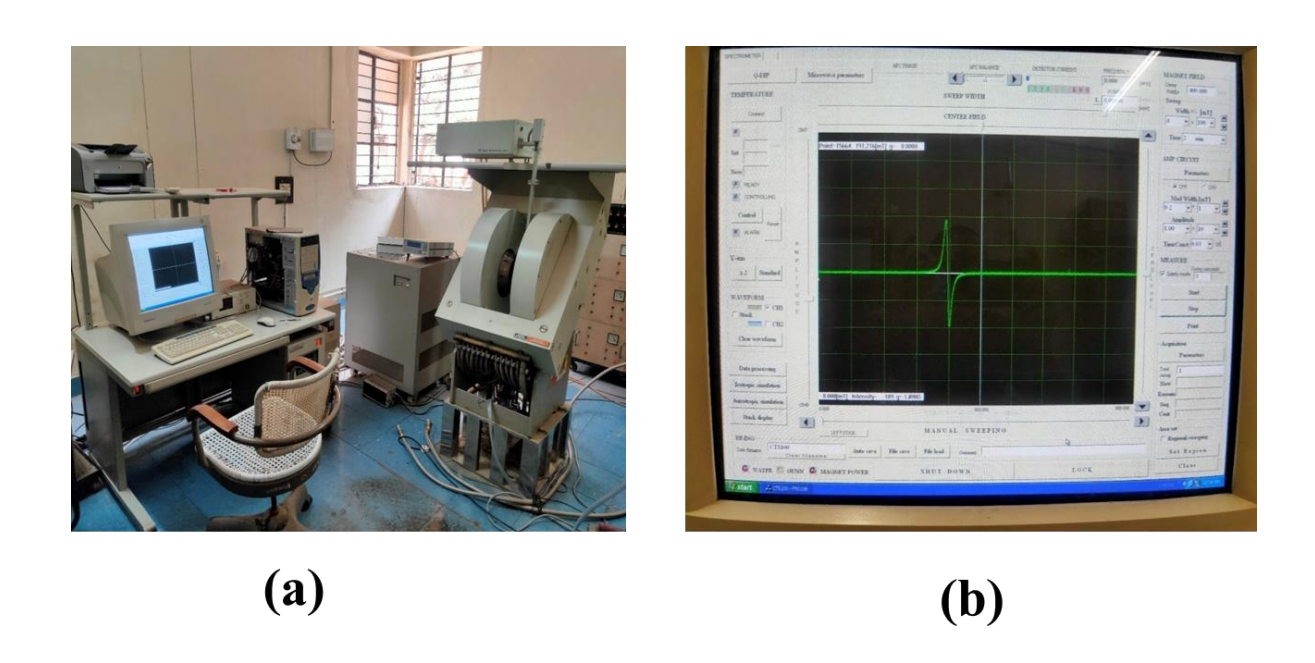


Fig. 2.6: (a) Cavity FMR setup, (b) A typical FMR spectra on an interface.

Under the influence of the external fields, the magnetic moments of the ferromagnetic material start precessing around the direction of the static magnetic field. After the Zeeman split, let the two energy levels be α and β corresponding to $M_S = + \left(\frac{1}{2}\right)$ and $M_S = -\left(\frac{1}{2}\right)$ respectively. The gap between the energy level can be varied with the strength of H. Resonance condition is satisfied when an energy $h\nu$ matches with the splitting energy ΔE , here ν is the frequency of the external radiation, i.e., resonance occur when the frequency of the external AC magnetic field matches the precession frequency of the magnetic moments. At this point, the energy absorption

by the material is maximized, leading to a peak in the absorption or reflection of the incident electromagnetic waves. With AC frequency of 9 GHz, for a typical unpaired electron system, the resonant field (H_r) is 0.3 T [8, 9].

The major components in an FMR setup are listed below:

- 1. **AC source:** The frequency of the AC field used in this experimental set up is in the microwave region of 9.45 GHz which corresponds to 32 mm wavelength. The microwave is generated using a klystron and transmitted into the cavity using a waveguide.
- 2. **Resonant cavity:** The microwave is admitted into the resonant cavity through an iris. The frequency of the source is tuned to the appropriate resonant frequency of the cavity. The corresponding resonant wavelengths are related to the dimensions of the cavity. The optimum operating condition is to maximize the AC frequency at the sample such that the sample sees a homogenous field. At resonance condition, the energy density in the resonance cavity is thousands of times to that in the waveguide, this maximizes the detection of resonant absorption in a sample.
- 3. **Magnetic field:** In FMR experiment, the variations of H correspond to the separation between the energy levels. A Hall sensor is used to measure the magnitude of H. Since every absorption line has a non-zero width, it is taken care that the sample sees a homogenous H which is placed within the cavity.
- 4. **Detector:** In the FMR experiment the AC field is fixed to 9.45 GHz, the static field H is varied and the FMR spectra is recorded. To improve the signal to noise ratio a field modulator is used. The field modulator acts as a frequency chopper and adds an AC component on the static DC magnetic field H which results in an alternating signal at the microwave detector which can be amplified using a narrow-band amplifier. Finally, the resulting signal is rectified and taken on a field dependence which gives the first derivative of the absorption line. The shape of the FMR spectra can be fitted using a Lorentzian function from which the *H_r* and Δ*H* is obtained.

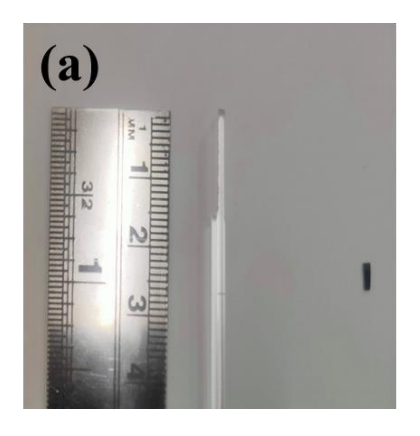






Fig. 2.7: (a) Half-cut quartz rod sample holder, (b) CFAS film placed on the sample holder for measurement, (c) resonance cavity of the FMR setup.

A commercial JEOL-FA200 ESR spectrometer which operates in the X-band of microwave frequency, f = 9.45 GHz, is employed to record the FMR spectra. The sample holder along with the sample and cavity is shown in Fig. 2.6. The CFAS thin films are cut to 3 x 3 mm sizes and placed in the holder. A half-cut quartz rod is used for measurements in *in-plane* configuration and a full rod, where the sample is placed at the base of the rod, is used for *out-of-pane* measurements. A Teflon tape is used to wrap and hold the sample to the holder. A goniometer is attached to the FMR spectra which is held above the resonant cavity, through which the sample is introduced into the cavity. This provides the provision for angular dependent measurements.

2.4.2 Temperature dependent FMR

Ferromagnetic resonance spectra were recorded at different temperatures, from 120 K to 300 K, using an X-band AC frequency of 9.5 GHz. The low temperature is achieved by circulating liquid Nitrogen vapour through the cavity. A controlled flow is regulated by controlling the Nitrogen gas from a pressurized Nitrogen gas cylinder which is introduced into the sealed liquid Nitrogen dewar. The sample is placed inside the cavity through a hollow quartz cylinder, which shields the liquid Nitrogen from the external environment. Once the temperature is stabilized to the required temperature, the FMR spectra is recoded. First, the FMR spectra is recoded during the cooling cycle (300 K to 120 K) by applying the external DC field along the easy magnetization axis (H_r is lowest) and during the warming cycle (120 K to 300 K), along the hard axis.

2.4.3 Broadband ferromagnetic resonance

A coplanar waveguide is composed of a coplanar arrangement of three conductors, these conductors are configured in a ground-signal-ground (GSG) layout on a dielectric substrate. The microwave signal is introduced to the central strip conductor, referred to as the signal line. Meanwhile, the two outer conductors function as ground planes.

A consistent microwave signal is administered to the coplanar waveguide (CPW) and the signal transmitted through the microwave diode is measured by a lock-in amplifier, synchronized to a frequency modulating the external magnetic field. The advantage of employing the CPW-FMR setup lies in its broadband capability (4 GHz to 18 GHz) enabling measurements in both frequency and field domains.

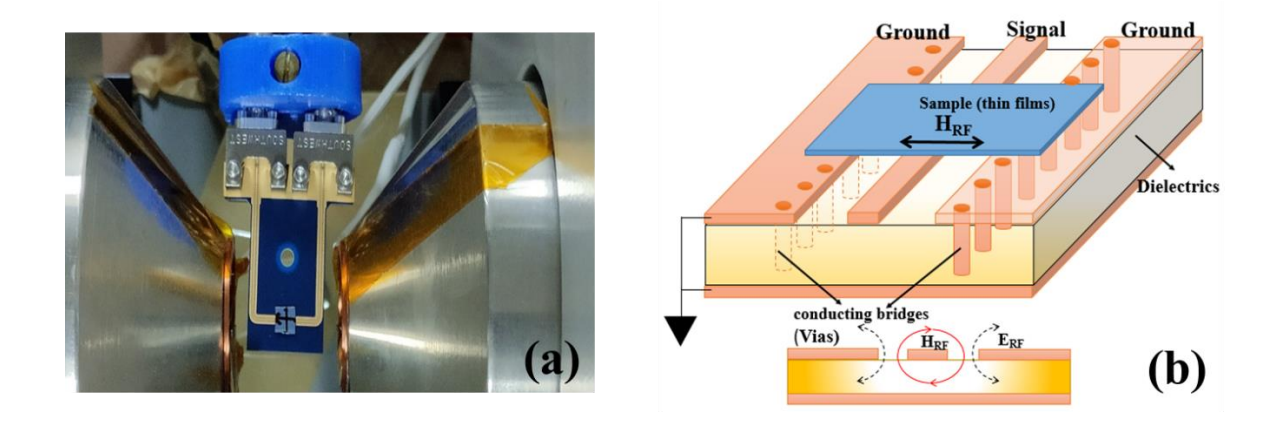


Fig. 2.8: (a) Image of the CPW strip placed between the magnet poles, (b) a schematic diagram of CPW with sample film placed on top of the signal line [10].

The CPW is positioned within the pole gap of an electromagnet generating an in-plane external magnetic field (strength from 0 to 4000 Gauss). The alignment ensures that the magnetic field direction is parallel to the straight section of the transmission line, on which sample is placed. The CPW receives a microwave (RF) signal from the microwave generator, allowing the propagation of the signal through the CPW and generating a microwave magnetic field (H_{Rf}). When the magnetic film is exposed to H_{Rf} , at the resonance condition microwave power is absorbed and consequently the transmitted microwave signal is reduced. The microwave diode at the input transforms the transmitted signal into DC voltage at the output. Generally, the DC voltage from the microwave diode output is sensitive to both input microwave power and frequency, this

may generate nonlinear background signals and parasitic signals that are independent of the magnetic properties of the sample. The signal-to-noise ratio (SNR) is enhanced by suppressing undesired non-magnetic signals through a field modulation [10].

The CFAS thin films for characterization were cut into 5 x 5 mm sizes, which are placed carefully on top of the waveguide. The measurement was carried out in *in-pane* (IP) configuration (IP) i.e., the external static magnetic field (H) is applied along the film plane and correspondingly, perpendicular to the microwave field (AC field). To ensure that the FMR spectra is measured along the easy-axis of magnetization, the spectra is recorded initially at varying IP angles with respect to the H, following which, the direction where the minimum H_r is obtained is taken as the IP easy axis.

2.5 Magneto Optic Kerr Effect.

The phenomena in which there is a shift in the polarization of the reflected light when it falls on a magnetized material is known as Magneto-optical Kerr effect (MOKE). Its difference with the Faraday effect is that in Faraday effect there is a change in polarization as the light passes through the magnetized material [12]. Depending on the configuration of the direction of incident plane of light and the easy axis of sample magnetization, Kerr effect can be carried out in three configurations. (i) Longitudinal Magneto-optical Kerr effect (L-MOKE), in this the incident plane of light is applied parallel to the magnetization direction which is along the plane of the film. (ii) Transverse Magneto-optical Kerr effect (T-MOKE), when the incident plane of light is perpendicular to the magnetization of the sample and the magnetization is along the film plane (iii) Polar Magneto-optical Kerr effect (P-MOKE) in which the magnetization of the sample is perpendicular to the film plane and the incident light is applied parallel to it. Thus, films with inplane magnetic anisotropy can be characterized using L-MOKE or T-MOKE and films with perpendicular magnetic anisotropy though P-MOKE.

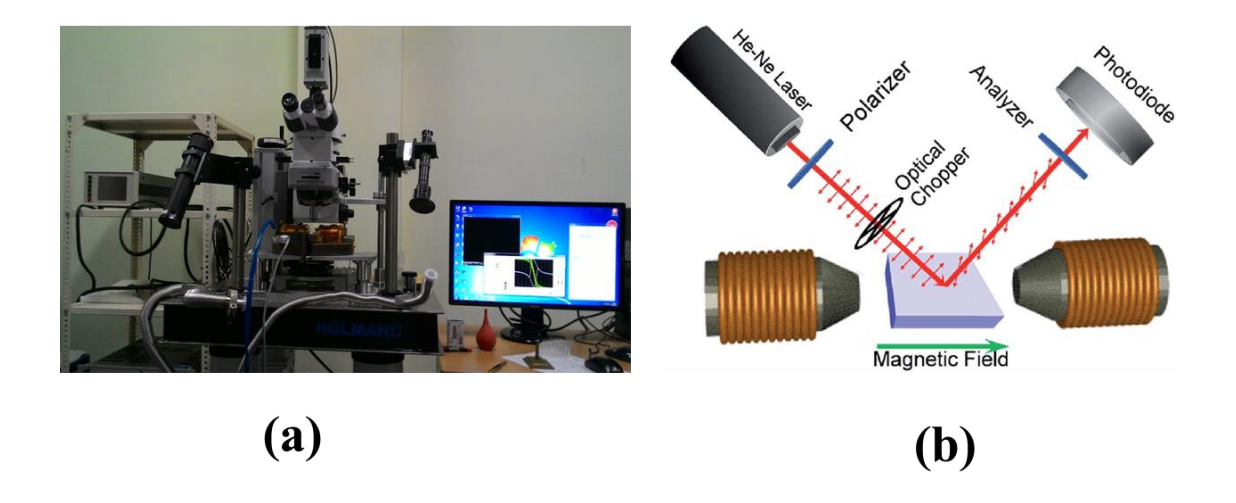


Fig. 2.9: (a) Photograph of MOKE setup used for CFAS films under study, (b) Schematic diagram of MOKE experimental setup [11].

A plane polarized light when incident on a magnetized material, after interaction with the sample, the polarization of the reflected light is shifted. The in-phase component of the reflected light is changed giving rise to the Kerr rotation and the Kerr ellipticity is given by the out-of-phase component of reflected light [13]. The Kerr rotation which is directly proportional to the sample magnetization, is recorded by measuring the change in reflected intensity by allowing the reflected light to pass through an analyser to a photo-diode.

The Kerr-hysteresis loops are recorded and domain images are captured, by rotating the CFAS films at different angles, using a longitudinal Kerr-microscopy attached with a magnetometer system, made by Evico Magnetics, Germany. The MOKE setup employs an LED for the light source, a moveable sample stage on which sample is placed, a double microscope capable of low and high resolution for capturing the change in magnetic domain images and the electromagnet that is rotatable for L-MOKE or T-MOKE configuration. The LED light source is fixed at 430 nm wavelength and a 1 x 1 cm CFAS sample is placed on the sample holder which can be rotated with an angle accuracy of 1°. To make sure that there is no remnant magnetization the film is first exposed to an AC field. Then the Kerr hysteresis loops are measurement in DC field of ± 100 Oe. For mapping a larger area (30 × 30 mm to 8 × 8 mm) domain pattern a low-resolution microscope is employed and for area of 100 μ m × 100 μ m to 300 × 300 nm a high-resolution microscope is used. For the CFAS films, the scan area was over 300 μ m × 300 μ m and

20X lens has been used. Both the Kerr hysteresis loops and the magnetic domain images are recorded simultaneously.

References:

- 1. S. Rossnagel, "Handbook of Thin-Film Deposition Processes and Techniques," 319 (Noyes Publications) (2002).
- 2. Chandrima Banerjee, Ph. D thesis, "Experimental Study of Spin Waves in Magnetic Thin Films and Nanostructures" Chapter 3, (2017)
- 3. Aref Saleh Baron, Ph. D thesis "Synthesis and Characterization of methyl ammonium lead trihalide Perovskite Compounds and their Applications in Photonic Devices" Chapter 3, (2019)
- 4. R. Wiesendanger, "Scanning Probe Microscopy and Spectroscopy", Cambridge University Press, Cambridge, UK (1994).
- 5. B. D. Cullity, "Elements of X-ray diffraction", Addison-Wesley publishing company, United States of America (1956).
- 6. Toru Mitsunaga, "x-ray thin-film measurement techniques II" The Rigaku journal, **25**(1) (2009)
- 7. Physical Property Measurement System (PPMS), User's Manual, Quantum Design, San Diego, CA, USA, 1084-100A, (2009).
- 8. K. K Darrow, "Magnetic Resonance", Pg. 74 99, (1953).
- 9. Allan H. Morrish, "The Physical Principles of Magnetism: Wiley-IEEE Press, pg. 106 111 (2001)
- 10. Han Kyu Lee, Ph. D thesis "Magnetic Anisotropy, Damping and Interfacial Spin Transport in Pt/LSMO Bilayers", Chapter 2, (2017)
- 11. R. Ciprian, P. Torelli, A. Giglia, et al. "New strategy for magnetic gas sensing" *RSC Advances* **86**, (2016)
- 12. A. Hubert and R. Schfer, Magnetic, "Domains: The Analysis of Magnetic Microstructures" Springer, Berlin (2009).
- 13. Manna Ali, Ph. D thesis, "Growth and study of magnetostrictive FeSiBC thin films for device application" (1999).

Chapter 3

Structure and surface morphology of Co₂FeAl_{0.5}Si_{0.5} Heusler alloy thin films

In this chapter, the effect of deposition temperature and film thickness on the structure and surface morphology of the $Co_2FeAl_{0.5}Si_{0.5}$ Heusler alloy thin films is discussed.

3.1 Experimental details

Grazing incidence x-ray diffraction (GIXRD) technique has been used to investigate the crystal structure of the $Co_2FeAl_{0.5}Si_{0.5}$ (CFAS) Heusler alloy thin films. GIXRD patterns were recorded at a grazing angle of 0.5° using Bruker D8 Discover X- ray diffractometer, with a Cu K_{α} source of wavelength 1.546 Å. The stoichiometry of the deposited CFAS films was optimized using energy dispersive x-ray spectroscopy (EDS) with micro-imaging capability provided by the Carl Zeiss field emission scanning microscope (FESEM) to which the EDS accessory is attached.

3.2 Crystallographic structure of the Heusler compound

The type of atomic structure (L2₁, B2, A2) and the strength of anti-site disorder in X₂YZ Heusler alloys is known to affect the density of states (DOS) at the Fermi energy (\in_f), which, in turn, influences the half-metallic property of full Heusler alloys [1, 2].

Depending on the amount of atomic site-disorder present, full Heusler X_2YZ alloys can exist in one of the three structures: L2₁, B2, A2 [3-5]. The structural properties of these systems are commonly studied using X-ray diffraction techniques. L2₁ structure is characterized by the superlattice reflections for which all the Miller indices (h k l) are odd, e.g., (111), (311). By contrast, B2 structure forbids odd superlattice reflections and only permits the even superlattice reflections satisfying the relation (h + k + l) = 4n + 2 (where n is an integer), e.g., (002), (222). A2 structure is marked by the absence of both odd and even superlattice reflections. Irrespective of the type of structure (L2₁ or B2 or A2), the underlying cubic structure manifests itself in the fundamental Bragg diffraction peaks, with the Miller indices obeying the relation (h + k + l) = 4

[6-8], e.g., the reflections (220), (400), (422). Furthermore, the site exchange between the X and Y atoms gives rise to DO₃ disorder [9]. Such a disorder is difficult to detect using Cu X-ray source in Co-Fe based full Heusler alloy because the atomic scattering factors of Co and Fe are similar to each other.

3.3 Structural investigation

3.3.1 Effect of deposition temperature

A single stoichiometric CFAS target (Co: 50; Fe: 25; Al: 12.5; Si: 12.5) was used to grow the films by DC magnetron sputtering. The base pressure in the sample chamber, prior to deposition, was 4×10^{-8} Torr. Composition of the CFAS thin films was determined by the energydispersive X-ray spectroscopic (EDS) attachment of the field emission scanning electron microscope (FESEM). The stoichiometry of the CFAS thin films was initially optimized using the films grown on GaAs substrates. The reason behind the choice of this substrate is that the desired thin film CFAS contains Si element which makes it difficult for composition analysis during EDS data quantification or analysis since the intensity count for the Si element will come from both the CFAS film as well as the Si substrate. Hence, the GaAs substrate helps to avoid this complication. 1 x 1 cm GaAs substrates were cleaned thoroughly with acetone and then with IPA in ultrasonicator for 10 min, after which the substrate was mounted into the vacuum chamber. The composition of the CFAS thin films was optimized close to the target composition by varying the power and argon pressure one at a time. Sputtering rate plays a very crucial role in optimizing the film deposition. First, the DC gun power is kept fixed, then the Ar pressure is varied to get the plasma and get a uniform sputtering rate for the CFAS film deposition, then the films are taken for composition analysis. This process is repeated over until the desired stoichiometry of the CFAS film is obtained (Table 3.1). To maintain the uniformity of the CFAS film deposited on the substrate, the substrate holder is rotated at 10 RPM.

To determine the stoichiometry and homogeneity a set of five different regions of the films are focused for scan, Fig. 3.1 (a) shows one such area where the sample has been scanned over a 6 μ m x 6 μ m area. Finally, the readings from the different regions are averaged. An optimum sputtering rate of 0.04 nm/sec was achieved at a DC power of 40W and 5 x 10⁻³ Torr argon pressure. Since GaAs cannot withstand deposition at higher temperature (TS > 500°C), the final depositions

are carried out on Si(100) substrates with and without a buffer layer of oxidized 300 nm SiO₂ layer, as shown in a schematic diagram in Fig. 3.2 (a) and (b). EDS analysis yielded the atomic composition of the as-deposited films as Co: 50.13, Fe: 24.50, Al: 12.82, Si: 12.54; EDS image is shown in Fig. 3.1(b). The final deposited films were then capped with a 4 nm Ta layer to protect the CFAS film from oxidation.

Table 3.1: Lists out the deposition parameter optimization process by varying DC power, Ar pressure and the corresponding atomic percentage for different depositions.

Sample	Power	Ar	Thickness	Rate of	Atomic Percentage (%)			
ID	(Watt)	pressure	from	deposition				
		(mTorr)	profilometer	(nm/sec)				
			(nm)					
					Co	Fe	Al	Si
D12A	70	5	150	0.077	48	24	14	14
D12B	70	8	167	0.062	50	23	13.5	13.5
D12C	70	10	190	0.058	50	23	13.5	13.5
D24A	50	5	125	0.038	50	24.5	12.8	12.5
D24B	50	8	160	0.039	50	23	13.5	13.5
D24C	50	10	195	0.041	49	24	13.5	13.5
D37A	30	5	100	0.018	47	21	16	16
D37B	30	8	107	0.023	46	23	15.5	15.5
D37C	30	10	112	0.022	48	22	10	10

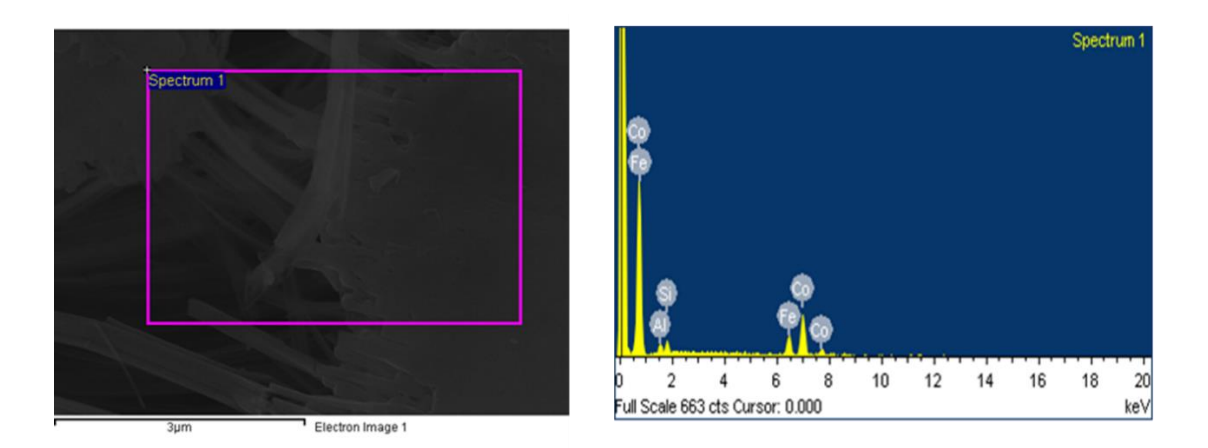


Fig. 3.1: (a) Surface of the CFAS thin film where the sample has been scanned over a rectangular area for EDS, and (b)the intensity or count of the Co, Fe, Si and Al elements from the CFAS thin film with their corresponding energy (in keV).

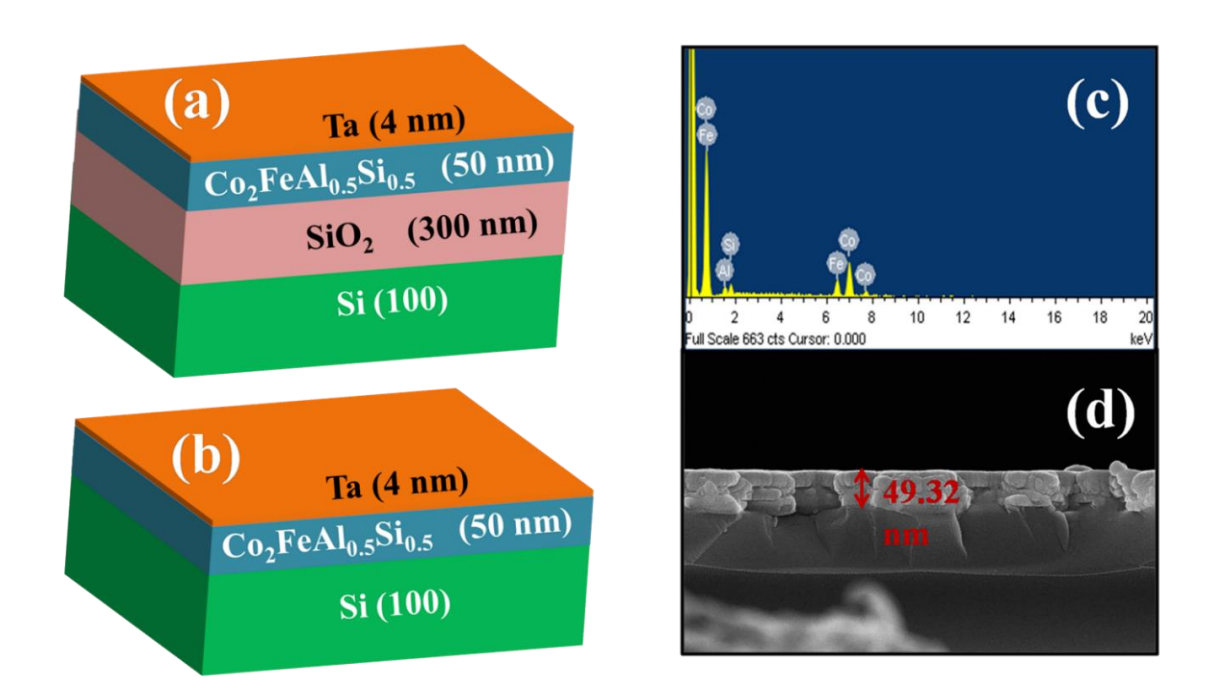
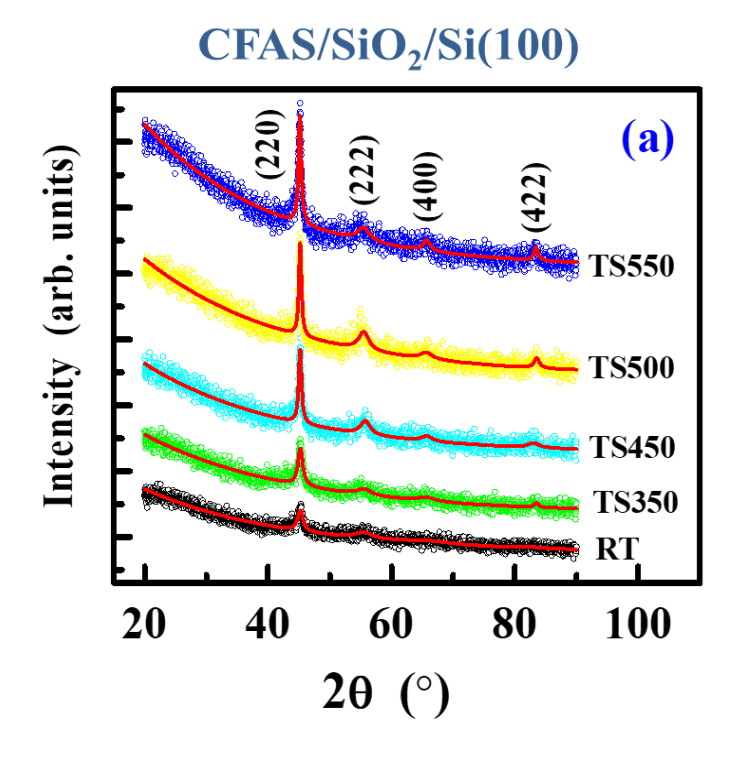


Fig. 3.2: (a) and (b): Schematic sketch of the film with and without the SiO_2 buffer layer in between the Si(100) substrate and the film. (c) EDS image of the as-deposited films indicating their chemical composition. (d) Cross-sectional FESEM image facilitating the visualization of the film thickness and the film-substrate interface.



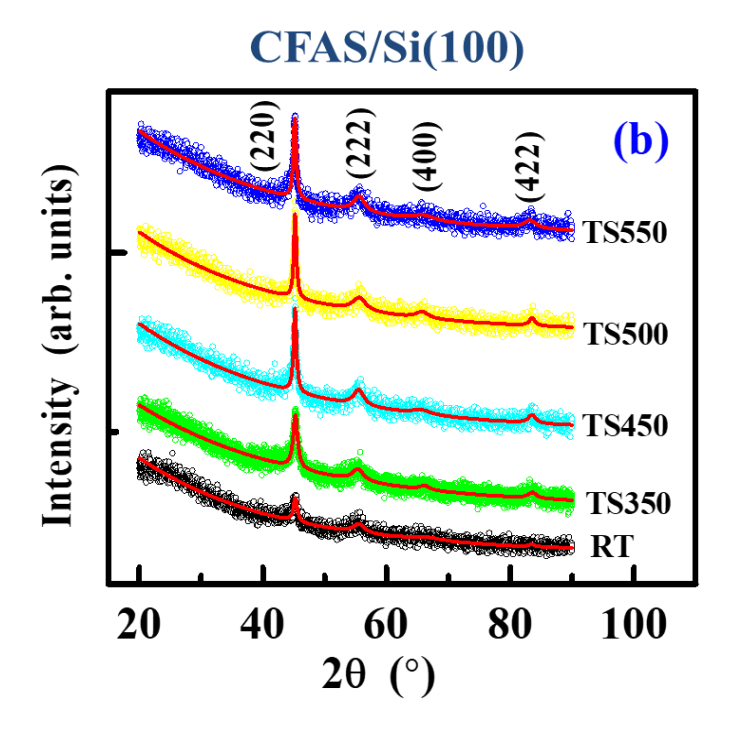


Fig. 3.3: Grazing incidence X-ray diffraction patterns of 50 nm thick $Co_2FeAl_{0.5}Si_{0.5}$ thin films deposited at substrate temperatures 27 °C, 350 °C, 450 °C, 500 °C and 550 °C on (a) $SiO_2/Si(100)$ and (b) Si(100) substrates.

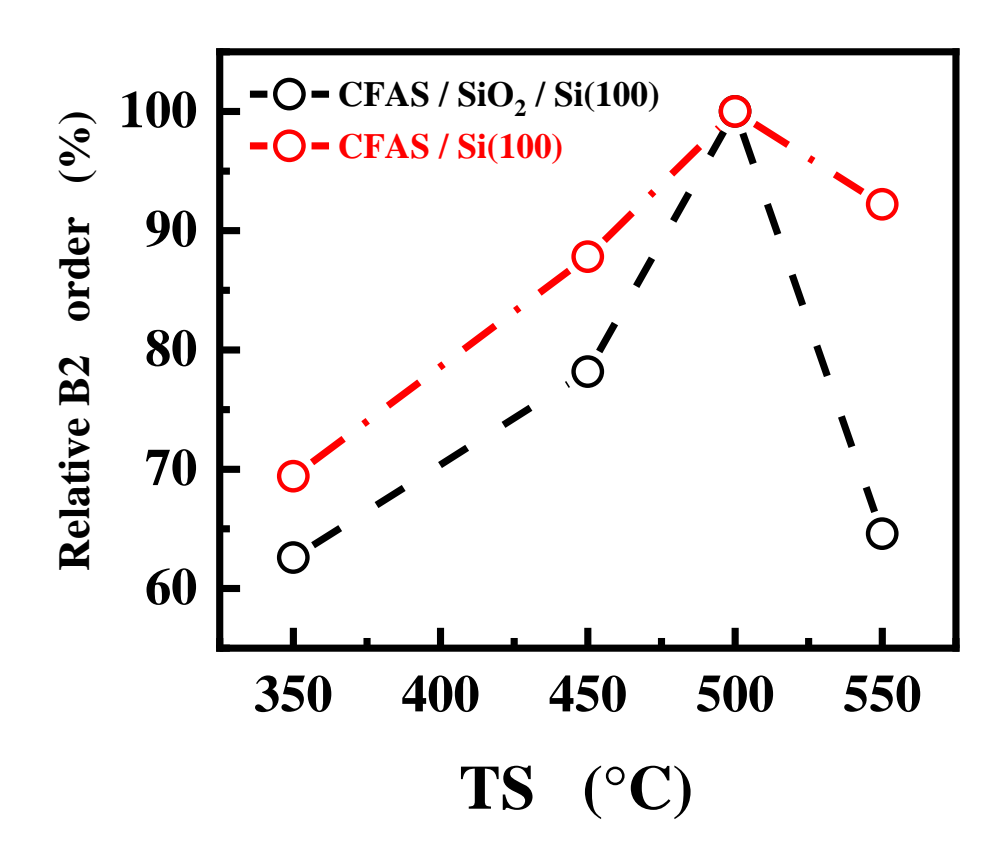


Fig. 3.4: The degree of atomic site order in B2 structure in the CFAS thin films, deposited on $SiO_2/Si(100)$ and Si(100) substrates, at different substrate temperatures.

Thin films of Co₂FeAl_{0.5}Si_{0.5} are grown at different substrate temperatures (i.e RT, TS350, TS450, TS500 and TS550) under the optimum stoichiometric conditions to tune the anti-site disorder.

The GIXRD patterns of the RT, TS350, TS450, TS500 and TS550 CFAS thin films, deposited at 27 °C, 350 °C, 450 °C, 500 °C and 550 °C on the Si(100) substrate with and without SiO₂ buffer layer are shown in Fig. 3.2 (a) and (b). Absence of the *odd* Bragg superlattice reflections such as (111), (311) completely rule out the presence of L2₁ structure in the CFAS thin films in question. Observation of the *even* superlattice reflection (222) in all the CFAS films, on the other hand, provides a strong evidence for the existence of B2 structure. The Bragg peaks, corresponding to the fundamental reflections (220), (400) and (422), progressively pick up in intensity as the substrate temperature increases from 27 °C to 550 °C. This observation implies that the crystalline order in the system improves with increasing substrate temperature [10,11] because the atoms have sufficient energy to move around and settle into their designated atomic sites. The percentage of relative B2 atomic order present in a given film is estimated by the integrated intensity ratio, $\frac{\binom{I^{(222)}}{I_{I}(220)}}{\alpha}$, where $\alpha = \binom{I_{I}(222)}{I_{I}(220)}$ It is evident from Fig. 3.4 that, (i) among all the CFAS films, the TS500 film with or without the SiO₂ buffer layer has the highest atomic site order (or equivalently, the least Y, Z anti-site disorder) within B2 structure and (ii) barring the TS500 film, the SiO₂ buffer layer reduces (B2) atomic site order in all other films.

3.3.2 Effect of film thickness

Fig. 3.5 shows the GIXRD patterns for the CFAS films of varying thickness, grown at 500 °C substrate temperature. Irrespective of the film thickness, the fundamental diffraction peaks (220), (400) and (422) are observed (even in the film of the lowest thickness 12 nm) which confirms the presence of underlying crystal structure in the system. For the films with t = 12 nm, 25 nm and 50 nm, in addition to the fundamental diffraction peaks, pronounced superlattice reflection (222), characteristic of B2 structure, is observed. The existence of (222) reflection indicates the presence of anti-site disorder where Fe and (A1, Si) atoms have partially exchanged their atomic sites [12]. An exception is the t = 75 nm film, where the (222) diffraction peak is not observed, but the fundamental diffraction peaks ((220), (400) and (422)) are still present, suggesting that the film with t = 75 nm has disordered A2 structure in which the Co, Fe and (A1, Si) atoms randomly occupy the X, Y and Z atomic sites.

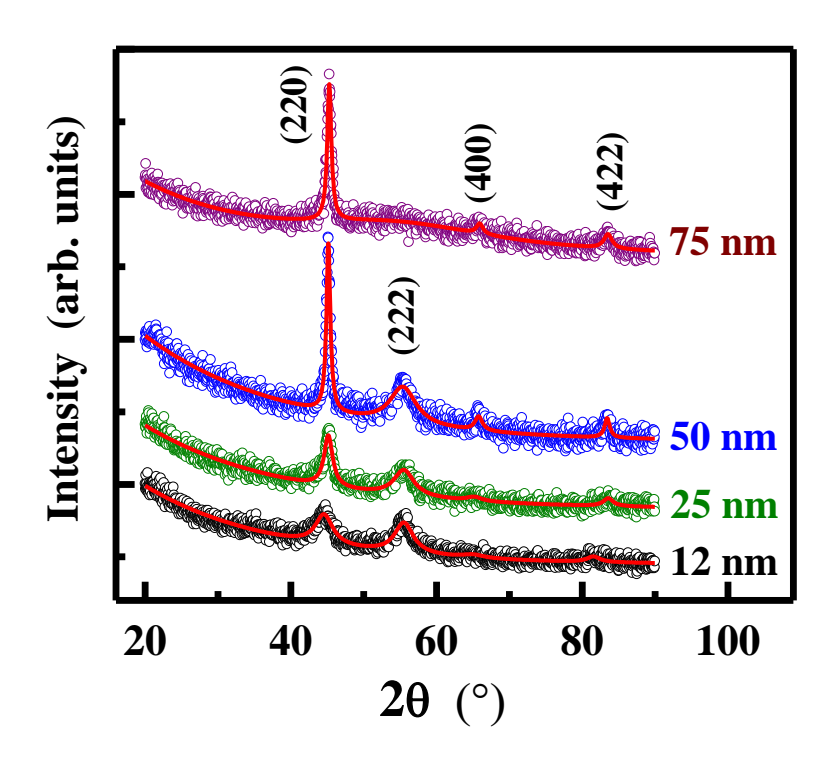


Fig. 3.5: GIXRD diffraction pattern for 12 nm, 25 nm, 50 nm and 75 nm CFAS films.

3.4 Conclusion

Co-based Heusler compound, Co₂FeAl_{0.5}Si_{0.5} (CFAS) thin films with varying degree of site-disorder were optimized by depositing on the Si(100) substrates with or without a 300 nm SiO₂ top layer using high vacuum DC magnetron sputtering. The stoichiometry of the deposited films has been confirmed using EDS. Irrespective of deposition temperature, detection of the (222) diffraction peak in all the films asserts the existence of B2 structure order with partial interchange of Fe and (Al, Si) atoms. The integrated intensity ratio goes through a peak at TS500 and the SiO₂ buffer layer reduces (B2) atomic site order in all other films. In the thickness series, the 12 nm, 25 nm and 50 nm films have B2 structure order while the 75 nm film shows A2 disorder.

References

- 1 G.H. Fecher and C. Felser, Substituting the main group element in cobalt—iron based Heusler alloys: Co2FeAl1-xSix, J. Phys. D: Appl. Phys. 40 (2007)1582. http://dx.doi.org/10.1088/0022-3727/40/6/S12.
- 2. B. Balke, G.H. Fecher, and C. Felser, Structural and magnetic properties of Co2FeAl1-xSix, Appl. Phys. Lett. 90(2007) 242503. https://doi.org/10.1063/1.2748341.
- 3. Lanuakum A Longchar, Mainur Rahaman, Binoy Krishna Hazra, R. Rawat, M. Manivel Raja, S.N. Kaul and S. Srinath. "Resistivity minima in disordered Co2FeAl0.5Si0.5 Heusler alloy thin films" Journal of Magnetism and Magnetic Materials 569 (2023) 170439.
- 4. C. Felser, L. Wollmann, S. Chadov, G.H. Fecher, and S.S. P. Parkin, Basics and prospective of magnetic Heusler compounds, APL Mater. 3 (2015) 041518. https://doi.org/10.1063/1.4917387.
- 5. I. Galanakis, P.H. Dederichs, and N. Papanikolaou, Slater-Pauling behavior and origin of the half-metallicity of the full-Heusler alloys, Phys. Rev. B 66 (2002) 174429. https://doi.org/10.1103/PhysRevB.66.174429.
- 6. K.R.A. Ziebeck and P.J. Webster, A neutron diffraction and magnetization study of Heusler alloys containing Co and Zr, Hf, V or Nb, J. Phys. Chem. Solids 35 (1974) 1-7. https://doi.org/10.1016/0022-3697(74)90002-X.
- 7. T. Saito, N. Tezuka, and S. Sugimoto, Structural and magnetic properties of Co2FeAl 0.5Si0.5 full-Heusler alloy thin films on GaAs substrates, Materials Transactions 52 (2011) 370–373. https://doi.org/10.2320/matertrans.MBW201004.
- 8. P.J. Webster and K.R.A. Ziebeck, Magnetic and chemical order in Heusler alloys containing cobalt and titanium, J. Phys. Chem. Solids 34 (1973)1647-1654. https://doi.org/10.1016/S0022-3697(73)80130-1.
- 9. Y. Takamura, R. Nakane, and S. Sugahara, Quantitative analysis of atomic disorders in full-Heusler Co2FeSi alloy thin films using X-ray diffraction with Co K α and Cu K α sources, J. Appl. Phys. 107 (2010) 09B111. https://doi.org/10.1063/1.3350914.

- 10. A.A. Lotin, O.A. Novodvorsky, D.A. Zuev, O.D. Khramova, L.S. Parshina, F.V. Lebedev, J.W. Bartha, and C. Wenzel, Influence of growth temperature on physical properties of ZnO films produced by pulsed laser deposition method, Opt. Mater. 35 (2013)1564-1570. https://doi.org/10.1016/j.optmat.2013.03.027.
- 11 M. Ohring, Materials Science of Thin Films, 2nd Edition. Academic press (2002) 520.
- 12. Lanuakum A. Longchar, Mainur Rahaman, Binoy Krishna Hazra, M. Manivel Raja, R. Rawat, S. N. Kaul and S. Srinath. "Effect of film thickness on the electrical transport in Co2FeAl0.5Si0.5 thin films", AIP Advances 13, (2023) 025106. https://doi: 10.1063/9.0000486.

Chapter 4

Effect of deposition temperature and film thickness on electrical resistivity and magnetoresistance in Co₂FeAl_{0.5}Si_{0.5} thin films

In this chapter, the effect of disorder and film thickness on electrical resistivity of Co₂FeAl_{0.5}Si_{0.5} thin films is clearly brought out from a systematic study of "zero-field" and "in-field" electrical resistivity as a function of temperature. The different scattering mechanisms responsible for the electrical resistivity have been extracted through a detailed analysis based on the theoretical models for electrical transport proposed in the literature. Furthermore, the mechanisms responsible for the magnetoresistance have also been studied. A negative anisotropic magnetoresistance has been observed.

4.1 Experimental details

Zero-field resistivity, ρ (T, H = 0), and *In-field* resistivity, ρ (T, H = 80 kOe), have been measured as a function of temperature, using the four-probe setup. ρ (T, H = 80 kOe) measurements were carried out in two geometries: (i) *Longitudinal configuration*, ρ^{\parallel} (T, H = 80 kOe), where both the current and magnetic field point in the same direction within the film plane, as shown in Fig. 4.1(a); (ii) *Transverse configuration*, ρ^{\perp} (T, H = 80 kOe), in which the current direction lies in the film plane while the magnetic field is applied perpendicular to the film plane, as depicted in Fig. 4.1(b).

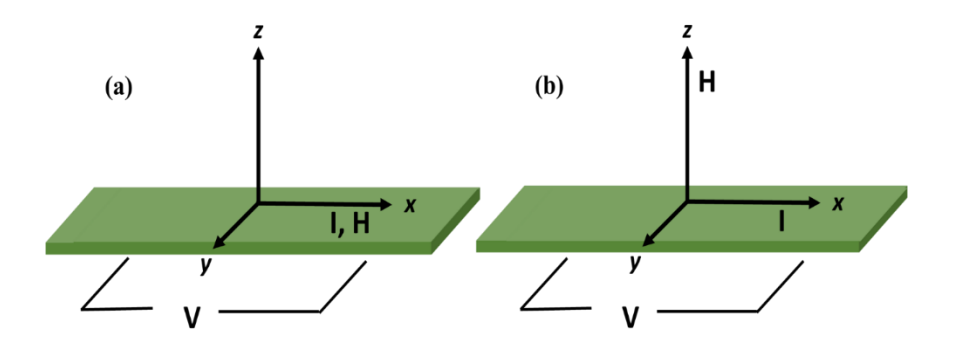


Fig. 4.1: Schematic diagram for the electrical resistivity measurement in the (a) Longitudinal configuration (b) Transverse configuration

4.2. Resistivity mechanisms at $T < T_{min}$

4.2.1 Scattering involving Kondo spin-flip/two-level tunnelling states/diffusons

The primary factors influencing the electrical resistivity in most metals at low temperatures is the scattering of conduction electrons from the impurity atoms as well as imperfections, present within the lattice structure [1]. In various disordered systems like amorphous ferromagnets [2–5] and disordered Heusler alloys [6], a logarithmic temperature dependence of electrical resistivity is observed at low temperatures. The observed phenomena can be explained either by i) single-channel Kondo spin-flip scattering [7,8], where the conduction electrons interact with a magnetic impurity having an unpaired electron spin, or ii) scattering from two-level tunneling states (TLS) [9,10], where localized defects or imperfections create additional energy levels that can interact with conduction electrons, or iii) the two-channel orbital Kondo effect for $T > T_K$, where T_K denotes the Kondo temperature [11–15] or iv) scattering of conduction electrons by *diffusons*, which are non-propagating longitudinal spin fluctuations [16]. The contribution to electrical resistivity at low temperatures from each of these scattering mechanisms is given by

$$\rho_{r}(T) = -\delta_{r} \ln T \tag{4.1}$$

In Eq. (4.1), δ_x is a direct measure of the magnitude of Kondo spin-flip, TLS or electron-diffuson scattering.

4.2.2 Enhanced electron-electron interaction (EEI)

At very low temperatures, disordered systems experience enhanced electron scattering, which, in turn, hinders the ability of electrons to effectively screen or shield one another, resulting in a significant increase in the electron-electron interaction (EEI) [17–19]. The contribution of enhanced electron-electron interaction (EEI) to resistivity in three-dimensional (3D) disordered systems can be expressed as follows [7,18]

$$\rho_{EEI}(T, H) = -\gamma_{EEI} T^{1/2} \tag{4.2}$$

here,

$$\gamma_{EEI} = \rho^2(0) \left(\frac{e^2}{4\pi^2\hbar}\right) \left(\frac{1.3}{\sqrt{2}}\right) \left(\frac{4}{3} - \frac{3}{2}F_\sigma\right) \left(\frac{k_B}{\hbar D_i}\right)^{\frac{1}{2}}$$
(4.3)

 D_i is the electron-diffusion constant and F_{σ} is the screening factor for coulomb interaction. Interestingly, the $-T^{1/2}$ power law is also predicted by the two-channel orbital Kondo model for $T < T_K$ [11–15].

4.2.3 Weak localization/quantum interference effect

In disordered systems, multiple elastic scattering at extremely low temperatures results in a phase *coherence* between the partial waves scattered from the nearby lattice ions which enhances the probability for an electron to return to its origin [18,20]. This phenomenon is termed as the weak-localization (WL) or *quantum interference* (QI) effect [3,4,20]. As temperature increases, various inelastic scattering processes come into play and progressively delocalize electrons by destroying the phase coherence. Depending upon the nature of inelastic scattering mechanism and the lattice dimensionality, the WL contribution varies as $T^{-p/2}$, - lnT and - $T^{p/2}$ for 1D, 2D and 3D disordered systems. The expression for WL in 3D systems is

$$\rho_{wl}(T, H) = -\xi_{WL} T^{p/2} \tag{4.4}$$

where

$$\xi_{WL} = \rho^2(0) \left(\frac{e^2}{\pi^2 \hbar}\right) \left(\frac{1}{\alpha}\right) \tag{4.5}$$

In Eq. (4.4), the index p assumes the values $\frac{3}{2}$, 2 and 3, depending on whether the scattering arises from the Coulomb interaction in the dirty limit (conductivity, $\sigma \leq 10^4 \ s/cm$), (e-e) inelastic interaction in the clean limit $(10^4 \leq \sigma \leq 10^6 \ s/cm)$ and electron-phonon (e-p) scattering [17,18]. α in Eq. (4.5) denotes the relevant microscopic length scale.

4.3 Resistivity mechanisms at $T > T_{min}$

With increasing temperature, the processes such as the inelastic electron-phonon (e - p) scattering, spin-orbit (SO) scattering, Zeeman splitting of spin sub-bands, electron-magnon (e - m) scattering and scattering from spin fluctuations tend to suppress the quantum corrections to resistivity arising from WL and EEI effects with the result that the classical Boltzmann ballistic transport behavior is progressively restored.

4.3.1 Electron-phonon scattering

In crystalline systems with or without weak anti-site disorder, the expression for the electronphonon scattering contribution to $\rho(T, H)$, $\rho_{e-p}(T)$, yielded by the Bloch-Grüneisen [21] and Bloch-Wilson [22] formalisms, has the following generalized form

$$\rho_{e-p}(T) = \alpha_{e-p} \left(\frac{T}{\theta_D}\right)^n \int_0^{\theta_D/T} \frac{x^n}{(e^x - 1)(1 - e^{-x})} dx \tag{4.6}$$

where θ_D is the Debye temperature.

Eq.(4.6) reduces to the well-known Bloch-Grüneisen (BG) and Bloch-Wilson (BW) forms, respectively, for n = 5 and n = 3. The BG expression describes the phonon-induced non-spin-flip single band $(s\uparrow\downarrow - s\uparrow\downarrow, d\uparrow\downarrow - d\uparrow\downarrow)$ scattering contributions to $\rho(T, H)$ and gives a correct description of the phonon contribution in non-magnetic alkali and noble metals. By contrast, the BW expression represents the phonon-induced non-spin-flip two-band $(s\uparrow\downarrow - d\uparrow\downarrow)$ scattering contributions to $\rho(T, H)$ and is more appropriate for the 3d-transition metals.

In amorphous systems with topological/quenched disorder, the contribution from e-p scattering is described by the modified diffraction model [23]. This model considers the scattering of conduction electrons from the potential of the disordered spatial arrangement of atoms and predicts the temperature dependence of resistivity as

$$\rho_{e-p}(T) = \alpha_{e-p} \left\{ 1 + \left[S_0(2k_f) - 1 \right] e^{-2 \left[W_{2k_f}(T) - W_{2k_f}(0) \right]} \right\}$$
(4.7)

The second term in Eq. (4.7) is the temperature-dependent structure factor $S_T(2k_f)$ which is defined as

$$S_T(2k_f) \cong 1 + [S_0(2k_f) - 1]e^{-2W_{2k_f}(T)}$$
 (4.8)

where $S_0(2k_f)$ is the equilibrium structure factor and $e^{-2W_{2k_f}(T)}$ is the Debye-Waller factor with $W_{2k_f}(T)$, in the Debye approximation, given by,

$$W_{2k_f}(T) = W_{2k_f}(0) + 4W_{2k_f}(0) \left(\frac{T}{\theta_D}\right)^2 \int_0^{\theta_D/T} \frac{x}{(e^x - 1)} dx$$
 (4.9)

and $W_{2k_f}(0) = \frac{3\hbar^2 k_f^2}{2Mk_B \Theta_D}$, M is the atomic mass, k is the wave vector and k_B is the Boltzmann constant.

4.3.2 Electron-magnon scattering

The electron-magnon scattering involves spin-flip $s^{\uparrow\downarrow}$ and $d^{\uparrow\downarrow}$ and $d^{\uparrow\downarrow}$ intraband and $s^{\uparrow\downarrow}$ d^{$\downarrow\uparrow$} interband transitions. According to the two-band models [24,25] of e - m scattering contributions to $\rho(T,H)$, $\rho_{e-m}(T,H)$, in 3d transition metal ferromagnets, the spin-flip s - d interband scattering contribution is at least two orders of magnitude larger than that arising from the spin-flip s - s intraband scattering. Thus, over the entire temperature range, the spin-flip s - s scattering essentially determines ρ_{e-m} .

The spin fluctuation theory [26,27], yields the magnon-induced spin-flip scattering [28] contribution to $\rho(T, H)$ as,

$$\rho_{e-m}(T, H = 0) = \beta_{e-m} \times \left(\frac{T}{D_{sw}(T)}\right)^2$$
(4.10)

where the coefficient β_{e-m} is given by

$$\beta_{e-m} = \left(\frac{\pi}{4}\right) \left[\left(\frac{m_s}{ne^2}\right) \zeta_{s-d}^2 N\left(E_f^d\right) N\left(E_f^s\right) \left(k_f^s\right)^{-4} \right]$$

$$\times \left[\Gamma(3)\zeta(2) \left(\frac{g\mu_B M_S(0)}{\hbar} \right) \right] (k_B)^2 \tag{4.11}$$

and

$$D_{sw}(T) = D_0 \left(1 - D_2 T^2 - D_{\frac{5}{2}} T^{\frac{5}{2}}\right)$$
(4.12)

In Eq. (4.11), n is the number density, m is the mass of s-electrons, ζ_{s-d} is the s - d electron coupling constant, $N\left(E_f^d\right)$ and $N\left(E_f^s\right)$ are the total density of states at the Fermi level, E_F , for d and s-electrons, k_f^s is the Fermi wave vector for s-electrons, $M_s(0)$ is the spontaneous magnetization at T=0 K. In Eq. (4.12), D_{sw} is the spin wave stiffness, D_0 is the value of D_{sw} at 0 K and D_2 and $D_{5/2}$ account for the thermal renormalization of D_{sw} due to electron-magnon and magnon-magnon interactions.

Both α_{e-p} and β_{e-m} give rise to the *positive* temperature coefficient of resistivity (TCR) and are primarily responsible for the increase in resistivity as temperature is raised above T_{min} .

4.4. Data analysis, results, and discussion

4.4.1 Effect of deposition temperature (CFAS-TS)

Figs. 4.2 and 4.3, display zero-field, ρ (T, H = 0), and in-field electrical resistivity, ρ (T, $H = 80 \, kOe$), for the Co₂FeAl_{0.5}Si_{0.5} thin films deposited on SiO₂/Si(100) substrate and Fig. 4.5 display zero-field, ρ (T, H = 0), and in-field electrical resistivity, ρ (T, $H = 80 \, kOe$), for the Co₂FeAl_{0.5}Si_{0.5} thin films deposited on Si(100) substrate. The striking features of these results are as follows,

- (i) In all the films, as a function of temperature, the resistivity goes through a minimum at a temperature, T_{min} . T_{min} is highest for the RT film (\approx 95 K) and shifts to lower temperatures with increasing T_S ; for the TS500 film $T_{min} \approx 23$ K.
- (ii) As T_S increases, ρ_{5K} , (i.e., the residual resistivity) falls rapidly from 407 $\mu\Omega$ cm for the RT film and attains the minimum value for the TS500 CFAS thin films (\approx 106 $\mu\Omega$ cm) deposited at T_S = 500°C. The observation (ii) is compatible with the highest atomic site order within the B2 structure in the TS500 films.
- (iii) The signatures in $\rho(T)$ at low temperatures, taken to be typical of half-metallicity, such as the exponential suppression [15] of the electron-magnon (e-m) scattering or the two-magnon scattering contribution to $\rho(T)$ varying as $\rho_{2m} \propto T^{9/2}$ at very low temperatures with a crossover

to $\rho_{2m} \propto T^{7/2}$ at higher temperatures [16], are not apparent in the present case. Instead, in conformity with the earlier reports [17-21, 23-28] on several Co-based Heusler alloy thin films, we observe an upturn in $\rho(T)$ at such temperatures resulting from the presence of anti-site atomic disorder. Since this upturn completely masks the anticipated two-magnon scattering crossover from $\rho_{2m} \propto T^{9/2}$ to $\rho_{2m} \propto T^{7/2}$, it is not possible to conclusively establish or refute the presence of half-metallicity in our samples.

Fig. 4.4 displays the residual resistivity (ρ_{5K}), T_{min} and residual resistivity ratio, as functions of substrate temperature, obtained from the longitudinal resistivity data (Fig. 4. 4 (a) - (c)) and transverse resistivity data (Fig 4.4 (d) - (f)) deposited on the SiO₂/Si(100). While, Fig. 4.5 shows the comparison of ρ_{5K} and T_{min} as functions of substrate temperature in the CFAS thin films deposited on the SiO₂/Si(100) and Si(100) substrate.

RRR, which is defined as the ratio of the electrical resistivity at room temperature (300 K) to the electrical resistivity at absolute zero (0 K) or lowest measurable temperature, provides insight into the purity and quality of a material system. In general, metals with higher RRR values have fewer impurities and defects, leading to better electrical conductivity [1]. RRR increases with an increase in TS. The structural results support the observed increase in RRR, with the TS500 film having the highest B2 structural order at very low temperatures with a crossover to $\rho_{2m} \propto T^{7/2}$ at higher temperatures [16], are not apparent in the present case. Instead, in conformity with the earlier reports [17-21, 23-28] on several Co-based Heusler alloy thin films, we observe an upturn in $\rho(T)$ at such temperatures resulting from the presence of anti-site atomic disorder. Since this upturn completely masks the anticipated two-magnon scattering crossover from $\rho_{2m} \propto T^{9/2}$ to $\rho_{2m} \propto T^{7/2}$, it is not possible to conclusively establish or refute the presence of half-metallicity in our samples.

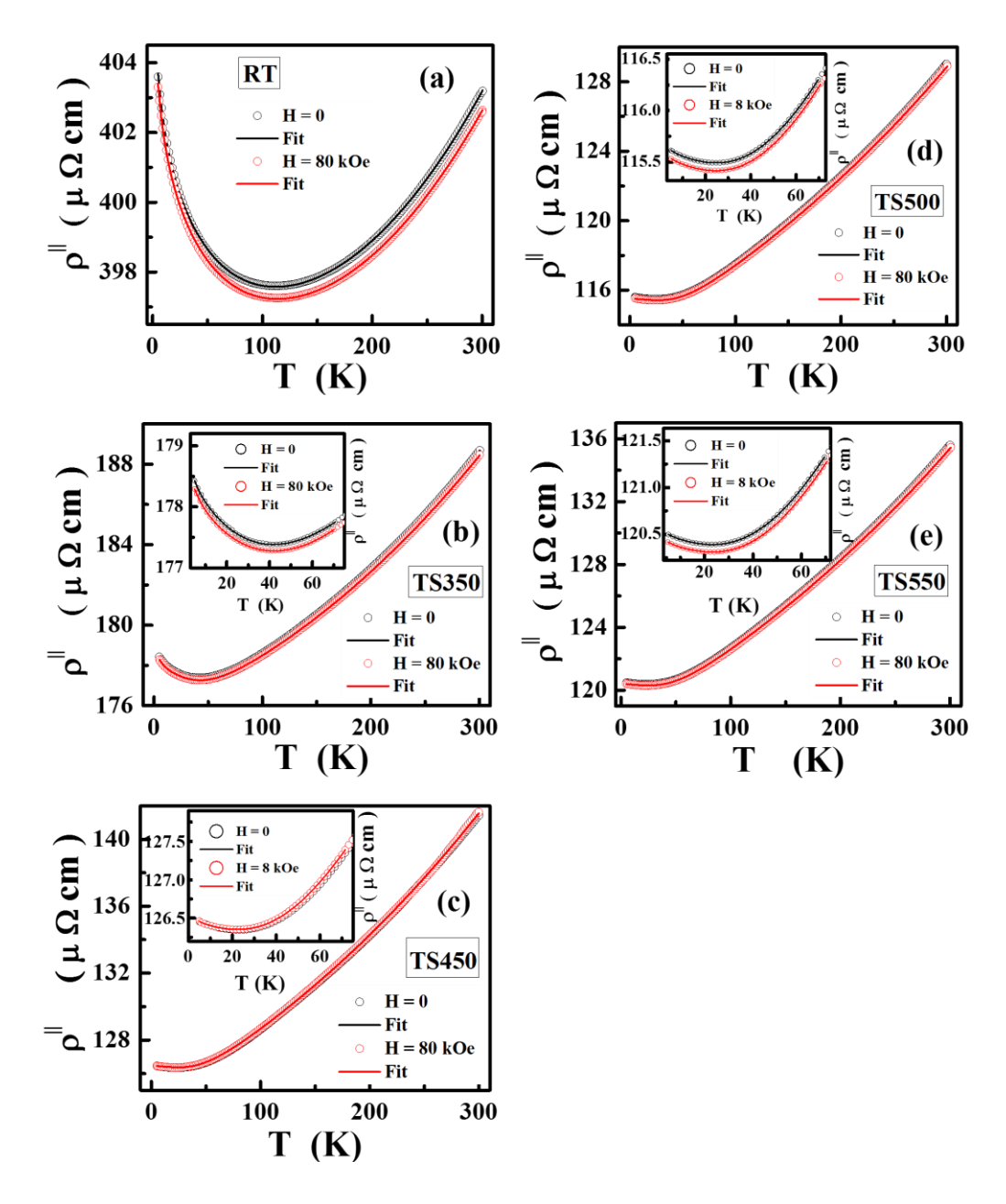


Fig. 4.2: Longitudinal resistivity ($\rho^{||}$): (a) data and fits for the RT films, based on Eq. (4.14) with the electron-phonon contribution given by the modified diffraction model. (b) – (e): Zero-field and in-field resistivity (black and red open circles) in the temperature range 5 - 300 K with theoretical fits (black and red continuous curves), based on Eq. (4.14) for TS350, TS450, TS500 and TS550 films deposited on SiO₂/Si(100). Insets (a-e) give the enlarged view of the zero-field and in-field resistivity (open circles) in the range 5-70 K with theoretical fits (continuous lines), based on Eq. (4.14) for the, TS350, TS450, TS500 and TS550 films.

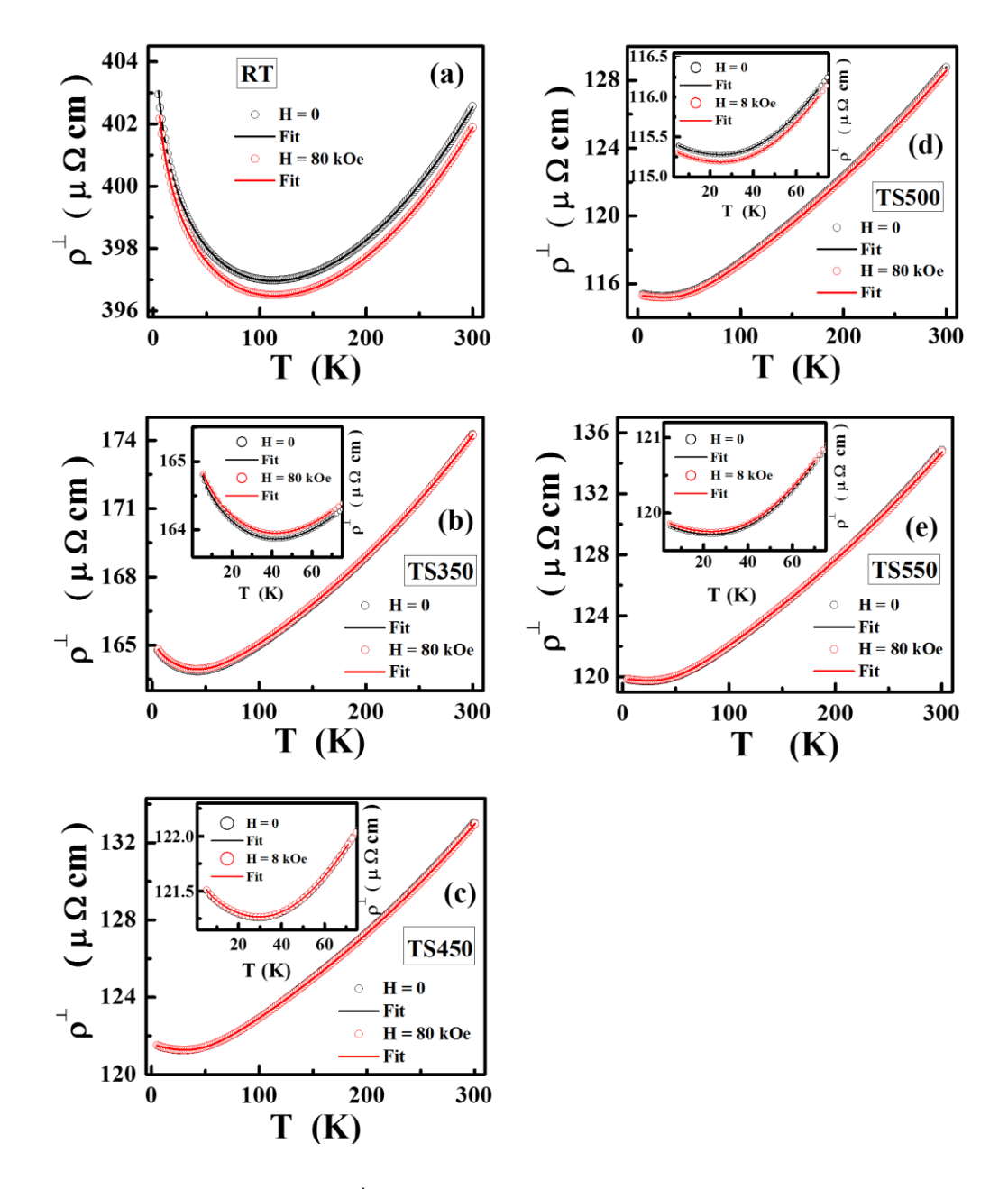


Fig. 4.3: Transverse resistivity (ρ^{\perp}): (a) data and fits for the RT films, based on Eq. (4.14) with the electron-phonon contribution given by the modified diffraction model. (b) – (e): Zero-field and in-field resistivity (black and red open circles) in the temperature range 5-300 K with theoretical fits (black and red continuous curves), based on Eq. (4.14), for TS350, TS450, TS500 and TS550 films deposited on SiO₂/Si(100). Insets (a-e) give the enlarged view of the zero-field and in-field resistivity (open circles) in the range 5-70 K with theoretical fits (continuous lines), based on Eq. (4.14), for the TS350, TS450, TS500 and TS550 films.

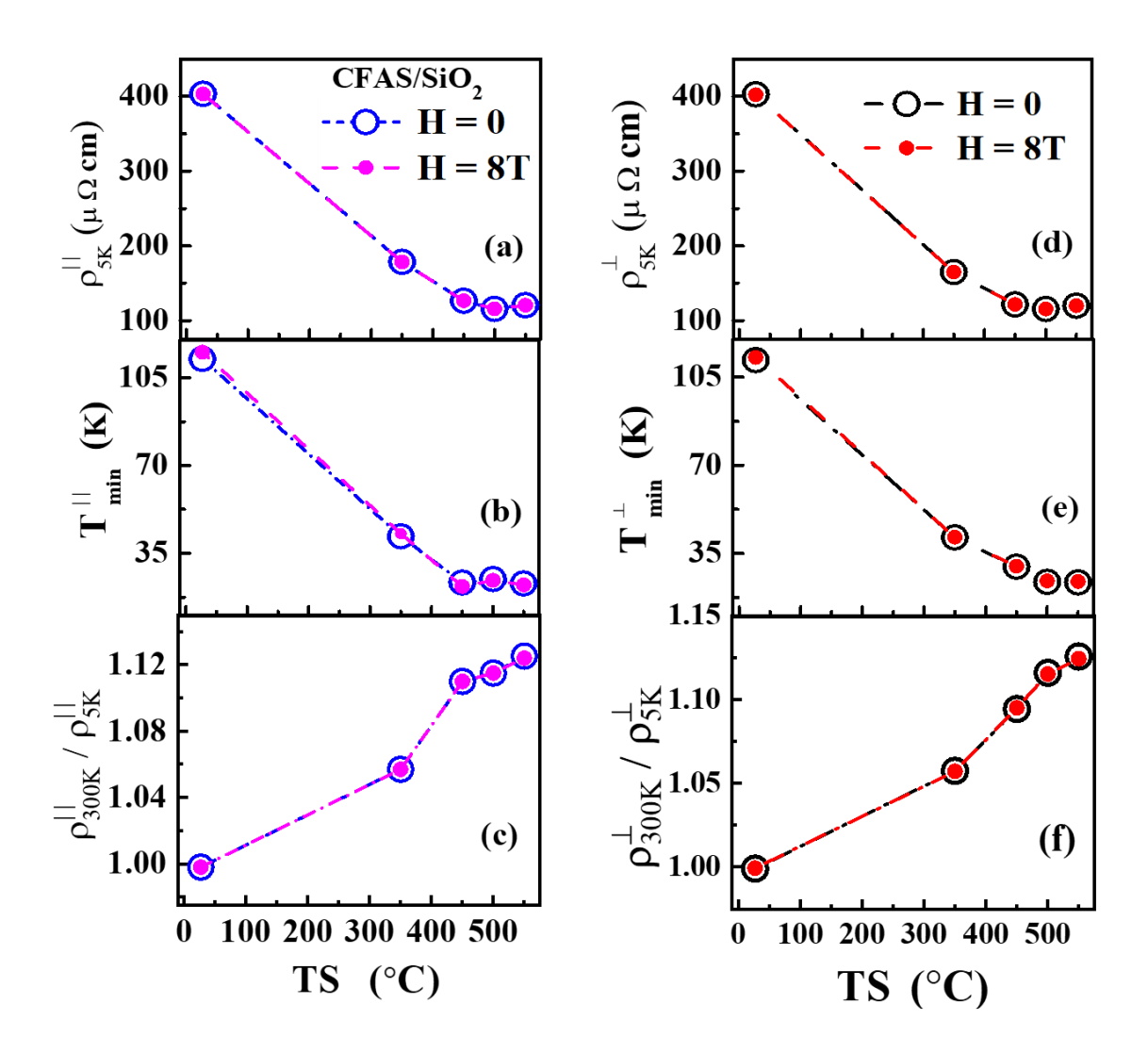


Fig. 4.4: (a) Residual resistivity (ρ_{5K}), (b) T_{min} and (c) residual resistivity ratio, as functions of substrate temperature in the CFAS thin films, obtained from longitudinal resistivity data. (d) Residual resistivity (ρ_{5K}), (e) T_{min} and (f) residual resistivity ratio, as functions of substrate temperature in the CFAS thin films, obtained from transverse resistivity data.

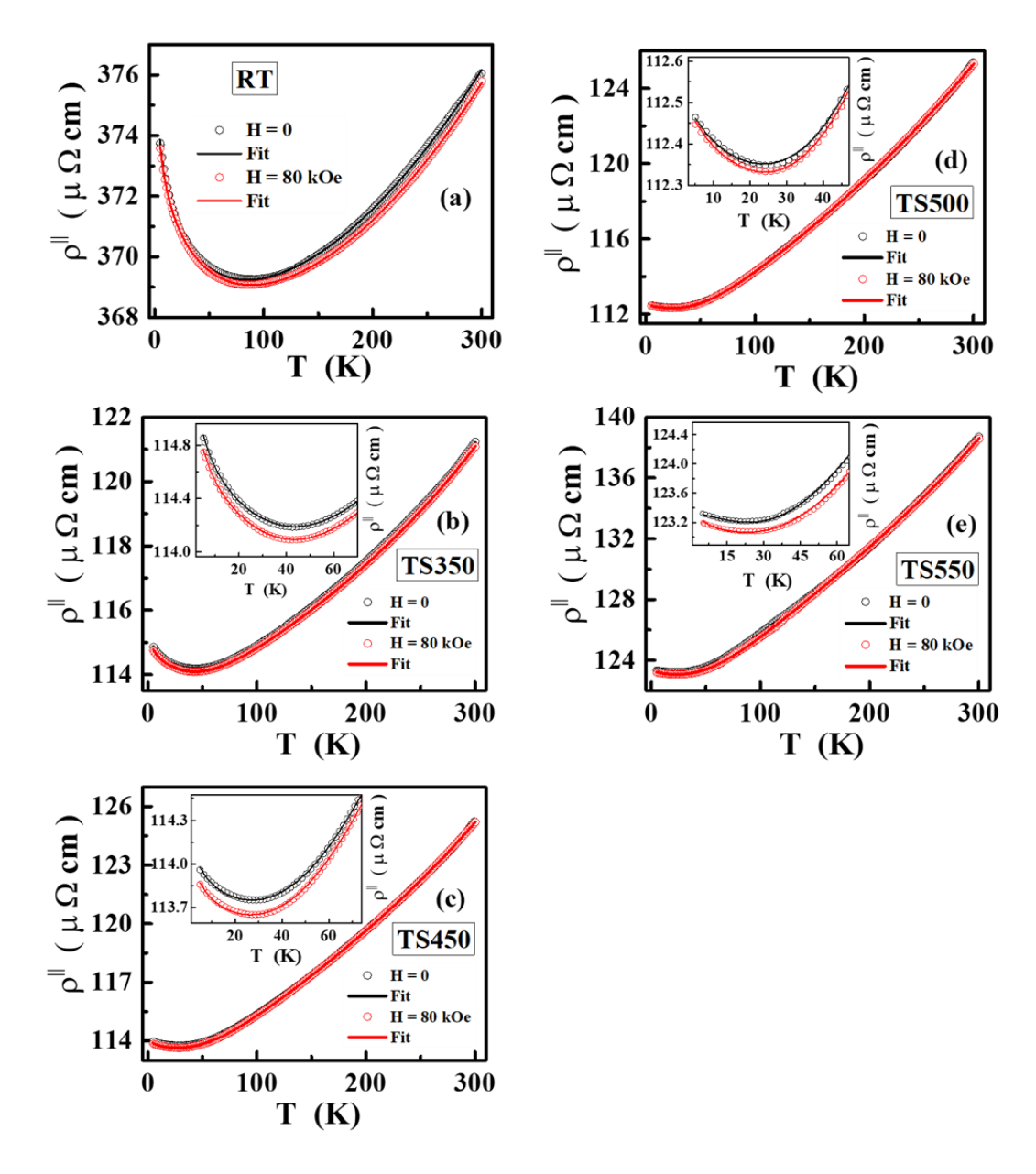


Fig. 4.5: Longitudinal resistivity (ρ^{\parallel}): (a) data and fits for the RT films, based on Eq. (4.14) with the electron-phonon contribution given by the modified diffraction model. (b) – (e): Zero-field and in-field resistivity (black and red open circles) in the temperature range 5 - 300 K with theoretical fits (black and red continuous curves), based on Eq. (4.14) for TS350, TS450, TS500 and TS550 films deposited on Si(100). Insets (a-e) give the enlarged view of the zero-field and in-field resistivity (open circles) in the range 5-70 K with theoretical fits (continuous lines), based on Eq. (4.14) for the, TS350, TS450, TS500 and TS550 films.

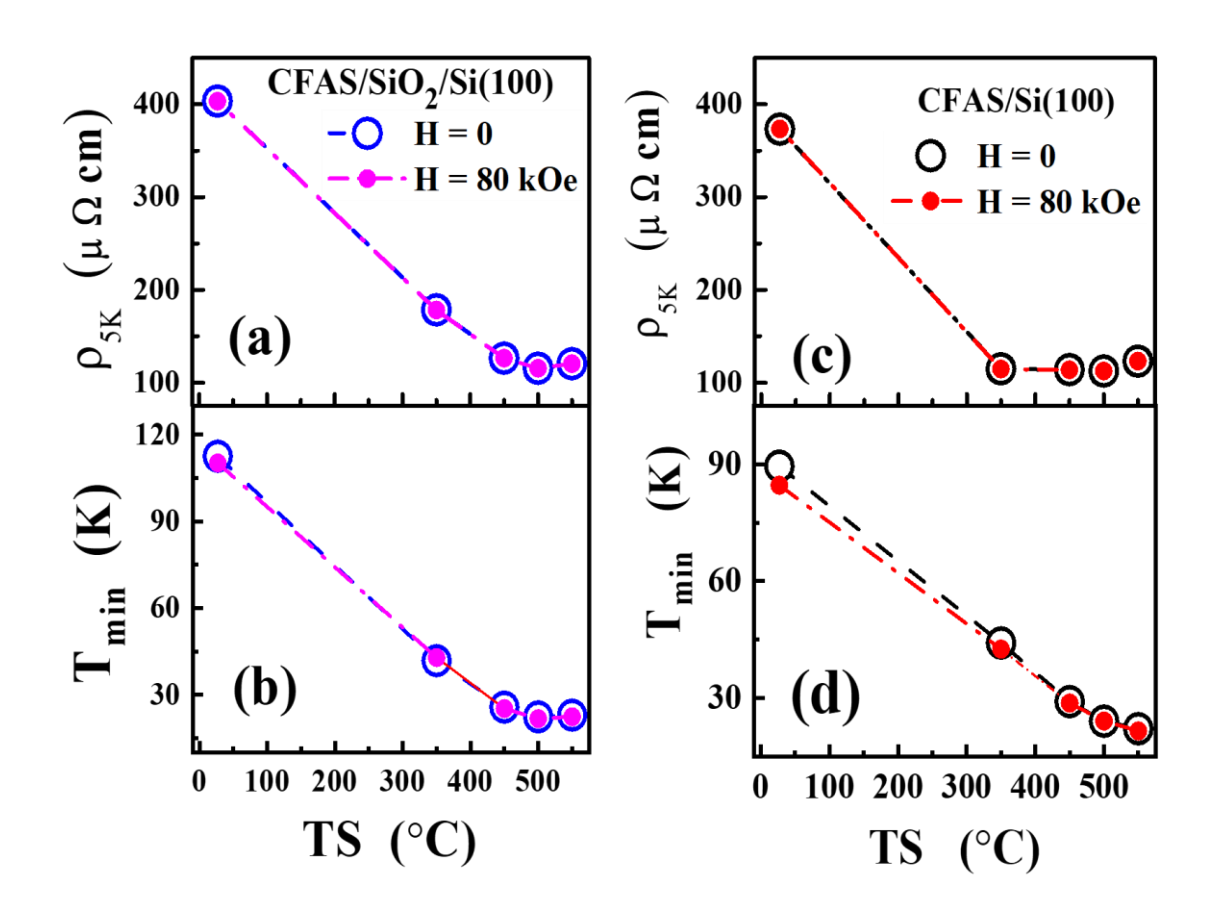


Fig. 4.6: Residual resistivity (ρ_{5K}) and T_{min} as functions of substrate temperature in the CFAS thin films deposited on the (a), (b): SiO2/Si(100) substrate, (c), (d): Si(100) substrate.

In numerous Co-based Heusler alloy thin films, the variation with temperature of the form $\rho(T) \sim -T^{1/2}$ has been reported below T_{min} . This behavior has been ascribed to either weak localization (WL) effect [29] or particle-particle channel EEI or particle-hole channel EEI [30] whereas the temperature variation $\rho(T) \sim -lnT$ is considered to have its origin in either the orbital two-channel Kondo effect [11–15] or electron-diffuson scattering [6,31,32].

Fig. 4.7 shows $\Delta \rho(T) = \rho(T) - \rho_{5K}$ against $\ln T$ and/or $T^{1/2}$ for the RT, TS350, TS450, TS500 and TS550 CFAS films deposited on CFAS/SiO₂/Si(100) and CFAS/Si(100) thin films.

Before embarking upon a detailed quantitative analysis of the resistivity data, we follow the customary practice of plotting $\Delta \rho(T) = \rho(T) - \rho_{5K}$ against $\ln T$ and/or $T^{1/2}$. We find that only the $\Delta \rho$ versus $\ln T$ plots for different CFAS films are linear over a wide temperature range (5K \leq $T \lesssim T_{min}$). Such plots, shown in Fig. 4.7, clearly demonstrate that the mechanism leading to $\ln T$ behavior makes a dominant contribution to $\Delta \rho$ (T) and this contribution is not affected by an external magnetic field (H) as strong as 80 kOe. As mentioned under sub-section 4.1.1., there are four possible sources for the $-\ln T$ variation: Kondo spin-flip scattering [7,8], scattering from TLS [9,10], two-channel orbital Kondo effect [11–15] or scattering of conduction electrons from diffusons [16]. The Kondo spin-flip scattering, intrinsic to dilute magnetic systems, is extremely sensitive to H, and hence cannot be responsible for the field-independent $-\ln T$ contribution. TLS come into being when an atom or group of atoms can tunnel between atomic configurations of equivalent energy separated by low energy barriers. Such dynamical atomic configurations are realized only in a non-crystalline material with topological disorder. The existence of TLS as well as the scattering of conduction electrons from TLS of non-magnetic origin cannot be sustained in a crystalline ferromagnet (as in the CFAS thin films) with site-disorder. It is evident from Fig. 4.7 that a crossover from $-\ln T$ to $-T^{1/2}$ variation as the temperature is lowered through T_K (which is a characteristic experimental signature of the two-channel orbital Kondo effect) is not observed in the present case. This leaves only the electron-diffuson (e - d) scattering as the most likely origin of the $-\ln T$ upturn in electrical resistivity below T_{min} . At this stage, it should be emphasized that an overwhelming - ln T contribution does not completely rule out possible contributions from the quantum corrections arising from the enhanced electron-electron interaction and weak localization effects

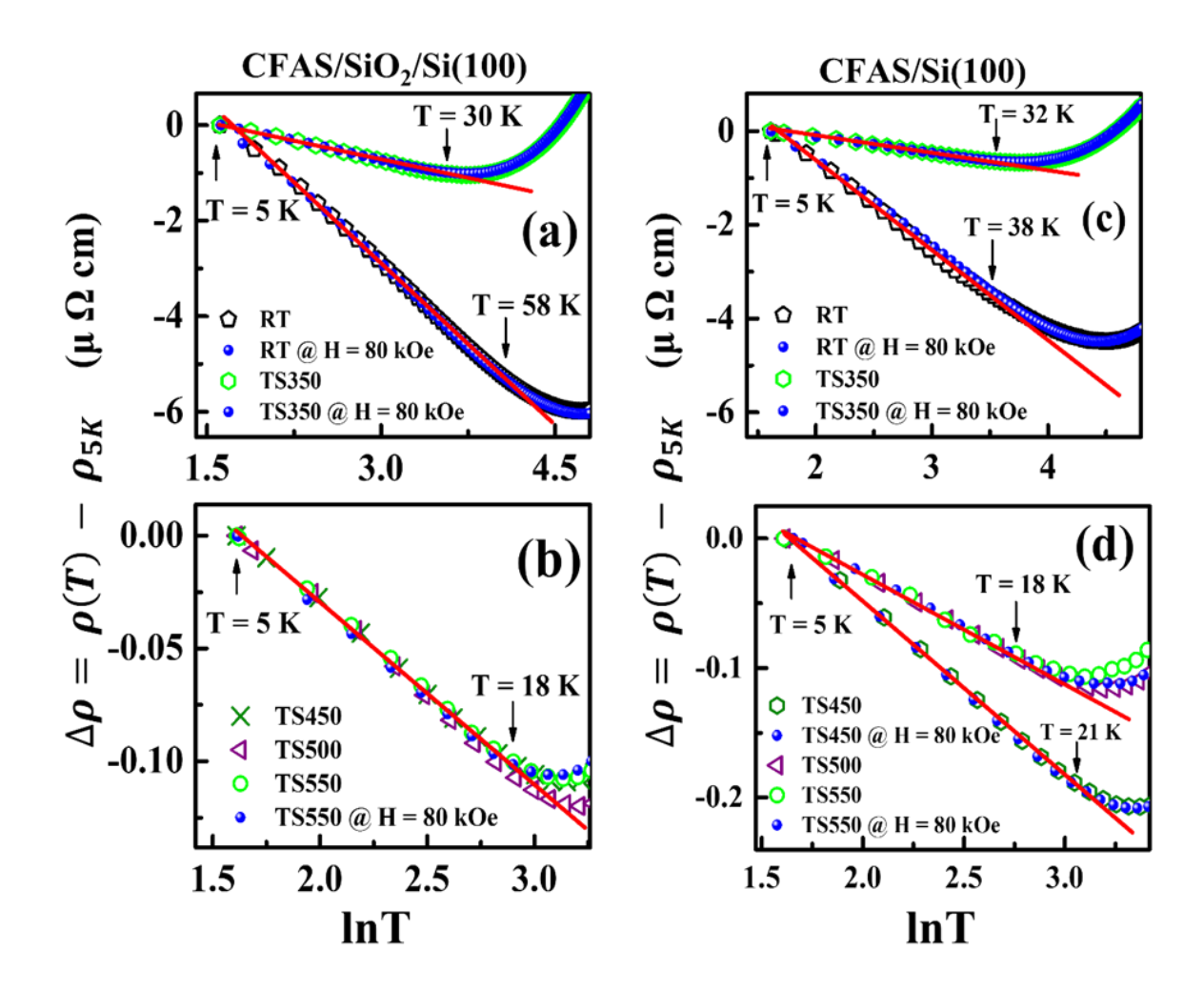


Fig. 4.7: Linear variation of $\Delta \rho$ with $\ln T$ at $T < T_{min}$ for (a), (c): RT and TS350, and (b), (d): TS450, TS500, and TS550 CFAS/SiO₂/Si(100) and CFAS/Si(100) thin films. The straight lines through the data symbols serve to highlight the linear relationship between $\Delta \rho$ and $\ln T$. Open symbols and solid circles denote the 'zero-field' (H = 0) and 'in-field' (H = 80 kOe) $\Delta \rho$ data, respectively.

In order to unravel the mechanisms responsible for the observed functional dependence of *zero-field* and *in-field* resistivity on temperature, $\rho(T, H = 0)$ and $\rho(T, H = 80 \ kOe)$ data for the CFAS/SiO₂/Si(100) and CFAS/Si(100) thin films, shown in Figs. 4.2, 4.3 and 4.5 are analyzed in terms of the expression that assumes the validity of Matthiessen rule and considers various contributions to $\rho(T, H)$ as additive, i.e.,

$$\rho(T,H) = \rho_0 + \rho_{e-d}(T) + \rho_{wl}(T,H) + \rho_{EEI}(T) + \rho_{e-m}(T,H) + \rho_{e-p}(T)$$
(4.13)

In the explicit form, Eq. (4.13) is given by.

$$\rho(T,H) = \rho_0 - \delta_{e-d} \ln T - \zeta_{wl} T^{\frac{p}{2}} - \gamma_{EEI} T^{\frac{1}{2}} + \beta_{e-m} \left[\frac{T}{1 - D_2 T^2} \right]^2 + \alpha_{e-p} \left(\frac{T}{\theta_D} \right)^n \int_0^{\frac{\theta_D}{T}} \frac{x^n}{(e^x - 1)(1 - e^{-x})} dx$$
(4.14)

where the residual resistivity, ρ_0 , accounts for the scattering of conduction electrons from grain boundaries, atomic disorder and defects/imperfections, while the coefficient β_{e-m} absorbs the $1/D_0^2$ term (refer to Eqs. (4.10) and (4.12)).

The best theoretical fits (continuous lines) to the $\rho(T, H = 0)$ and $\rho(T, H = 80 \, kOe)$ data (open circles), based on Eq.(4.14), shown in Figs. 4.2, 4.3 and 4.5, have been obtained as follows: we have considered all possible combinations of the contributions to $\rho(T, H)$ arising from the electron-diffuson (e - d) scattering, weak localization (WL), enhanced electron-electron interaction (EEI), electron-magnon (e - m) and electron-phonon (e - p) scattering. For instance, we covered the cases in Eq.(4.14), where [33] (i) $\delta_{e-d} \neq 0$, $\zeta_{wl} = 0$, $\gamma_{EEI} = 0$, $\beta_{e-m} \neq 0$ and $\alpha_{e-p} \neq 0$, (ii) $\delta_{e-d} = 0$, $\zeta_{wl} \neq 0$, $\gamma_{EEI} = 0$, $\beta_{e-m} \neq 0$ and $\alpha_{e-p} \neq 0$, (iii) $\delta_{e-d} = 0$, $\zeta_{wl} \neq 0$, $\gamma_{EEI} \neq 0$

to 0 in the e-m term. The form of $\rho_{e-p}(T)$ is given by either the Bloch-Grüneisen (BG) model [21] or the Bloch-Wilson (BW) model [22] or the modified diffraction model [23].

The reduced chi-square, χ_r^2 , has the lowest magnitude in all the TS-CFAS films when the EEI contribution to $\rho(T, H=0)$ and $\rho(T, H=80\ kOe)$ is zero, p=3 in the WL term, D_2 is finite and the electron-phonon scattering term has the form given by the BW model. However, for RT films, χ_r^2 is minimum when $D_2=0$ and $\rho_{e-p}(T)$ has the form given by modified diffraction model with the remaining contributions to similar to that of the remaining TS films.

Apart from the resultant fits to the $\rho(T, H = 0)$ (black open circles) and $\rho(T, H = 80 \ kOe)$ (red open circles) data, based on Eq. (4.14), Fig. 4.8 gives a visual demonstration of how the relative magnitudes of the contributions ρ_{e-d} , ρ_{wl} , ρ_{e-m} and ρ_{e-p} vary with temperature. It is evident from this figure that ρ_{e-d} and ρ_{wl} dominate over ρ_{e-m} and ρ_{e-p} for $T < T_{min}$ whereas the reverse is true for $T > T_{min}$. Furthermore, magnitude-wise $\rho_{e-d} > \rho_{wl}$ for $T < T_{min}$ and $\rho_{e-p} > \rho_{e-m}$ in most of the temperature range above T_{min} . The external magnetic field, H, has no effect on ρ_{e-d} and ρ_{e-p} but tends to suppress ρ_{wl} and ρ_{e-m} , which is clearly noticed for the RT film in Fig. 4.8.

This result is representative of other TS-CFAS films as well. Non-propagating longitudinal spin fluctuations (diffusons), involved in the e-d scattering, are insensitive to H [16] and so is ρ_{e-d} . If the spin-phonon coupling is negligibly small, H is not expected to have any influence on ρ_{e-p} . On the contrary, H tends to suppress ρ_{wl} as it progressively destroys the phase coherence and thus delocalizes the electrons. H creates a gap in the spin-wave spectrum and thereby increases the energy cost for exciting spin waves. Consequently, number of magnons available for the e-m scattering reduces with increasing H.

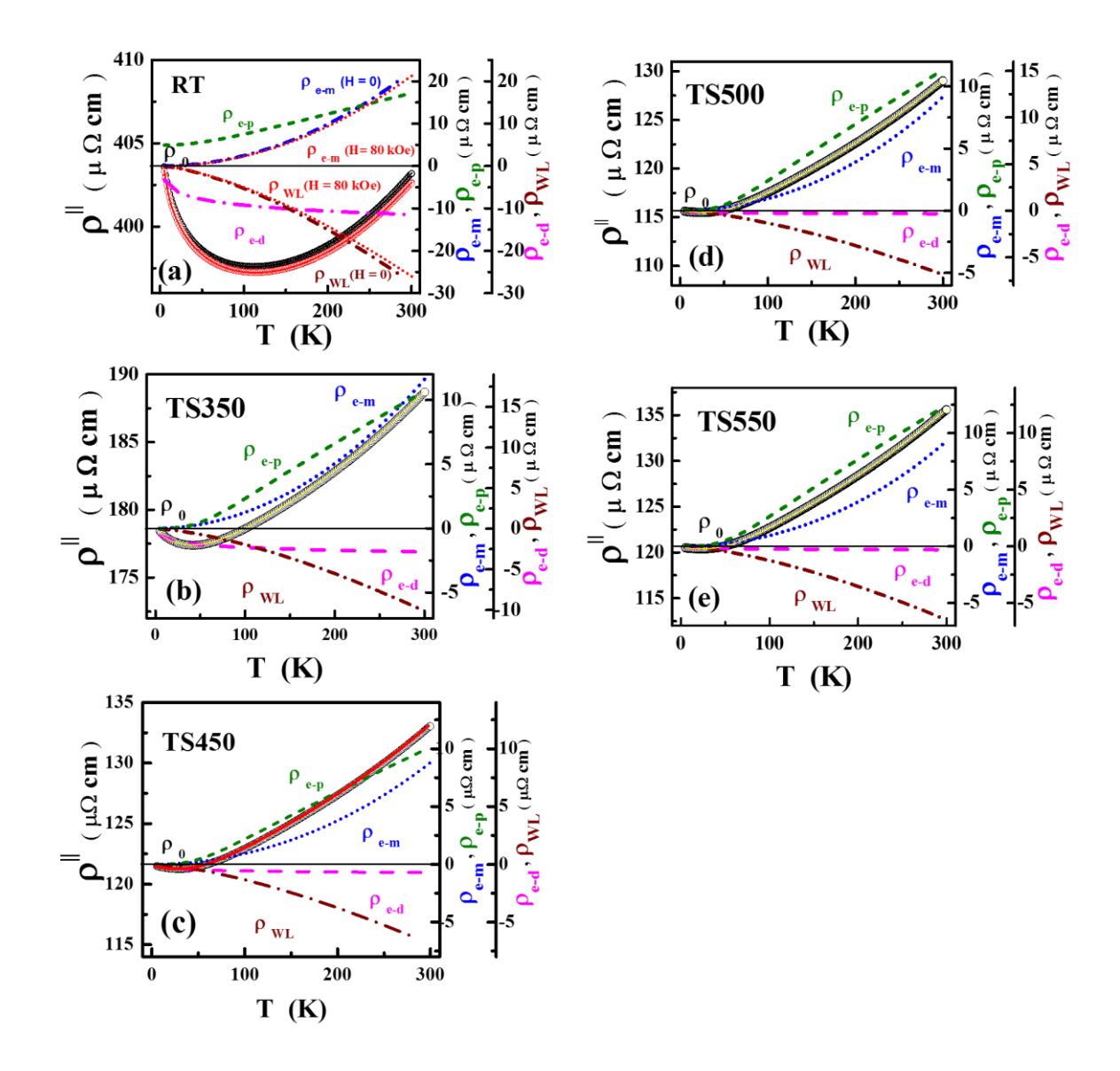


Fig. 4.8: (a) Zero-field, $\rho(T, H = 0)$, and in-field resistivity, $\rho(T, H = 80 \text{ kOe})$, (open circles) as functions of temperature with theoretical fits (continuous lines), based on Eq. (4.14), and the temperature variations of the contributions from the e-d scattering (ρ_{e-d}), WL (ρ_{WL}), e-m (ρ_{e-m}) and e-p (ρ_{e-p}) scattering for the RT film. Magnetic field of strength H=80 kOe leaves ρ_{e-d} and ρ_{e-p} unaltered in the entire temperature range but tends to suppress ρ_{WL} and ρ_{e-m} . (b) - (d) Zero-field resistivity, $\rho(T, H = 0)$, (open circles) as a function of temperature, with theoretical fits (continuous lines), based on Eq. (4.14), and the temperature variations of ρ_{e-d} , ρ_{WL} , ρ_{e-m} and ρ_{e-p} for TS350, TS500 and TS550.

In order to determine which form of the e-p (e-m) term in Eq. (4.14), BG or BW, ($D_2=0$ or $D_2 \neq 0$, i.e., $\rho_{e-m} \sim T^2$ or $\rho_{e-m} \sim (T/D_{sw}(T))^2$) gives correct description of $\rho_{e-p}(T)$ ($\rho_{e-m}(T)$), the percentage deviation of the $\rho(T, H=0)$ data, ρ_{exp} , from the corresponding fit values, ρ_{fit} , i.e., $\left\lfloor (\rho_{exp}-\rho_{fit})/\rho_{exp} \right\rfloor \times 100$, is plotted against temperature for all the CFAS films in Fig. 4.9.

In Fig. 4.10, percentage deviation for the TS500 CFAS thin film is compared for $BG + T^2$ and $BW + T^2$ in (a), $BG + T^2$ and $BG + (T/D_{sw}(T))^2$ in (b), and $BW + T^2$ and $BW + (T/D_{sw}(T))^2$ in (c). Evidently, the combination $BW + (T/D_{sw}(T))^2$ alone yields the statistical deviations while all the other combinations exhibit very large (~ 20 times larger) systematic deviations.

This result, which is representative of other CFAS thin films as well, permits us to conclude that in the crystalline TS350, TS450, TS500 and TS550 CFAS films, the thermal renormalization of the spin-wave stiffness due to the electron-magnon interaction, i.e., $D_{sw}(T) = D_0(1 - D_2 T^2)$ with $D_2 \neq 0$, contributes significantly to $\rho_{e-m}(T)$ and the BW model correctly describes the functional dependence of ρ_{e-p} on temperature. The validity of BW model asserts that the *phonon-induced* non-spin-flip two-band ($s\uparrow\downarrow$ - $d\uparrow\downarrow$) scattering dominantly contributes to $\rho(T,H)$.

In sharp contrast, for the RT CFAS films with the least atomic order, (i) the inclusion of the thermal renormalization of spin wave stiffness does not result in any significant improvement in the fit quality, and (ii) neither the BG model nor the BW model but the modified diffraction model yields minimum deviations as it takes into account the contribution to e - p scattering from the potential of the disordered spatial arrangement of atoms.

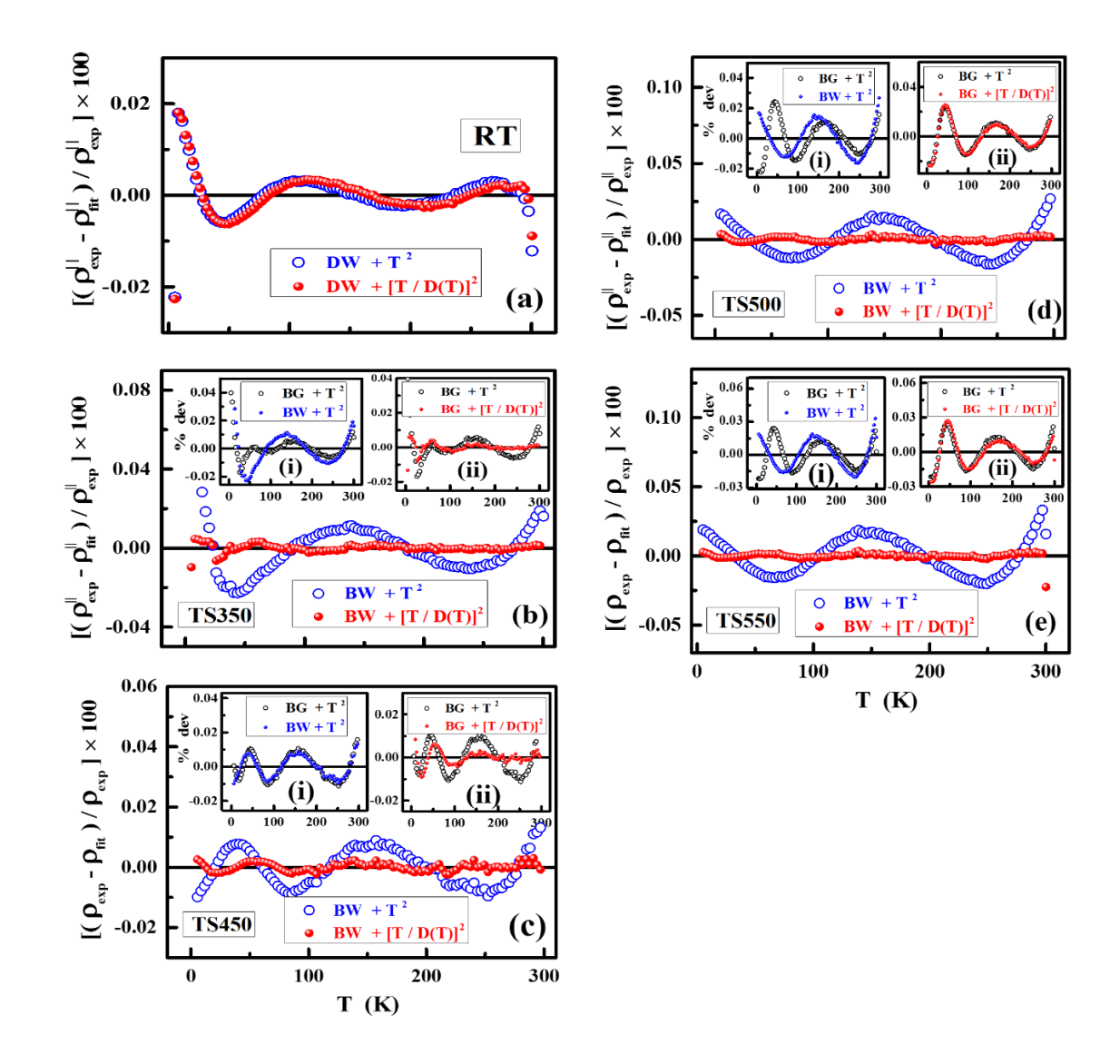


Fig. 4.9: (a) Comparison of the percentage deviations from the $DW + T^2$ and $DW + [T/D_{SW}(T)]^2$ fits (b)-(e) Comparison of the percentage deviations from the $BW + T^2$ and $BW + [T/D_{SW}(T)]^2$ fits (based on Eq. (14)) in RT, TS350, TS450 TS500 and TS550 CFAS thin films. For all the figures, inset (i) Displays the percentage deviations from the $BG + T^2$ and $BW + T^2$ fits, inset (ii) Compares the percentage deviations from the $BG + T^2$ and $BG + [T/D_{SW}(T)]^2$ fits. See the text for details about different types of theoretical fits.

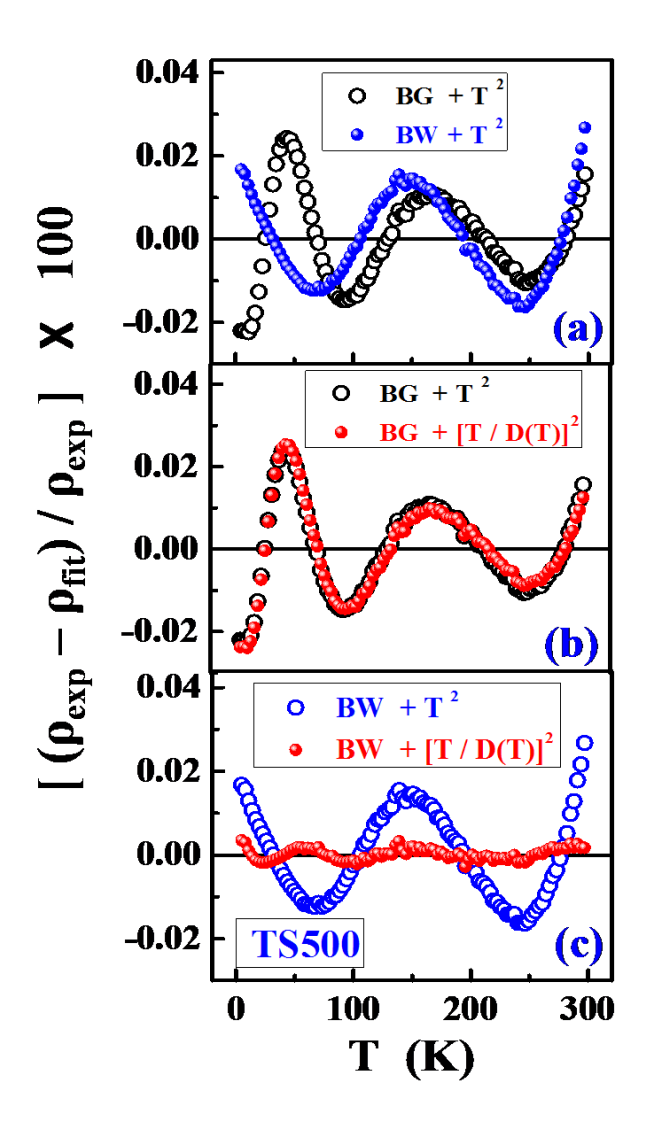


Fig. 4.10: TS500 CFAS thin film as an example; (a) displays the percentage deviations from the $BG + T^2$ and $BW + T^2$ fits. (b) Compares the percentage deviations from the $BG + T^2$ and $BG + [T/D_{SW}(T)]^2$ fits. (c) Comparison of the percentage deviations from the $BW + T^2$ and $BW + [T/D_{SW}(T)]^2$ fits (based on Eq. (4.14)). See the text for details about different types of theoretical fits.

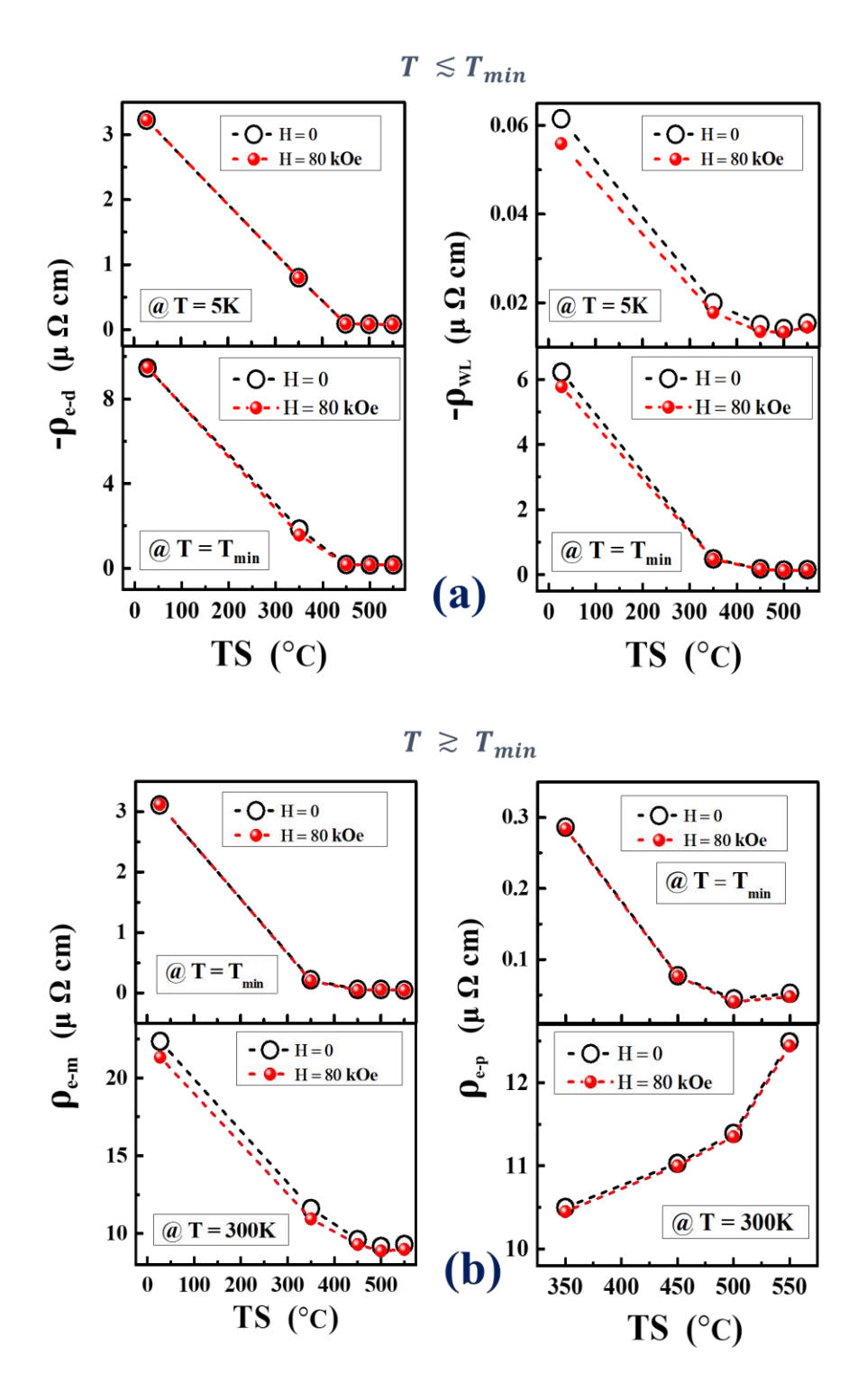


Fig. 4.11: (a) ($T \lesssim T_{min}$) Variation with the substrate temperature of ρ_{e-d} and ρ_{WL} at 5 K and T_{min} for CFAS thin films (b) ($T \gtrsim T_{min}$) Variation with substrate temperature of ρ_{e-m} , ρ_{e-p} at T_{min} and 300 K. The open black and filled red dots indicate the zero-field and in-field data, respectively.

The data presented in Figs. 4.8, 4.11(a) and 4.11(b), illustrate that, at any given temperature, ρ_{e-d} , ρ_{wl} and ρ_{e-m} decrease in magnitude while ρ_{e-p} increases as the atomic order improves with increasing TS. As TS promotes (B2) crystalline order, ballistic rather than diffusive motion of electrons is energetically favored, the phase coherence is progressively lost and electrons get delocalized with the result that both ρ_{e-d} and ρ_{wl} decline. Since the magnon – induced spin-flip s -d inter-band $(s^{\uparrow\downarrow}-d^{\downarrow\uparrow})$ transitions essentially govern ρ_{e-m} , decrease in ρ_{e-m} is a manifestation of the suppression of $(s^{\uparrow\downarrow} - d^{\downarrow\uparrow})$ scattering with increasing atomic order caused by the depletion of the minority-spin \downarrow density of states at E_F . This observation is consistent with the earlier reports of half-metallicity and substantially higher spin polarization in L2₁ ordered bulk CFS [34]and CFAS thin films [8]. On the other hand, ρ_{e-p} increases because the *phonon-induced* non-spin-flip two-band s^{\uparrow} - d^{\uparrow} transitions become more and more frequent as the majority-spin \uparrow density of states at E_F increases with atomic order. Another important result is that, irrespective of the value of TS, the quantities ρ_{e-d} , ρ_{wl} , ρ_{e-m} and ρ_{e-p} have systematically higher magnitudes for the CFAS films deposited on the SiO₂/Si(100) substrates than on the Si(100) substrates. The only exception is TS500 CFAS thin film that have comparable values for the two types of substrates. The SiO₂ buffer layer sustains higher atomic site disorder (in all but the TS500 film) which, in turn, gives rise to the systematically higher values of ρ_{e-d} , ρ_{wl} , ρ_{e-m} and ρ_{e-p} .

4.4.1.1 Effect of deposition temperature on Magnetoresistance

The suppression of weak localization (WL)/quantum interference (QI) effect and electron-magnon (e-m) scattering by the external magnetic field (H) are exclusively responsible for the negative magnetoresistance (MR). Moreover, the WL/QI contribution to magnetoresistance (MR $_{WL}$) is negligibly small compared to that arising from the e-m scattering (MR $_{e-m}$). This is because the WL effect is, to a large extent, already suppressed by the internal exchange field, which is orders of magnitude stronger than the external field, H. Being just a perturbation, H thus generates a very small MR $_{WL}$. To verify if the observed MR is essentially due to the suppression of the e-m scattering contribution to

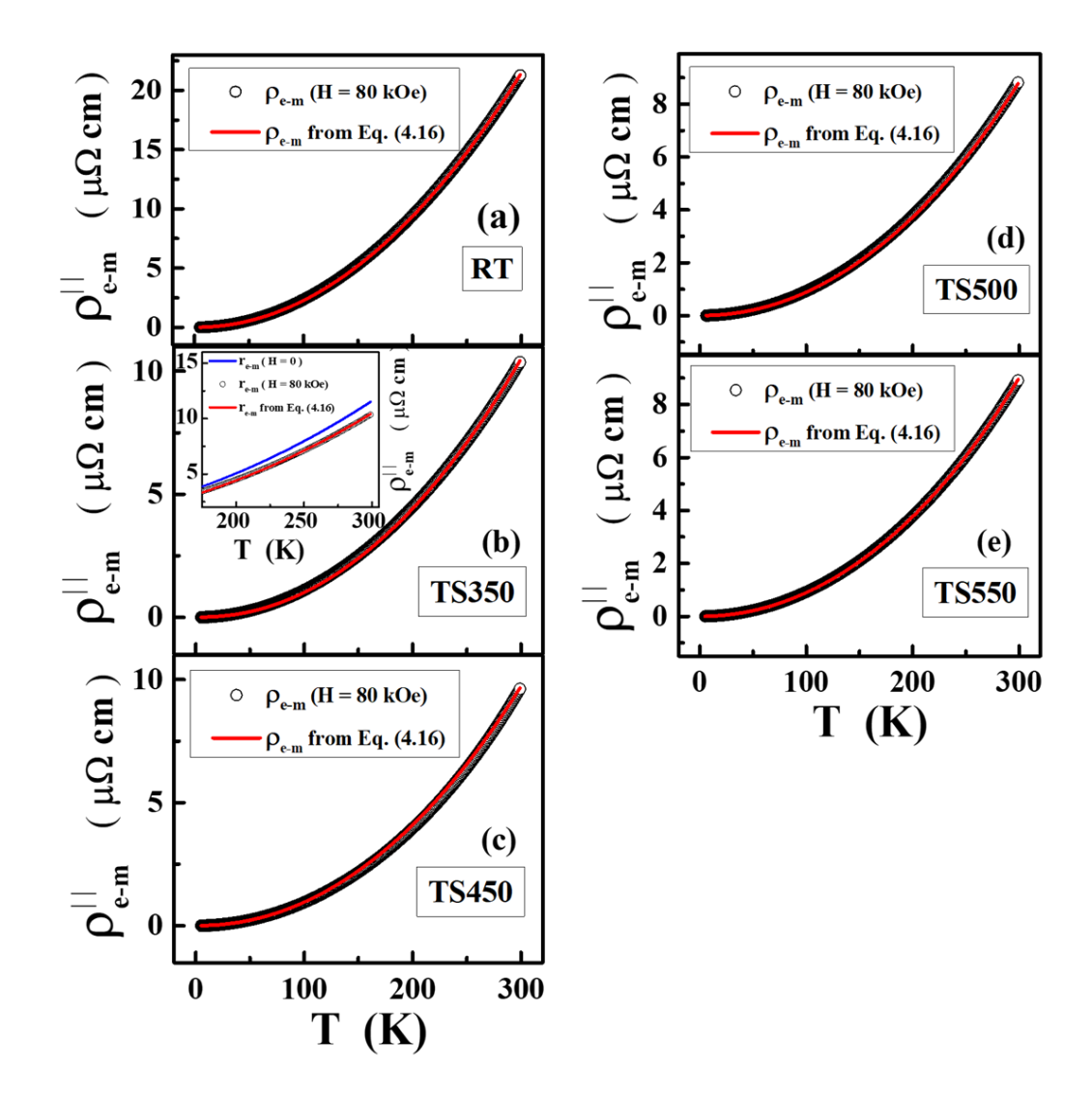


Fig. 4.12: (a) – (d) Comparison of the observed ρ_{e-m}^{\parallel} (T, H = 80 kOe) (open circles) with the ρ_{e-m}^{\parallel} (T, H = 80 kOe) computed (red curves) from ρ_{e-m}^{\parallel} (T, H = 0 kOe)) using the theoretical expression, Eq. (4.16). Inset (b) clearly bears out the suppression of ρ_{e-m} (T) at H = 80 kOe.

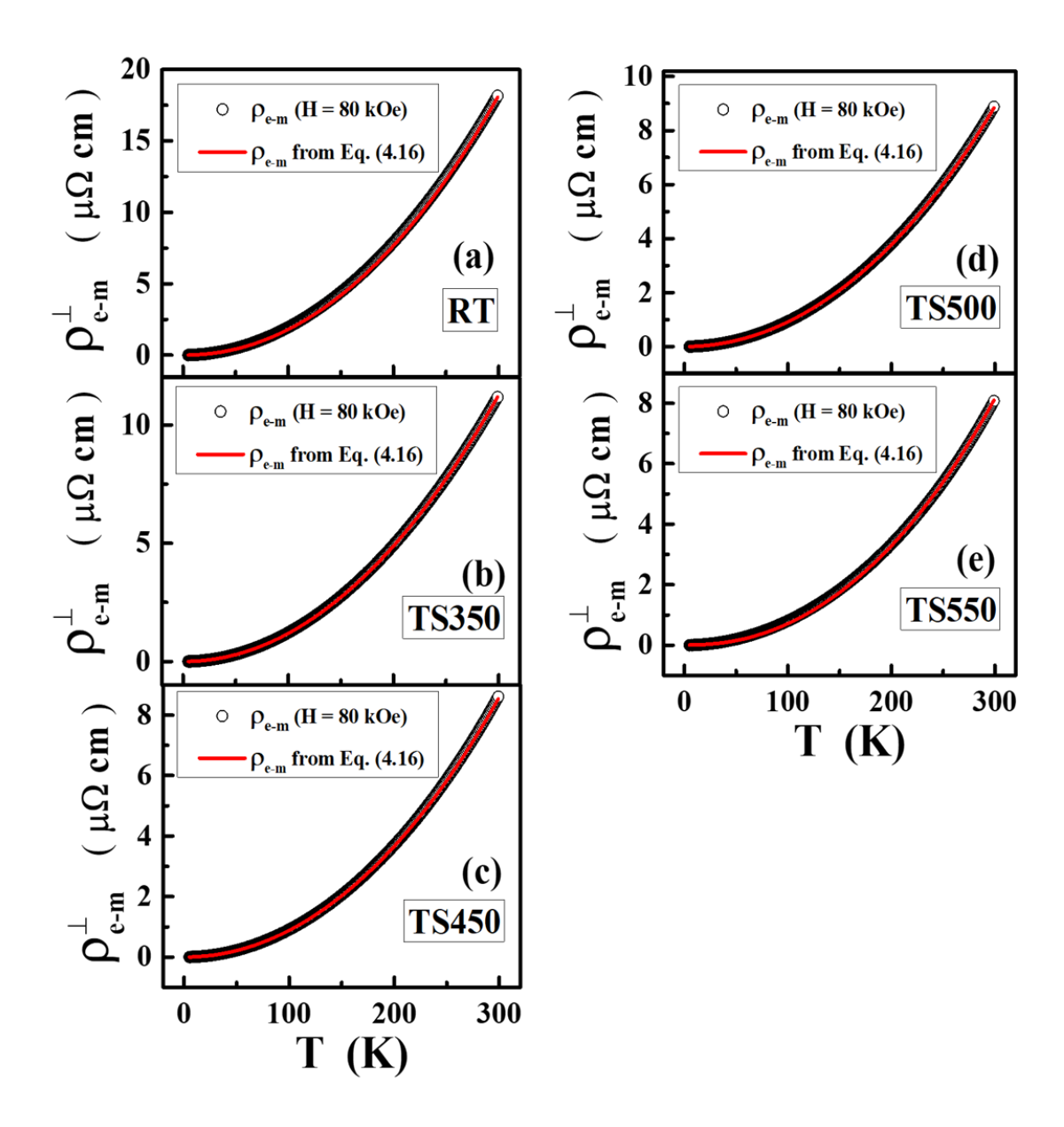


Fig. 4.13: (a) – (e) Comparison of the observed ρ_{e-m}^{\perp} (T, H = 80 kOe) (open circles) with the ρ_{e-m}^{\perp} (T, H = 80 kOe) computed (red curves) from ρ_{e-m}^{\perp} (T, H = 0 kOe) using the theoretical expression, Eq. (4.16).

 $\rho(T, H = 0)$ by H, instead of using the standard definition of magnetoresistance.

$$\left(\frac{\Delta\rho}{\rho}\right) = \frac{\rho(T,H)}{\rho(T,H=0)} - 1 , \qquad (4.15)$$

 $\rho_{e-m}(T,H)$ is calculated from $\rho_{e-m}(T,H=0)$ employing the expression for $\rho_{e-m}(T,H)$ given by the spin fluctuation theory [26–28]

$$\rho_{e-m}(T,H) = \rho_{e-m}(T,H=0) \left[1 + \eta \left(h \ln h - 2h + \frac{h^2}{2} \right) \right]$$
 (4.16)

where $h = g \mu_B H/k_B T$ and η is a material parameter which varies from sample to sample. Note that $\rho_{e-m}(T, H=0) = \beta_{e-m} \left[\frac{T}{1-D_2 T^2}\right]^2$ is obtained from the fits to the $\rho(T, H=0)$ data, based on Eq. (4.14) (refer to the Fig. 4.2 and 4.3). The inset of Fig. 4.12 (b) shows a typical behavior of negative MR as a function of temperature at H=80 kOe. $\rho_{e-m}(T, H=80 \ kOe)$ is computed from $\rho_{e-m}(T, H=0)$ using Eq. (4.16) and the agreement between the observed (black open circles) and computed (red continuous curves) $\rho_{e-m}(T, H=80 \ kOe)$ is optimized by treating η as the lone fitting parameter. Fig. 4.12 and 4.13 clearly bears out that the red curves accurately reproduce the observed $\rho_{e-m}(T, H=80 \ kOe)$ over the entire temperature range $5 \ K \le T \le 300 \ K$. As far as the theoretical fits are concerned, only the leading term, $h \ln h$, within the parenthesis in Eq. (4.16), is significant.

4.4.1.2 Effect of deposition temperature on Anisotropic Magnetoresistance (AMR)

The anisotropic magnetoresistance (AMR) effect is a well-known phenomenon observed in ferromagnetic materials, wherein the electrical resistivity undergoes changes based on the relative angle between the directions of current flow and magnetization. AMR ratio is generally defined as

$$\left(\frac{\Delta\rho}{\rho}\right)_{AMR} = \frac{\rho_{||} - \rho_{\perp}}{\rho_{\perp}} \tag{4.17}$$

where $\rho_{||}$ represents the longitudinal resistivity, when the current is applied along the magnetization direction, which lies in the film plane and ρ_{\perp} is the resistivity when the directions of current and magnetization are perpendicular to each other. AMR has its origin in the scattering

of conduction s-electrons from localized d-electrons when the hybridization of s- and d-states is caused by the spin-orbit interaction [35–37].

A negative magnetoresistance (AMR ratio) has been observed [38–40] in half-metallic systems in which no minority spin density of states exists at the Fermi energy, ϵ_f . Within the framework of the two-current conduction model with spin-orbit interaction, *Kokado et al.* [40] showed that the sign of the AMR ratio is determined by the dominant s - d scattering process. Thus, crucial information about the scattering mechanism responsible for the spin-polarized conduction state in a given ferromagnetic system can be obtained from the observed sign of the AMR ratio.

Since the density of states (DOS) in either spin-up or spin-down sub-band at the Fermi level (ϵ_f) is absent in a half-metal, sign of the AMR ratio should always be negative due to the dominant $s \uparrow \to d \uparrow$ or $s \downarrow \to d \downarrow$ scattering. A negative AMR ratio originates from the s-d scattering wherein the $s \uparrow$ electrons scatter into the $d \uparrow$ sub-band and the magnitude of negative AMR is directly proportional to the density of states (DOS) of the d spin-up $(d \uparrow)$ sub-band at ϵ_f [35,40].

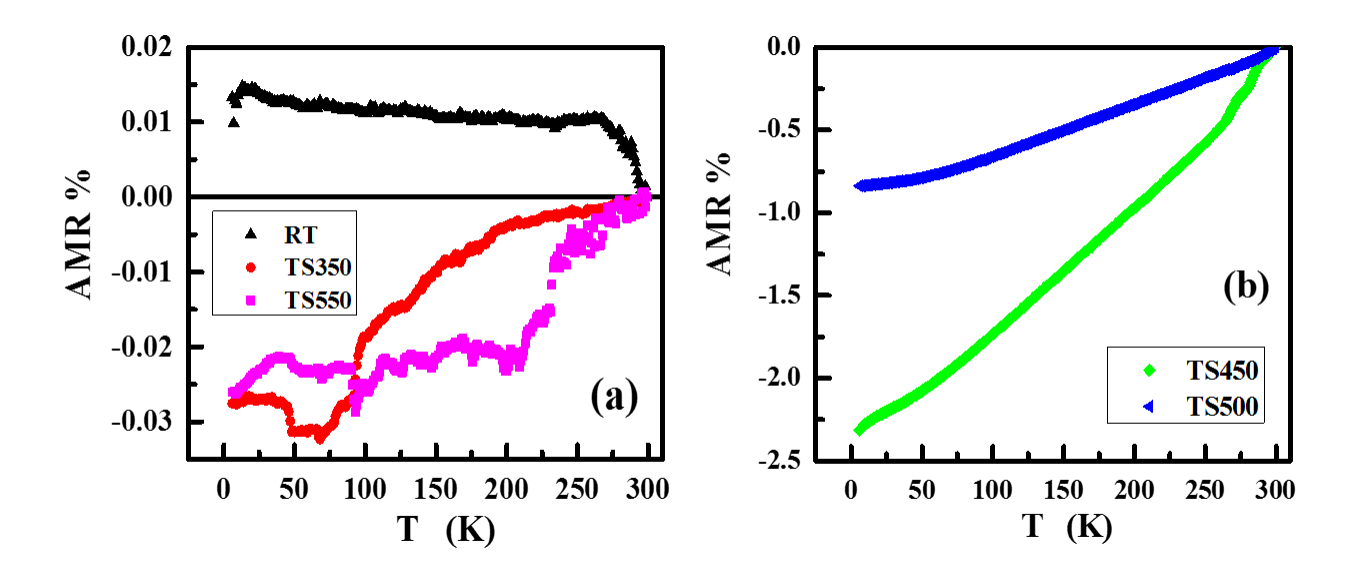


Fig. 4.14: Temperature dependence of AMR % for the RT, TS350, TS450, TS500 and TS550 CFAS films.

The In-field longitudinal and transverse electrical resistivity (Fig. 4.1(a) and (b)), measured in the presence of external magnetic field, H = 80 kOe, is used to obtain the AMR ratio for the CFAS films.

Since the difference between the measured values of $\rho^{||}(T)$ and $\rho^{\perp}(T)$ is very small, slight uncertainty in the sample dimensions can mask the actual behaviour of the AMR ratio. For this reason, the $\rho_{||}(T)$ and $\rho_{\perp}(T)$ in Eq. (4.17) are redefined as $\rho_{||}(T) = \frac{\rho^{||}(T)}{\rho^{||}(300K)}$ and $\rho_{\perp}(T) = \frac{\rho^{\perp}(T)}{\rho^{\perp}(300K)}$, As is evident from Fig. 4.14(a) that, over the entire temperature range from 5K to 300 K, the AMR ratio for the RT film is *positive* whereas it is *negative* for the more structurally-ordered films, TS350, TS450, TS500 and TS550. At 5 K, AMR% has the maximum value of - 0.03 in the TS350 and TS550 films and - 2.31 and - 0.84, respectively, for the TS450 and TS500 films.

In view of the theory proposed by *Kokado et al.* [40], the dominant $s \uparrow \to d \downarrow$ or $s \downarrow \to d \uparrow$ *spin-flip* scattering process gives rise to the positive AMR ratio in the RT film whereas the $s \downarrow \to d \downarrow$ or $s \uparrow \to d \uparrow$ *non-spin-flip* scattering process is responsible for the negative AMR ratio in the TS350, TS450, TS500 and TS550 films. The dominant $s \uparrow \to d \uparrow$ *non-spin-flip* scattering in these ordered films indicates that the films TS350, TS450, TS500 and TS550 could be half-metallic in nature.

The temperature dependence of the AMR ratio for CFAS thin films (TS350, TS450, TS500, TS500) indicates a degradation of spin polarization at ϵ_f with increasing temperature. The RT film with the highest degree of anti-site disorder is an exception in that the AMR % retains the value of $\approx +0.01$ over a wide temperature range. This observation suggests that the RT films have finite DOS in both spin-up and spin-down sub-bands. Table 4.1 shows the reported experimental values of AMR ratio for different ferromagnetic systems.

Table 4.1: AMR ratios of various ferromagnets reported in the literature. WI - FM, SI - FM and FM stand for Weak itinerant-electron ferromagnet, Strong itinerant-electron ferromagnet and ferromagnet, respectively.

Category	System	AMR ratio		Reference
			at 300 K	
WI - FM	bcc Fe		0.0030	ref. [41]
SI- FM	fcc Co		0.020	ref. [41]
	fcc Ni		0.018, 0.022	ref. [36], [41]
Half-metallic	L2 ₁ Co ₂ MnSi	- 0.002 at 10 K	- 0.0015	ref. [39]
FM	B2 Co ₂ FeAl		- 0.001	ref. [39]
	L2 ₁ Co ₂ FeSi	- 0.003 at 20 K		ref. [38]

4.4.2 Effect of CFAS film thickness

The variations of residual resistivity (ρ_{5K}), T_{min} and residual resistivity ratio (RRR = ρ_{300K} / ρ_{5K}) with thickness (t) are shown in Fig. 4.15. ρ_{5K} decreases from t=12 nm ($\sim250.6~\mu\Omega$ cm) and goes through a minimum at t=50 nm ($\sim115.39~\mu\Omega$ cm). Irrespective of the film thickness, resistivity as a function of temperature for all the films goes through a minimum at the temperature T_{min} , which decreases from 105 K at 12 nm to 23.7 K at 50 nm. The residual resistivity ratio as a function of thickness exhibits a peak at t=50 nm.

As the film thickness is reduced, the contributions to resistivity arising from the scattering of conduction electrons at surfaces and interfaces become increasingly important compared to those from the core. In the case of 12 nm and 25 nm films, the surface and interface contributions to $\rho(T)$ are expected to be significantly larger than those caused by the underlying anti-site disorder (B2 structure). Thus, $\rho(T)$ has a large value in the range of $220 - 250 \,\mu\Omega$ cm for the films with t = 12 nm and 25 nm. For the films with t = 50 nm, $\rho(T)$ drops to nearly half ($\sim 120 \,\mu\Omega$ cm) the value of t = 12 nm and/or t = 25 nm films, indicating that the scattering from surface and interface is

much weaker. However, with further increase in thickness to t = 75 nm, the resistivity assumes values ~ 220 $\mu\Omega$ cm because the film with t = 75 nm has the maximum anti-site disorder, as revealed by the GIXRD data (A2 structure). This result is consistent with the minimum in ρ_{5K} at t = 50 nm.

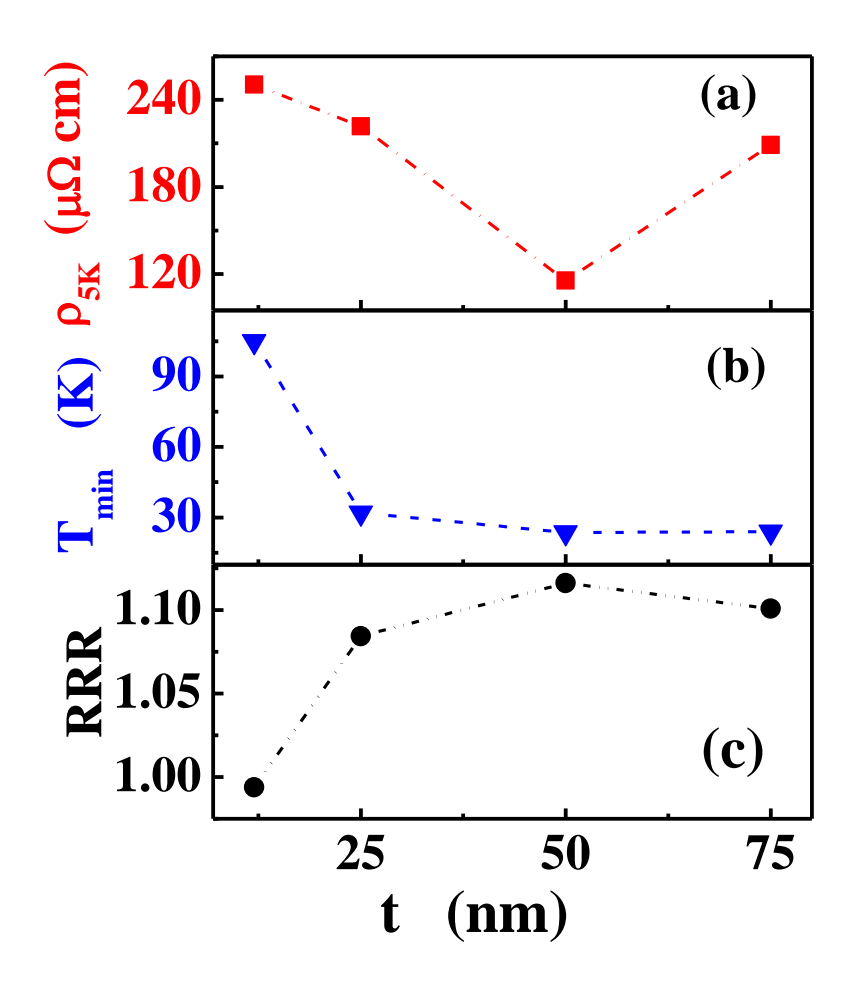


Fig. 4.15: Variations of the residual resistivity ρ_{5K} , T_{min} , and the residual resistivity ratio (RRR) with the thickness, t, for the CFAS thin films.

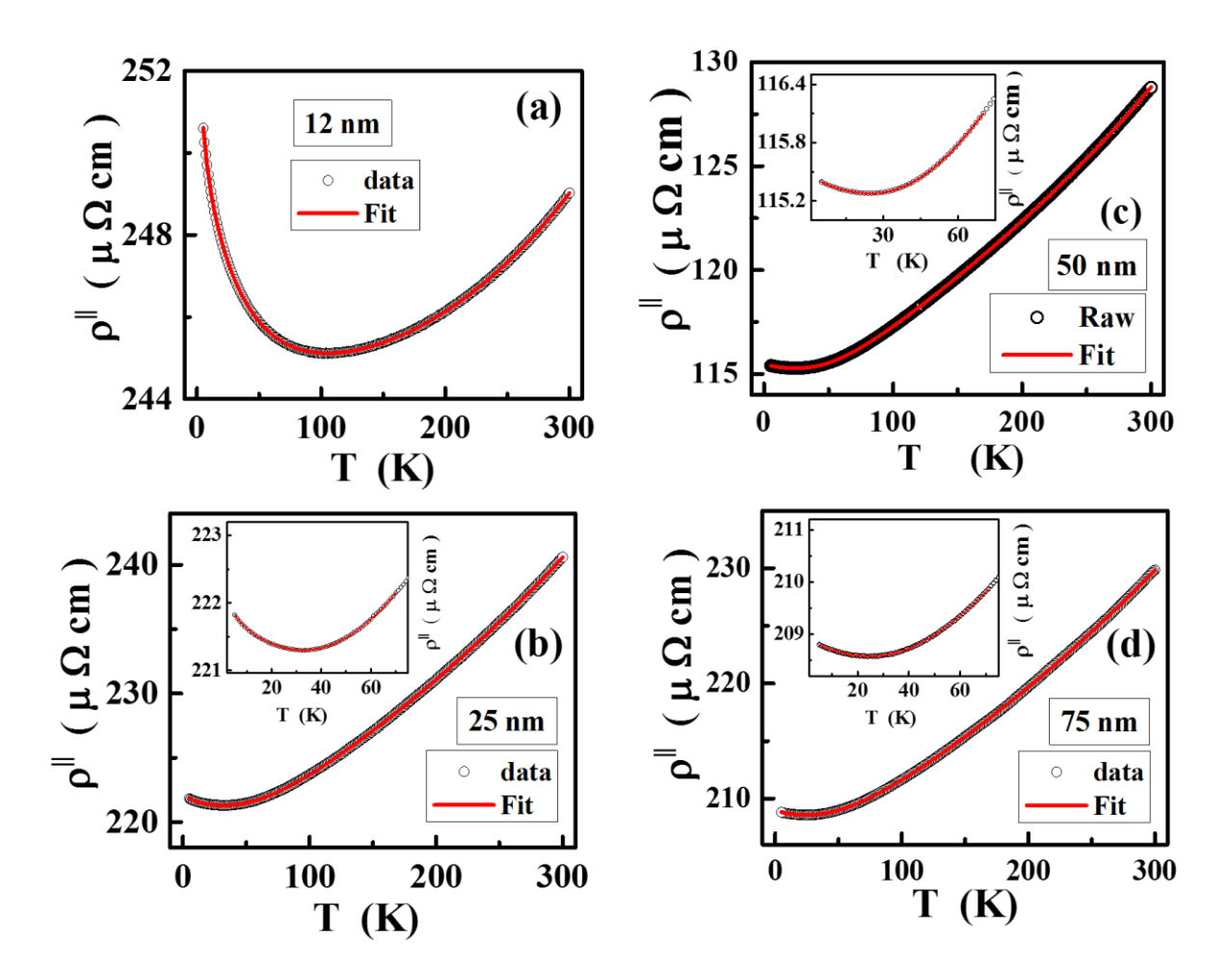


Fig. 4.16: (a) - (d) Longitudinal resistivity, $\rho(T, H = 0)$ (open circles), as a function of temperature along with theoretical fits (red solid lines), based on Eq. (4.14). Insets of sub-figures (b) - (d) show enlarged view of $\rho(T, H = 0)$ data (open circles) and the theoretical fits over the temperature range 5 K - 70 K to highlight the minimum in resistivity.

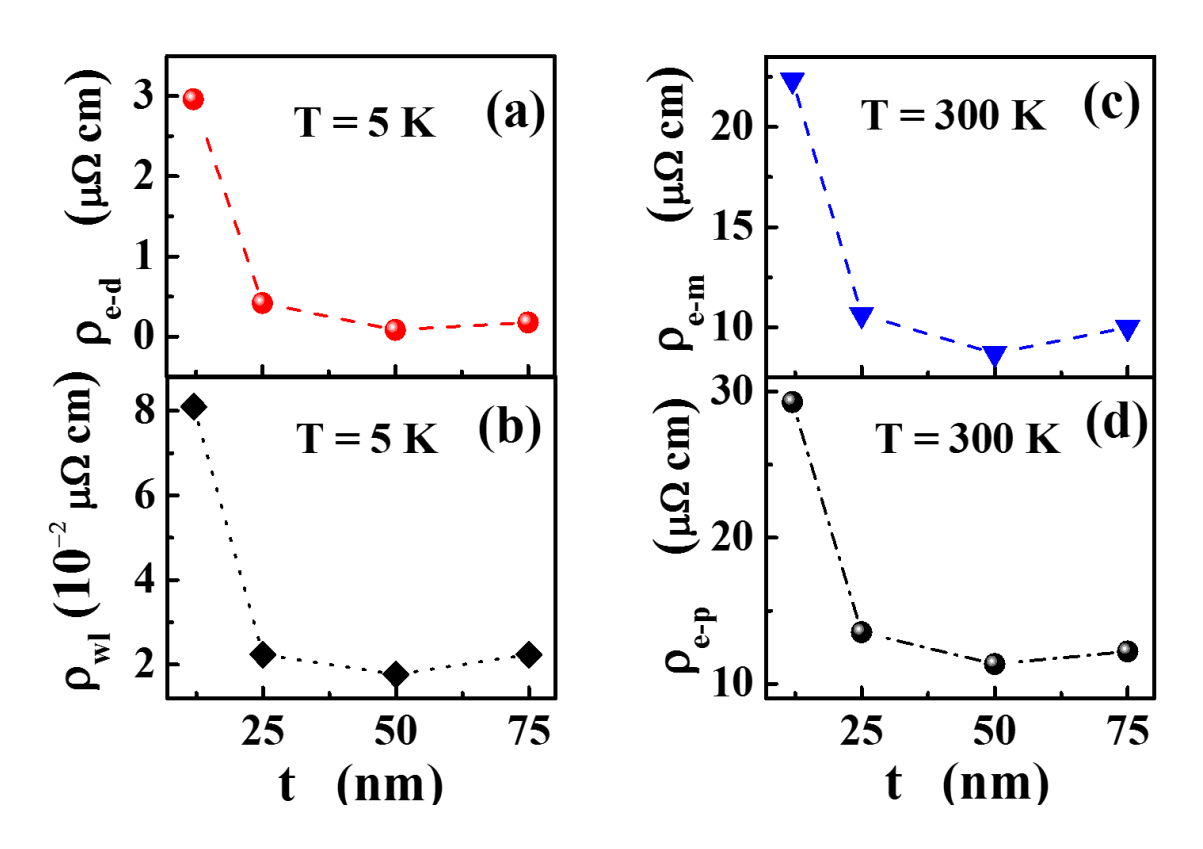


Fig. 4.17: Variation of (a) ρ_{e-d} , (b) ρ_{wl} , (c) ρ_{e-m} and (d) ρ_{e-p} with the film thickness.

Fig. 4.16 shows the longitudinal resistivity, $\rho(T,H=0)$, for the CFAS thin films with thickness t=12 nm, 25 nm, 50 nm and 75 nm, plotted as a function of temperature from 5K to 300K. The best theoretical fits (red continuous curves) to the $\rho(T,H=0)$ data (open circles) based on Eq. (4.14) are also depicted in this figure.

While the upturn in $\rho(T, H = 0)$ for $T < T_{min}$ has its origin in ρ_{e-d} and ρ_{wl} , ρ_{e-m} and ρ_{e-p} entirely account for the positive TCR at $T > T_{min}$. Furthermore, the thermal renormalization of the spin-wave stiffness, i.e., $D_{sw}(T) = D_0(1 - D_2 T^2)$ with $D_2 \neq 0$, turns out to be important in the CFAS films in question. Note that, in the thickness series case, $\rho_{e-p}(T)$ is correctly described by the BW model. The fact that the BW model is more appropriate implies that the phonon-induced non-spin-flip two-band ($s\uparrow\downarrow$ - $d\uparrow\downarrow$) scattering significantly contributes to $\rho_{e-p}(T)$.

Fig. 4.17 shows the magnitudes of ρ_{e-d} , ρ_{wl} , ρ_{e-m} and ρ_{e-p} as functions of the CFAS film thickness. Note that, in this figure, the extreme values of ρ_{e-d} and ρ_{wl} , computed at T = 5 K, and those of ρ_{e-m} and ρ_{e-p} , computed at T = 300 K, are shown. It is evident that all the contributions, ρ_{e-d} , ρ_{wl} , ρ_{e-m} and ρ_{e-p} , have minimum values at t=50 nm. This behavior is consistent with the fact that, in the entire temperature range, $\rho(T,H=0)$ for the 50 nm film is the lowest, ranging from ρ_{5K} = 115.39 $\mu\Omega$ cm to ρ_{300K} = 129.02 $\mu\Omega$ cm. Furthermore, irrespective of the film thickness, ρ_{e-d} makes larger contribution to $\rho(T,H=0)$ than ρ_{wl} at any temperature T < T_{min} whereas ρ_{e-p} > ρ_{e-m} at T > T_{min}.

4.5. Summary and conclusion

For an in-depth study of the effect of anti-site disorder on the electrical- and magneto-transport properties of Co-based Heusler compounds, 50 nm thick Co₂FeAl_{0.5}Si_{0.5} (CFAS) thin films with varying degree of site-disorder were deposited on Si(100) substrates with 300 nm SiO₂ top oxidized layer at the substrate temperatures TS = 27° C, 350° C, 450° C, 500° C and 550° C. An extensive quantitative analysis of the longitudinal and transverse 'zero-field', $\rho(T, H=0)$ and 'in-field', $\rho(T, H=0)$ and 'in-field', $\rho(T, H=0)$ and 'in-field', $\rho(T, H=0)$ and 'analysis of the longitudinal and transverse 'zero-field' theoretical models for diffusive and ballistic transport mechanisms, permits us to unambiguously draw the following conclusions.

- Variations in both the substrate temperature, TS, (RT, TS350, TS450, TS500 and TS550) and thickness (12nm, 25nm, 50 nm and 75 nm) of the CFAS thin films, the electron-diffuson (e-d) scattering and weak localization (WL) mechanisms, responsible for *negative* temperature coefficient of resistivity (TCR) for T < T_{min}, compete with the *positive* TCR mechanisms, electron-magnon (e-m) and electron-phonon (e-p) scattering, to produce the resistivity minimum at T_{min}. ρ_{e-d} and ρ_{wl} dominate over ρ_{e-m} and ρ_{e-p} for $T < T_{min}$ whereas the reverse is true for $T > T_{min}$.
- (ii) At any given temperature, ρ_{e-d} , ρ_{wl} and ρ_{e-m} decrease while ρ_{e-p} increases as the atomic order improves with increasing substrate temperature, TS.
- (iii) The SiO₂ buffer layer increases the strength of anti-site disorder in the CFAS films and hence the magnitudes of ρ_{e-d} , ρ_{wl} , ρ_{e-m} and ρ_{e-p} in all the TS CFAS thin films is higher than the films deposited on Si(100) without the SiO₂. The only exception is the TS500 film (which has the least anti-site disorder) in that the presence of the SiO₂ buffer layer does not seem to make any appreciable difference in the values of ρ_{e-d} , ρ_{wl} , ρ_{e-m} and ρ_{e-p} .
- (iv) In the thickness series of CFAS thin films, ρ_{e-d} , ρ_{wl} , ρ_{e-m} and ρ_{e-p} go through a minimum at 50 nm CFAS films, which agrees with the highest RRR for 50 nm, thereby confirming that this CFAS film has the lowest degree of disorder or equivalently, the highest structural order.
- (v) While the *phonon-induced* non-spin-flip two-band ($s\uparrow\downarrow$ $d\uparrow\downarrow$) scattering accounts for ρ_{e-p} , magnon-induced spin-flip s d interband ($s\uparrow\downarrow$ $d\downarrow\uparrow$) transitions essentially determine ρ_{e-m} .
- (vi) In the crystalline TS350, TS450, TS500 and TS550 CFAS films, the thermal renormalization of the spin-wave stiffness due to the electron-magnon interaction, i.e., $D_{sw}(T) = D_0(1 D_2 T^2)$ with $D_2 \neq 0$, contributes significantly to $\rho_{e-m}(T)$. This is also true for the CFAS films of different thicknesses.

- (vii) Negative magnetoresistance (MR) results from a progressive suppression of the WL effect and e-m scattering by external magnetic field. The 'zero-field' $\rho_{e-m}(T, H=0)$ data, when used in the expression given by the spin fluctuation model, Eq. (4.16), permits an accurate determination of $\rho_{e-m}(T, H=80 \ kOe)$ over the entire temperature range $5 \ K \le T \le 300 \ K$. This observation, in turn, implies that the WL contribution to MR is negligibly small.
- (viii) The CFAS film deposited at RT shows a positive AMR %. By contrast, the films TS350, TS450, TS500 and TS550 show a negative AMR. Another important conclusion is that the large AMR % found in the TS450 and TS500 films with the highest B2 order is due to the scattering of the *s*↑ electrons into the empty states in the d↑ spin sub-band. This inference asserts that the TS450 and TS500 films are good candidates for half-metallicity.

References

- 1. Charles Kittel, John Wiley & Sons, Inc. pg. 149-151(2005).
- 2. S. N. Kaul, W. Kettler, and M. Rosenberg, *Phys. Rev. B* **33**, (1986).
- 3. P. D. Babu, S. N. Kaul, L. Fernandez Barquin, J. C. Gomez Sal, W. H. Kettler, and M. Rosenberg, *Int. J. Mod. Phys. B* **13**, 141 (1999).
- 4. S. Srinivas, S. N. Kaul, and S. N. Kane, J. Non. Cryst. Solids 248, 211 (1999).
- 5. S. N. Kaul, W. Kettler, and M. Rosenberg, *Phys. Rev. B* **35**, (1987).
- 6. B. K. Hazra, S. N. Kaul, S. Srinath, M. M. Raja, R. Rawat, and A. Lakhani, *J. Magn. Magn. Mater.* **481**, 194 (2019).
- 7. R. Nandini and N. Kumar, *Phys. Stat. Sol.* (b) **63**, (1974).
- 8. M. S. Gabor, M. Belmeguenai, T. Petrisor, C. Ulhaq-Bouillet, S. Colis, and C. Tiusan, *Phys. Rev. B: Condens Matter Mater. Phys.* **92**, (2015).
- 9. A. Zawadowski, *Phys. Rev. Lett.* **45**, (1980).
- 10. R. W. Cochrane, R. Hariss, J. O. Strom-Olson, and M. J. Zuckermann, *Phys. Rev. Lett.* **35**, 517 (1975).
- 11. S. Tong, X. Zhao, D. Wei, and J. Zhao, *Phys. Rev. B* **101**, (2020).
- 12. Ph. Nozières and A. Blandin, Journal de Physique 41, 193 (1980).
- 13. P. Schlottmann and P. D. Sacramento, *Adv. Phys.* **42**, 641 (1993).
- 14. L. J. Zhu, S. H. Nie, P. Xiong, P. Schlottmann, and J. H. Zhao, *Nat. Commun.* 7, 10817 (2016).
- 15. Y. Huang, X. Yao, F. Qi, W. Shen, and G. Cao, Appl. Phys. Lett. 121, 162403 (2022).
- 16. M. A. Continentinot and N. Rivier, J. Phys. F: Metal Phys. 8, (1978).
- 17. B. L. Altshuler and A. G. Aronov, Elsevier Science Publisher B.V. 1 (1985).

- 18. P. A. Lee and T. V Ramakrishnan, *Rev. Mod. Phys.* **57**, 287 (1985).
- 19. M. A. Howson, J. Phys. F: Met. Phys. 14, 25 (1984).
- 20. G. Bergmann, *Physics Reports (Review Section of Physics Letters)* **107**, 1 (1984).
- 21. J. M. Ziman, Oxford University Press, New York pg. 364 (1960).
- 22. A. H. Wilson, *Proc. R. Soc. A* **167**, 580 (1938).
- 23. S. R. Nagel, *Phys. Rev. B* **16**, (1977).
- 24. B. Raquet, M. Viret, E. Sondergard, O. Cespedes, and R. Mamy, *Phys. Rev. B: Condens Matter Mater. Phys.* **66**, 244331 (2002).
- 25. D. A. Goodings, *Physical Review* **132**, (1963).
- 26. S. N. Kaul, J. Phys.: Condens. Matter 11, 7597 (1999).
- 27. S. N. Kaul, Journal of Physics Condensed Matter 17, 5595 (2005).
- 28. P. V. P. Madduri and S. N. Kaul, *Phys. Rev. B* **95**, (2017).
- 29. M. Aftab, G. Hassnain Jaffari, S. K. Hasanain, T. A. Abbas, and S. Ismat Shah, *J. Phys. D: Appl. Phys.* **45**, (2012).
- 30. L. J. Zhu and J. H. Zhao, Sci. Rep 7, (2017).
- 31. B. K. Hazra, S. N. Kaul, S. Srinath, M. M. Raja, R. Rawat, and A. Lakhani, *Phys. Rev. B* **96**, (2017).
- 32. B. K. Hazra, M. M. Raja, R. Rawat, A. Lakhani, S. N. Kaul, and S. Srinath, *J. Magn. Magn. Mater.* **448**, 371 (2018).
- 33. L. A. Longchar, M. Rahaman, B. Krishna Hazra, R. Rawat, M. Manivel Raja, S. N. Kaul, and S. Srinath, *J. Magn. Magn. Mater.* **569**, (2023).
- 34. D. Bombor, C. G. F. Blum, O. Volkonskiy, S. Rodan, S. Wurmehl, C. Hess, and B. Büchner, *Phys. Rev. Lett.* **110**, (2013).

- 35. A. P. Malozemoff, *Phys. Rev. B* (1985).
- 36. S. N. Kaul, J. Phys. F: Met. Phys. 7, 2091(1977).
- 37. I. A. Campbell, A. Fert, and O. Jaoul, J. Phys. C: Solid State Phys. 3 S95, (1970).
- 38. F. J. Yang, C. Wei, and X. Q. Chen, Appl. Phys. Lett. 102, (2013).
- 39. Y. Sakuraba, S. Kokado, Y. Hirayama, T. Furubayashi, H. Sukegawa, S. Li, Y. K. Takahashi, and K. Hono, *Appl. Phys. Lett.* **104**, (2014).
- 40. S. Kokado, M. Tsunoda, K. Harigaya, and A. Sakuma, J. Physical Soc. Japan 81, (2012).
- 41. T. R. Mcguire, J. A. Aboaf, and E. Klokholm, IEEE Trans. Magn. 20, (1984).
- 42. L. A. Longchar, M. Rahaman, B. K. Hazra, M. M. Raja, R. Rawat, S. N. Kaul, and S. Srinath, *AIP Adv.* **13**, (2023).

Chapter 5

Effect of deposition temperature and film thickness on magnetization, magnetic anisotropy, and Gilbert damping parameter in Co₂FeAl_{0.5}Si_{0.5} thin films

In this chapter, a systematic investigation reveals the impact of disorder and film thickness on magnetization, magnetic anisotropy, and the Gilbert damping parameter by studying the angular variation of resonance field and linewidth in "in-plane" and "out-of-plane" configurations. Both broad-band as well as x-band ferromagnetic resonance has been studied. Additionally, ferromagnetic resonance spectra at different temperatures are recorded to study the temperature dependance of magnetization in the CFAS thin films.

5.1 Theoretical background.

A magnetic dipole in the presence of an external magnetic field (H), experiences a torque due to which it precesses around the H direction. This is known as Larmor precession and the frequency of precession is given by the expression,

$$\omega_L = \gamma H \tag{5.1}$$

where $\gamma = g\mu_B/\hbar$ is the gyromagnetic ratio of the electron. If this precessing magnetic dipole is placed in an external microwave radiation field of frequency $\omega = \omega_L$ resonant absorption of energy occurs. The direction of the microwave field must be perpendicular to that of the static magnetic field. The condition for resonance can be written as,

$$\hbar\omega = g\mu_B H \tag{5.2}$$

This phenomenon is known as electron spin resonance (ESR) occurring within an unpaired electron spin system where magnetic moments exhibit no interaction with each other. By contrast, in a ferromagnetic material, the spins are interacting. Exchange interaction forces the spins to align

in the parallel configuration in a ferromagnetic system which results in a large internal field or spontaneous magnetization. When a ferromagnetic material encounters an external magnetic field, the spins experience the influence of both the external magnetic field (H) and an internal field which resulting from exchange interaction. Thus, ferromagnetic resonance (FMR) [1], differs from ESR by the presence of an additional internal field [1]. So, the resonance condition, Eq. (5.2), must be modified for ferromagnetic samples by replacing H by an effective field H_{eff} , which includes besides the external field, internal exchange field and anisotropy fields.

The phenomenological equation of motion for magnetization, proposed by Landau and Lifshitz (LL) [2], is given by the following expression.

$$\frac{d\vec{M}}{dt} = \gamma \left(\vec{M} \times \vec{H}_{eff} \right) - \frac{\lambda}{M_s^2} (\vec{M} \times \vec{M} \times \vec{H}_{eff})$$
 (5.3)

The initial expression on the right side signifies the torque encountered by magnetization (\vec{M}) in an effective field H_{eff} , where $H_{eff} = \vec{H} + \vec{h} (t) - \vec{H}_{dem} + \vec{H}_k + \vec{H}_{ex}$ where \vec{H} is the applied static magnetic field, $\vec{h} (t)$ represents the microwave/alternating magnetic field, \vec{H}_{dem} is the demagnetizing field, \vec{H}_k denotes the anisotropy field, \vec{H}_{ex} is the exchange field, and M_s refers to the saturation magnetization. The second term in Eq. (5.3) represents the LL damping torque that gives rise to relaxation towards the equilibrium and λ determines the relaxation rate. Further, Gilbert (G) [3] modified this damping term so that it is also suitable for low frequencies. Thus,

$$\frac{d\vec{M}}{dt} = \gamma \left(\vec{M} \times \vec{H}_{eff} \right) - \frac{\lambda}{\gamma M_s^2} \left(\vec{M} \times \frac{d\vec{M}}{dt} \right) \tag{5.4}$$

Eq. (5.4) is the Landau-Lifshitz-Gilbert (LLG) equation where λ is the LLG damping parameter.

5.2 Lineshape calculation

Consider an ellipsoidal ferromagnetic specimen exposed concurrently to a uniform static magnetic field (\vec{H}) aligned with the z-axis and an alternating (AC) magnetic field, $\vec{h}(t) = \vec{h} e^{i\omega t}$ acting within the xy plane, such that the magnitude of the AC field is smaller than that of the static field. The total magnetization of the sample is the sum of the magnetization originating from the static field and AC field, i.e., $\vec{M} = \vec{M}_s + \vec{m}(t)$ with $\vec{m}(t) = \vec{m} e^{i\omega t}$ and $|\vec{m}(t)| << |\vec{M}_s|$. It is assumed that the static field is sufficiently strong to saturate the system, so that both M_s and H

point in the same direction. The effective magnetic field $H_{eff} = \vec{H} + \vec{h} \ (t) - \vec{H}_{dem} + \vec{H}_k + \vec{H}_{ex}$ where $\vec{H}_{dem} = -\mathbf{D} \cdot \vec{M}$ is the demagnetizing field, $\vec{H}_k = \vec{D}_k \cdot \vec{M}$ is the uniaxial anisotropy field with the easy axis along \vec{H} . The anisotropy is taken as uniaxial type to simplify the calculation. Since exchange stiffness constant is very small, which results in a small exchange field, and hence is neglected to simplify the calculation. \vec{D} and \vec{D}_k are diagonal tensors and M is the saturation magnetization. Substituting the value of \vec{M} and H_{eff} in Eq. (5.4) yields [4–7].

$$\frac{d\vec{m}(t)}{dt} = \gamma [\vec{M}_s \times \vec{h}(t) + \vec{m}(t) \times \vec{H} - \vec{M} \times (\vec{D} \cdot \vec{M}) - \vec{M} \times (\vec{D}_k \cdot \vec{M}) - \frac{\lambda}{\gamma M^2} ([\vec{M}_s + \vec{m}(t)] \times \frac{d}{dt} [\vec{M}_s + \vec{m}(t)])]$$
(5.5)

where the term γ [$\vec{m}(t) \times \vec{h}(t)$] has been dropped due to the smaller magnitude and $\frac{dM_S}{dt} = 0 = \gamma$ ($\vec{M}_S \times H$) is used to simplify the Eq. (5.5). Using the relation $\vec{m}(t) = \vec{m}e^{i\omega t}$. Disregarding the terms of the second order, the cartesian elements of Eq. (5.5) are simplified to:

$$\left(\frac{i\omega}{\gamma}\right)m_x + \left[H + \left(D_y + D_{ky} - D_z - D_{kz}\right)M_s + i\Gamma\right]m_y = M_s h_y \tag{5.6}$$

$$-[H + (D_x + D_{kx} - D_z - D_{kz})M_s + i\Gamma]m_x + \left(\frac{i\omega}{\gamma}\right)m_y = -M_s h_x$$
 (5.7)

$$m_z = 0 (5.8)$$

where $\Gamma = \frac{\lambda \omega}{\gamma^2 M_s}$, is known as the FMR LLG linewidth. Eliminating m_y from Eqs. (5.6) and (5.7) gives.

$$m_x = \chi_{xx} h_x + \chi_{xy} h_y \tag{5.9}$$

with
$$\chi_{xx} = [H + (D_y + D_{ky} - D_z - D_{kz})M_s + i\Gamma]M_s\eta^{-1}$$
 (5.10)

$$\chi_{xy} = (i\omega/\gamma)M_s\eta^{-1} \tag{5.11}$$

and

$$\eta = [H + (D_x + D_{kx} - D_z - D_{kz})M_s][H + (D_y + D_{ky} - D_z - D_{kz})M_s] - \Gamma^2$$

$$-\left(\frac{\omega}{\gamma}\right)^2 + i\Gamma[2H + (D_x + D_y + D_{kx} + D_{ky} - 2D_z - 2D_{kz})M_s]$$
(5.12)

Elimination of m_x instead of m_y from Eqs. (5.6) and (5.7) resulted in,

$$m_{\mathcal{V}} = \chi_{\mathcal{V}\mathcal{X}} h_{\mathcal{X}} + \chi_{\mathcal{V}\mathcal{V}} h_{\mathcal{V}} \tag{5.13}$$

where $\chi_{xx} = \chi_{yy} = \chi$ is the dynamic susceptibility and $\chi_{xy} = -\chi_{yx} = i G$, \vec{G} is the gyration vector. Since the dynamic susceptibility and dynamic permeability μ are complex, i.e., $\chi = \chi' - i \chi''$ and $\mu = \mu' - i \mu''$, using the relation $\mu = 1 + 4 \pi \chi$, the real and imaginary parts of the dynamic permeability are given by [4-7]

$$\alpha \{ [H + (D_y + D_{ky} - D_z - D_{kz}) M_x] [B + (D_x + D_{kx} - D_z - D_{kz})] - \Gamma^2$$

$$\mu' = \frac{-\left(\frac{\omega}{\gamma}\right)^2 \} + \beta \Gamma(B + H) + (D_x + D_y + D_{kx} + D_{ky} - 2D_z - 2D_{kz}) M_s]}{(\alpha^2 + \beta^2)}$$
(5.14)

$$\mu'' = \frac{\{-\alpha\Gamma[(B+H_k)-(H+H_k)] + \beta[(B+H_k)-(H+H_k)]\}}{\times [H+(D_y+D_{ky}-D_z-D_{kz})M_s]\}}$$
(5.15)

with

$$\alpha = [H + (D_x + D_{kx} - D_z - D_{kz})M_s][H + (D_y + D_{ky} - D_z - D_{kz})M_s]$$
$$-\Gamma^2 - \left(\frac{\omega}{\gamma}\right)^2 \qquad (5.16)$$

$$\beta = \Gamma \left[2H + \left(D_x + D_y + D_{kx} + D_{ky} - 2D_z - 2D_{kz} \right) M_s \right]$$
 (5.17)

and

$$B = H + 4\pi M_s \tag{5.18}$$

Considering a flat plane where H is oriented along the symmetry axis (z-axis) in terms of uniaxial anisotropy and lies within the sample plane (parallel configuration), $D_x = D_z = 0$, $D_y = 4\pi$ (The choice is made for the x-axis to align with the polar axis), $D_{kx} M_s = D_{ky} M_s = H_k$ and $D_{kz} = 0$. Substituting these component values of \vec{D} and \vec{D}_k , Eqs. (5.14) - (5.17) are simplified to yield [4 – 7]

$$\mu' = \frac{\left[(H + H_k)(B + H_k) - \Gamma^2 - \left(\frac{\omega}{\gamma}\right)^2 \right] \left[(B + H_k)^2 - \Gamma^2 - \left(\frac{\omega}{\gamma}\right)^2 \right] + 2\Gamma^2(B + H_k)(B + H + 2H_k)}{\left[(H + H_k)(B + H_k) - \Gamma^2 - \left(\frac{\omega}{\gamma}\right)^2 \right]^2 + \Gamma^2(B + H + 2H_k)^2}$$
(5.19)

$$\mu'' = \frac{-2\Gamma((B+H_k)\left[(B+H_k)(B+H_k)-\Gamma^2-\left(\frac{\omega}{\nu}\right)^2\right]+\Gamma(B+H+2H_k)\left[(B+H_k)^2-\Gamma^2-\left(\frac{\omega}{\nu}\right)^2\right]}{\left[(B+H_k)(B+H_k)-\Gamma^2-\left(\frac{\omega}{\nu}\right)^2\right]^2+\Gamma^2(B+H+2H_k)^2}$$
(5.20)

The microwave power absorbed by the specimen, linked to the surface impedance [8], in the parallel configuration is expressed as:

$$P_{\parallel} \propto [(\mu'^2 + \mu''^2)^{\frac{1}{2}} + \mu'']^{1/2}$$
 (5.21)

The theoretical calculation of the derivative of power absorption with respect to magnetic field $(\frac{dP_{\parallel}}{dH})$ can be determined by combining the Eqs. (5.19) - (5.21) and taking the field derivative of Eq. (5.21). The resonance frequency ($\omega = \omega_r$) can be calculated from Eqs. (5.6) and (5.7) by the condition that m_x and m_y have non-trivial solutions only when $h_x = h_y = 0$. This implies that,

$$\begin{vmatrix} i\omega_{res}/\gamma & \{-[H_{res} + (D_y + D_{ky} - D_z - D_{kz})M_s + i\Gamma]\} \\ \{-[H_{res} + (D_x + D_{kx} - D_z - D_{kz})M_s + i\Gamma]\} & i\omega_{res}/\gamma \end{vmatrix}$$

$$= 0$$

(5.22)

where H_{res} is the resonance field corresponding to ω_{res} . After solving the determinant of Eq. (5.22) and simplifying, we find

$$\left[\left(\frac{\omega}{\gamma} \right)^2 + \Gamma^2 \right] = \left[H_{res} + \left(D_y + D_{ky} - D_z - D_{kz} \right) M_s \right]$$

$$\times [H_{res} + (D_x + D_{kx} - D_z - D_{kz})M_s]$$
 (5.23)

Throughout the experiment, the microwave frequency (ω) remains constant, while the static field is systematically varied to meet the resonance condition. If, $D_x = D_z = 0$, $D_y = 4\pi$, $D_{kx}M_s = D_{ky}M_s = H_k$ and $D_{kx} = 0$, then Eq. (5.23) reduces to

$$\left[(\omega / \gamma)^2 + r_{||h}^2 \right] = \left(H_{res}^{||h} + 4\pi M_S + H_k \right) \left(H_{res}^{||h} + H_k \right) \tag{5.24}$$

and if $D_x = D_z = 0$, $D_y = 4\pi$, $D_{kx}M_s = D_{ky}M_s = H_k$ and $D_{kx} = 0$, then Eq. (5.23) reduces to

$$\left[\left(\frac{\omega}{\gamma} \right)^2 + r_{\parallel \nu}^2 \right] = \left(H_{res}^{\parallel h} + H_k \right) \tag{5.25}$$

With the assumption of $H_k \ll 4\pi M_s$, Eq. (5.25) can be rewritten in a form similar to Eq. (5.24) as

$$\left[\left(\omega/\gamma\right)^{2}+r_{||}^{2}\right]=\left(H_{res}^{||}+4\pi M_{S}-H_{k}\right)\left(H_{res}^{||\gamma}+H_{k}\right) \tag{5.26}$$

Putting $H_k = 0$ in Eqs. (5.24) and (5.26), results in

$$\left[\left(\frac{\omega}{\gamma} \right)^2 + r_{||\nu|}^2 \right] = \left(H_{res}^{||\nu|} + 4\pi M_s - H_k \right) \left(H_{res}^{||h|} + H_k \right)$$
 (5.27)

and

$$(H_{res}^{||} + 4\pi M_S) H_{res}^{||} = (H_{res}^{||\gamma} + 4\pi M_S - H_k) (H_{res}^{||\gamma} - H_k)$$
 (5.28)

where H_{res} represent the resonance field in the absence of uniaxial anistropy, i.e., $H_k = 0$. This is possible only when,

$$H_{res}^{||} = H_{res}^{||h} + H_k \text{ or } H_{res}^{||h} = H_{res}^{||} - H_k$$
 (5.29)

$$H_{res}^{||} = H_{res}^{||\nu} + H_k \text{ or } H_{res}^{||\nu} = H_{res}^{||} + H_k$$
 (5.30)

From Eqs. (5.29) and (5.30) it follows that

$$H_k = \frac{H_{res}^{||v} - H_{res}^{||h}}{2} \tag{5.31}$$

Therefore, 'in-plane' uniaxial anisotropy can be determined from Eq. (5.31) by measuring the resonance field in horizontal-parallel ('in-plane' easy axis) and vertical-parallel ('in-plane' hard axis) sample configurations.

5.3 Angular variation of the resonance field

Imagine a coordinate system where the xy plane signifies the plane of the film, and the z-axis is perpendicular to the film plane. The angle θ_H (θ_M) represents the inclination between the magnetic field (magnetization) and the normal to the film. The magnetic field's (magnetization's) projection onto the xy plane forms an angle φ_H (φ_M) with the x-axis. It is assumed that the anisotropy field lies in the xy plane, forming an angle φ_k with the x-axis. Various components contributing to the free energy density, F, in a film with 'in-plane' uniaxial anisotropy, as per the chosen coordinate system, are outlined below.

- (i) Zeeman energy $(F_z) = -MH \left[\sin \theta_m \sin \theta_H \cos(\varphi_M \varphi_H) + \cos \theta_M \cos \theta_H \right]$
- (ii) Shape anisotropy $(F_s) = 2\pi M^2 \cos^2 \theta_M$
- (iii) Uniaxial anisotropy $(F_u) = K_u [1 \sin^2 a \cos^2 (\varphi_M \varphi_k)]$

Therefore, total energy can be written as

$$F = F_2 + F_s + F_u$$

$$= -MH \left[\sin \theta_m \sin \theta_H \cos(\varphi_M - \varphi_H) + \cos \theta_M \cos \theta_H \right]$$

$$+ 2\pi M^2 \cos^2 \theta_M + K_u \left[1 - \sin^2 \cos^2(\varphi_M - \varphi_k) \right]$$
(5.32)

Now, $\frac{\partial F}{\partial \theta_M} = 0$ and $\frac{\partial F}{\partial \varphi_M} = 0$ are the equilibrium conditions. The resonance condition is given by [9]

$$\left(\frac{\omega}{\nu}\right)^{2} = \frac{1}{M^{2}\sin^{2}\theta_{M}} \left[\left(\frac{\partial^{2}F}{\partial\theta_{M}^{2}}\frac{\partial^{2}F}{\partial\varphi_{M}^{2}}\right) - \left(\frac{\partial^{2}F}{\partial\theta_{M}\partial\varphi_{M}}\right)^{2} \right]$$
(5.33)

In order to get the resonance condition, first and second derivatives of free energy (F) with respect to θ_M and φ_M have to be calculated. The first derivative of F with respect to θ_M and φ_M are given by following expressions.

$$\frac{\partial F}{\partial \theta_M} = -MH \left[\cos \theta_M \sin \theta_H \cos(\varphi_M - \varphi_H) - \sin \theta_M - \cos \theta_H \right] + 2\pi M^2 \sin 2\theta_M$$
$$-K_u \sin 2\theta_M \cos^2(\varphi_M - \varphi_k)$$

$$\frac{\partial F}{\partial \varphi_M} = MH \sin \theta_M \sin \theta_H \sin(\varphi_M - \varphi_H) - K_u \sin^2 \theta_M \sin 2(\varphi_M - \varphi_k)$$
(5.35)

Considering $\frac{\partial F}{\partial \theta_M} = 0$, yields:

$$H_{res} \left[\sin \theta_M \cos \theta_H - \cos \theta_M \sin \theta_H \cos(\varphi_M - \varphi_H) \right]$$

$$= 2\pi M \sin 2\theta_M + \frac{H_k}{2} \sin 2\theta_M \cos^2(\varphi_M - \varphi_k)$$
(5.36)

where $H_k = 2 K_u/M$. Similarly, $\frac{\partial F}{\partial \varphi_M} = 0$, gives

$$H_{res}\sin\theta_H\sin(\varphi_M-\varphi_H) = \frac{H_k}{2}\sin\theta_M\sin2(\varphi_M-\varphi_k)$$
 (5.37)

(5.34)

The second-order derivatives are given by the following expressions.

$$\frac{\partial^2 F}{\partial^2 \theta_M^2} = M H_{res} [\sin \theta_m \sin \theta_H \cos(\varphi_M - \varphi_H) + \cos \theta_M \cos \theta_H]$$

$$- M \cos 2\theta_M [4\pi M + H_k \cos^2(\varphi_M - \varphi_k)]$$
(5.38)

$$\frac{\partial^2 F}{\partial \varphi_M^2} = M \sin^2 \theta_M \left[H_{res} \left(\cos \theta_M \cos \theta_H + \sin \theta_M \sin \theta_H \cos (\varphi_M - \varphi_H) \right) \right] - (4\pi M + H_k \cos^2 (\varphi_M - \varphi_k)) \cos^2 \theta_M + H_k \cos^2 (\varphi_M - \varphi_k)$$
(5.39)

$$\frac{\partial^2 F}{\partial \theta_M \partial \varphi_M} = M H_{res} \cos \theta_M \sin \theta_H \sin(\varphi_M - \varphi_H) + K_u \sin 2\theta_M \sin 2(\varphi_M - \varphi_k)$$
(5.40)

Substituting the value of $\frac{\partial^2 F}{\partial^2 \theta_M^2}$, $\frac{\partial^2 F}{\partial \phi_M^2}$, $\frac{\partial^2 F}{\partial \theta_M \partial \phi_M}$ into the Eq. (5.33) and simplifying, the resonance condition is given by

$$\left(\frac{\omega}{\nu}\right)^{2} = \left\{ \begin{bmatrix} H_{res}(\sin\theta_{M}\sin\theta_{H}\cos(\varphi_{M} - \varphi_{H}) + \cos\theta_{M}\cos\theta_{H}) \\ -\cos2\theta_{M}(4\pi M + H_{k}\cos^{2}(\varphi_{M} - \varphi_{k})) \end{bmatrix} \right. \\
\times \left[\left(H_{res}(\cos\theta_{M}\cos\theta_{H} + \sin\theta_{M}\sin\theta_{H}\cos(\varphi_{M} - \varphi_{H})) \right) \\ - \left(4\pi M + H_{k}\cos^{2}(\varphi_{M} - \varphi_{k}) \right)\cos^{2}\theta_{m} + H_{k}\cos2(\varphi_{M} - \varphi_{k}) \right\} \\
- \left[\frac{H_{k}}{2}\cos\theta_{m}\sin2(\varphi_{M} - \varphi_{k}) \right]^{2} \tag{5.41}$$

(a) The 'In-plane' case

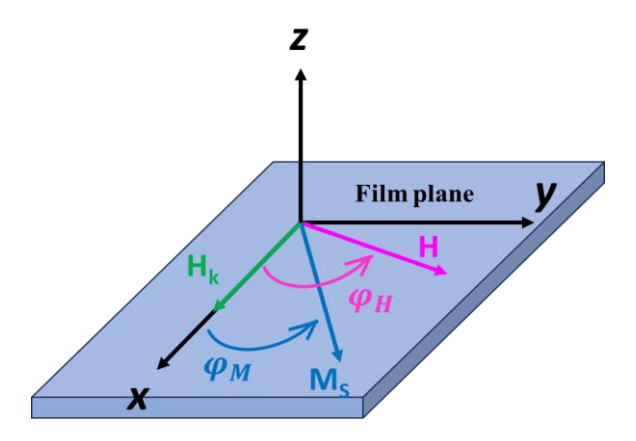


Fig. 5.1: In-plane configuration geometry.

Considering M_s and H along the sample plane (xy plane) gives the in-plane configuration, i.e., $\theta_M = \theta_H = \pi/2$ and the angles φ_M , φ_H and φ_k are determined relative to the x-axis within the sample plane, refer Fig. 5.1. The resonance condition and equilibrium condition for magnetization are derived from the Eqs. (5.41) and (5.37), substituting the value of $\theta_M = \theta_H = \pi/2$, as resonance condition

$$(\omega / \nu)^{2} = \left[H_{res}^{||} \cos(\varphi_{H} - \varphi_{M}) + 4\pi M + H_{k} \cos^{2} \varphi_{M} \right] \left[H_{res}^{||} \cos(\varphi_{H} - \varphi_{M'}) + H_{k} \cos(2\varphi_{M'}) \right]$$
$$= H_{1}^{||} H_{2}^{||}$$

(5.42)

where, $H_1^{||} \equiv \left[H_{res}^{||} \cos(\varphi_H - \varphi_M) + 4\pi M + H_k \cos^2 \varphi_M \right]$ and $H_2^{||} \equiv \left[H_{res}^{||} \cos(\varphi_H - \varphi_M) + H_k \cos(2\varphi_M) \right]$ are stiffness fields for IP case.

Now the relation $[\partial F/\partial \varphi_M = 0]$

$$2H_{res}^{||}\sin(\varphi_H - \varphi_M) = H_k\sin(\varphi_M)$$
(5.43)

 H_{res}^{\parallel} as function φ_H can be calculated by the solving the Eq. (5.42) and equilibrium condition of magnetization, i.e., Eq. (5.43). For simplicity φ_k is taken as zero, i.e., along the x direction.

(b) The 'Out-of-plane' case

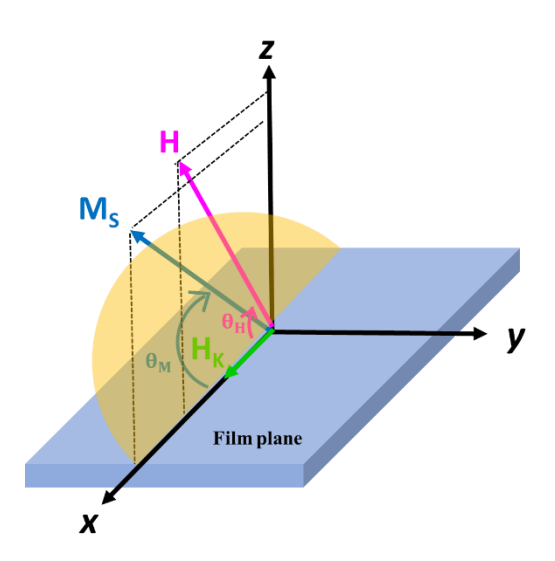


Fig. 5.2: Out-of-plane configuration geometry.

For 'out-of-plane' configuration, H and M_s are along to the xz plane, Fig. 5.2. The resonance condition and equilibrium condition for magnetization are obtained with value of $\varphi_H = \varphi_M = \varphi_K = 0$ from the Eqs. (5.41) and (5.36).

Resonance condition

$$\left(\frac{\omega}{\nu}\right)^{2} = \left[H_{res}^{\perp}\cos(\theta_{H} - \theta_{M}) - (4\pi M + H_{k})\cos 2\theta_{M}\right]
\times \left[H_{res}^{\perp}\cos(\theta_{H} - \theta_{M}) - 4\pi M\sin^{2}\theta_{\mu} + H_{k}\cos^{2}\theta_{m}\right] = H_{1}^{\perp}H_{2}^{\perp}$$
(5.44)

Where, $H_1^{\perp} \equiv [H_{res}^{\perp} \cos(\theta_H - \theta_M) - (4\pi M + H_k) \cos 2\theta_M]$ and $H_2^{\perp} \equiv [[H_{res}^{\perp} \cos(\theta_H - \theta_M) - 4\pi M \sin^2 \theta_\mu + H_k \cos^2 \theta_m]$ represent stiffness fields in OP configuration.

Under the condition that $[\partial F/\partial \varphi_M = 0]$

$$\frac{\cos \theta_H}{\cos \theta_M} - \frac{\sin \theta_H}{\sin \theta_M} = \frac{4\pi M + Hk}{H_{res}^{\perp}}$$
(5.45)

By solving the Eq. (5.44) numerically at equilibrium condition (i.e., Eq. (5.45)), 'out-of-plane' resonance field (H_{res}^{\perp}) as function of 'out-of-plane' field angle (θ_H) can be deduced.

5.4 Angular variation of linewidth

The ferromagnetic resonance "peak-to-peak" value linewidth, ΔH , indicates the rate at which magnetization returns to its equilibrium state after the static magnetic field is turned off. In accordance with the Arias and Mills framework [10 –13], encompassing intrinsic and extrinsic damping mechanisms, the ferromagnetic resonance (FMR) linewidth can be expressed as:

$$\Delta H = \Delta H^{LLG} + \Delta H^{TMS} \tag{5.46}$$

The first term of Eq. (5.46) is Gilbert damping contribution, which is the intrinsic contribution is given by:

$$\Delta H^{LLG} = \frac{2}{\sqrt{3}} \frac{\alpha \omega}{\gamma M_c \Xi} \tag{5.47}$$

In Eq. (5.47), α is Gilbert damping constant. When the external field angle deviates from the equilibrium magnetization angle, it results in the displacement of magnetization by the field. This displacement is quantified through the dragging function, which is defined as

$$\Xi = \frac{1}{H_1 + H_2} \frac{d(\omega/\nu)^2}{dH_{res}} \tag{5.48}$$

The second term in Eq. (5.46), is the two-magnon scattering (TMS) contribution which is extrinsic,

$$\Delta H^{TMS} = \frac{\Gamma}{\gamma \Xi} \tag{5.49}$$

 Γ is rate at which two-magnon scatter and is dependent on the frequency and magnetic field angle. The TMS has its origin from the nonuniform magnon modes having wave vector $k \neq 0$ [14, 15].

Additionally, angular spread of crystallite misorientation and inhomogeneity in the magnetization cause an inhomogeneous broadening of the linewidth, as proposed by *Chappert et. al.*, [16, 17]. The inhomogeneous broadening contributions are given by the following expressions,

$$\Delta H^{inhom} = \Delta H^{4\pi Meff} + \Delta H^{\varphi_H \text{ or } \theta_H}$$
 (5.50)

Here,
$$\Delta H^{4\pi M_{eff}} = |\frac{\partial H_{res}}{\partial (4\pi M_{eff})}|\Delta (4\pi M_{eff})$$
 (5.51)

$$\Delta H^{\varphi_H \theta_H} = \left| \frac{\partial H_{res}}{\partial \varphi_H} \right| \Delta(\varphi_H \text{ or } \theta_H)$$
 (5.52)

where $\Delta(4\pi Meff)$ and $\Delta(\varphi_H \ or \ \theta_H)$ are the distributions of $4\pi Meff$ and the average distribution of anisotropy axis in the film plane. Different contributions to the linewidth are evaluated for the IP and OP configurations in the next section.

The 'In-plane' case

The dragging function (Ξ) can be calculated for the IP configuration from Eqs. (5.42) and (5.48) and gives $\Xi = cos(\varphi_H - \varphi_M)$. If 'in-plane' anisotropy is small, applied magnetic field and magnetization are parallel, i.e., $\varphi_H = \varphi_M$, and hence $\Xi = 1$.

(I) Substituting the value of dragging function in Eq. (5.47), the Gilbert damping contribution reduces to

$$\Delta H^{LLG} = \frac{2}{\sqrt{3}} \frac{\alpha \omega}{\gamma Ms} \tag{5.53}$$

It can be seen from the above equation that Gilbert damping contribution in IP, is not angular dependent but depends on the frequency.

(II) The modified two-magnon scattering (TMS) contribution to the linewidth in IP geometry is given by [18–20]

$$\Delta H^{TMS} = \Gamma_0 + \Gamma_2 \cos 2(\varphi_H - \varphi_2) + \Gamma_4 \cos 4(\varphi_H - \varphi_4) / \arcsin\left(\frac{f}{\sqrt{f^2 + f_0^2 + f_0}}\right)$$
(5.54)

where Γ_2 , Γ_4 are strength of the two-fold, four-fold symmetry, respectively.

(III) The inhomogeneous contribution due to the inhomogeneity in the magnetization can be derived from Eqs. (5.42) and (5.51) and is given by

$$\Delta H^{4\pi M_{eff}} = \frac{H_2^{\parallel}}{\left(H_1^{\parallel} + H_2^{\parallel}\right)\cos(\varphi_H - \varphi_M)} \Delta \left(4\pi M_{eff}\right) \tag{5.55}$$

(**IV**) The inhomogeneous contribution due to the angular distribution of crystallite, deduced from Eqs. (5.42) and (5.52) and is given by

$$\Delta H^{\varphi_H} = H_r^{||} \tan(\varphi_H - \varphi_M) \Delta \varphi_H \tag{5.56}$$

The 'Out-of-plane' case

In 'out-of-plane' (OP) configuration, magnetization lags behind the applied magnetic field, which results in the equilibrium magnetization angle different from the applied field angle. The dragging function (\mathcal{E}) can be calculated for the OP configuration from Eqs. (5.44) and (5.48) and the result is $\mathcal{E} = \cos(\theta_H - \theta_M)$.

(I) Substituting the value of dragging function in Eq. (5.47), the Gilbert damping contribution can be expressed as

$$\Delta H^{LLG} = \frac{2}{\sqrt{3}} \frac{\alpha \omega}{\gamma M_S \cos(\theta_H - \theta_M)}$$
 (5.57)

It is evident from the above expression that Gilbert damping contribution in the OP configuration strongly depends on field angle (θ_H) and frequency.

(II) Two-magnon scattering (TMS) contribution to the linewidth in the OP geometry is given by [12]

$$\Delta H^{TMS} = \frac{2}{\sqrt{3}} \Gamma(H_0, \theta_H) \sin^{-1} \sqrt{\frac{H_1^{\perp}}{H_1^{\perp} + M_{eff}}} \times \frac{\cos(2\theta_m)}{\cos^2 \theta_M}$$
 (5.58)

$$\Gamma(H_0, \theta_H) = \frac{8^{H_K^2 b^2 p} / \pi D}{(H_1^{\perp} + H_2^{\perp})^2 \Xi} \left(\left\langle \frac{C}{a} \right\rangle - 1 \right) (H_2^{\perp} \times H_2^{\perp})$$

$$+ \left(\left\langle \frac{a}{C} \right\rangle - 1 \right) \times \left[H_1^{\perp} \cos(2\theta_M) + H_2^{\perp} \cos^2 \theta_m \right]^2 + \left[H_1^{\perp} \cos(2\theta_M) - H_2^{\perp} \sin^2 \theta_M \right]^2 \right]$$
(5.59)

where D is the exchange stiffness constant for the ferromagnetic film. In this formalism, defects are assumed to be rectangular in shape with lateral dimensions a and c and height b, if defect is an island; p is the fraction of film surface covered by the defects. Eq. (5.58) bears out that TMS becomes inactive [12] for angle $\theta_M > \pi/4$.

(III) The contribution to the linewidth due to the inhomogeneity in magnetization can be calculated from Eqs. (5.44) and (5.51) with the result

$$\Delta H^{4\pi M_{eff}} = \frac{H_2^{\perp} \sin^2 \theta_M - H_1^{\perp} \cos 2\theta_M}{(H_1^{\perp} + H_2^{\perp}) \cos(\theta_H - \theta_M)} \Delta (4\pi M_{eff})$$
 (5.60)

(IV) The contribution to linewidth arising from the angular distribution of crystallites calculated from Eqs. (5.44) and (5.52) and is given by

$$\Delta H^{\theta_H} = H_{res}^{\perp} \tan(\theta_H - \theta_M) \Delta \theta_H \tag{5.61}$$

5.5 Data analysis, results, and discussion.

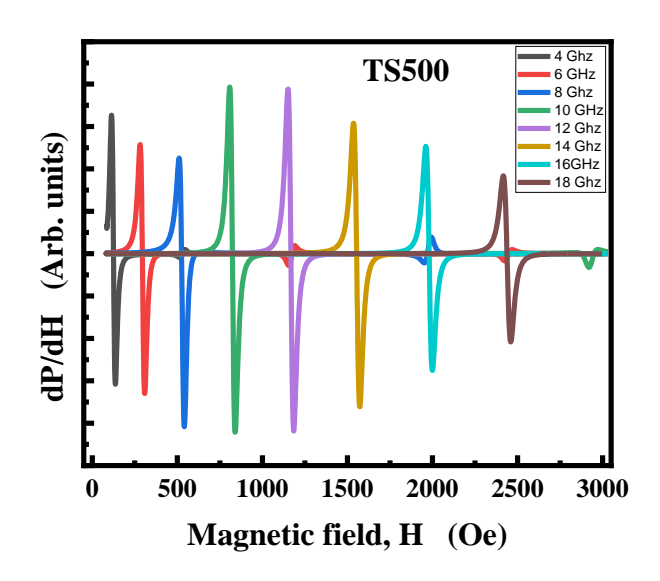
5.5.1 Effect of deposition temperature

5.5.1.1 Broad band FMR

The resonance signal, S_{12} or the ferromagnetic resonance (FMR) spectra has been recorded using a coplanar-wave guide broad-band FMR at different frequencies from 4 GHz to 18 GHz at 0.5 GHz intervals. Fig. 5.3(a) shows the FMR spectra of TS500 CFAS films. To record the FMR spectra, first the frequency is fixed, after that the static magnetic field (H) is swept up to a maximum of 3500 Gauss. The thin films for characterization, were cut into 5×5 mm sizes, which are placed carefully on top of the signal line of the CPW. The measurements were carried out in in-pane configuration (IP), i.e. H is applied along the film plane and correspondingly, perpendicular to the microwave field (H_{AC}). To ensure that the FMR spectra is measured along the easy-axis of magnetization, the spectra is initially recorded at varying in-plane angles with respect to the H, following which, the direction where the minimum resonance field is obtained is taken as the IP easy axis. Fig. 5.3(b) shows the field derivative of transmission signal $\left(\frac{dS_{12}}{dH}\right)$ as a function of static magnetic field (H) recorded at 8 GHz for TS500. From the plots, the recorded FMR spectra is not symmetric, thus, in order to extract the resonance field, H_{res}^{\parallel} and linewidth, ΔH^{\parallel} , the FMR spectra is fitted and analysed using an asymmetric Lorentzian function [21] given by:

$$\frac{dS_{12}}{dH} = a - b \frac{2\Delta H^{2} (H - H_{res}^{\parallel})}{\left[(H - H_{res}^{\parallel})^{2} + \Delta H^{\parallel^{2}} \right]^{2}} - c \frac{\Delta H \left[(H - H_{res}^{\parallel})^{2} - \Delta H^{\parallel^{2}} \right]}{\left[(H - H_{res}^{\parallel})^{2} + \Delta H^{\parallel^{2}} \right]^{2}}$$
(5.62)

The asymmetric Lorentzian function given by Eq. (5.62) considers both the absorptive and the dispersive contributions to the FMR spectra. Here, the derivative of the transmission signal of the co-planar waveguide is the same as the field derivative of the FMR spectra in a resonance cavity,



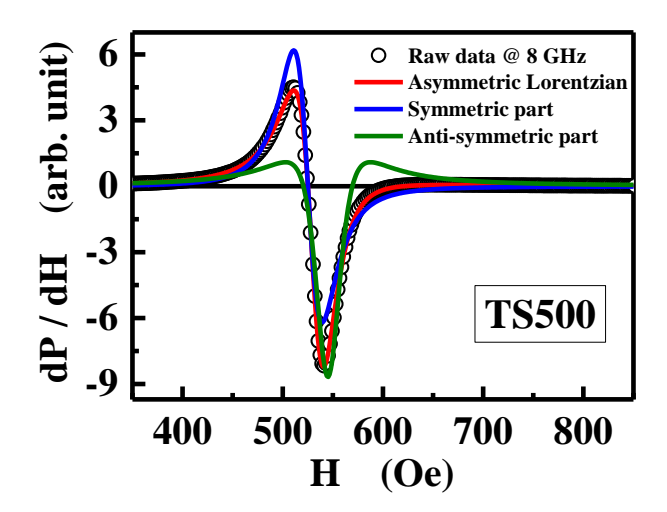


Fig. 5.3: (a) FMR spectra recorded from 4 to 18 GHz for TS500 CFAS film and (b)Asymmetric Lorentzian fit showing the symmetric (absorptive) and anti-symmetric (dispersive) terms.

 $\frac{dS_{12}}{dH} \propto \frac{dP}{dH}$. The second term in Eq. (5.62) attributes for the symmetric part where *b* is the absorptive coefficient and the third term considers the anti-symmetric part with *c* as the measure of dispersive contribution.

During the fit, $H_{res}^{||}$ and $\Delta H^{||}$ are set as free fitting parameters. As seen in Fig. 5.3(b), it is evident that the symmetric and anti-symmetric part alone (represented by the blue and green continuous lines respectively) do not fit the observed $\frac{dS_{12}}{dH}$ spectra. Whereas the asymmetric Lorentzian function given by Eq. (5.62) with both the absorptive and the dispersive contributions, describes the observed FMR spectra very well, such a fit is represented by the red continuous lines. The value of $H_{res}^{||}$ and $\Delta H^{||}$ obtained from such a fit is plotted against the frequency ($\omega = 2\pi f$) and is presented in Fig. 5.5 and 5.6.

The variation of $H_{res}^{||}$ with ω (= $2\pi f$) is fitted using the Kittel resonance condition [22], which is given by the expression.

$$\omega = \gamma \sqrt{\left(H_{res}^{||} + H_{k}^{||}\right) \times \left(H_{res}^{||} + H_{k}^{||} + 4\pi M_{s}\right)}$$
 (5.63)

here, $\gamma = g \mu_B/\hbar$, the gyromagnetic ratio, g is the Landé splitting factor, M_s is the saturation magnetization and H_k^{\parallel} is the IP anisotropy field.

The fit to the data using Eq. (5.63) is shown in Fig. (5.4) by the red continuous lines. As seen in figure, the Kittel resonance condition accurately describes the observed variation of $H_{res}^{||}$ with ω (= $2\pi f$). The Landé g-factor, M_s and $H_k^{||}$ obtained from the Kittel fit is tabulated in Table 5.1. The saturation magnetization, M_s increases with increasing deposition temperature and has the highest, $M_s = 1304$ G, for TS500 CFAS film. This can be attributed to the increased crystallinity with TS and TS500 CFAS films having the highest B2 crystalline order [23,24]. The Landé g-factor for the TS500 CFAS film is obtained to be equal to 2.025(3), which is very close to the expected value of g = 2 for spin system. From TS350 to TS550 the value of g does not have much variation. Fig. 5.4 shows the variation of Landé g-factor and M_s with TS.

Table 5.1: Landé g - factor, M_s , ΔH_{inhomo} , α and TMS contribution obtained from the fits using Eqs. (5.63) and (5.64) along with the frequency range over which the linewidth is fitted.

Sample	Frequency	Lande-g	M_s	$\Delta \boldsymbol{H}_{inhomo}$	α	TMS
ID	range, (ω)	factor	(G)	(Oe)		(Oe)
	GHz					
RT	25.16 - 113.04	2.101(5)	715	0.11	1.72 x 10 ⁻²	0.9
TS350	43 - 87	2.092(6)	917	10	1.0 x 10 ⁻³	0.05
TS450	25.16 - 91.06	2.082(2)	1030	18	1.3 x 10 ⁻³	0
TS500	25.16 - 75.36	2.025(3)	1107	7	1.35 x 10 ⁻⁴	0.50
TS550	25.16 - 65.94	2.030(8)	1055	2	9.8 x 10 ⁻³	0.3

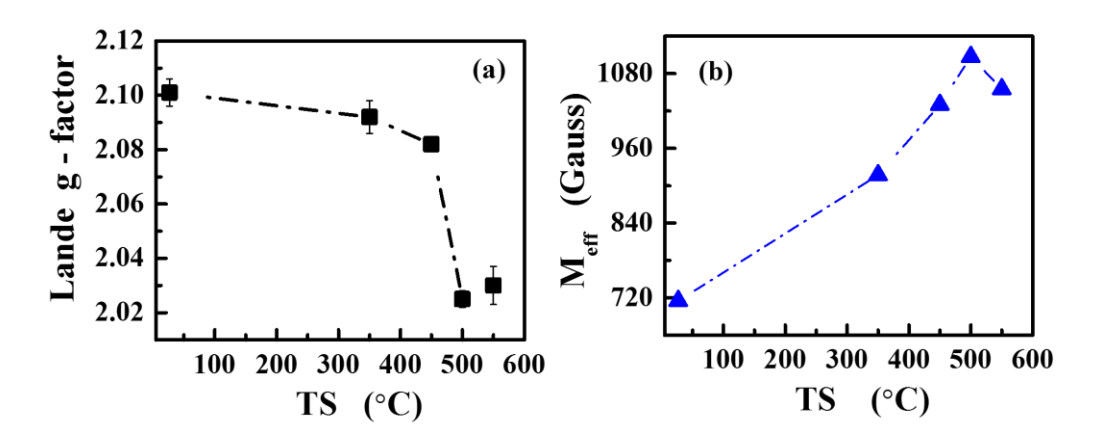


Fig. 5.4: Variation of (a) Landé g – factor and (b) M_s , with substrate temperature.

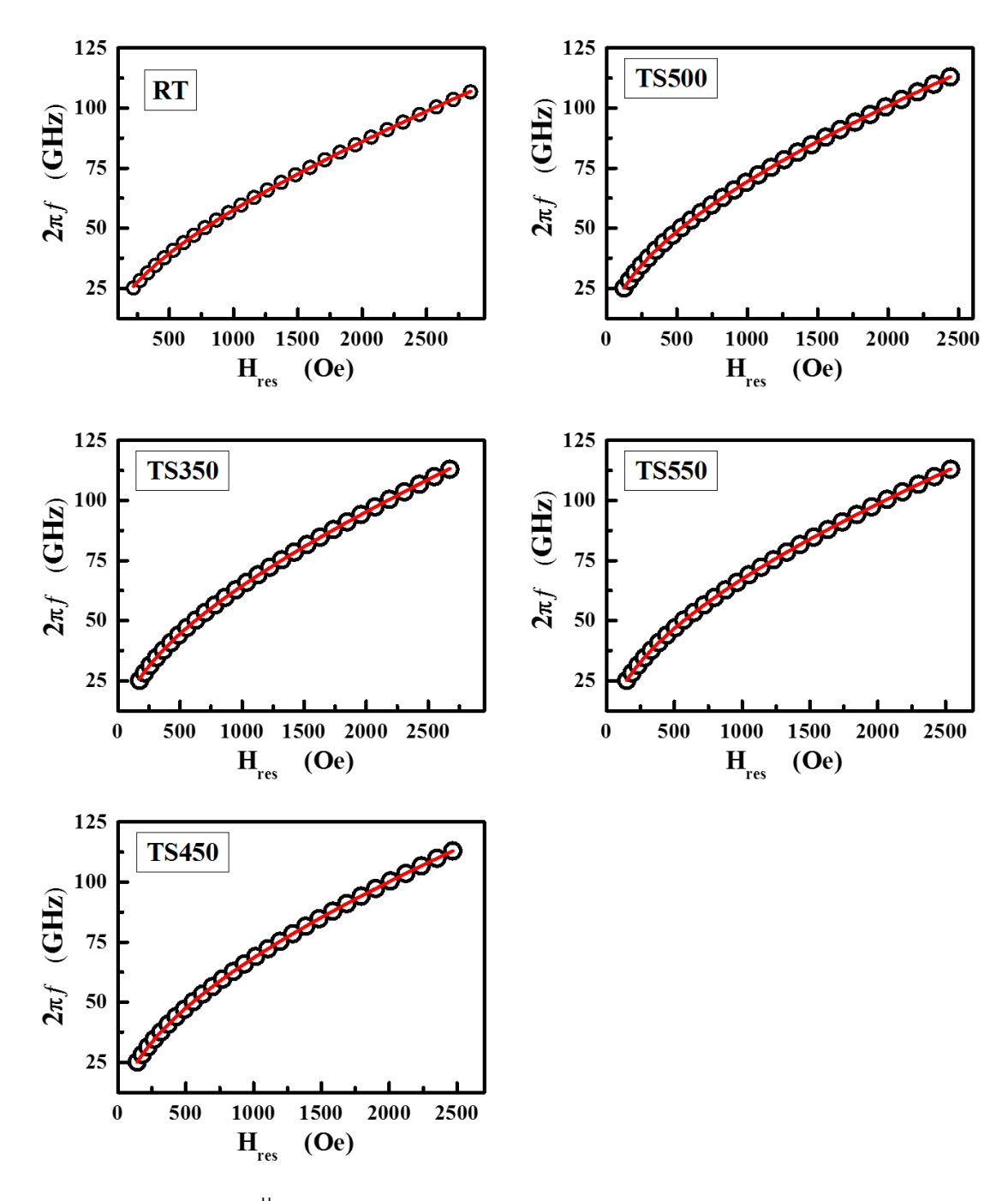


Fig. 5.5: The value of $H_{res}^{||}$ obtained from the fit using Eq. (5.62) is plotted against the frequency $(\omega = 2\pi f)$. The red solid curves represent the Kittel fit.

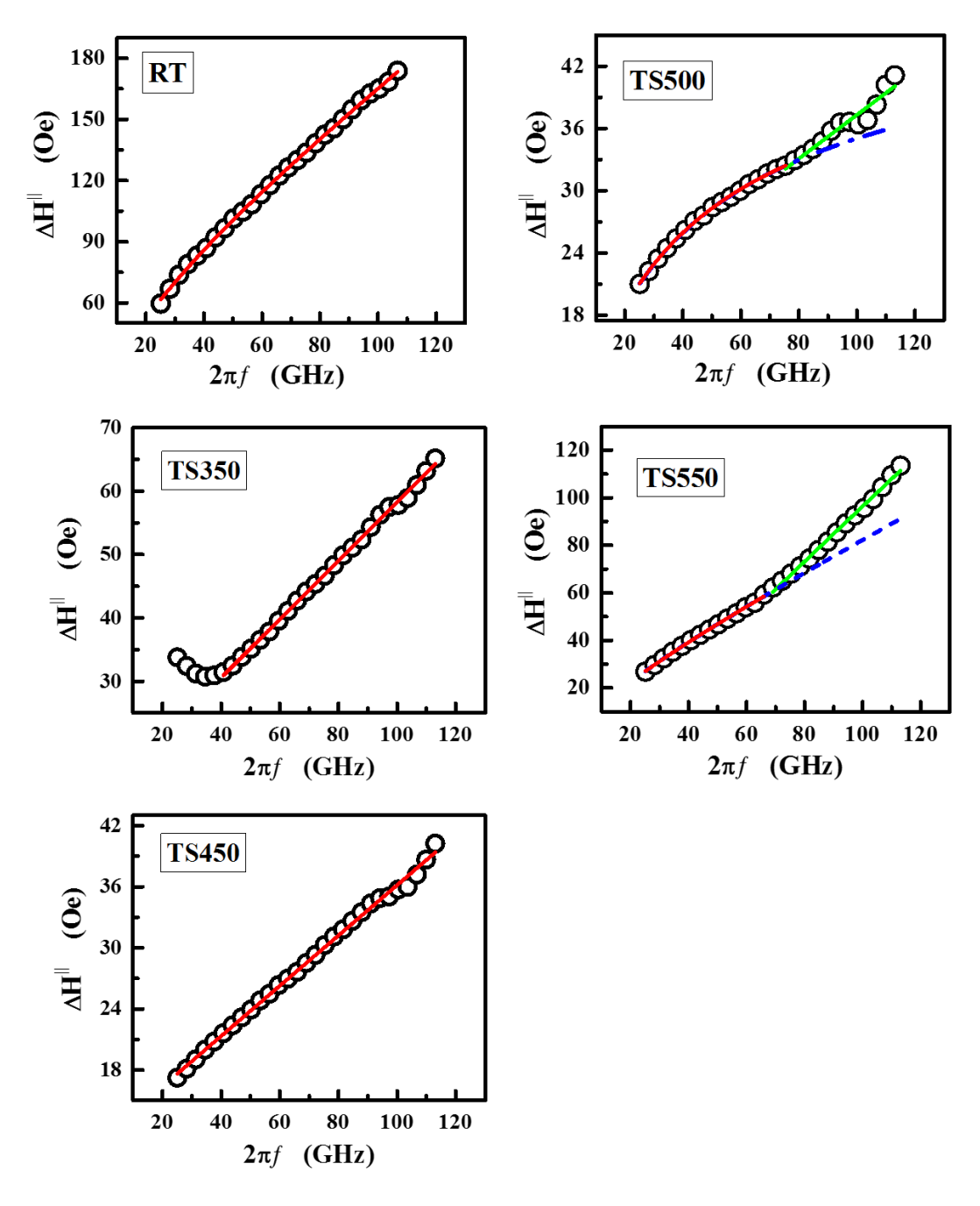


Fig. 5.6: $\Delta H^{||}$ obtained from the Kittel fit using Eq. (5.62), plotted against the frequency ($\omega = 2\pi f$). The solid red curves represent the fits using Eq. (5.64).

The $\Delta H^{||}$ of the FMR spectra is directly related to the damping of the spin dynamics and to the inhomogeneity such as sample roughness, porosity, defects, etc. present in the film [25, 26]. From Fig. 5.6, it can be observed that $\Delta H^{||}(f)$ does no vary linearly but has some curvature and this curvature is dependent on the frequency range. To account for such behaviour, $\Delta H^{||}(f)$ has been analysed by taking the intrinsic contribution which is the Landau-Lifshitz-Gilbert (LLG) term and the extrinsic two magnon scattering (TMS) terms along with the ΔH_{inh} contribution [27].

$$\Delta H = \Delta H_{inh} + \frac{2\pi\alpha}{\sqrt{3}M_S} f + \Delta H^{TMS}$$
 (5.64)

here, α is the intrinsic Gilbert damping constant in the LLG expression. The TMS expression is given by Eq. (5.54). Since the FMR spectra is measured along the easy axis of magnetization i.e., $\varphi_H = \varphi_M$, then we can write $\cos 2(\varphi_H - \varphi_M) = 1$ in (Eq. 5.54). And ΔH_{inh} is a frequency independent term. During the fit, M_s obtained from the Kittel fit is fixed and α and TMS coefficient are used as free fitting parameters. The values of ΔH_{inh} , α and TMS contribution obtained from the fit using Eq. (5.64) is given in Table 5.1.

In the TS500 CFAS film, the Eq. (5.64) fits the observed variation of $\Delta H^{||}(f)$ from $\omega = 25.16$ GHz to 75.36 GHz (i.e f=4 to 12 GHz). Such a fit is represented by the red continuous line in Fig. 5.6(d) for TS500. The blue dash line is the projection of the fit extrapolated by using the obtained parameters within the range of fit. The green continuous line represents the fit using only $(\Delta H_{inh} + \frac{2\pi\alpha}{\sqrt{3}\,M_S}f)$ without the ΔH^{TMS} term. Similar analysis is carried out for the TS550 CFAS film. Evidently, the TMS contribution is low for TS350 ($\Delta H^{TMS} = 0.05$ Oe) and negligible in TS450 films. In the TS500 film, $\Delta H^{TMS} = 0.5$ Oe.

The variation of α with the TS is plotted in Fig. 5.7. ΔH_{inh} gradually decreases with increasing TS, except for the RT film which gives a low value from the fit. The Gilbert damping constant for RT is 0.017 and decreases with increasing TS. The lowest value of $\alpha = 1.35 \times 10^{-4}$ is obtained for the TS500 CFAS film. For the TS550 film, $\alpha = 0.0098$, Such a variation of α with TS can be explained using the torque correlation model [28-30], which is given by:

$$\alpha = (1/\gamma M_s \tau) \mu_B^2 N(E_F) (g-2)^2$$
 (5.65)

here, τ is the scattering time of conduction electron, $N(E_F)$ is the total spin density of state, both $(S \uparrow \text{ and } S \downarrow)$ at the Fermi energy level E_F . From the Kittel expression, the value of g does not vary much with TS, and hence the variation in $(g-2)^2$ does not significantly affect the α value. Thus, from this relation, α is directly dependant on $N(E_F)$ [28]. From the structural analysis, B2 structural order increases with TS. Consequently, the decrease in α with TS reflects that $N(E_F)$ decreases with increasing structural order. The low value of α for TS500 CFAS film suggest that this system has low density of state at the E_F . A low value of α , with large magnetization and large TMS contribution has also been reported in Co₂MnSi system [31].

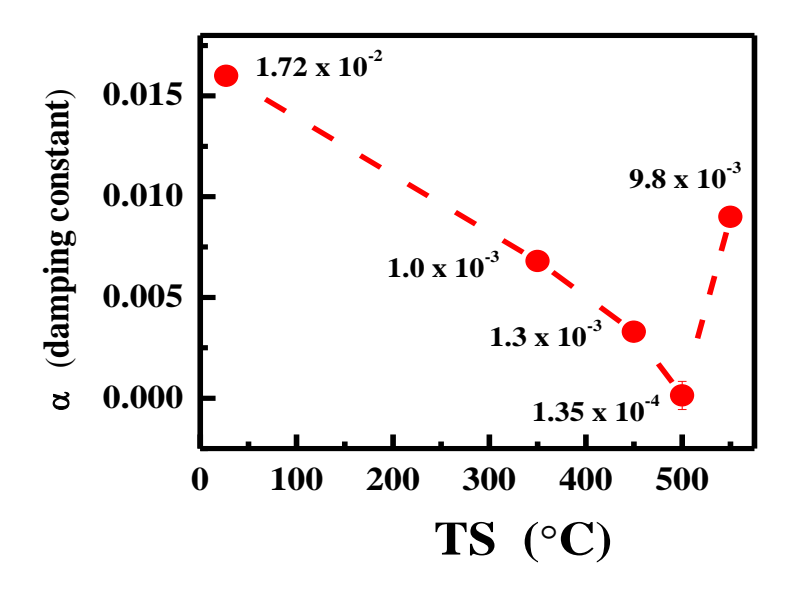


Fig. 5.7: α obtained from the fit using Eq. (5.64) plotted as a function of deposition temperature.

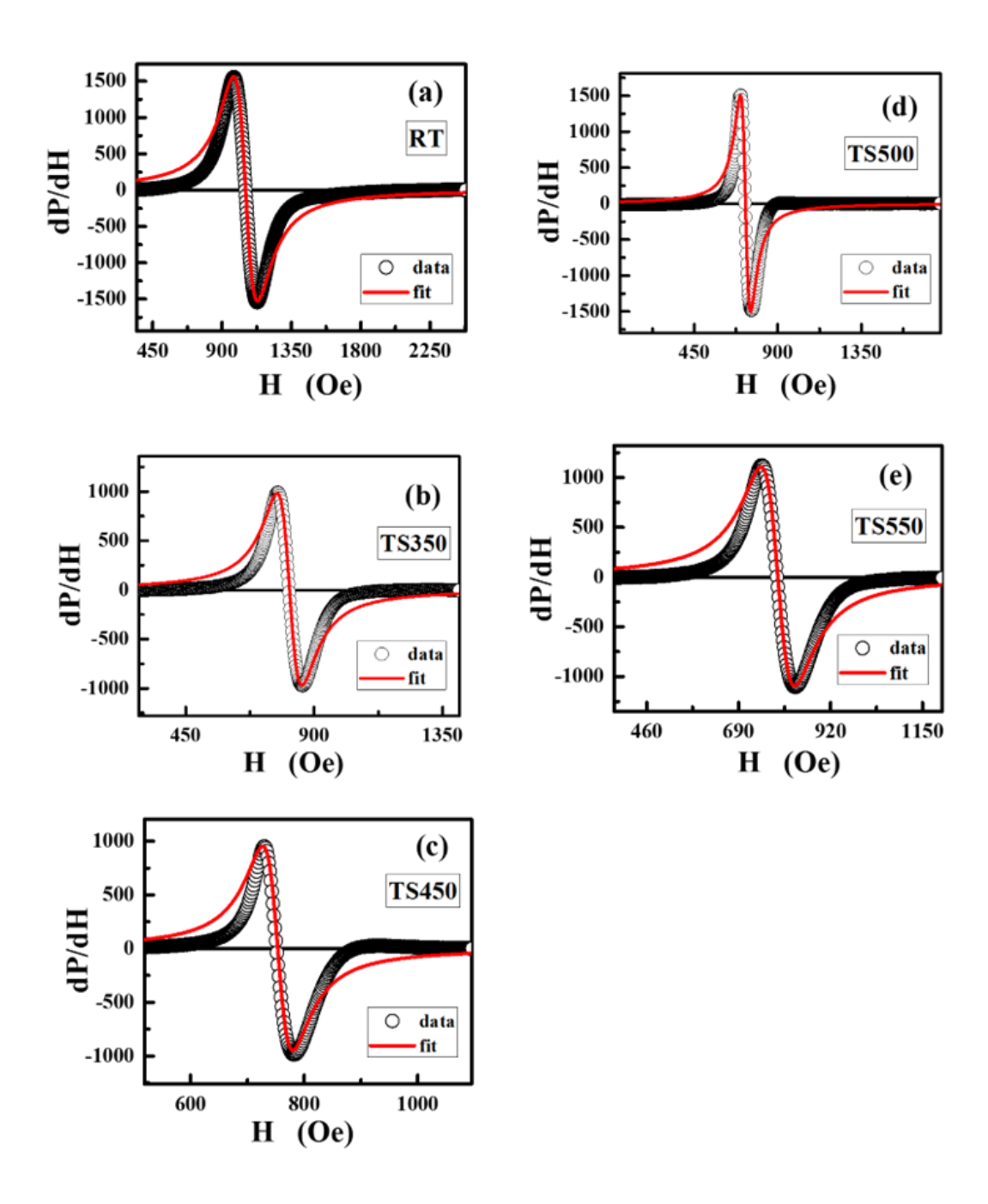


Fig. 5.8: In-plane magnetization and anisotropy field as a function of deposition temperature.

5.5.1.2 Angular dependent Ferromagnetic resonance

(I) Lineshape analysis

For RT, TS350, TS450, TS500 and TS550 CFAS thin films, field derivative of the microwave power absorption $\left(\frac{dP}{dH}\right)$ were recorded at varying angles of φ_H , in IP configuration and θ_H in OP configuration. To obtain the saturation magnetization (M_S), Landé splitting factor (g), anisotropy field (H_K) and FMR linewidth (ΔH) from the FMR spectra, lineshape (LS) analysis has been carried out by considering, M_S, g, H_K and ΔH as free-fit parameters. For the lineshape analysis, the $\frac{dP}{dH}$ FMR spectra recorded at $\varphi_H = 0^\circ$ is used. During the fit, M_S and g for all the films were first initiated with values obtained from CPW-FMR Kittel fits. Regardless, the value of the Landé splitting factor has the value g = 2.04(2). The final value of M_S and H_K thus obtained in IP configuration LS analysis is listed in Table 5.2. As observed in the broad-band FMR results, the TS500 has the highest magnetization, M_S^{||} ≈ 1054 Gauss and lowest anisotropy field H_K^{||} = 8 Oe. The best fit to the data is given in Fig. 5.8.

(II) In-plane angular variation.

Polar plots of $H_{res}^{||}(\phi_H)$ for RT, TS350, TS450, TS500 and TS550 CFAS thin films are shown in Fig. 5.9. In the IP angular variation, $H_{res}^{||}(\phi_H)$ has minima at $\phi_H = 0^\circ$ and $\phi_H = 180^\circ$ and maxima at $\phi_H = 90^\circ$ and $\phi_H = 270^\circ$. Irrespective of the degree of anti-site disorder with respect to TS, the observation of the two-fold symmetry in $H_{res}^{|||}(\phi_H)$ clearly affirms 'in-plane' uniaxial anisotropy in the CFAS films.

The fit to the $H_r(\phi_H)$ data is achieved by adopting a self-consistent procedure considering the ϕ_M with ϕ_H , M_S and H_K as free fit parameters. The final fit thus achieved is shown in Fig. 5.9 as continuous lines to the raw data.

 M_S and H_K obtained from the fit are plotted with TS in Fig. 5.10(a). As observed in previous analysis, M_S is maximum for the TS500 CFAS film and correspondingly H_K is lowest. The equilibrium magnetization angle (ϕ_M) obtained from the fit, for all the CFAS films, is plotted against the field angle (ϕ_H) in Fig. 5.10(b). The observation that $\phi_M \cong \phi_H$ in Fig. 5.10(b) suggests that the 'in-plane' anisotropy field is so insignificantly small compared to the external magnetic

field that, regardless of the φ_H value, the magnetization vector aligns with the magnetic field direction.

 $\Delta H^{||}(\varphi_H)$ for different CFAS thin film samples, is shown in Fig. 5.11. It is to be noted that the maxima (or minima) in $\Delta H^{||}(\varphi_H)$ and $H_r(\varphi_H)$ do not correspond at the same value of (φ_H) . The IP linewidth variation is maximum for the RT film with $[\delta(\Delta H)] \sim 12$ Oe, which decreases with increasing TS and has the lowest $[\delta(\Delta H)] \sim 2$ Oe for TS500 CFAS films. For all the films, except the film deposited at RT, two-fold symmetry is observed in $\Delta H^{||}(\varphi_H)$.

Table 5.2: H_{res}^{\parallel} at $(\varphi_H = 0^{\circ})$ and $(\varphi_H = 90^{\circ})$, M_s , and H_k obtained from the fits, based on equations (5.42) and (5.43), for the RT, TS350, TS450, TS500 and TS550 CFAS thin films.

Sample ID	H_{res}^{\parallel} $(\boldsymbol{\varphi}_{H} =$	H_{res}^{\parallel} $(\varphi_H = 90^\circ)$	$H_k^{\parallel} = [H_{res}^{\parallel} (\varphi_H) - 90^{\circ}) -$	Ms from $H_{res}^{\parallel}\left(\mathbf{\varphi}_{H} ight)$ fit	H_{K} from $H_{res}^{\parallel}\left(oldsymbol{arphi}_{H} ight)$ fit	Ms from LS fit	H _K from LS fit
	0°) (Oe)	(Oe)	$H_{res}^{\parallel}(\varphi_H = 0^{\circ})]/2$	(Gauss)	(Oe)	(Gauss)	(Oe)
RT	1000	1103	103	962	54	712	-19
TS350	810	845	35	922	18	970	-13
TS450	751	770	20	1015	9	1047	1.7
TS500	722	750	28	1054	8	1130	17
TS550	785	808	23	966	11	1056	-2

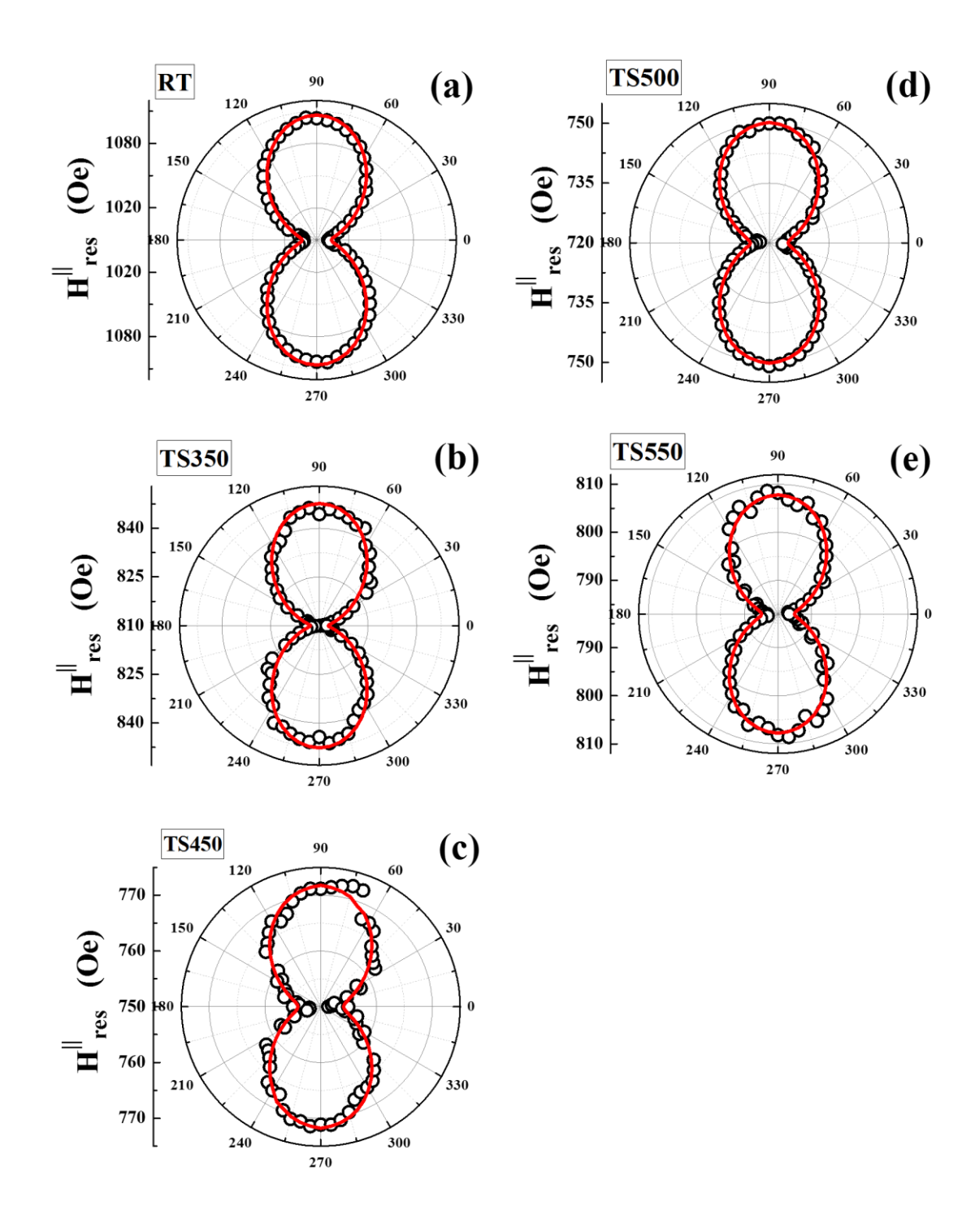


Fig. 5.9: Variation of the $H_{res}^{||}(\varphi_H)$ along with fits for RT, TS350, TS450, TS500 and TS550 CFAS thin films.

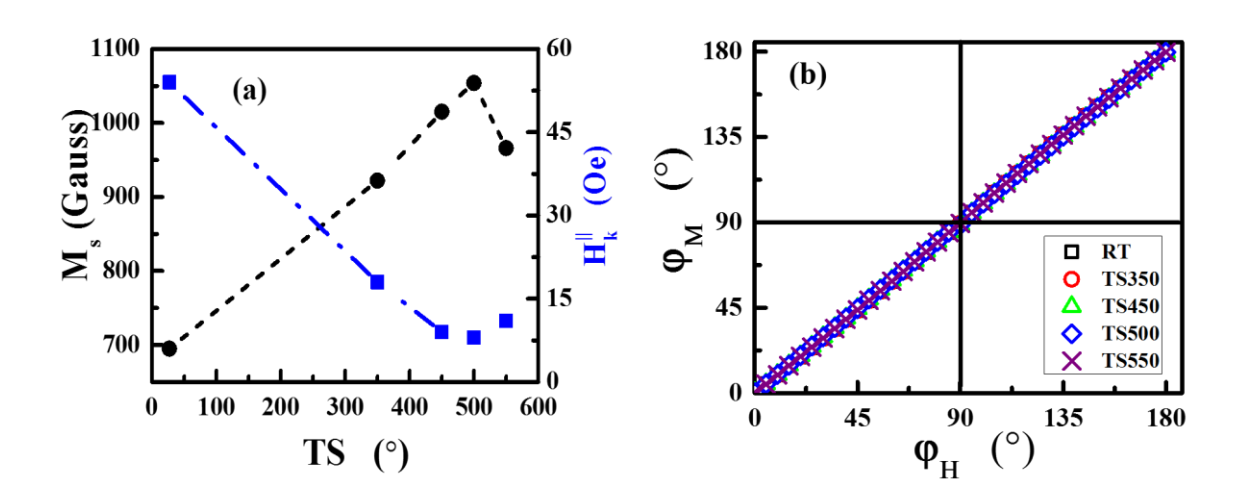


Fig. 5.10: (a) Variation of M_S and H_K with deposition temperature, (b) Variation of the φ_M with φ_H for RT, TS350, TS450, TS500 and TS550 CFAS thin films

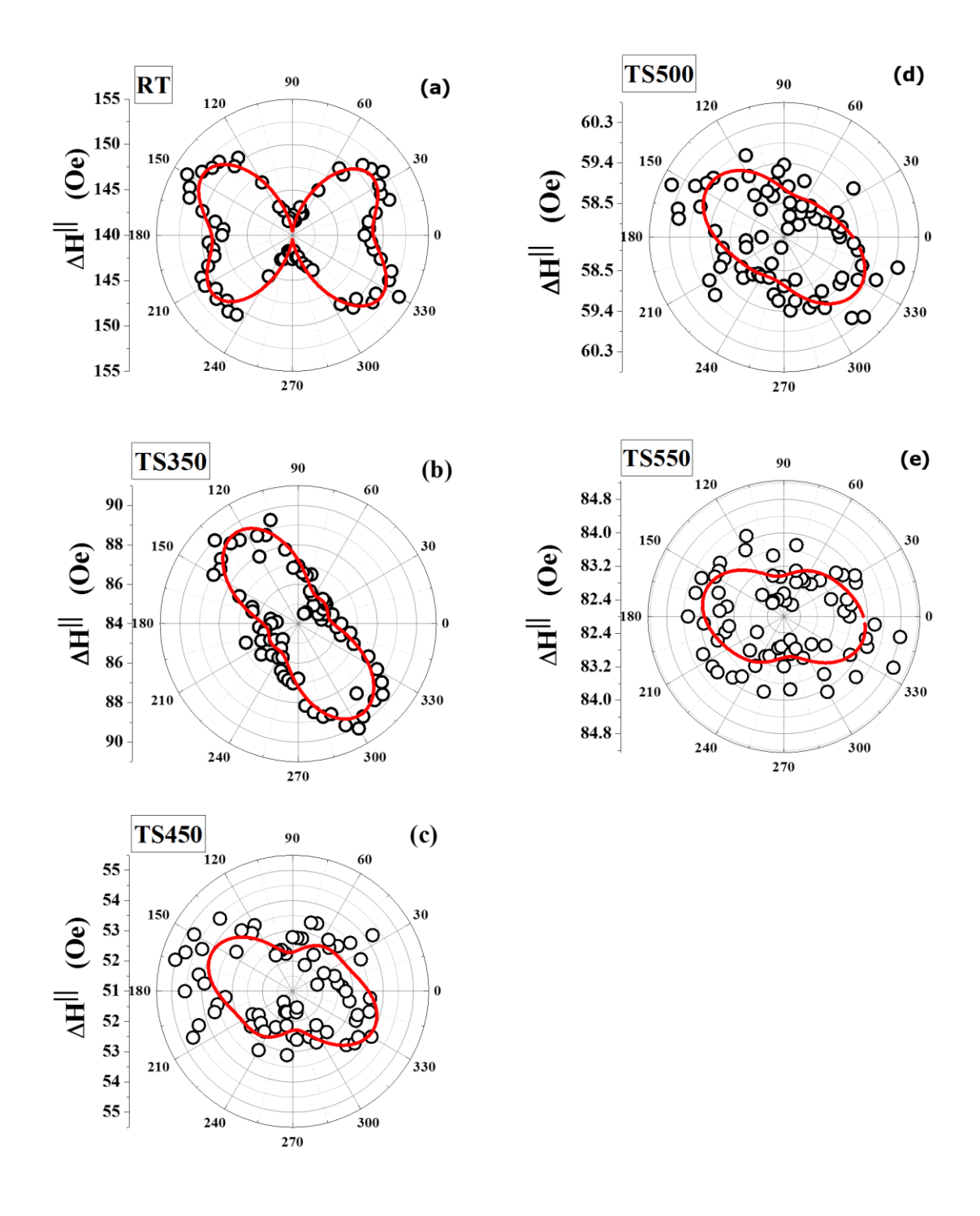


Fig. 5.11: Variation of the $\Delta H^{\parallel}(\varphi_H)$ along with fits for RT, TS350, TS450, TS500 and TS550 CFAS thin films.

The linewidth is a measure of the rate at which the magnetization relaxes back to equilibrium position once the static magnetic field is switched off and its broadening has contributions from intrinsic damping, which is given by the LLG contribution, (ΔH^{LLG}) and extrinsic damping mechanisms, two-magnon scattering (ΔH^{TMS}) [32, 33]. In addition, angular spread in crystallite misorientation, ($\Delta H^{\theta H}$) and inhomogeneity in magnetization ($\Delta H^{4\pi M_{eff}}$) causes an inhomogeneous broadening in the linewidth [34-37].

Table 5.3: H_{res}^{\perp} , M_s , and H_k obtained from the fits, based on equations (5.44) and (5.45), for the RT, TS350, TS450, TS500 and TS550 CFAS thin films.

Sample ID	H_{res}^{\perp}	$M_{\rm S}$ from $H_{res}^{\perp}\left(heta_{H} ight)$ fit	H_{K} from $H_{res}^{\perp}(\theta_{H})$ fit	M _S from LS fit	H _K from LS fit
	$(\boldsymbol{\theta}_{H} = 0^{\circ})$	(Gauss)	(Oe)		(Oe)
	(Oe)			(Gauss)	
RT	1030	683	136	697	120
TS350	810	884	133	887	130
TS450	733	986	125	993	119
TS500	712	1016	118	1022	120
TS550	760	962	115	956	120

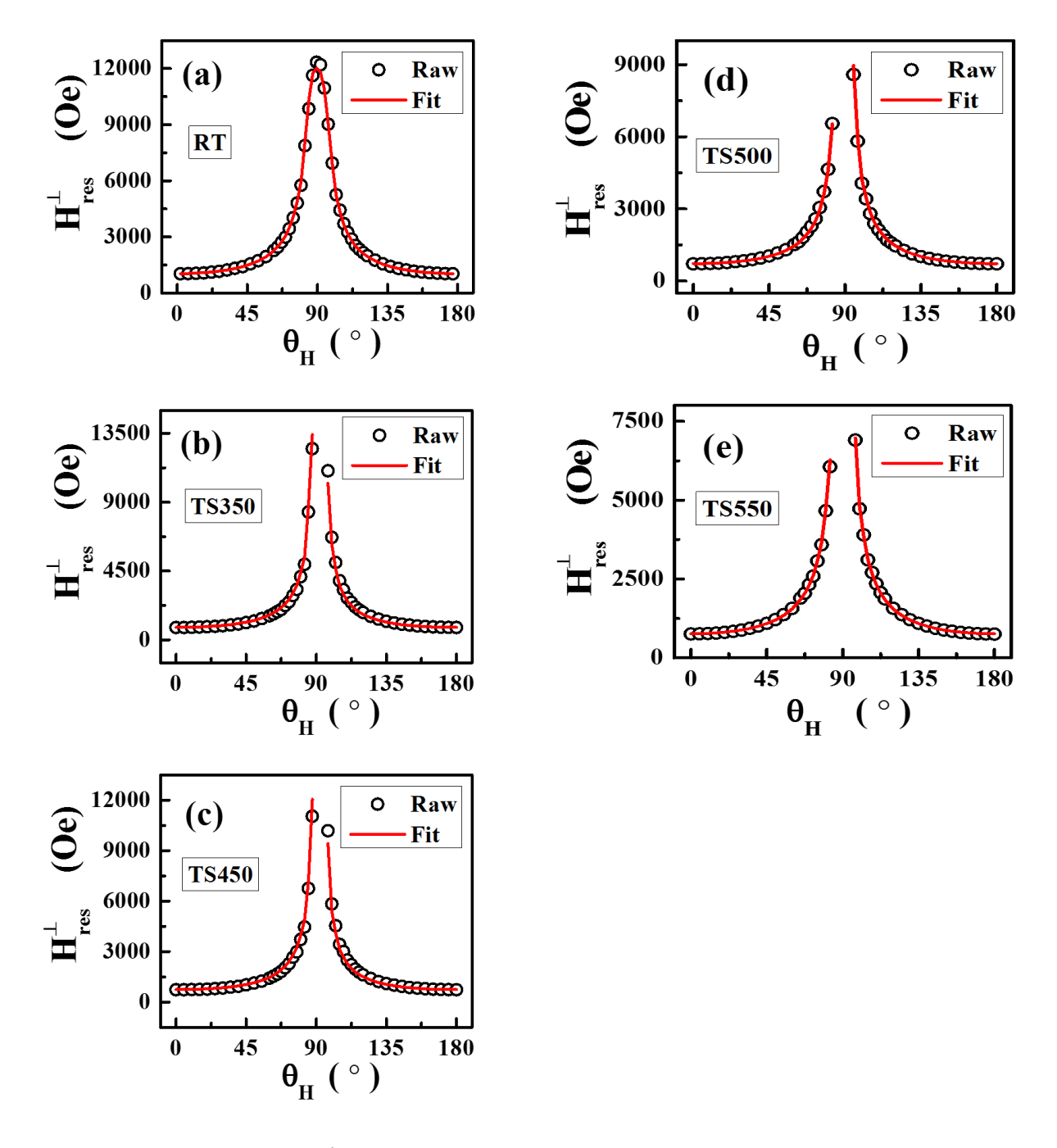


Fig. 5.12: Variation of the $H_{res}^{\perp}(\theta_H)$ along with fits for RT, TS350, TS450, TS500 and TS550 CFAS thin films.

(III) Out-of-plane angular variation

 $H_{res}^{\perp}(\theta_H)$ for TS series CFAS thin films, are displayed in Fig. 5.12. Similar to the IP, in the OP angular variation, irrespective of the degree of anti-site disorder with respect to TS, the two-fold symmetry is observed in $H_{res}^{\perp}(\theta_H)$ (polar plots) in all the CFAS films.

For the TS450, TS500 and TS550 film, as θ_H approaches 90° the resonance field is large and hence, H_{res}^{\perp} shift to higher fields. This is because as θ_H approaches 90° the magnetization vector points out-of-the film plane toward the hard axis.

The value of M_s and H_k obtained from the LS analysis are used as initial parameters for the angular dependant analysis. The quality of fit is monitored by noting the change in χ^2 . After several iteration the fit with the minimum χ^2 is taken as the best fit. The final M_s and H_k thus obtained is plotted with TS in Fig. 5.14 (a). The θ_H dependence of equilibrium magnetization (θ_M) is shown in Fig. 5.14(b). For smaller angles, θ_M follows θ_H and then as θ_H approaches 90°, θ_M lags behind θ_H in the out-of-plane case.

Different contributions to the linewidth are evaluated for the OP configuration considering the Eqs. (5.57 – 5.61). In the OP configuration, given in Fig. 5.13, shows $\Delta H^{\perp}(\theta_H)$ along with the best fit and the individual contributions from ΔH^{LLG} , ΔH^{TMS} , $\Delta H^{4\pi M_{eff}}$ and ΔH^{θ_H} . Since the crystalline order and magnetization increases with TS, the contribution from $\Delta H^{4\pi M_{eff}}$ to the total linewidth becomes negligible with TS and this is further affirmed from the obtained fits which gives $\Delta H^{4\pi M_{eff}} \cong 0$ for TS350, TS450, TS500 and TS550. Furthermore, ΔH^{LLG} , and ΔH^{θ_H} has dominant contributions to the ΔH^{\perp} .

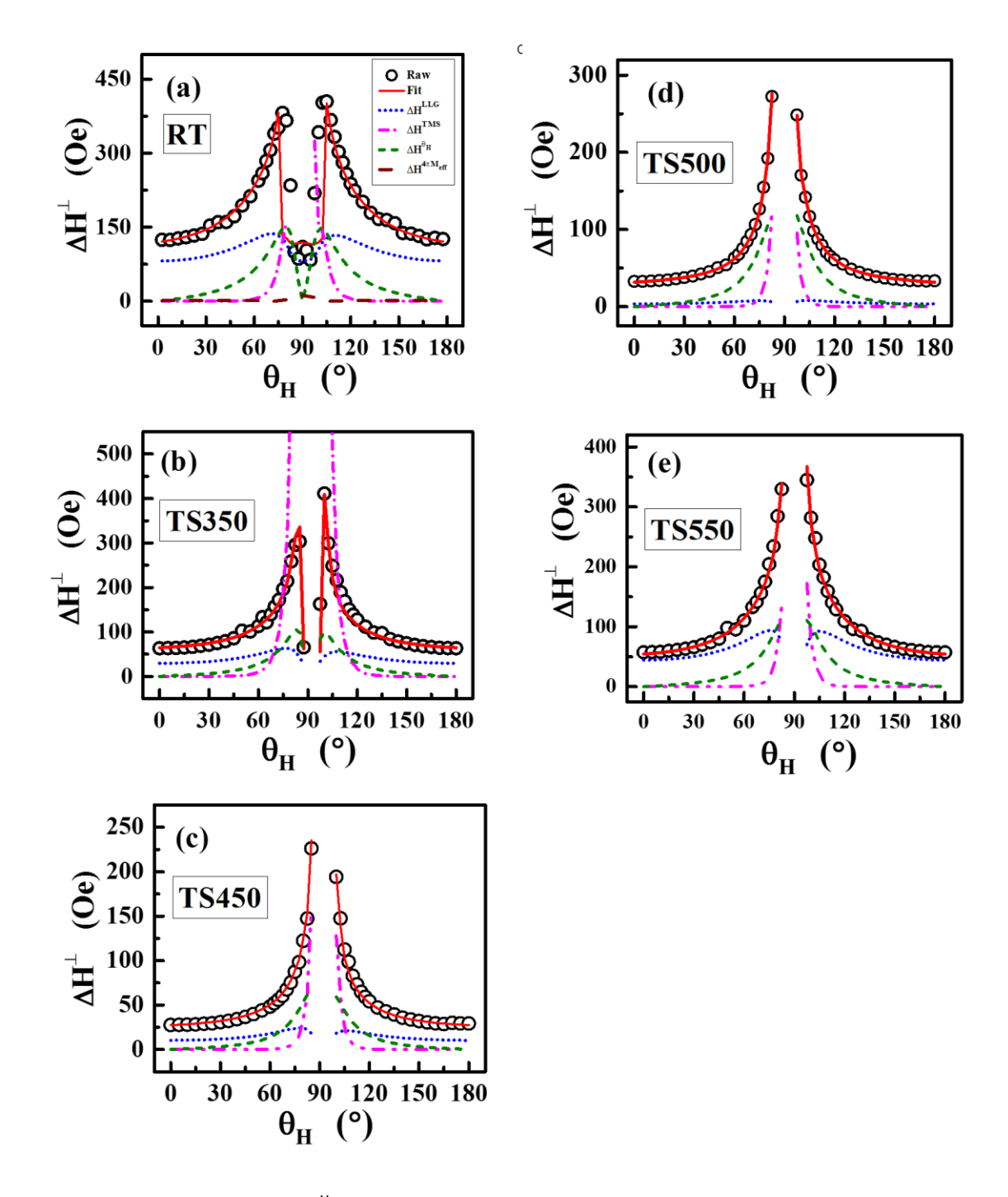


Fig. 5.13: Variation of the $\Delta H^{\parallel}(\theta_H)$ along with fits for RT, TS350, TS450, TS500 and TS550 CFAS thin films.

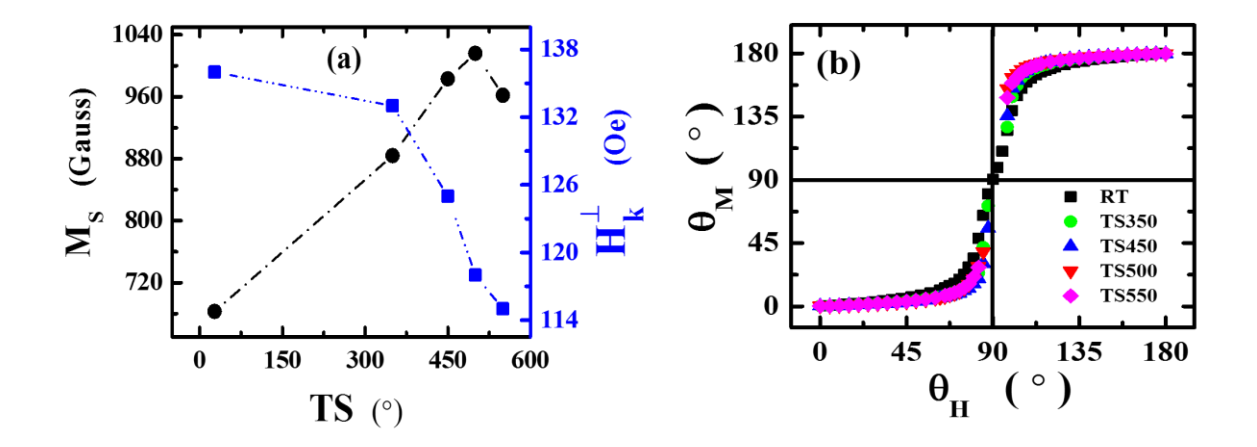


Fig. 5.14: Variation of (a) M_s with TS, (b) θ_M vs θ_H

5.5.1.3 Temperature dependence of FMR.

The FMR spectra in IP-easy axis ($\varphi_H = 0^\circ$) and IP-hard axis ($\varphi_H = 90^\circ$) has been recorded at temperatures ranging from 120 K to 300 K with 10 K temperature steps. H_{res} as a function of temperature increase with temperature while ΔH show a decreasing trend with increasing temperature. As the magnitude of magnetization decreases with increasing temperature, $H_{res}(T)$ increases with temperature.

The anisotropic field is estimated by using the relation (similar in form to Eq. (5.31)),

$$H_K(T) = \frac{[H_{res} (T, \varphi_H = 90^\circ) - H_{res} (T, \varphi_H = 0^\circ)]}{2}$$
 (5.65)

Saturation magnetization (M_S) obtained from the lineshape analysis (along with the fit) is plotted in Fig. 5.15 as a function of temperature. $M_S(T)$ is fitted using the well-known spin wave expression [38-40] given by,

$$M(T,H) = M(0,H) - g\mu_B \left[Z(3/2,t_H) \left(\frac{k_B T}{4\pi D(T)} \right)^{\frac{3}{2}} \right] + 15\pi \beta Z(5/2,t_H) \left(\frac{k_B T}{4\pi D(T)} \right)^{\frac{5}{2}}$$
(5.66)

where, $Z(s,t_H)$ is the Bose-Einstein integral function, with $t_H=\frac{g\mu_B H_{eff}}{k_B T}$. The main observation is that the $T^{\frac{3}{2}}$ term in Eq. (5.66) alone completely accounts for the observed $M_S(T)$ and the thermal renormalization of the spin wave stiffness, D(T) improves the quality of the fit. The thermal variation $D(T)=D(0)[1-D_2T^2]$ characteristic of the itinerant ferromagnet, yield much better fit than the $D(T)=D(0)\left[1-D_{\frac{5}{2}}T^{\frac{5}{2}}\right]$,

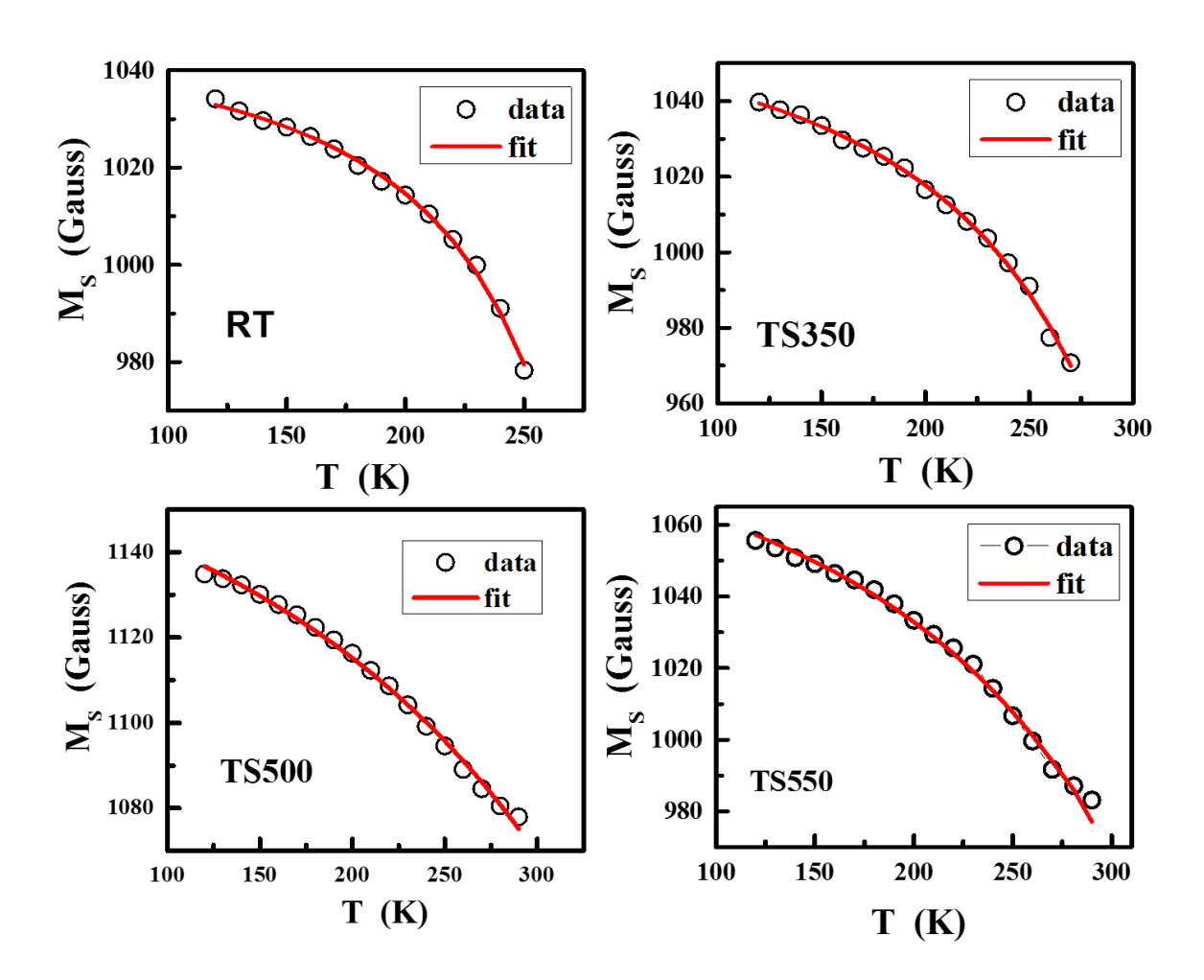


Fig. 5.15: Saturation magnetization (M_S) as a function of temperature. $M_S(T)$ is fitted using the spin wave expression.

5.5.2 Effect of film thickness

5.5.2.1 Broadband FMR

The FMR spectra were recorded at different frequencies ranging from 8 GHz to 39 GHz. The thin films are placed on top of the signal line of co-planar wave guide strip and the static magnetic field (H) is varied perpendicular to the applied microwave field along the film plane.

It is to be noted that the FMR spectra could not be recorded for the 12 nm CFAS thin film. The reason could be that the resonance field is beyond the field range of the experimental setup. As observed in the structural analysis and resistivity, the anti-site disorder in 12 nm film is large in comparison to the other films in the thickness series.

The resonance field ($H_{res}^{||}$) and linewidth ($\Delta H^{||}$) are obtained from the best fit to the FMR spectra by using the asymmetric Lorentzian function given by Eq. (5.62). The $H_{res}^{||}$ and $\Delta H^{||}$ thus obtained are plotted with the frequency as shown in Fig. 5.16 and 5.17 for the 25 nm, 50 nm and 75 nm films.

Table 5.4: Lande g-factor, M_s , ΔH_{inhomo} , α and TMS contribution obtained from the best fits along with the frequency range over which the linewidth is fitted and the corresponding values are obtained.

Thickness	Frequency	Lande	M_s	$\Delta \boldsymbol{H_{inhomo}}$	α	TMS	
(nm)	range, (ω)	g-	(Gauss)			(Gauss)	
	GHz	factor					
25	25.16-244.92	2.02	1008	17	0.0034	0.08	
50	25.16-75.36	2.025(3)	1107	10	1.305	0.50	
					x10 ⁻⁴		
75	25.16-238.6	2.03(8)	1045	13	0.0058	0.3	

In order to obtain the saturation magnetization (M_s) and anisotropic field (H_k) , the frequency dependence of $H_{res}^{||}$ is analysed using the Kittel resonance condition given by Eq. (5.63). M_s and H_k thus obtained are plotted against the thickness (t), shown in Fig. 5.17. In the thickness series, M_s increases from 1226(\pm 25) Gauss to 1304(\pm 27) Gauss and then decreases to 1249(\pm 29) Gauss as the thickness is varied from 25 nm to 75 nm respectively. The parameters obtained from the Kittel fit is given in Table 5.4.

In full Heusler alloy, magnetization results from the hybridization of the orbital states and in turn depends on the environment the atoms are sitting. Thus, the magnetization is directly affected by the anti-site disorder in these systems. Though the 25 nm film and 50 nm film both have B2 ordering, the anti-site disorder is more in the 25 nm film, whereas the 75 nm film has A2 disorder, as confirmed from the structural analysis by X-ray diffraction study. This result directly correlates to the variation of M_s with thickness. Thus, the highest M_s obtained for the 50 nm film can be attributed to the increased B2 crystalline order. This result is also in agreement with the highest residual resistivity ratio (RRR) obtained for the 50 nm CFAS film. The obtained H_k has also similar variation with thickness, with 50 nm having the highest $H_k = 36(\pm 7)$ Oe. In the Kittel resonance expression (Eq. (5.62)), both M_s and H_k are additive terms, thus the variation of H_k in orders of tens is negligible in comparison to the effective magnetization, $4\pi M_s$ which is in the order of few thousands.

In order to deduce the contribution to linewidth broadening, frequency dependence of ΔH^{\parallel} is analysed using Eq. (5.64). The obtained α parameter from the fit is plotted with the film thickness in Fig. 5.19. Since α is directly related to the density of state (DOS) of the system at ε_f [48-51], the lowest value of α for the 50 nm film confirms higher spin polarization than the 25 nm or 75 nm CFAS films. Thus, by varying the thickness of the thin film, the α parameter can be tuned for required spintronic applications

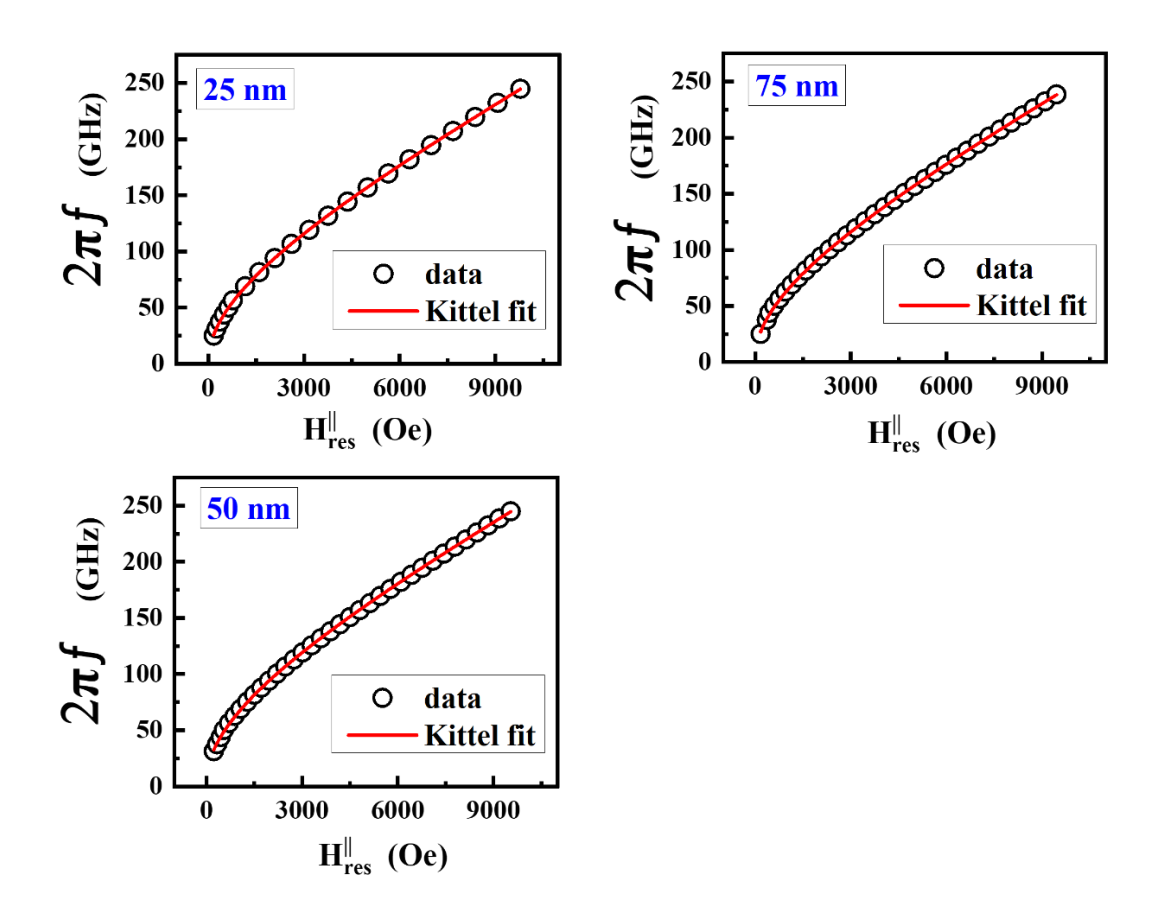


Fig. 5.16: $H_{res}^{||}$ variation with frequency. Open circles denote the raw data and red continuous line denote the fit.

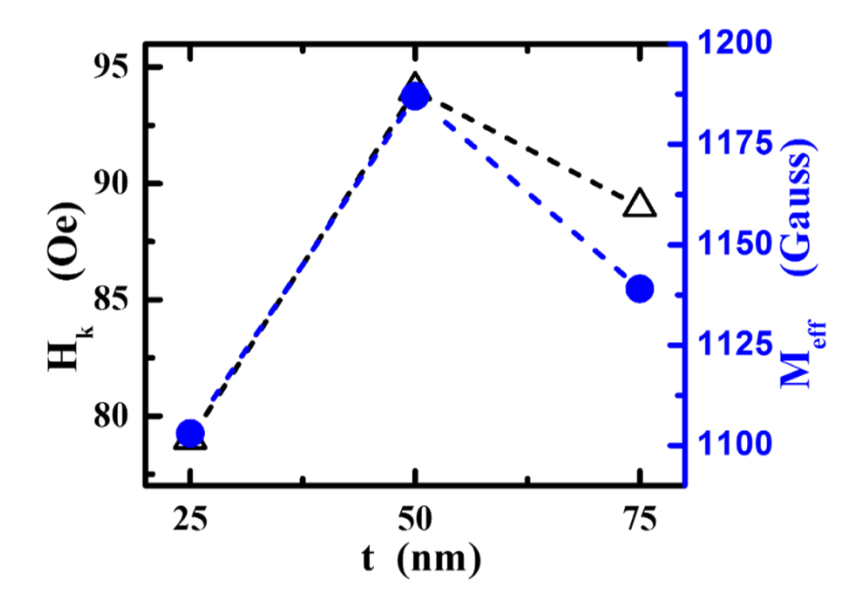


Fig. 5.17: Thickness variation of M_s and H_k

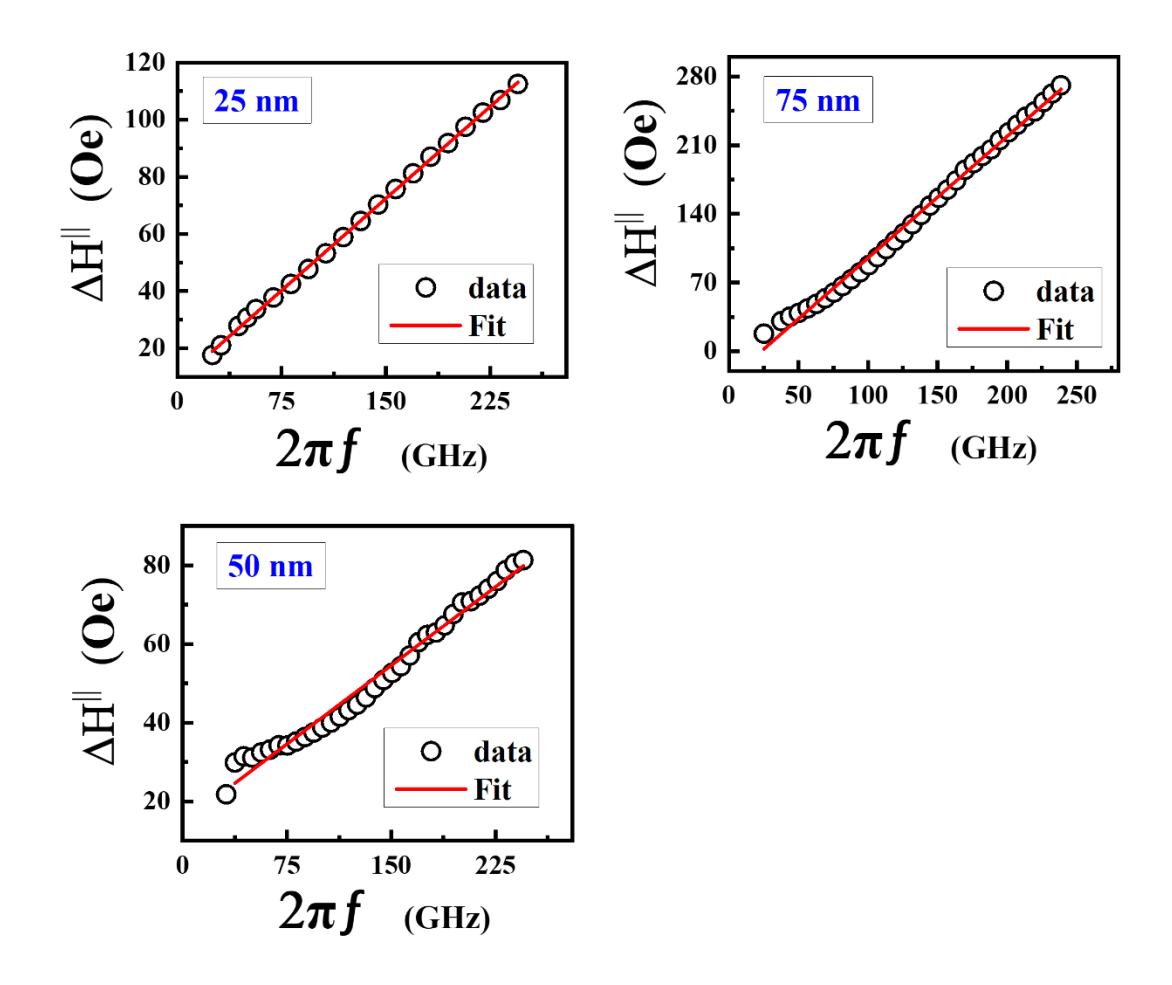


Fig. 5.18: Frequency dependence of $\Delta H^{||}$. Open circles denote the raw data and red continuous line denote the fit.

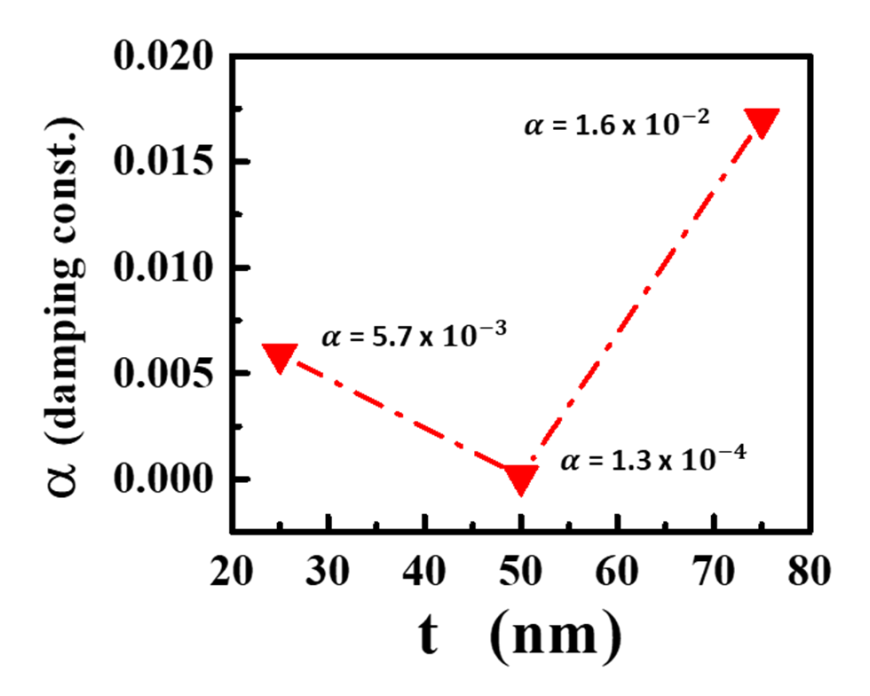


Fig. 5.19: Gilbert damping constant (α) plotted for different thickness.

5.5.2.2 Angular dependent Ferromagnetic resonance

(I) Lineshape analysis

Similar to the TS series, $\left(\frac{dP}{dH}\right)$ is recorded at different angles both in IP as well as OP configurations for the thickness series films (25 nm, 50 nm and 75 nm). Eq. (5.19) - (5.21) are used to fit the FMR spectra. To achieve the best fit, peak to peak linewidth (ΔH_{pp}) and intensity of $\left(\frac{dP}{dH}\right)$ obtained from the FMR spectra along with the effective magnetization (M_{eff}), anisotropy field (H_k) and Land´e splitting factor (g), obtained from the broadband FMR analysis, were used as initial input parameters for the lineshape analysis. The values thus obtained from the fit is listed in Table 5.5

(II) In-plane angular variation.

The angular variation of H_{res} is plotted in Fig. 5.20. Like the TS series, all the films show in-plane uniaxial anisotropy. The $H_{res}(\varphi_H)$ is fitted using a self-consistent procedure by employing the values of M_{eff} and H_k obtained from the lineshape analysis. The quality of fit is monitored by the computed value of χ^2 . The best fit to the $H_r(\varphi_H)$ data produced a low χ^2 of 10^{-2} order. The

obtained values of M_s , H_k and fit parameters are presented in the Table 5.5. The film with thickness, t = 50 nm has the highest magnetization. Similar variation has been observed from the broadband FMR analysis.

Fig. 5.22 shows the applied magnetic field angle (φ_H) dependence of equilibrium magnetization angle (φ_M) . A linear dependence of φ_H on φ_M shows that magnetization always follows the applied magnetic field direction, further implying that in-plane anisotropy field in these films are small. The fit parameters obtained from the best fit using Eq. (5.52) - (5.43) is listed in Table 5.5.

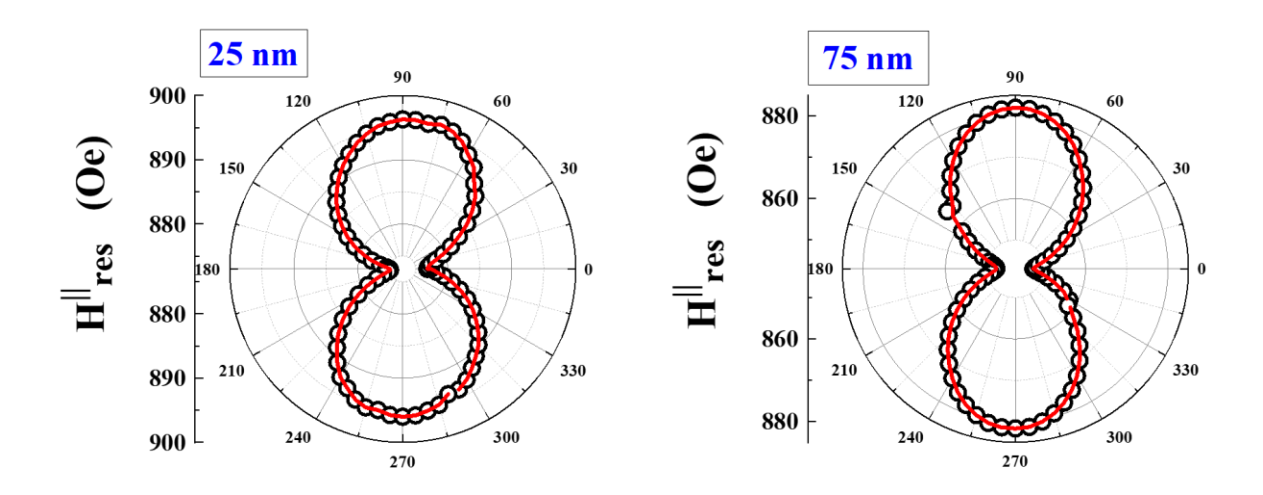


Fig 5.20: Angular variation of H_{res}^{\parallel} for 12 nm and 7 nm CFAS films along with the fits.

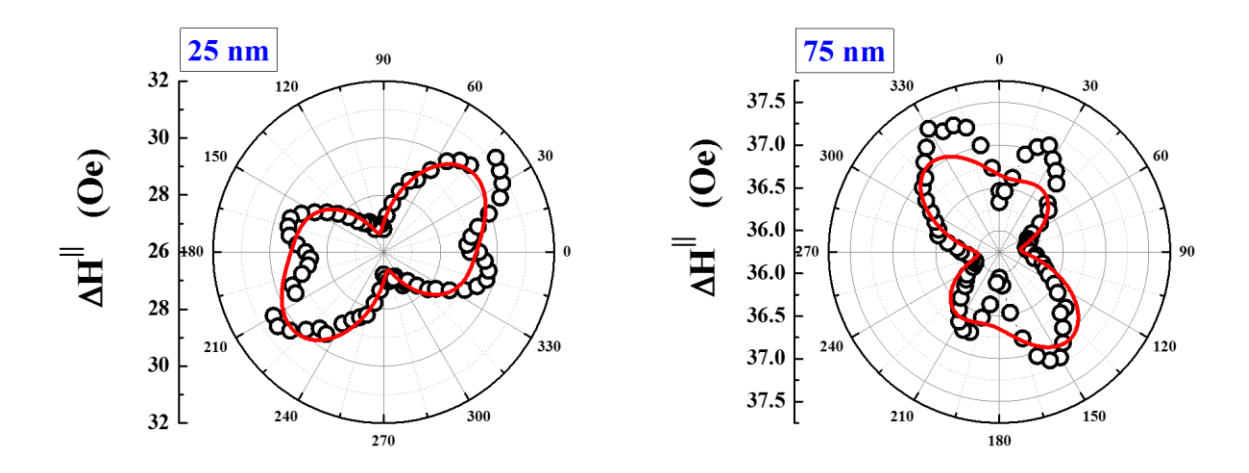


Fig. 5.21: Angular variation of $\Delta H^{||}$ for the thickness series along with the fits.

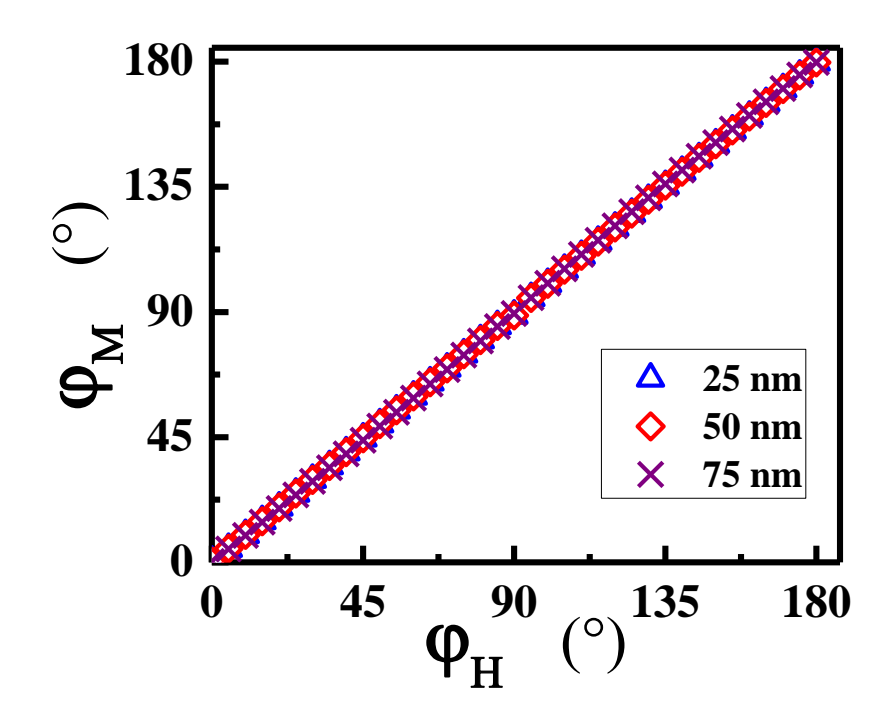


Fig. 5.22: Variation of the ϕ_M with ϕ_H 25 nm, 50 nm and 75 nm CFAS thin films.

The $\Delta H^{||}$ obtained from the FMR spectra are plotted as angular variation of φ_H . In contrast to the two-fold variation observed in $H_{res}(\varphi_H)$, a four-fold variation is observed in $\Delta H^{||}(\varphi_H)$. The total variation in $\Delta H^{||}$ from $\varphi_H = 90^\circ$ to $\varphi_H = 0^\circ$ is ± 4 Oe, while for the 75 nm film the total variation is only ± 1.5 Oe. To determine the linewidth broadening mechanisms contributing to the total $\Delta H^{||}$. The angular variation of $\Delta H^{||}$ is analysis using Eq. (5.57) – (5.61). Since the ΔH_{inho} term and LLG term are angular independent, ΔH_{inho} is obtained as a free fitting parameter whereas the value of the LLG term is computed by taking the value of α from the broadband linewidth analysis. In Eq. (5.58) the isotropic term is neglected since the $\Delta H^{||}$ variation shows an angular dependence. Both Γ_2 and Γ_4 are considered at $\varphi_H = 0^\circ$. The fit to the data is shown in Fig. 5.21. Fits have been attempted using $\Gamma_2 \neq 0$, $\Gamma_4 = 0$ and with $\Gamma_2 = 0$, $\Gamma_4 \neq 0$, regardless the best fit to the data is obtained by considering both the terms.

Table 5.5: H_{res}^{\parallel} at $(\varphi_H = 0^{\circ})$ and $(\varphi_H = 90^{\circ})$, M_s , and H_k obtained from the fits, based on equations (5.42) and (5.43), for the 25 nm and 75 nm CFAS thin films.

Thick ness (nm)		$H_{res}^{ }$ $(\theta_H = 90^\circ)$	$H_k^{ } = [H_{res}^{ } (\psi_H = 90^\circ) -$	Ms from $H_{res}^{\parallel}(\theta_H)$ fit	H_{K} from $H_{res}^{ }\left(heta_{H} ight)$ fit	Ms from LS fit	H _K from LS fit
	(Oe)	(Oe)	$H_{res}^{\perp}(\psi_H = 0^{\circ})]/2$	(Gauss)	(Oe)	(Gauss)	(Oe)
25	860	895	25	985	7	1105	12
50	722	750	28	1054	8	1130	17
75	840	883	27	1015	5	1127	13

(III) Out-of-pane angular variation.

 $\frac{dP}{dH}$ were also recorded at different angles for the 25 nm, 50 nm and 75 nm thin films in out-of-plane configuration. The out-of-plane resonance field, H_{res}^{\perp} obtained from the lineshape analysis of the FMR spectra is plotted with the field angle θ_H as presented in Fig. 5.23. For the 50 nm and 75 nm film, as θ_H approaches 90° the resonance field is large and hence shift to higher fields. This is because as θ_H approaches 90° the magnetization vector points out-of-the film plane toward the hard axis. The θ_H dependence of equilibrium magnetization (θ_M) is shown in Fig. 5.24. For smaller angles, θ_M follows θ_H and then as θ_H approaches 90°, θ_M lags behind θ_H in the out-of-plane case.

Table 5.6: H_{res}^{\perp} M_s , and H_k obtained based on equations (5.44) and (5.45) for 25 nm, 50 nm and 75 nm CFAS films.

Thickne ss (nm)	H_{res}^{\perp} $(\theta_H = 0^{\circ})$	Ms from $H_{res}^{\perp}(\theta_H)$ fit	H_{K} from $H_{res}^{\perp}\left(heta_{H} ight)$ fit	Ms from LS fit	H _K from LS fit
	(\mathbf{Oe})	(Gauss)	(Oe)	(Gauss)	(Oe)
25	1530	985	110	995	125
50	712	1016	118	1022	120
75	975	998	115	1004	112

The angular variation of ΔH^{\perp} are shown in Fig. 5.21. As carried out in the TS series linewidth analysis, LLG contribution (ΔH^{LLG}), inhomogeneous broadening due to crystallite misorientation (ΔH^{θ_H}), inhomogeneous broadening due to magnetization ($\Delta H^{4\pi M_{eff}}$) and TMS contribution (ΔH^{TMS}) have been taken into account to fit the angular variation of ΔH^{\perp} . The equilibrium 'out-of-plane' magnetization angle, obtained from $H^{\perp}_{res}(\theta_H)$, is used to evaluate the different contributions to linewidth. The fit (red solid line) to the $H^{\perp}_{res}(\theta_H)$, data, based on Eqs. (5.57) - (5.61), is illustrated in Fig.5.22. The individual contributions are plotted for all the thicknesses in the same figure. The following results can be drawn from the fit to $\Delta H^{\perp}(\theta_H)$; (i) ΔH_{LLG} contributions is dominant over the angular range and it gives rise to a dip at around $\theta_H = 90^{\circ}$. (ii) From all the figures, it is clear that TMS is not sensitive up to $\theta_H = 30^{\circ}$, beyond this angle TMS contribution rises rapidly. This TMS essentially explains the sharp rise in linewidth. As $\theta_H \rightarrow 90^{\circ}$, TMS scattering is more effective since $K \neq 0$ spin wave modes are excited in the perpendicular configuration.

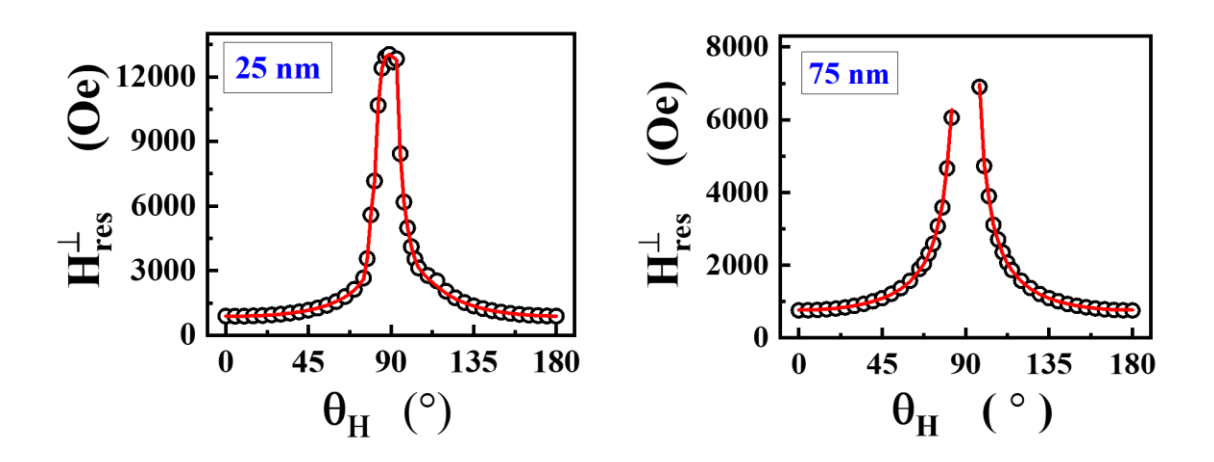


Fig. 5.23: Variation of the $H_r^{||}(\theta_H)$ along with fits for 25 nm and 75 nm CFAS thin films.

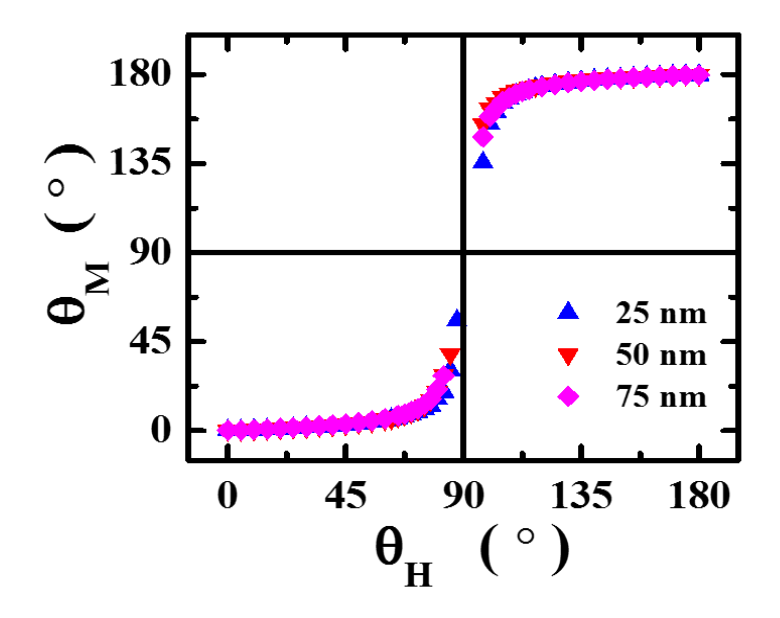


Fig. 5.24: Variation of the θ_M with θ_H for 25nm, 50 nm and 75 nm CFAS thin films

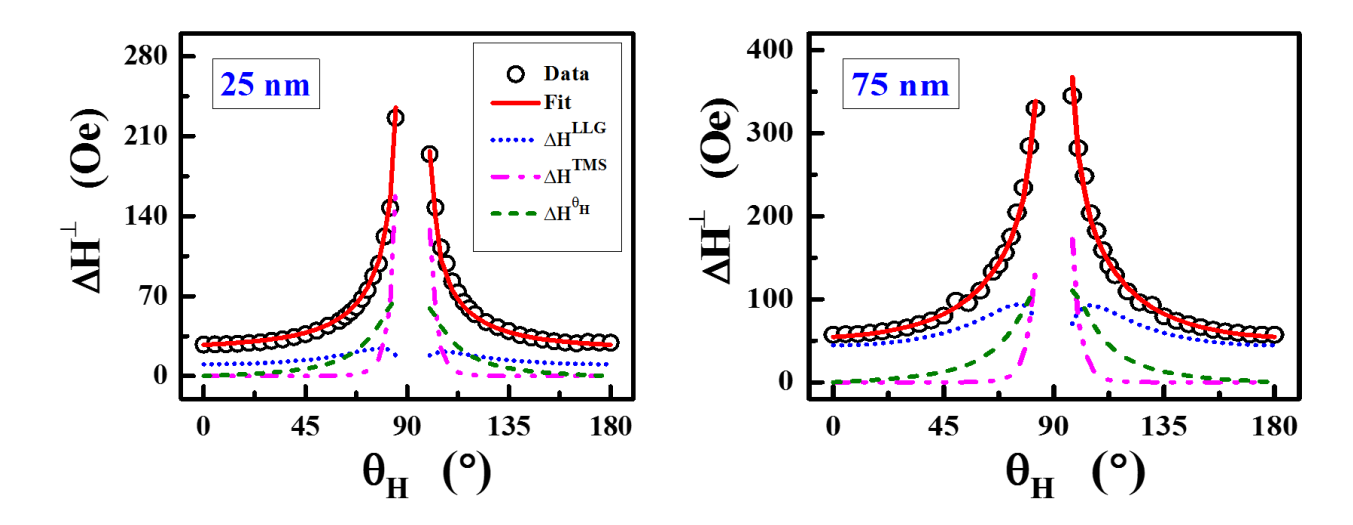


Fig. 5.25: Variation of ΔH^{\perp} with $\theta_{\rm H}$ for the thickness series along with the fits showing contribution of ΔH^{LLG} , ΔH^{TMS} and $\Delta H^{\theta_{\rm H}}$.

5.6 Conclusion

Ferromagnetic resonance studies have been carried out in CFAS thin films. The effect of anti-site disorder and thickness on the M_s , H_k , and α has been investigated. The various contributions to linewidth have been investigated by taking into consideration the various mechanisms that contributes to ΔH . Following are the results:

- 1. In the thickness series, the H_r variation with frequency is well described by the Kittel resonance expression. M_s and H_k are obtained from the fit and plotted with the TS. Among all the films in TS series, TS500 has the highest magnetization.
- 2. From the linewidth analysis of the broadband FMR, TS500 has the lowest α value. Such as low value of α validated the high spin polarization in the CFAS system.
- 3. The ΔH_{inh} and LLG term alone does not reproduce the frequency dependence of ΔH . Taking into account the TMS contribution best describes the ΔH bhaviour.
- 4. In the TS series, irrespective of the anti-site disorder, all the films show in-plane uniaxial anisotropy.
- 5. From the angular variation of ΔH , the LLG contribution and angular spread in the crystalline misorientation dominantly contribute to the broadening of linewidth.

6.	In the thickness series, 50 nm film has the highest magnetization and anisotropy field with the lowest α . This is attributed to the increased B2 crystalline order in this thickness.

References:

- 1. H. E. Griffiths, Nature **158**, 670 (1946).
- 2. L. Landau and E. Lifshitz, Phys. Z. Sowjetunion 8, 153 (1935).
- 3. T.L. Gilbert, Phys. Rev. **100**, 1243 (1955).
- 4. S. N. Kaul and V. Siruguri, J. Phys. F: Met. Phys. 17, L255 (1987).
- 5. S. N. Kaul and V. Siruguri, J. Phys.: Condens. Matter 4, 505 (1992).
- 6. S. N. Kaul and P. D. Babu, Phys. Rev. B 45, 295 (1992).
- 7. V. Siruguri and S. N. Kaul, J. Phys.: Condens. Matter **8**, 4545 (1996).
- 8. Allan H. Morish, "THE PHYSICAL PRINCIPLES OF MAGNETISM".
- 9. H. Suhl, Phys. Rev. 97, 55 (1955).
- 10. R. Arias and D. L. Mills, Phys. Rev. B 60, 7395 (1999).
- 11. P. Landeros, R. E. Arias, and D. L. Mills, Phys. Rev. B 77, 214405 (2008).
- 12. J. Linder et. al., Phys. Rev. B **80**, 224421 (2009).
- 13. I. Barsukov et. al., Phys. Rev. B **85**, 014420 (2012).
- 14. M. J. Hurben and C. E. Patton, J. Appl. Phys. **83**, 4344 (1998).
- 15. G. Woltersdorf and B. Heinrich, Phys. Rev. B 69, 184417 (2004).
- 16. C. Chappert, K. L. Dang, P. Beauvillain, H. Hurdequint, and D. Renard, Phys. Rev. B 34, 3192 (1986).
- 17. 17. S. Mizukami, Y. Ando, and T. Miyazaki, Jpn. J. Appl. Phys. 40, 580 (2001).
- 18. D. L. Mills and R. Arias, Physica B 384, **147** (2006).
- 19. R. Arias and D. L. Mills, J. Appl. Phys. **87**, 5455 (2000).
- 20. M. Belmeguenai et. al., Phys. Rev. B 87, 184431 (2013).

- 21. N. Mecking, Y. S. Gui and C. M. Hu, Phys. Rev. B **76** (2007) 224430.
- 22. C. Kittel, Phys. Rev. 73 (1948) 155.
- 23. B. K. Hazra, S. N. Kaul, S. Srinath and M.M. Raja, J. Phys. D: Appl. Phys. **52**, 325002 (2019)
- Y. V. Kudryavtseva, V. A. Oksenenkoa, V. A. Kulagina, J. Dubowikb and Y. P. Lee, J. Magn. Magn. Mater. 310 (2007) 2271.
- 25. N. Mo, J. Hohlfeld, M. Islam, C. S. Brown, E. Girt, P. Krivosik, W. Tong, A. Rebei and C. E. Patton, Appl. Phys. Lett. **92** (2008) 022506.
- 26. B. Heinrich, J. F. Cochran, and R. Hasegawa, J. Appl. Phys. 57 (1985) 3690.
- 27. C. E. Patton, J. Appl. Phys. **39** (1968) 3060.
- 28. Kambersky V 1970 Can. J. Phys. **48** 2906
- 29. Kambersky V 2007 Phys. Rev. B 76 134416
- 30. Sakuma A 2015 J. Phys. D: Appl. Phys. 48 164011
- 31. Andrieu S, Neggache A, Hauet T, Devolder T, Hallal A, Chshiev M, Bataille A M, Fevre P L and Bertran F 2016 Phys. Rev. B **93** 094417
- 32. J. F. Cochran, R. W. Qiao, and B.Heinrich, Phys. Rev. B **39**, 4399 (1989)
- 33. B. Heinrich and J. F. Cochran, R. Hasegawa, J. Appl. Phys. **57**, 3690 (1985).
- 34. Mikihiko Oogane, Resul Yilgin, Masatsugu Shinano, Satoshi Yakata, Yuya
- 35. Sakuraba, Yasuo Ando, and Terunobu Miyazaki, J. Appl. Phys. 101, 09J501 (2007).
- M. Oogane, T. Kubota, Y. Kota, 1 S. Mizukami, H. Naganuma, A. Sakuma, and Y. Ando,
 Appl. Phys. Lett. 96, 252501 (2010).
- 37. F. J. Yang, C. Wei, and X. Q. Chen, Appl. Phys. Lett. **102**, 172403 (2013)
- 38. G. A. Basheed, S. N. Kaul and A. Michels. Appl. Phys. Lett. **91**, 033105 (2007)

- 39. V. Siruguri and S. N. Kaul, J. Phys.: Condens. Matter **8**, 4545 (1996)
- 40. S. N. Kaul and P. D. Babu, Phys. Rev. B **50,** 9308 (1994)

Chapter 6

Effect of deposition temperature and film thickness on magnetization reversal and magnetic anisotropy

This chapter provides a comprehensive exploration of the impact of disorder and film thickness on magnetization reversal and magnetic anisotropy, focusing on the "in-plane" configuration. A thorough analysis of observed changes in hysteresis loops with the angular variation, along with the accompanying magnetic domain images, effectively elucidating the mechanisms for the magnetization behavior in the Co₂FeAl_{0.5}Si_{0.5} thin films are presented

6.1 Experimental details

Static Kerr hysteresis loops are recorded at varying 'in-plane' magnetic field angles (φ_H), along the film plane, by rotating the CFAS films with respect to the applied field (H) direction by using Longitudinal magneto-optic Kerr effect (L-MOKE) spectroscopy. Simultaneously, domain images are captured at different field val2ues of the hysteresis curve.

6.2 Theoretical Background

6.2.1 Introduction to magnetic domains and domain walls

Weiss proposed that in ferromagnetic materials, the atomic magnetic moments (or spins) interact with each other [1]. He suggested that these atomic moments tend to align parallel to each other within small regions, which are termed as "magnetic domains." Inside each domain, the magnetic moments reinforce each other, creating a strong local magnetic field. However, between neighboring domains, the magnetic moments point in different directions, leading to the cancellation of magnetic effects on a larger scale [2]. Weiss's mode l provided an explanation for phenomena like hysteresis (the lag in magnetization with changing external magnetic field) and the ability of ferromagnetic materials to retain their magnetization after the external field is removed.

For a ferromagnetic specimen, the total free energy in the presence of an external magnetic field is given by [1, 2]:

$$F_T = F_H + F_e + F_k + F_D + F_{\sigma} \tag{6.1}$$

Where, F_H is the Zeeman energy when an external magnetic field H is applied, F_e is the exchange energy, F_k represents the magnetocrystalline energy, F_D is the demagnetization energy and F_σ is the magnetostrictive energy [1]. Now, consider a single crystal, in the shape of a parallelepiped, where the extended axis denotes the preferred easy axis of magnetization direction. In the absence of an external magnetic field and under the assumption that there are no internal or external stresses affecting the sample then,

$$F_H = F_\sigma = 0 \tag{6.2}$$

When all the moments are aligned along the easy axis of magnetization, i.e, along the long edge of the parallelepiped, then the system is in a 'single domain' configuration. In this single domain, F_e will be minimum, but since all the moments are aligned in one direction, it will induce north and south poles at the edges. These induced poles will in turn produce a large demagnetization field whose direction is opposite to the internal field. To minimize such large demagnetization field, the single domain is broken into two reverse domains with the moments in each domain opposite to each other (180° with respect to each other). This ensures that the magnetic lines originating from either of the poles to close with the adjacent reversed-pole of the reverse domain, such that the F_D of a single domain is reduced by a factor of half. However, in the process, F_e and F_k are increased because all moments are not aligned parallel and are not pointed in the easy direction within the domain wall that separates the 180° domain. However, the total magnetic energy for this configuration is much lower than the single domain configuration. Thus, as the number of domains is increased, F_D will decrease at the expense of F_e and F_k . The boundary region between the two domains is called the 'domain wall and the competition between F_e and F_k decides the domain wall width. Since large F_e is required to flip a nearest-neighbor spin, F_e tends to make the domain wall wider. By contrast, F_k forces the spin to be aligned along the same direction and hence tends to decrease the domain wall width. For a uniaxial system, the domain wall width can be calculated by minimizing the F_e and F_k and is given by [2]:

$$\delta = \pi \sqrt{\frac{J S^2}{K a}} \tag{6.3}$$

In the expression, S is the electron spin, K is the anisotropy constant, J is the exchange integral and 'a' is the lattice parameter. A 180° domain wall separates the domains of opposite magnetization whereas 90° domain wall separates the domains where one domain makes an angle 90° to another one.

6.2.2 Stoner and Wohlfarth model

The Stoner-Wohlfarth model [3,4] is a theoretical framework which provides insights into the behavior of magnetic materials, in the presence of an applied external magnetic field. The model starts by assuming that the material is a single magnetic domain consisting of non-interacting particles exhibiting uniaxial anisotropy. Ferromagnetic materials often have multiple magnetic domains with different magnetization directions [1]. However, considering a single domain simplifies the analysis and serves as a useful starting point. The magnetization reversal occurs primarily via coherent rotation, with minimal impact from thermal effects on magnetization [5].

The model accounts for two key energy contributions: F_H and F_k when the magnetic moments align parallel to the external field, F_H is minimized, making this configuration energetically favorable. F_k favors the magnetic moments to align along a specific direction within the material along the "easy axis."

The SW model predicts that in the presence of an external magnetic field, there are two stable states for the magnetic domain: One state is the parallel alignment state, when the external field is applied parallel to the easy axis, the atomic magnetic moments align with the field direction. This configuration has the lowest total energy because both Zeeman and anisotropy energies are minimized. Another is the antiparallel alignment state, when the field opposes the easy axis, the magnetic moments align against the field direction. This state also has lower energy because it minimizes the anisotropy energy at the expense of increased Zeeman energy. Accordingly, as the external magnetic field strength is gradually increased or decreased, the magnetization of the material traces a hysteresis loop. This loop represents the transition between the two stable states as the field changes.

At T=0 K, consider an ellipsoid shaped grain carrying a single magnetic moment, 'm', with uniform magnetization throughout possesses a uniaxial anisotropy and is subjected to an externally applied static magnetic field H. The orientation of M is decided by the competition of uniaxial anisotropy energy and Zeeman energy due to H [5]. Therefore, at T=0 K, the energy per unit volume is then given by,

$$E = E_k + E_H = K \sin^2 \varphi_M - HM_s \cos(\varphi_M - \varphi_H)$$
 (6.4)

The anisotropic energy $K \sin^2 \varphi_M$ is minimum when $\varphi_M = 0$ for K > 0. If we add the demagnetization term to the anisotropy, then the effective anisotropy, K_{eff} can be written as:

$$K_{eff} = [K + 2\pi M_s (N_{\perp} - N_{\parallel})] \sin^2 \varphi_M \tag{6.5}$$

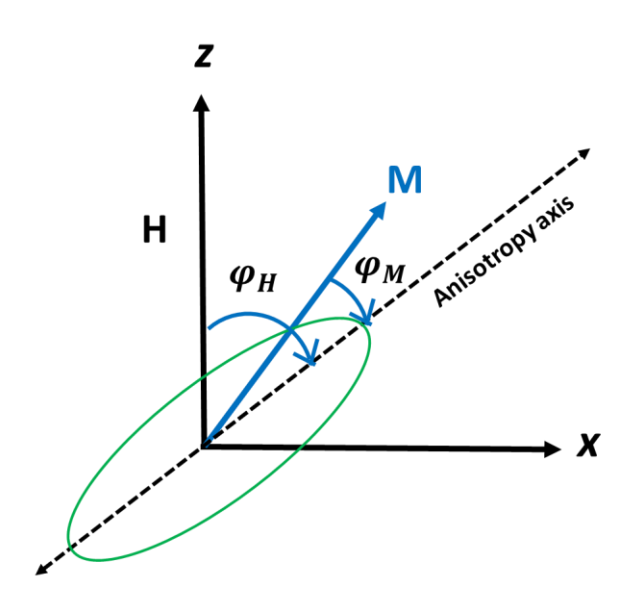


Fig. 6.1: Considering a single domain system with the easy axis of magnetic anisotropy axis, external magnetic field and magnetization directions.

Here, N_{\parallel} and N_{\perp} are the parallel and perpendicular demagnetization coefficients to the z-axis respectively. Now, the total energy of the SW model can be rewritten as,

$$E = K_{eff} \sin^2 \varphi_M - HM_s \cos(\varphi_M - \varphi_H)$$
 (6.6)

The minimum energy is achieved when $\varphi_M = \varphi_M^*$, where φ_M^* is the angle along which the magnetization prefers to align in equilibrium condition, refer Fig. 6.1. The minimum condition at φ_M^* is given by:

$$\left(\frac{\partial E}{\partial \theta}\right)_{\varphi_M = \varphi_M^*} = 0 \tag{6.7}$$

and

$$\left(\frac{\partial^2 E}{\partial \theta^2}\right)_{\varphi_M = \varphi_M^*} \ge 0 \tag{6.8}$$

Applying the above conditions to Eq. (6.6) yields,

$$[\sin\varphi_M \cos\varphi_M + h \sin(\varphi_M - \varphi_H)]_{\varphi_M = \varphi_M^*} = 0 \tag{6.9}$$

and

$$[\cos 2\varphi_M + h\cos(\varphi_M - \varphi_H)]_{\varphi_M = \varphi_M^*} \ge 0 \tag{6.10}$$

Magnetization, M, as a function of magnetic field, H, can be obtained from the values of φ_M , obtained from Eq. (6.9) and Eq. (6.10). The longitudinal magnetization, i.e., the projection of magnetization vector along the magnetic field direction, is given by [5,6]:

$$m_{\parallel} = \cos(\varphi_M - \varphi_H) \tag{6.11}$$

And the projection of M perpendicular to H, which is the transverse magnetization, is given by:

$$m_{\perp} = \sin(\varphi_M - \varphi_H) \tag{6.12}$$

The critical field h_c (which is equal to the coercive field (H_c) at $\varphi_H = 0$) for which magnetization reversal is obtained from Eq. (6.9) and Eq. (6.10) with the result,

$$H_s(\varphi_H) = \frac{H_k}{\left[\sin^{2/3}\varphi_H + \cos^{2/3}\varphi_H\right]^{3/2}}$$
(6.13)

For $0 < \varphi_H < 45^\circ$, H_c coincides with the switching field (H_s):

$$H_c = H_s(\varphi_H) = \frac{H_k}{\left[\sin^{2/3}\varphi_H + \cos^{2/3}\varphi_H\right]^{3/2}}$$
(6.14)

And for $45^{\circ} < \varphi_H < 90^{\circ}$,

$$H_c = \frac{H_k}{2\sin 2\omega_H} \tag{6.15}$$

6.2.3 Two-phase model

The Kondorsky model [7] predicts the angular dependance of coercivity during the process of magnetization reversal, primarily driven by domain wall motion. According to this model, magnetization reverses take place when the Zeeman energy exceeds the energy associated with the domain walls [7,8].

$$H_c^{Kon}(\varphi_H) = \frac{H_c(0)}{\cos \varphi_H} \tag{6.16}$$

It is evident from the Eq. (6.16) that H_c diverges at $\varphi_H = 90^\circ$. However, in a real material, H_c has a finite value at $\varphi_H = 90^\circ$. Thus, the above relation does not reproduce the angular dependence of coercivity at all angles (more so near $\varphi_H = 90^\circ$.)

Suponev et al. [9] proposed the two-phase model which generalizes the Kondorsky model [7]. The model is constructed by considering a system with two phases or two types of magnetic domains and the magnetization reversal occurs either by domain wall movement or coherent rotation, based on the range of the magnetic field. For an ellipsoid system having a uniaxial anisotropy, the angular dependance of H_c is given by the expression [9-15]:

$$H_c^{two-phase}(\varphi_H) = \frac{H_c(0)\cos\varphi_H}{(1/y)\sin^2\varphi_H + \cos^2\varphi_H}$$
(6.17)

where,

$$y = \frac{(N_x + N_N)}{N_Z} \tag{6.18}$$

Therefore, Eq. (6.17) gives:

$$H_c^{two-phase}(\varphi_H) = H_c(0) \frac{(N_x + N_N)\cos\varphi_H}{N_z\sin\varphi_H + (N_x + N_N)\cos^2\varphi_H}$$
(6.19)

 N_x and N_z are the demagnetization factors of the ellipsoid along the x and z directions. $N_N=H_A/M_S$, is the demagnetizing factor arising from anisotropy apart from the shape anisotropy [9, 7, 15]. When, $z\to\infty$, the expression (Eq. (6.19)) reduces to the Kondorsky formula (Eq. (6.16)). This is realized in the case of an infinite thin film with $N_x=N_z=0$.

Further, by taking two uniaxial anisotropies (UA₁ and UA₂) with significantly different magnitudes and considering that the direction of their easy axis is perpendicular to each other [16, 17], the original expression of the two-phase model i.e. Eq. (6.17) for the angular dependance of H_c is modified to:

$$H_c^{Modified\ TP}(\varphi_H) = H_c(0) \left[\frac{\cos \varphi_H}{(1/y_1) \sin^2 \varphi_H + \cos^2 \varphi_H} + \frac{\sin \varphi_H}{(1/y_2) \cos^2 \varphi_H + \sin^2 \varphi_H} \right]$$
(6.20)

 y_1 and y_2 gives the strength of the primary and secondary uniaxial anisotropies respectively.

6.3 Data analysis, results and discussion

6.3.1 Effect of deposition temperature

The static Kerr hysteresis loops were recorded at various "in-plane" field angle (φ_H) from 0° to 360° by rotating the sample with respect to the applied field direction. In Fig. 6.2, the Kerr loops at selected field angles, φ_H , for the films deposited at RT, TS350, TS450, TS500 and TS550 is shown. At $\varphi_H = 0^\circ$, rectangular hysteresis loops are observed for RT, TS350 and TS500. In

order to characterize the observed Kerr loops, the normalized squareness ratio and the coercive field (H_C) are obtained from the loops. The normalized squareness ratio is given by $\frac{M_r}{M_S}$, where M_r is the remanent magnetization and M_S is the saturation magnetizations. A perfect square or rectangular hysteresis loop should give $\frac{M_r}{M_S}\cong 1$. For the TS450 CFAS film, $\frac{M_r}{M_S}<1$ at $\varphi_H=0^\circ$ (i.e. along the easy axis) and for the TS550 CFAS film the Kerr loops are not perfectly square or rectangle which show that these films do not follow the SW model [5].

 $\frac{M_r}{M_S}$ and H_C extracted at different field angle (φ_H) are plotted in Fig. 6.3 and 6.4, as functions of φ_H . From the plots, following features are observed:

- (i) In the RT, TS350 and TS500 CFAS thin films, the angular variation of $\frac{M_r}{M_S}$ ratio and H_C shows a two-fold symmetry (shown in Fig. 6.3 and Fig. 6.4)
- (ii) The angular (φ_H) variation of $\frac{M_r}{M_S}$ ratio, for the TS450 and TS550 films (Fig. 6.3(c) and (e)) goes through four maxima at $\varphi_H = 0^\circ$, 90°, 180° and 270° (and four minima $\varphi_H = 70^\circ$, 110°, 250° and 300°).
- (iii) Similarly, four maxima at $\varphi_H = 0^\circ$, 90° , 180° and 270° (and four minima $\varphi_H = 70^\circ$, 110° , 250° and 300°) in the angular (φ_H) variation of H_C is observed for the TS450 and TS550 films.

In alignment with the two-fold angular variation of resonance field $(H_{res}^{||})$ from the FMR study, the two-fold angular variation of $\frac{M_r}{M_S}$ ratio and H_C confirms that the CFAS films have in-plane uniaxial anisotropy and the uniaxial anisotropy persist up to a high deposition temperature of 500 °C. Thin films of Cobalt-based Heusler alloy have also been previously reported with uniaxial anisotropy [18-20]. During the CFAS film deposition process, the films are grown at an oblique-angle deposition, resulting in 'self-shadowing' effect [21-24] which influences uniaxial anisotropy (UA) in the films.

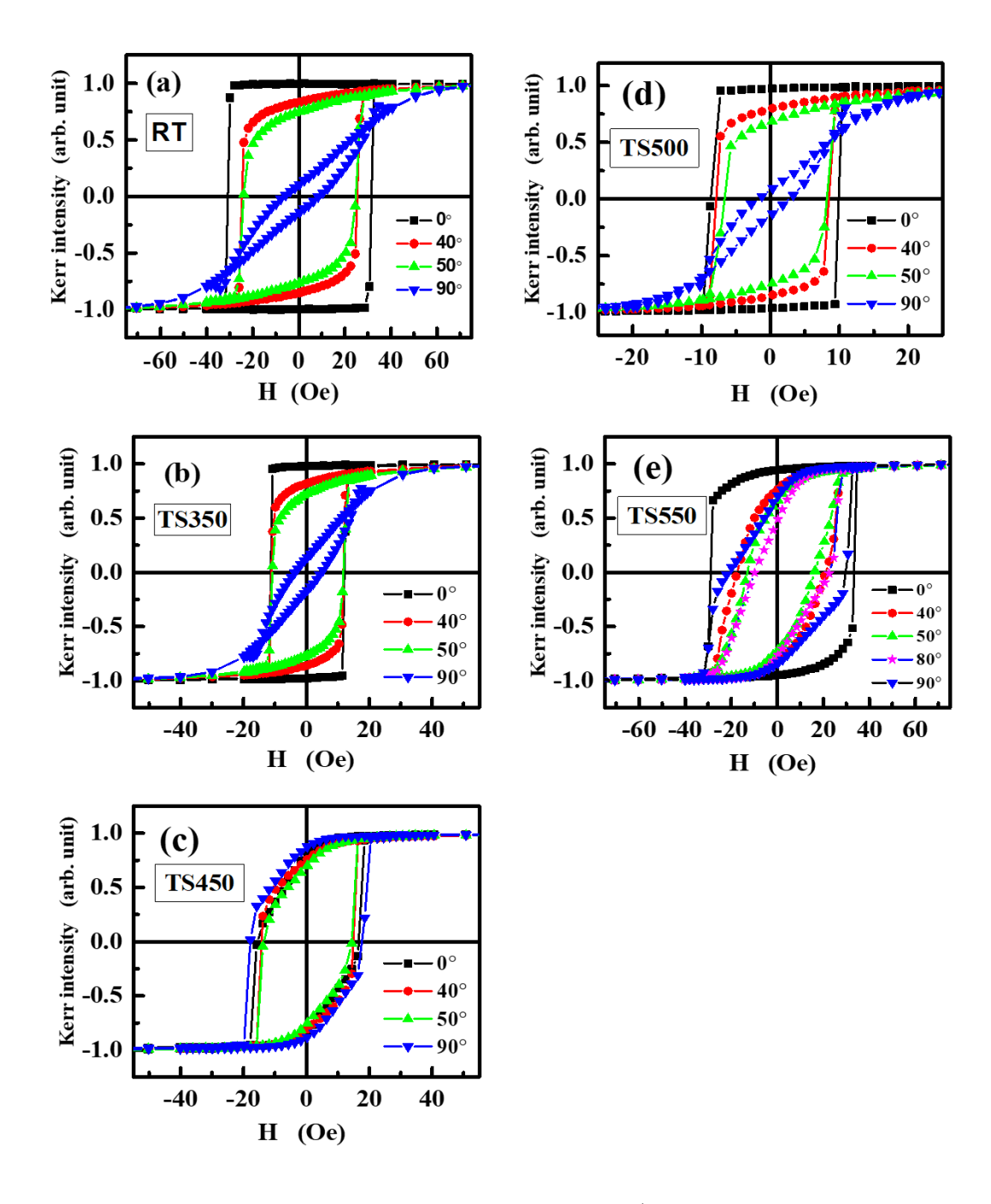


Fig. 6.2: Kerr hysteresis loops recorded at $\varphi_H = 0^{\circ}, 40^{\circ}, 50^{\circ}, 90^{\circ}$ for the TS series CFAS thin films.

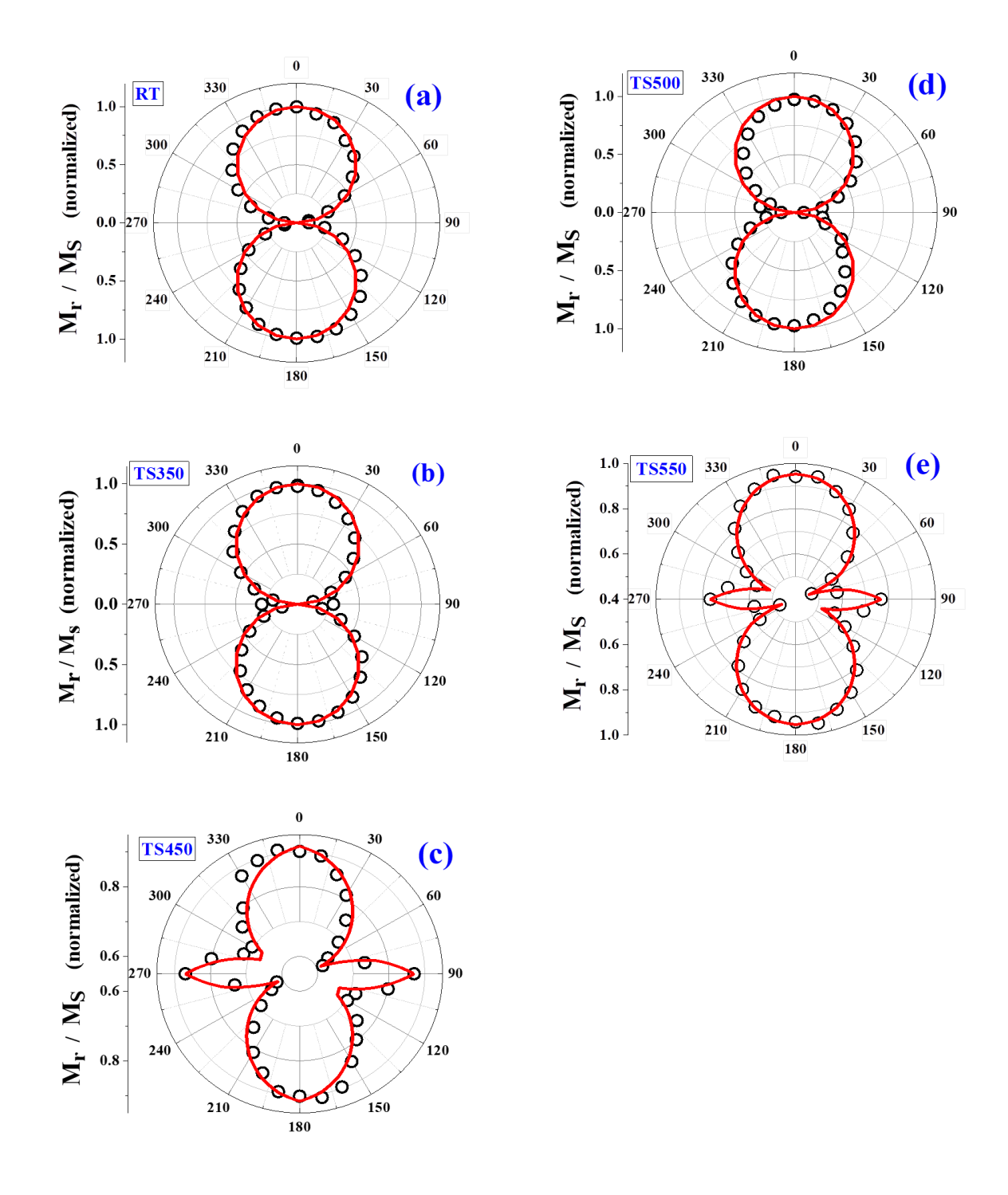


Fig. 6.: $\frac{M_r}{M_S}$ (φ_H) plot for the (a) RT, (b) TS350, (c)TS450, (d) TS500 and (e) TS550 CFAS thin films. The red continuous lines represent the fit and open circles represent the raw data.

The observation of maxima at the nominal hard axis of uniaxial anisotropy, $\varphi_H = 90^\circ$ or $\varphi_H =$ 270° has been previously reported by O. Idigoras et al. [13, 14] in the epitaxially grown uniaxial Co thin films. In the Co thin film with complete epitaxial alignment, there is a total absence of the such maxima around the hard axes. However, as the degree of epitaxial order decreases due to the increase in crystalline misorientation and disorder, these maxima or peak becomes more prominent in the range of $\varphi_H = 90^\circ \pm 2^\circ \text{ or } 270^\circ \pm 2^\circ$ for the angular variation of $\frac{M_r}{M_S}$ and H_C . In this case, the two-grain Stoner-Wohlfarth (SW) model has been used to elucidate the result [13, 14]. It is worth noting that this model is not suitable for the CFAS films under examination because in TS450 and TS550 CFAS films, the observed maxima is spread over a large angular range of ±50° around HA compared to the narrow angular range of $\pm 2^{\circ}$ around HA in the disordered Co thin films. In addition, owing to the polycrystalline characteristics of the TS450 and TS550 CFAS thin films, a measurable misalignment angle between the easy magnetization directions of the neighbouring grains is inevitably present. Similar observations have been reported for the CFS thin film systems Furthermore, when considering cubic magnetocrystalline anisotropy (MCA) as well [17]. characterized by a four-fold symmetry, $H_C(\varphi_H)$ displays four maxima at $\varphi_H = 45^\circ$, 135° , 225° , and 315°, along with four minima at $\varphi_H = 0^\circ$, 90°, 180°, and 270°, all with equal magnitudes [2]. Therefore, the observed variation of $\left[\frac{M_T}{M_S}\right](\varphi_H)$ and $H_C(\varphi_H)$ in the TS450 and TS550 CFAS films (Figs. 6.3 and 6.4) cannot be attributed to cubic MCA or conventional uniaxial anisotropy.

The anisotropy present in the CFAS films can be greatly influenced by the deposition and growth conditions of the films. The angular variation of $\frac{M_r}{M_S}$ can be reproduced by using the expression $\frac{M_r}{M_S}$ (φ_H) = cos (φ_H). Such a fit is represented by the red continuous lines (fit lines) in Fig. 6.3.

To understand the magnetization reversal process in CFAS thin films, analysis of $H_C(\varphi_H)$ has been conducted, involving the application of the SW model (Eq. 6.13), TP model (Eq. 6.17), and modified TP model (Eq. 6.20). The parameters (H_k and H_C) utilized for fitting these theoretical models to the $H_C(\varphi_H)$ plots are obtained as follows:

(i) The anisotropy field, H_k , corresponds to the field value at the onset of saturation magnetization on the Kerr-loops recorded at hard-axis ($\varphi_H = 90^\circ$) (Fig. 6.2)

(ii) The coercive field, H_C , is taken at the coercive field value on the Kerr-loop recorded along the easy axis ($\varphi_H = 0^\circ$) of magnetization.

In the RT films, the $H_C(\varphi_H)$ data has been analyzed by considering the SW model (Eq. 6.13), TP model (Eq. (6.17)) and the modified TP model (Eq. (6.20)). The individual models do not entirely reproduce the observed behavior $H_C(\varphi_H)$. In contrast, in this film both the SW and TP models contribute to $H_C(\varphi_H)$.

In the case of TS350 and TS500 films where a dominant two-fold variation of $H_C(\varphi_H)$ is observed, the TP model given by Eq. (6.17) entirely accounts for the H_C variation with φ_H .

The best fit to the $H_C(\varphi_H)$ data for the TS450 and TS500 CFAS film is obtained based on Eq. (6.20) (modified TP model) by taking y_1 and y_2 as free-fitting parameters and fix the H_C and H_k values. Fig. 6.4 shows the fit to the $H_C(\varphi_H)$ for the CFAS films. Evident from the figure, for the T450 and TS550, the modified TP model fits which are represented by the continuous red lines throughout the raw data (open circles), shows that the model describes $H_C(\varphi_H)$ behavior very well. The values H_C and H_k obtained from the Kerr loops and y_1 and y_2 from the fit are listed in Table 6.1.

From table 6.1, irrespective of TS, the relation $H_C < H_k$ is observed. This further justifies that the consideration of TP model and modified TP model to describe the $H_C(\varphi_H)$ holds good, since the pinning model is applicable only when $H_C < H_k$. The non-applicability of the SW model concludes that the CFAS film are multi domain systems.

With the increase in deposition temperature (TS), both H_C and H_k gradually decreases from H_C = 33 Oe and H_k = 61 Oe for RT to TS500 film (H_C = 9 Oe and H_k = 20 Oe). For the TS550, the value of H_C and H_k is higher than the TS500 films. Such a variation of H_C with TS in numerous thin films of Co-based Heusler alloys has been observed [21, 22].

Table 6.1: H_C and H_k obtained from the Kerr loops at $\varphi_H = 0^\circ$ and $\varphi_H = 90^\circ$ field angle respectively, along with the obtained values of y_1 and y_2 , from the fit for TS series CFAS films.

Sample ID	$H_{\mathcal{C}}$ (Oe)	$H_k(Oe)$	<i>y</i> ₁	<i>y</i> ₂	$H_k^{ }(Oe)$
					from FMR
RT	33	61			54
TS350	12	60	2.52(3)		18
TS450	16	40	1.33(3)	0.06(3)	9
TS500	9	20	1.8(2)		8
TS550	33	40	0.45(1)	0.03(2)	11

The variations observed in H_C and H_k with TS can be understood as follows: The impurities, defects or disorder present in the system acts a pinning center for the domain walls [2] and obstructs the domain wall motion during magnetization reversal process. To detach the domain walls from such pinning centers, large field are required to overcome the local anisotropy energy barriers. Thus, the CFAS films with higher degree of disorder (like the RT film) have higher H_C and switching fields. As the deposition temperature is increased, the films are more homogenized and the pinning centers due to defects decreases which in turn reduces the H_C and H_k . However, above 500° C deposition temperature, interdiffusion between the substrate and the film increases the magnetic inhomogeneity. Such an observation has been directly reflected in the sudden increase in the residual resistivity [Chapter 3] and the FMR linewidth [Chapter 5] in the case of TS550 CFAS films. This explains the increase in H_C and H_k in TS550 CFAS films.

In the TS450 and TS550 CFAS films, the parameter $y_1 \gg y_2$ as determined by Eq. (6.20) is a result of a significantly larger area under the lobes $\varphi_H = 0^\circ$ and 180° lobes compared to those under the $\varphi_H = 90^\circ$ and 270° lobes. This observation infers that the uniaxial anisotropy (UA₁) with an easy axis along $\varphi_H = 0^\circ$ or 180° predominates over the easy axis along $\varphi_H = 90^\circ$ or 270° (UA₂).

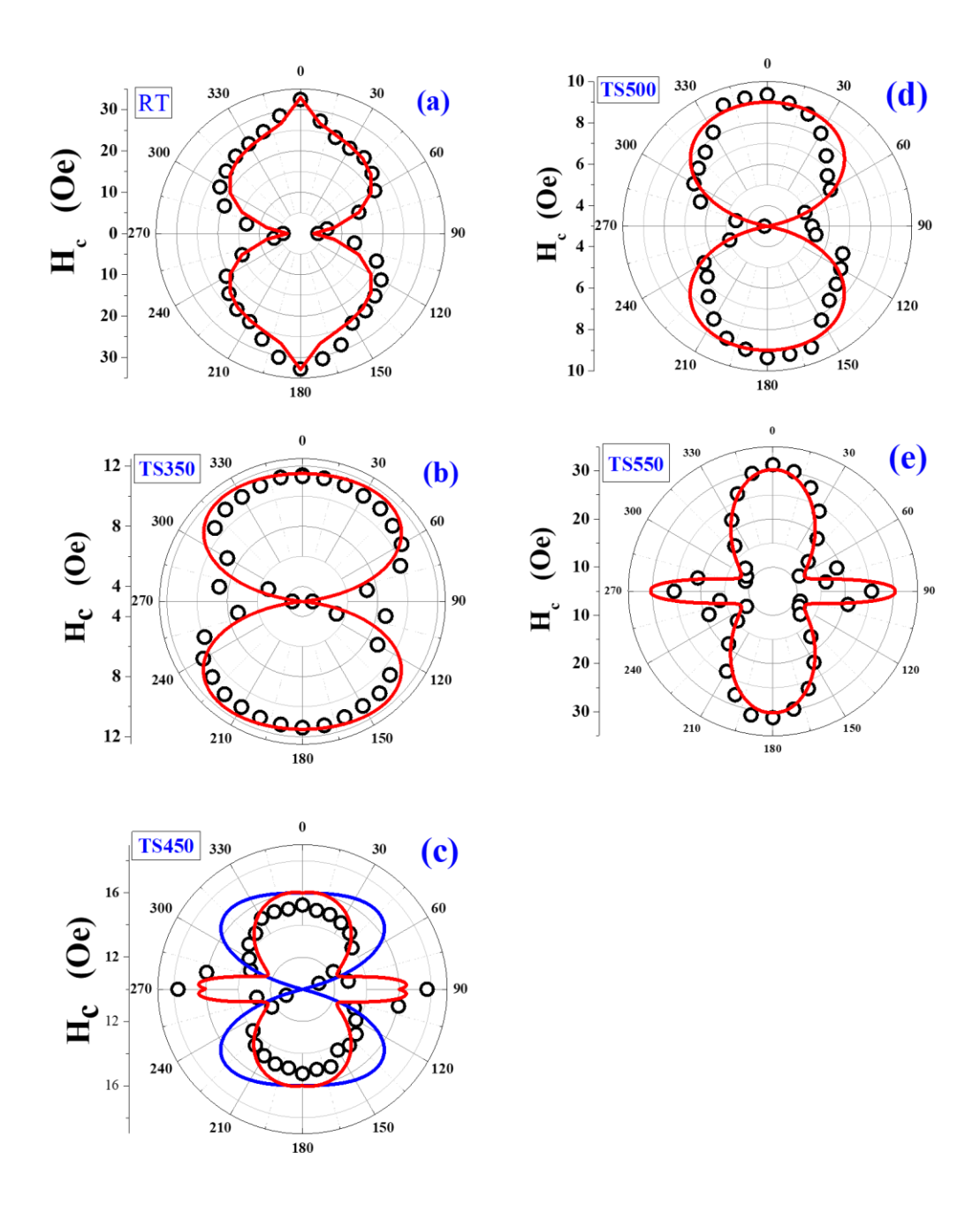


Fig. 6.4: $H_C(\varphi_H)$ plot for (a)RT, (b) TS350, (c) TS450, (d) TS500 and (e) TS550, CFAS film along with the fit, red lines, obtained from Eq. (6.13) and (6.17) and (6.20) as illustrated in the text.

The progression of domain images with changing magnetic fields allows for a visual description of the magnetization reversal process. Capturing domain images at different points along the magnetic hysteresis in the sample configurations facilitates this characterization. The images of domains, corresponding to the positions identified on the hysteresis loops, are displayed in Fig. 6.5 - 6.7. These images are captured at specific "in-plane" field angles, namely at $\varphi_H = 0^{\circ}$, 45° and 90°, for all the CFAS films.

Before starting the measurement, an alternating field was used to eradicate the residual magnetization in the films. A magnetic field, whether positive or negative and greater the coercive field strength, was employed to completely saturate the film. The process of capturing domain images entailed reducing the magnetic field from the saturation level. Regions with a bright (dark) contrast indicate domains where the magnetization vector aligns with the positive (negative) direction of the magnetic field. The blue (red) arrow represents the magnetization orientation within the domain along the positive (negative) direction of the magnetic field, while the yellow arrow indicates the direction of the magnetic field. Following are the observations when H is applied along different angles

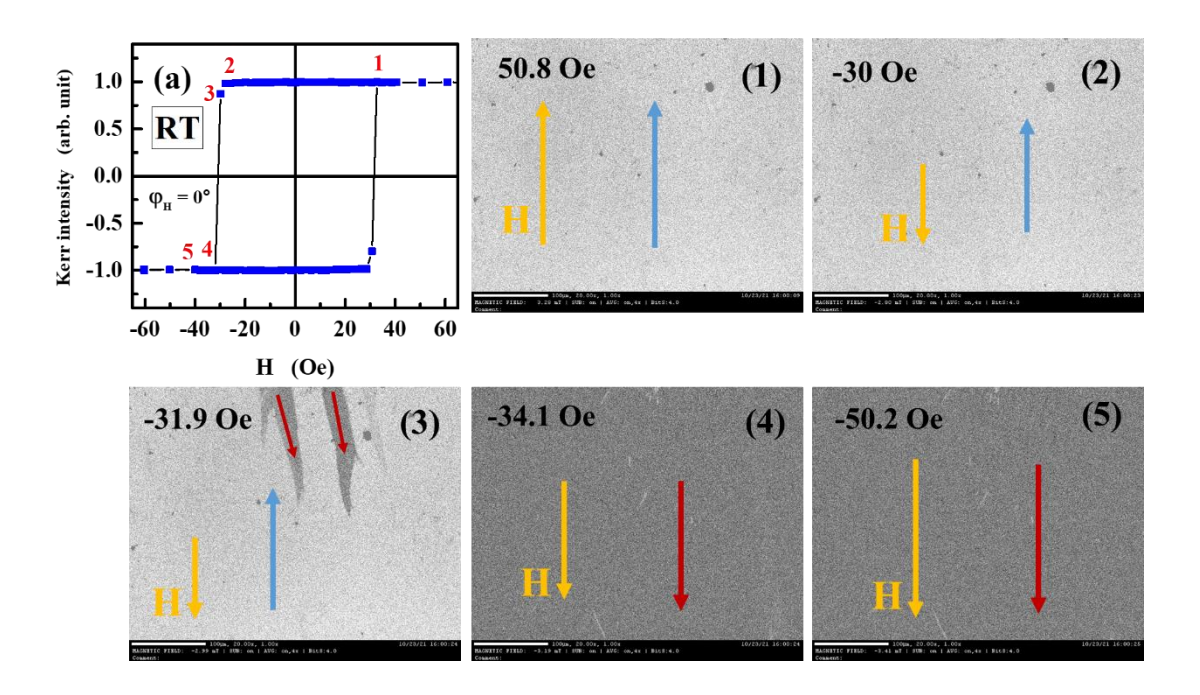
(i)
$$\varphi_H = 0^\circ$$

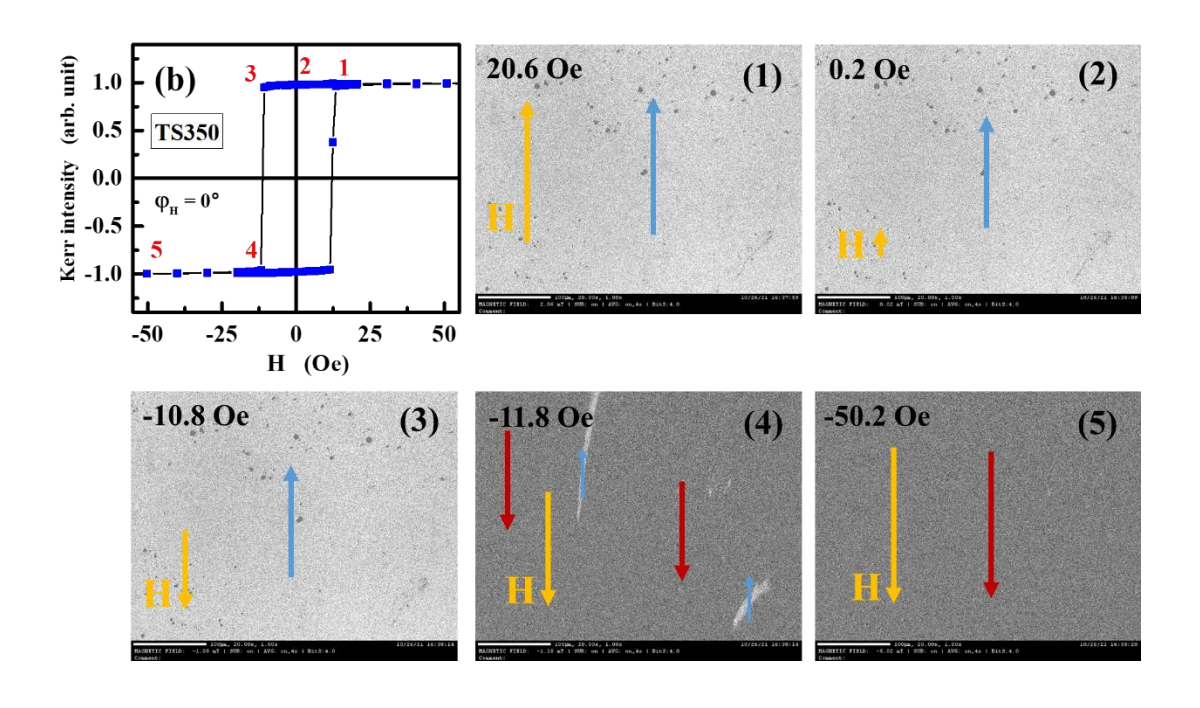
When H is applied along $\varphi_H = 0^\circ$, the magnetic field points along the 'in-plane' *easy-axis* of magnetization of the films. In films RT, TS350 and TS500, the magnetic domains (given by bright contrast) retain its orientation up to a certain field ($\sim H_c$) and then beyond this field, there is a quick transition to the reverse domains (given by dark contrast) as indicated by the sharp transition in the Kerr loops. The amount of inhomogeneity dictates both the density and strength of pinning centers in the films. The growth of reverse domain with field is captured in the RT film at *stage 3* of the hysteresis at H = -31.9 Oe (Fig. 6.5 (a)). At this stage of the field both the domains exist simultaneously but a slight increase in H (\sim 2 Oe) completely reverses the domain and brings to the saturated state.

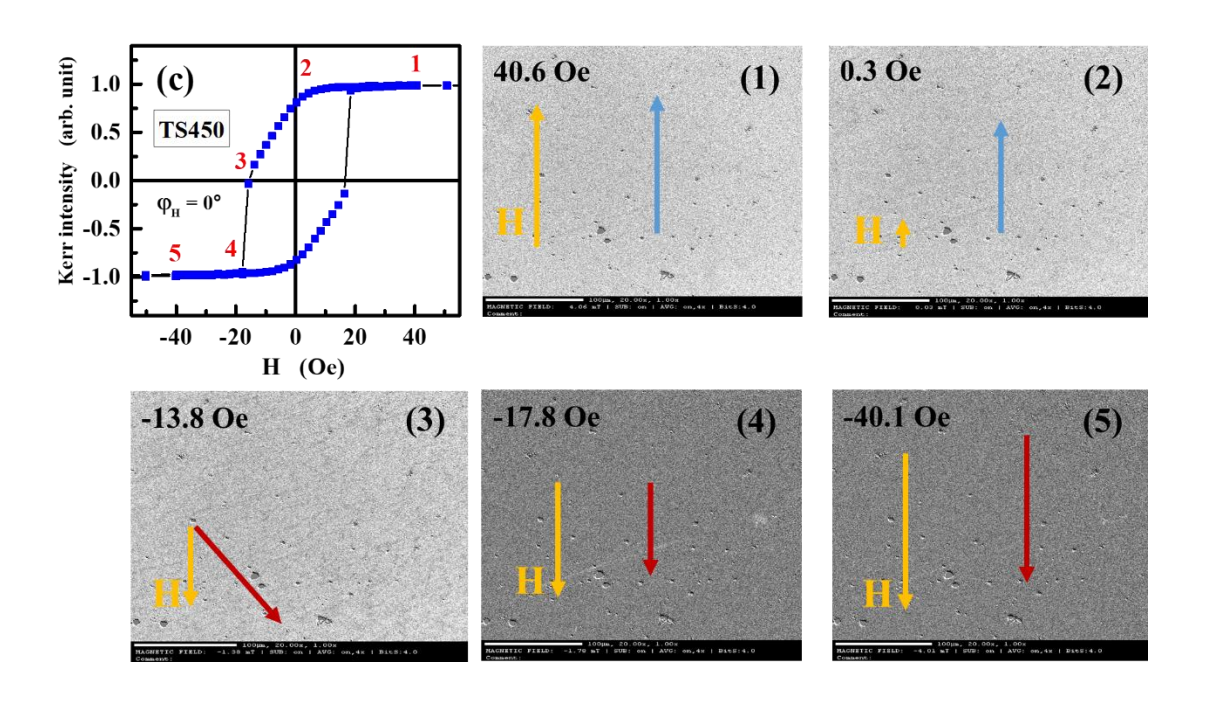
Similar observation is captured at *stage 4* of TS350 at -11.8 Oe (Fig. 6.5 (b)). Here the reverse domain is much larger and dominant. The field in *stage 3* and *stage 4* is H = 10.8 Oe and H = 11.8 Oe respectively, which means that even for a small change in $H (\sim 1 \text{ Oe})$ the domain gets completely reversed.

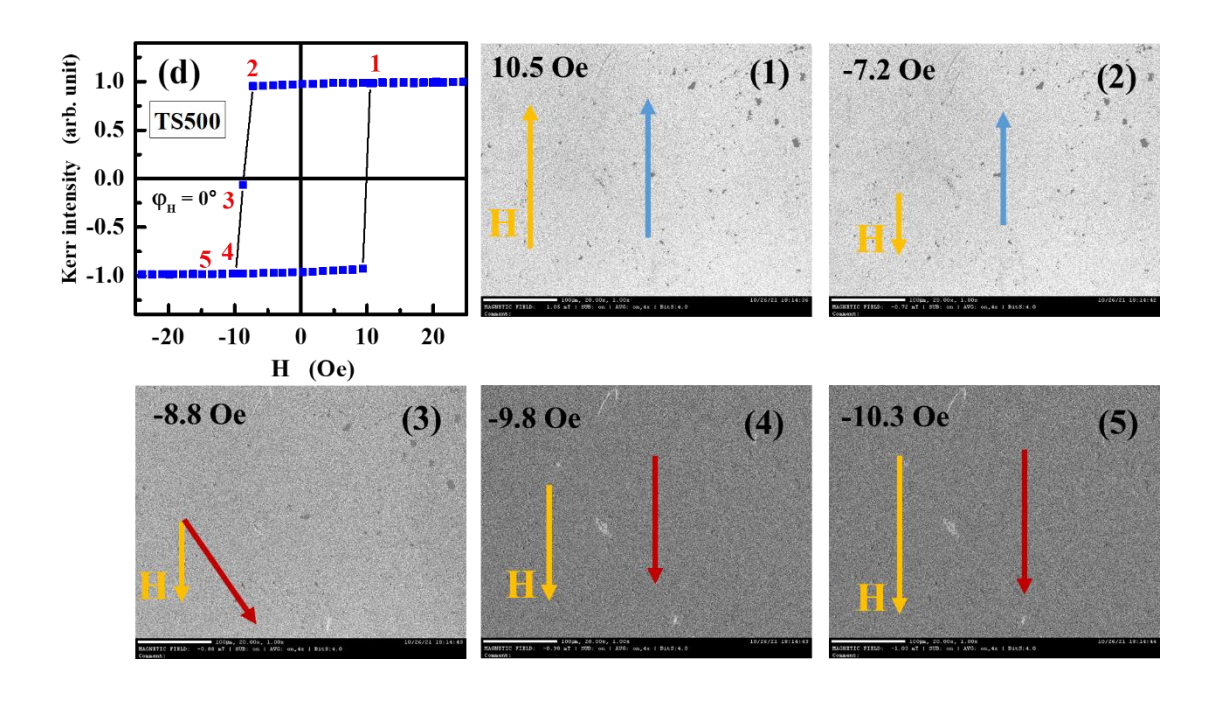
Thus, in RT, TS350 and TS500 CFAS films, the reverse domains nucleate as H approaches H_c and grow through the movement of domain wall when H surpasses H_c . With an increase in substrate temperature, the size of domains along the easy axis becomes larger and is easier to magnetize owing to which, in the TS500 film, the formation of reverse domains is abrupt and occurs quickly over a very small change in H, hence, the change in domain was not possible to record because the movement of domain walls occurs on a timescale significantly shorter than the temporal resolution of the current Kerr microscopy.

In the TS450 and TS550 CFAS films, coherent rotation takes place as the field increases to H_c , beyond which abrupt formation of reverse domain is observed. This is seen in the gradual decrease in Kerr intensity from the hysteresis loop. As indicated in the Fig. 5 (c) and (e), a small increase in field of H ~ 4 Oe (in TS450) and H ~ 2 Oe (in TS550) completely saturates the domain in the reverse direction. Thus, in TS450 and TS550, magnetization reversal occurs through both rotation (coherent) as well as growth.









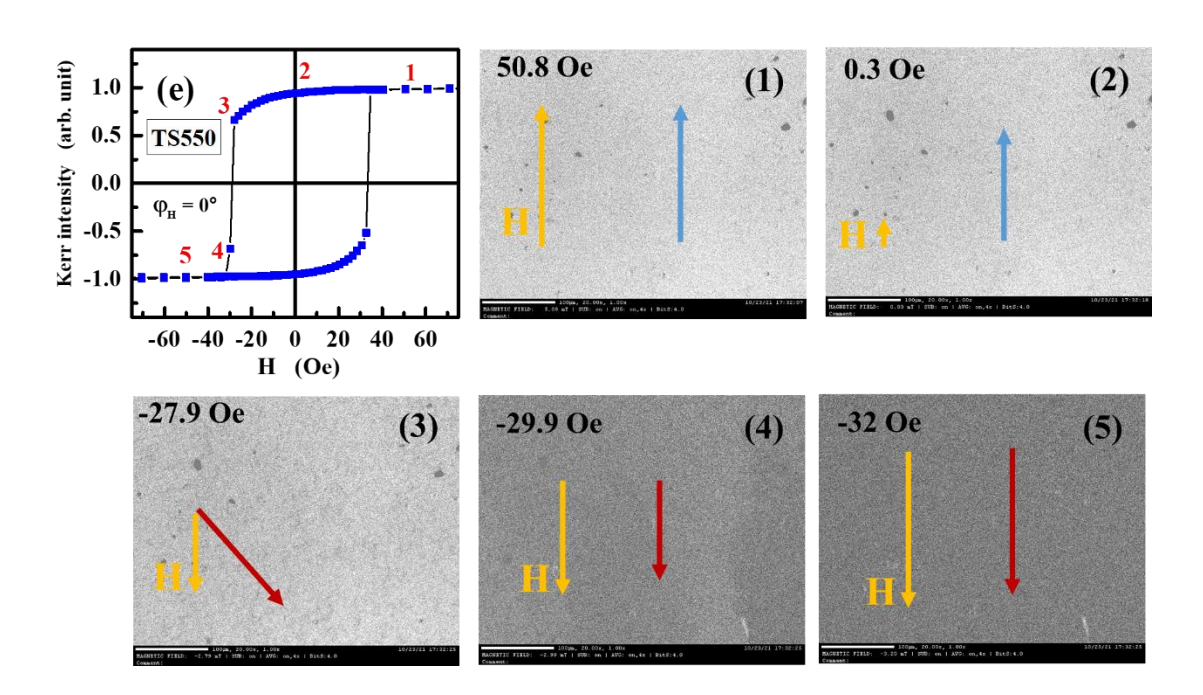
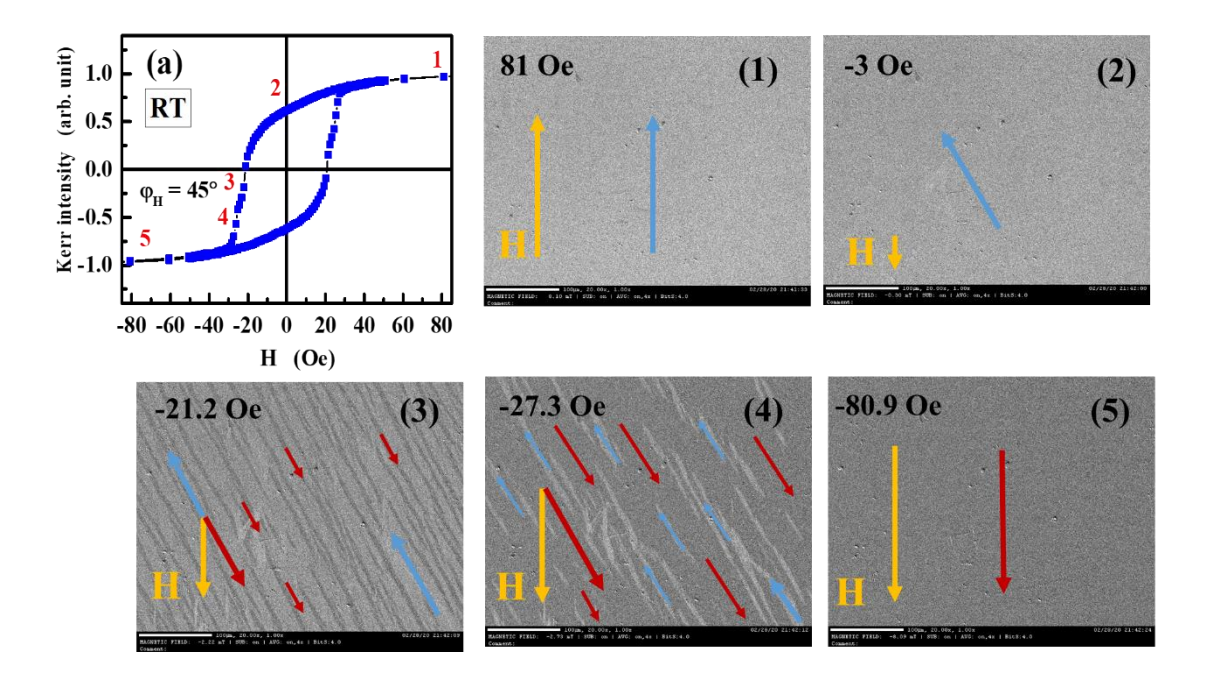
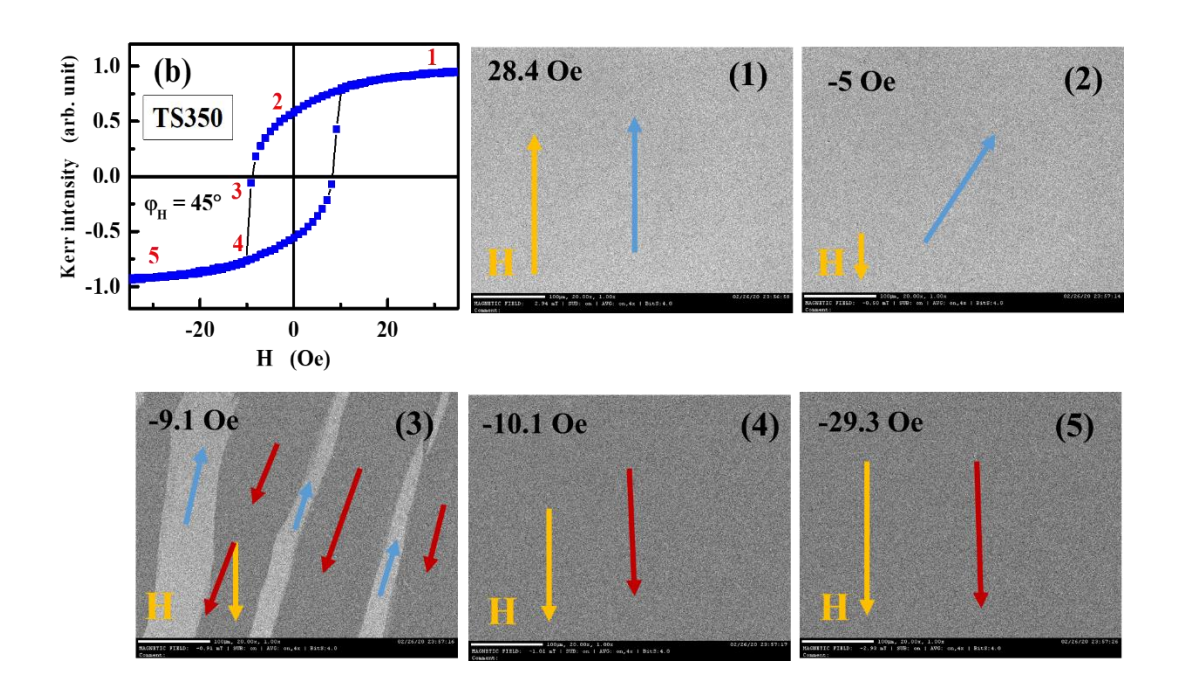


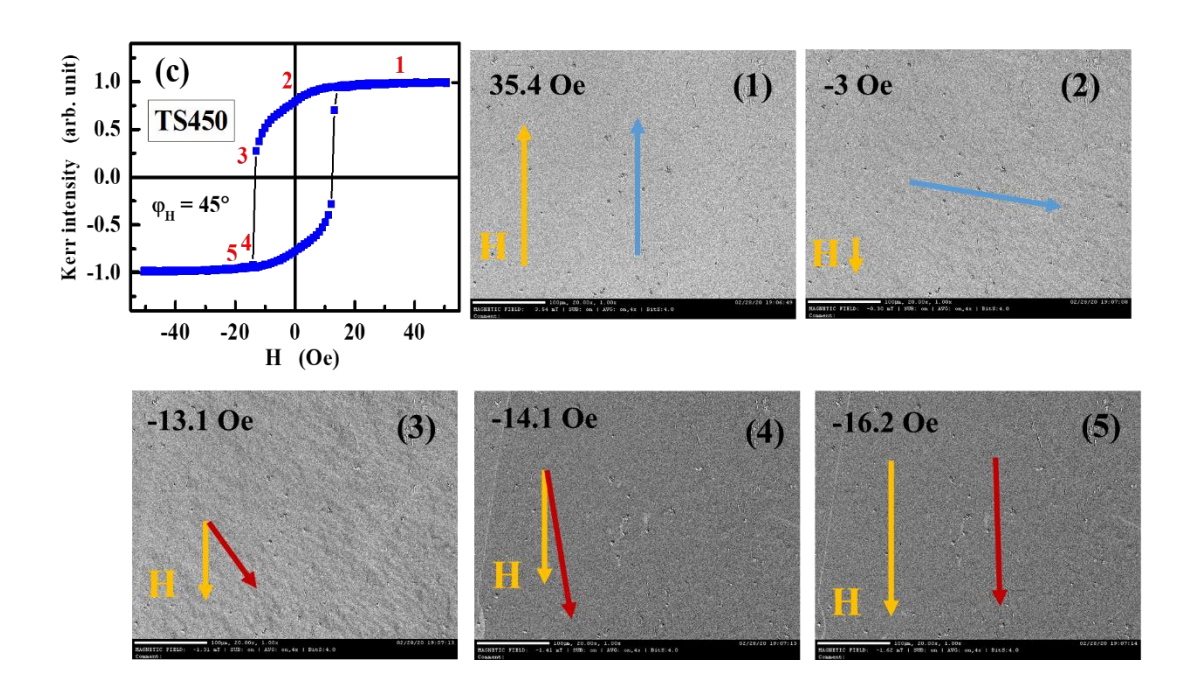
Fig. 6.5: Domain images taken at various points along the hysteresis curve at $\varphi_H = 0^{\circ}$ for (a) RT, (b) TS350, (c) TS450, (d) TS500 and (e) TS550, CFAS films

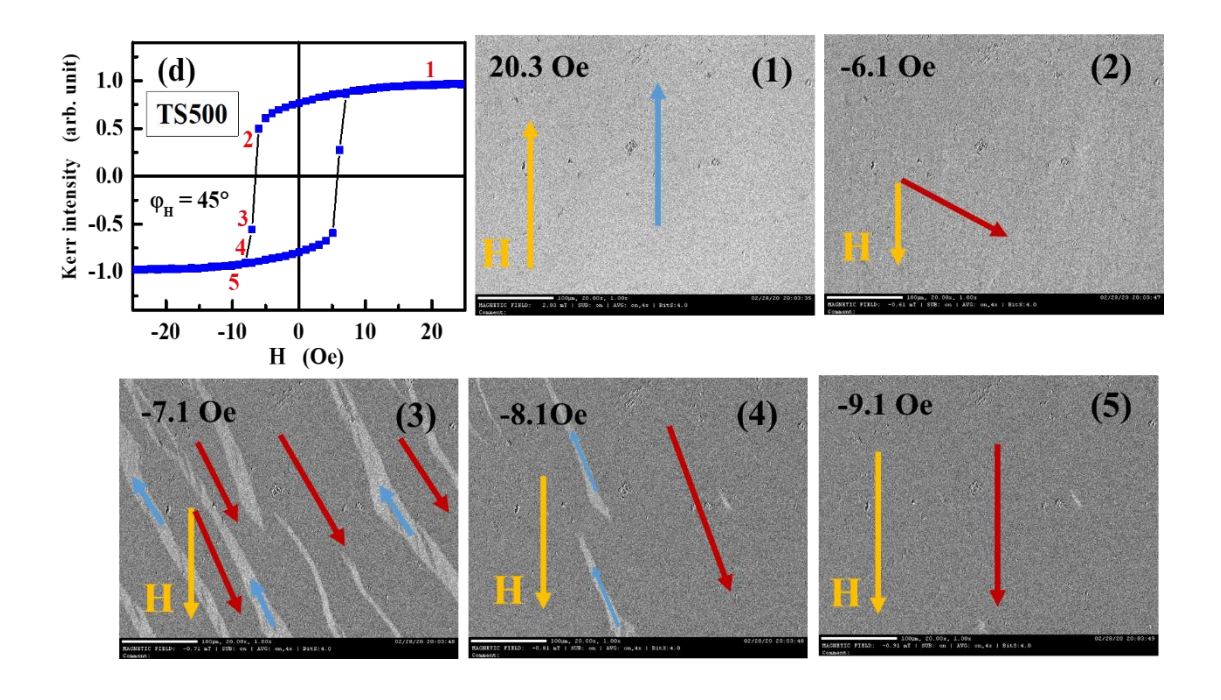
(ii)
$$\varphi_H = 45^\circ$$

When the magnetic field is directed at an angle of $\varphi_H = 45^{\circ}$ to the magnetization's easy axis, the reversal of magnetization occurs through a combination of rotation and growth. As H decreases, the magnetization vector endeavors to align itself with the easy axis, leading to its rotation towards the easy axis. Since the field required to saturate is quite large compared to the easy axis, rotation cannot be coherent giving rise to a stripe domain observation as seen in RT, TS350, TS450 and TS500, refer Fig. 6.6 (a) - (d). In the TS550 film nucleation of a large number of reverse domains is observed (Fig. 6.6 (e)).









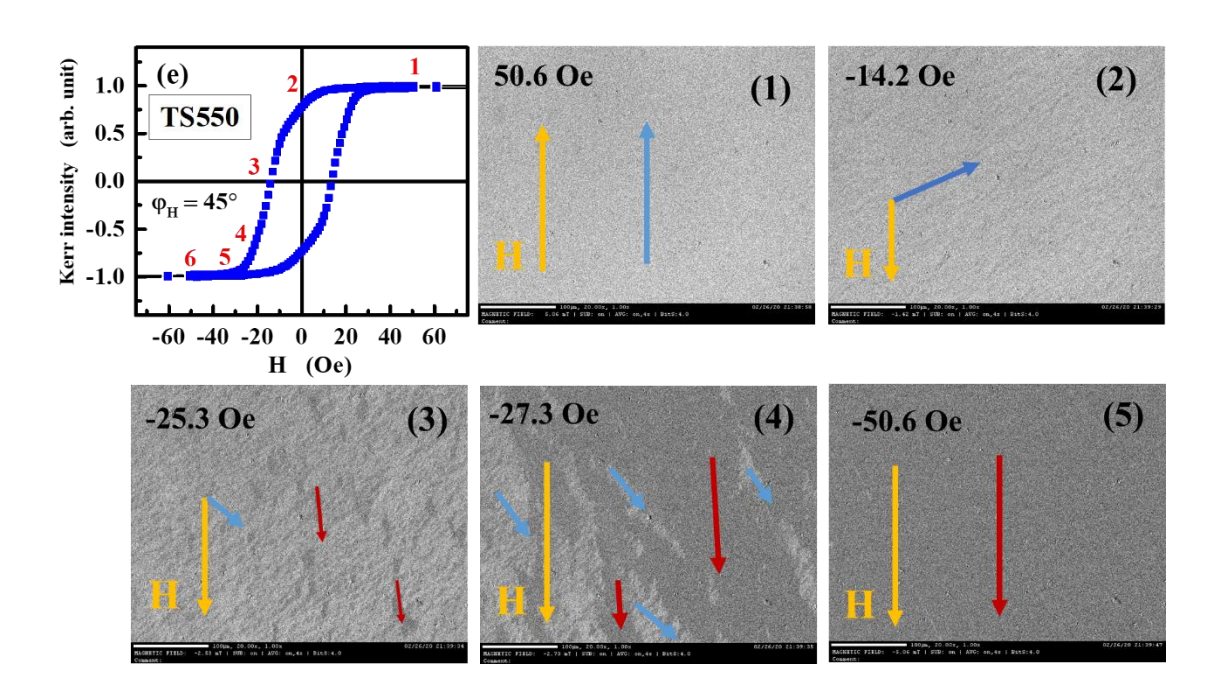
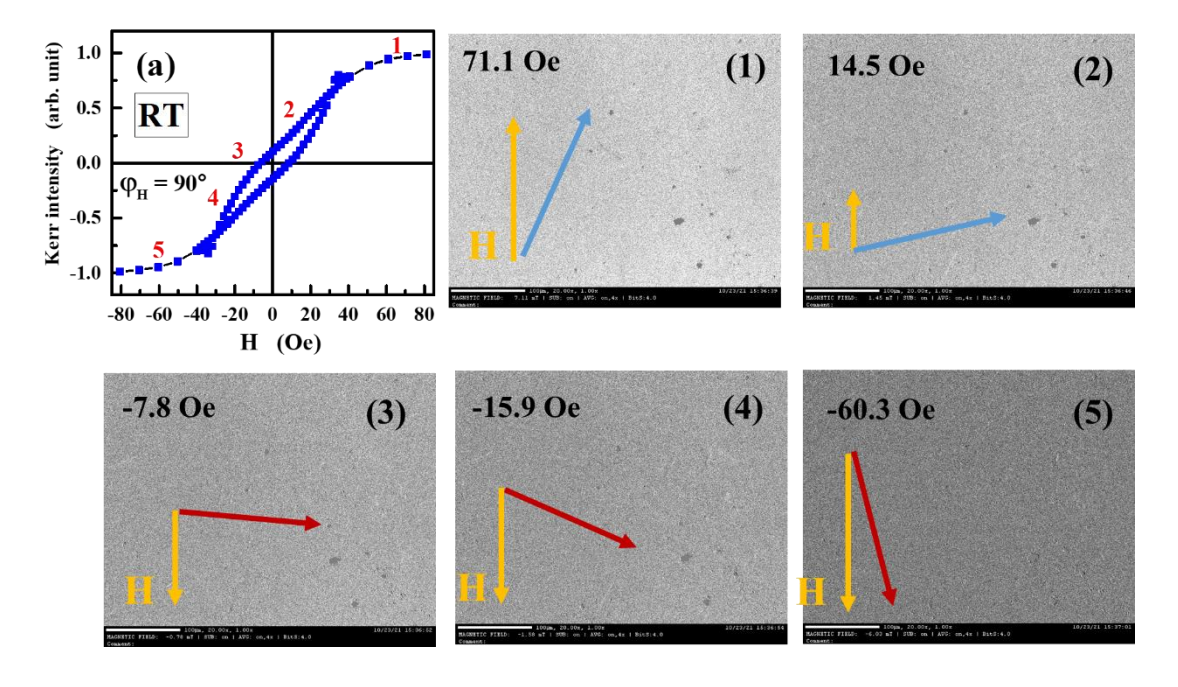
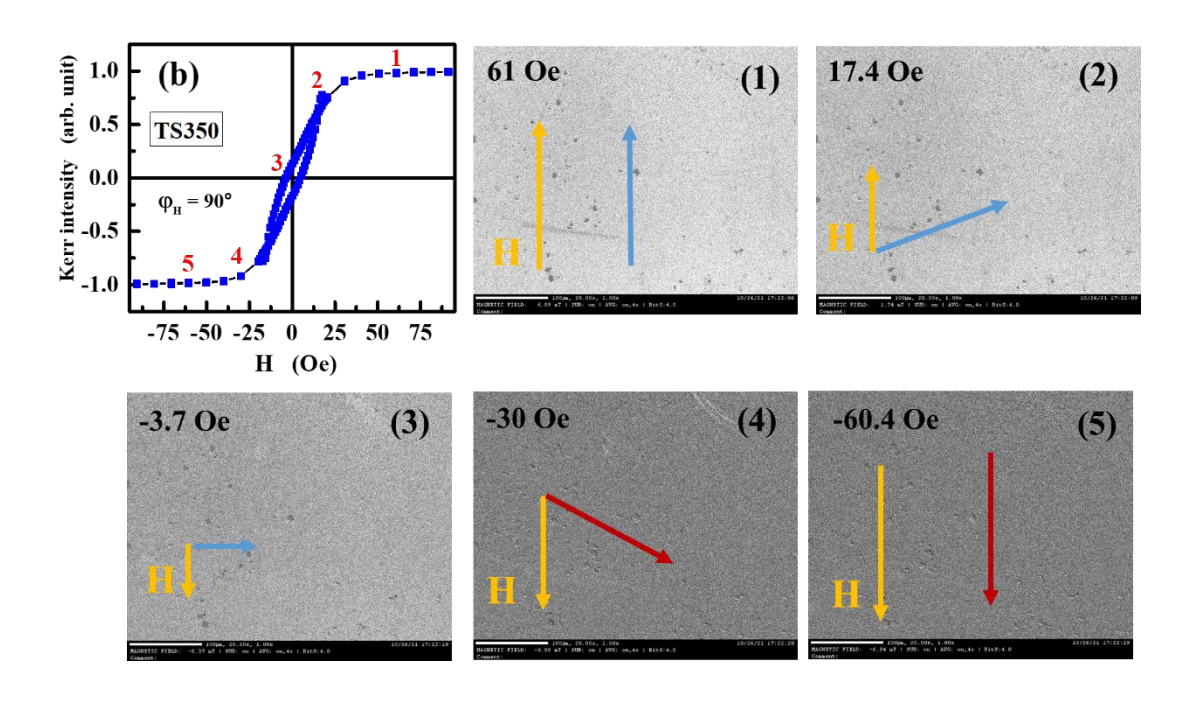


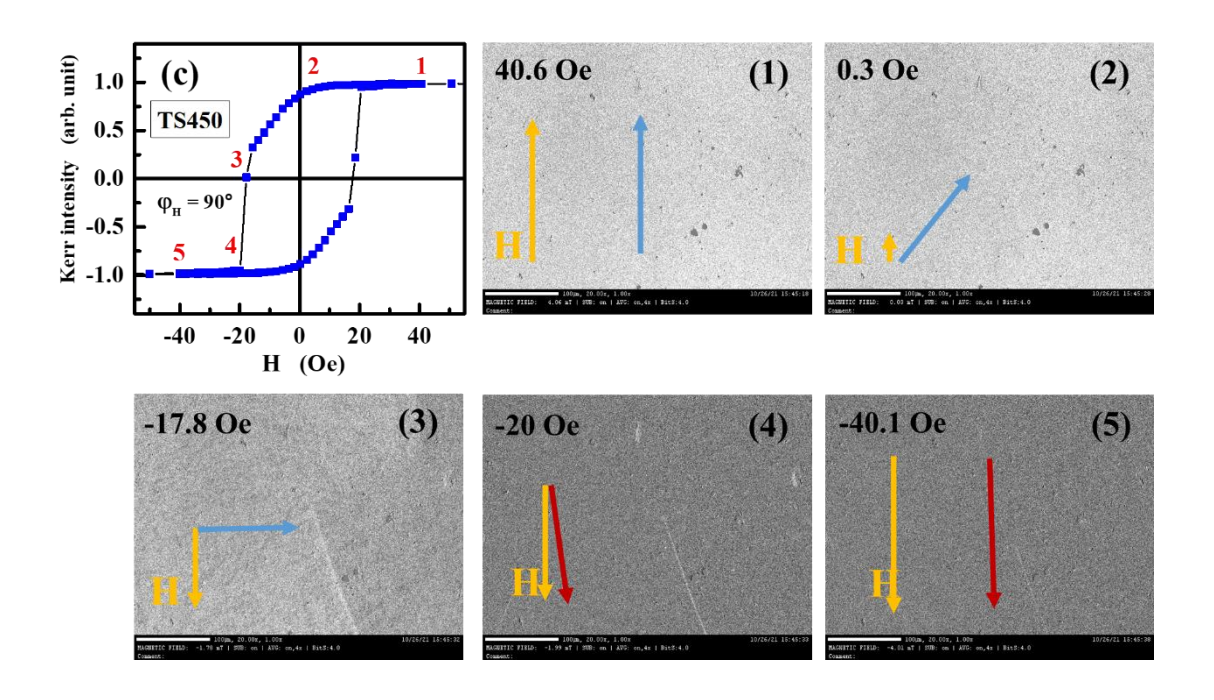
Fig. 6.6: Domain images taken at various points along the hysteresis curve at $\varphi_H = 45^{\circ}$ for (a) RT, (b) TS350, (c) TS450, (d) TS500 and (e) TS550, CFAS films

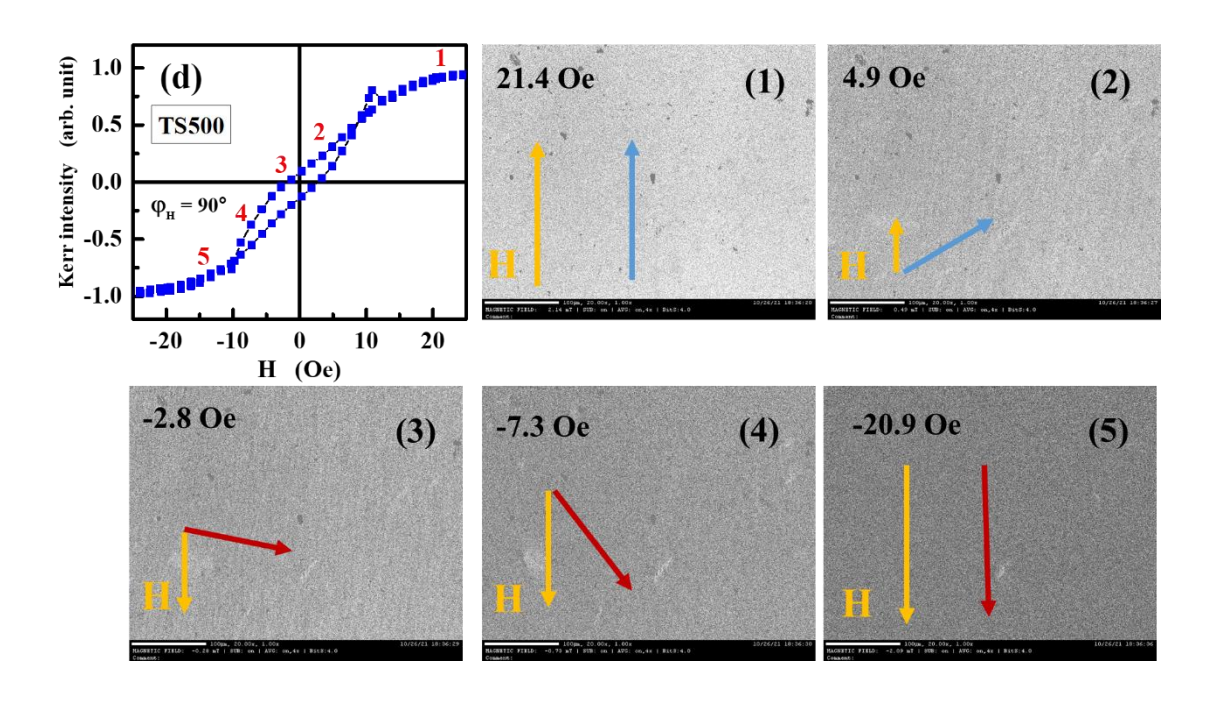
(iii)
$$\varphi_H = 90^\circ$$

When a magnetic field H is applied in the direction of the hard axis ($\varphi_H = 90^\circ$), the domains in the RT and TS350 films exhibit a subtle contrast between the dark and light regions. This occurs because, with the application of the field, the longitudinal component of magnetization decreases along the hard axis. In the stage 3 of the hysteresis loop of TS450 (and TS500), Fig. 6.7 (c) and (d), at H \sim -18 Oe (\sim -9 Oe) both the domains are simultaneously captured. In the TS450 and TS550 films (where the peaks at $\varphi_H = 90^\circ$ and 270° become more pronounced) there exist two uniaxial anisotropies (UAs) with easy axes perpendicular to each other. The hard axis of the primary UA₁ (i.e., $\varphi_H = 90^\circ$) serves as the easy axis of the secondary UA₂, and vice versa. When the magnetic field is oriented along $\varphi_H = 90^\circ$, even a small field strength of 20 Oe is adequate to saturate magnetization since the secondary UA2 is relatively weak. Upon reversing the field direction with a small magnitude of H (approximately 2 Oe), reverse domains initiate and expand, displacing the domains (characterized by blue arrows) due to the movement of 180° domain walls. [23, 24] [Figs. 6.7(c) and 2-5]. The exception is the TS550 film in which nucleation of a large number of reverse domains, is observed which occurs simultaneously (Fig. 6.7 (e)). This may arise due to large defect density in the TS550 film with interdiffusion. Increase in residual resistivity [25, 26] and FMR linewidth confirms the increase in disorder in this









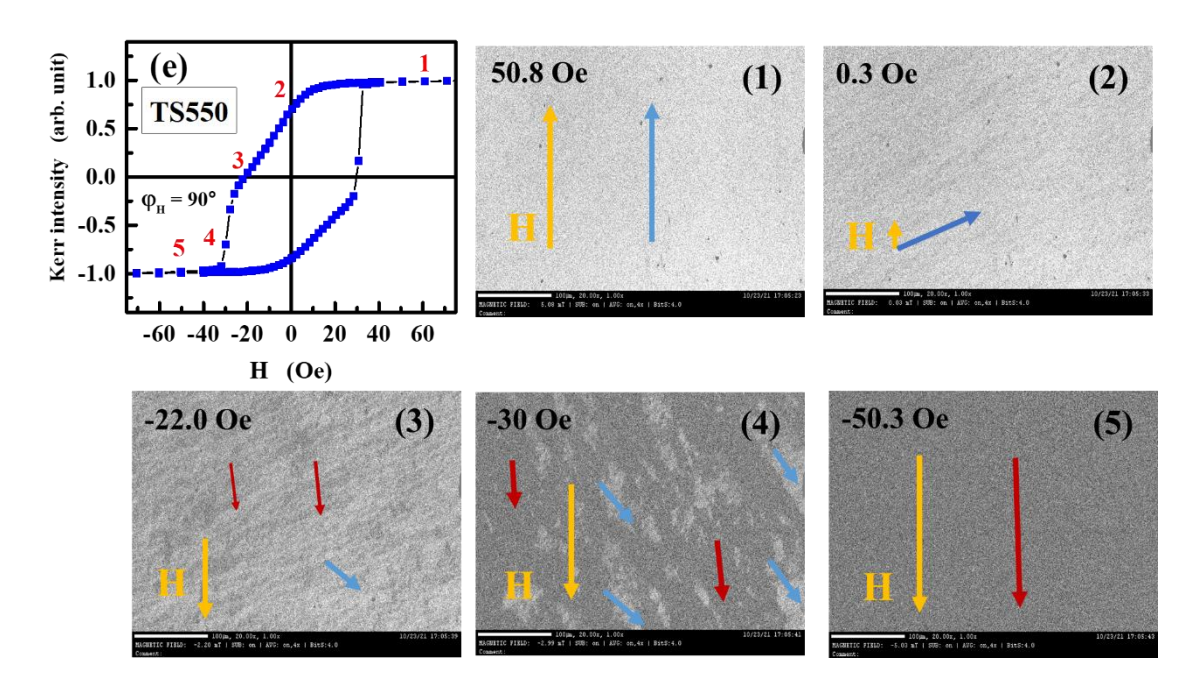


Fig. 6.7: Domain images taken at various points along the hysteresis curve at $\varphi_H = 90^{\circ}$ for (a) RT, (b) TS350, (c) TS450, (d) TS500 and (e) TS550, CFAS films.

6.3.2 Effect of thickness

To investigate how changes in thickness impact anisotropy and magnetization reversal mechanisms, static hysteresis loops and corresponding domain images were obtained at various angles (φ_H) relative to the magnetization's easy axis. This analysis was conducted on CFAS thin films with thicknesses of 12 nm, 25 nm, 50 nm, and 75 nm.

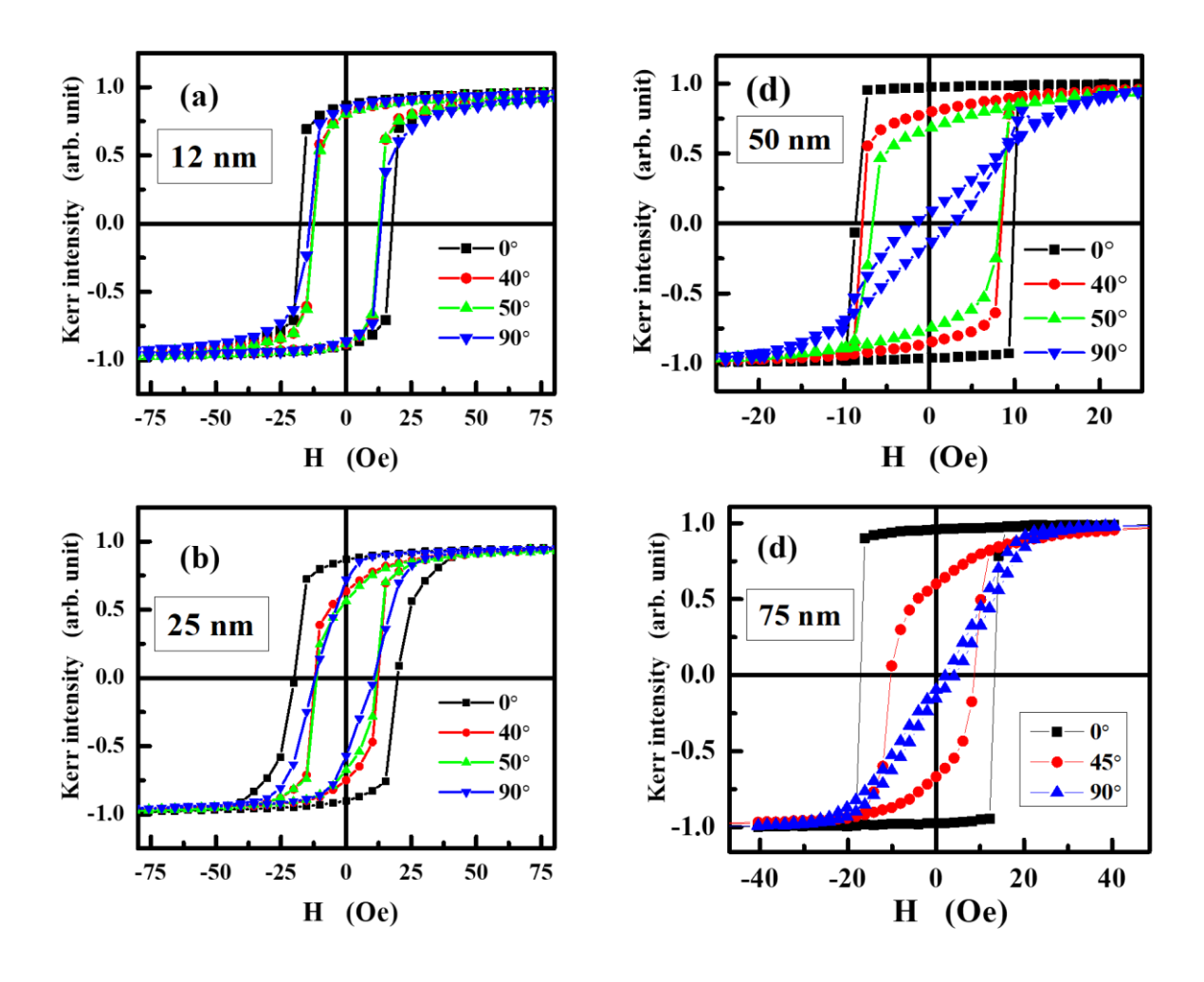


Fig. 6.8: Kerr hysteresis loops recorded at $\varphi_H = 0^\circ$, 40° , 50° , 90° for (a) 12 nm, (b) 25 nm, (c) 50 nm and (d) 75 nm, CFAS thin films.

The Kerr hysteresis curves for a different value of φ_H are plotted in Fig. 6.8. In the 12 nm and 25 nm films, the Kerr loops at $\varphi_H = 0^\circ$ (easy axis) does not show a square or rectangular loop, for which the $\frac{M_r}{M_S}$ ratio is less than 1. While for the higher thickness, the 50 and 75 nm films, $\frac{M_r}{M_S} \simeq 1$.

The $\frac{M_r}{M_S}$ ratio and the coercive field, H_c , extracted from the hysteresis loops, are plotted as functions of φ_H in Figs. 6.9 and 6.10. Following are the observations from the angular variation of $\frac{M_r}{M_S}$ and H_c :

- (i) Irrespective of the thickness, the angular variation of $\frac{M_r}{M_S}$ and H_c for all the films show a dominant two-fold symmetry which confirms the existence of in-plane uniaxial anisotropy in these films.
- (ii) In the 12 nm and 25 nm films, four maxima at $\varphi_H = 0^\circ$, 90° , 180° and 270° in the angular (φ_H) variation of $\frac{M_r}{M_S}$ and H_C is observed. The maxima at $\varphi_H = 90^\circ$, and 270° decreases with thickness in both $\frac{M_r}{M_S}$ (φ_H) and H_C (φ_H)
- (iii) In the 50 nm and 75 nm film, the hysteresis loop at $\varphi_H = 90^\circ$ (Fig. 6.8 (d)) closes in accordance with the SW model. In addition, the maxima at $\varphi_H = 90^\circ$ and 270° in the angular variation of $\frac{M_r}{M_S}$ and H_C is completely absent in the 50 and 75 nm film.

In the case of the films with thickness t = 12 nm and 25 nm (where four maxima at $\varphi_H = 0^\circ$, 90° , 180° and 270° in the angular (φ_H) variation of $\frac{M_r}{M_S}$ and H_C is observed), the optimum theoretical fits to the $\frac{M_r}{M_S}$ (φ_H) and H_C (φ_H) data is adequately described by the modified two-phase model (Eq. (6.20)). The fits are represented by the continuous red curves in Figs. 6.10 (and open circles represent the raw data). The corresponding values for the fit parameters are listed in Table 6.2. The variation of H_C from 12 nm to 25 nm ($H_C \cong 20 \ Oe$) is negligible (note that the field variation is caried out at 5 Oe steps), while it For system with t = 50 nm and 75 nm films, the two-phase model given by Eq. (6.17) describes the observed H_C (φ_H) behavior very well.

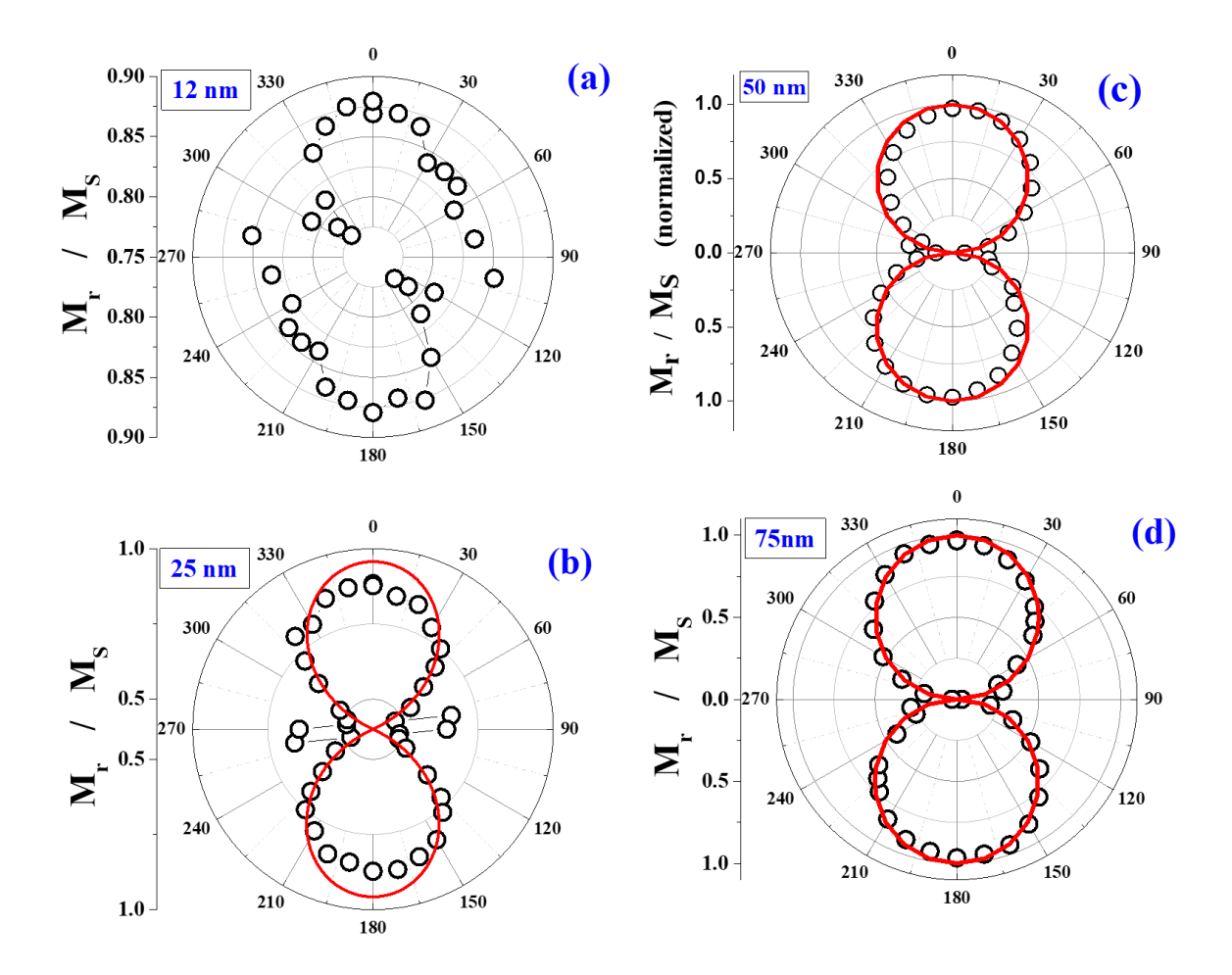


Fig. 6.9: Angular variation of $\frac{M_r}{M_S}$ for (a) 12 nm, (b) 25 nm, (c) 50 nm and (d) 75 nm, CFAS thin films. The red continuous lines represent the fit and open circles represent the raw data.

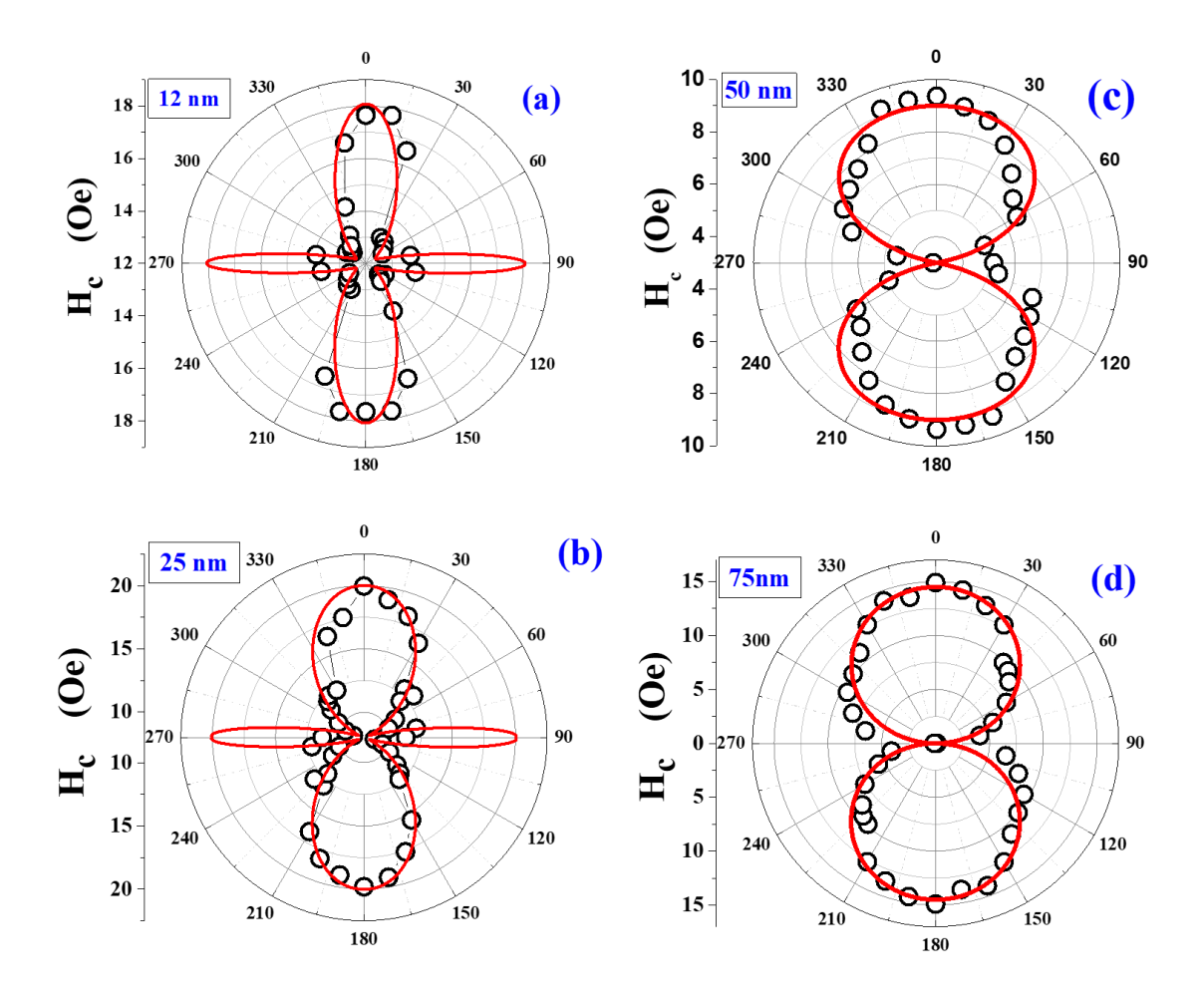


Fig. 6.10: $H_c(\varphi_H)$ plot for (a) 12 nm, (b) 25 nm, (c) 50 nm and (d) 75 nm, CFAS thin films along with the fit, red lines, obtained from Eq. (6.13) and (6.17) and (6.20) as illustrated in the text.

A clear crossover is observed from two UAs (for t = 12 nm and 25 nm) to a single UA (t = 50 nm and 75 nm). For both 50 nm and the 75 nm films, there is only one dominant in-plane uniaxial anisotropy (see Fig. 6.10 (d) and (e)). decreases to 9 Oe for the 50 nm film and then increases to 15 Oe for the 75 nm film. Thus, a minimum at H_C is observed for the 50 nm film. It is evident from the parameter values given in the table that $y_1 \gg y_2$ (for 12 nm and 25 nm). The value of y_1 increases with thickness and peaks at 50 nm film. The modified two-phase model considering two UAs which are mutually perpendicular to each other, the larger magnitude of y_1 (in comparison to y_2) confirms that the primary UA₁ is dominant and increases with thickness.

The crossover from uniaxial to cubic MCA with thickness variation has been reported in Co₂FeAl [27, 28] and Fe thin films [29]. Such a crossover has been explained using the Stoner–Wohlfarth (SW) model. At lower thickness, the uniaxial anisotropy is dominant over the small cubic anisotropy present in the system. As the thickness increases the strength of the cubic anisotropy grows such that after a certain thickness, the cubic anisotropy becomes the dominant anisotropy. However, in the present case i.e., the CFAS thin films under study, the hysteresis loops observed at different φ_H do not follow the SW model even by taking into consideration both the uniaxial and cubic anisotropies. Moreover, the magnetization reversal in SW model follows single domain coherent rotation but, in our case, the magnetization reversal occurs through nucleation and growth of the reverse domains through the domain wall motion.

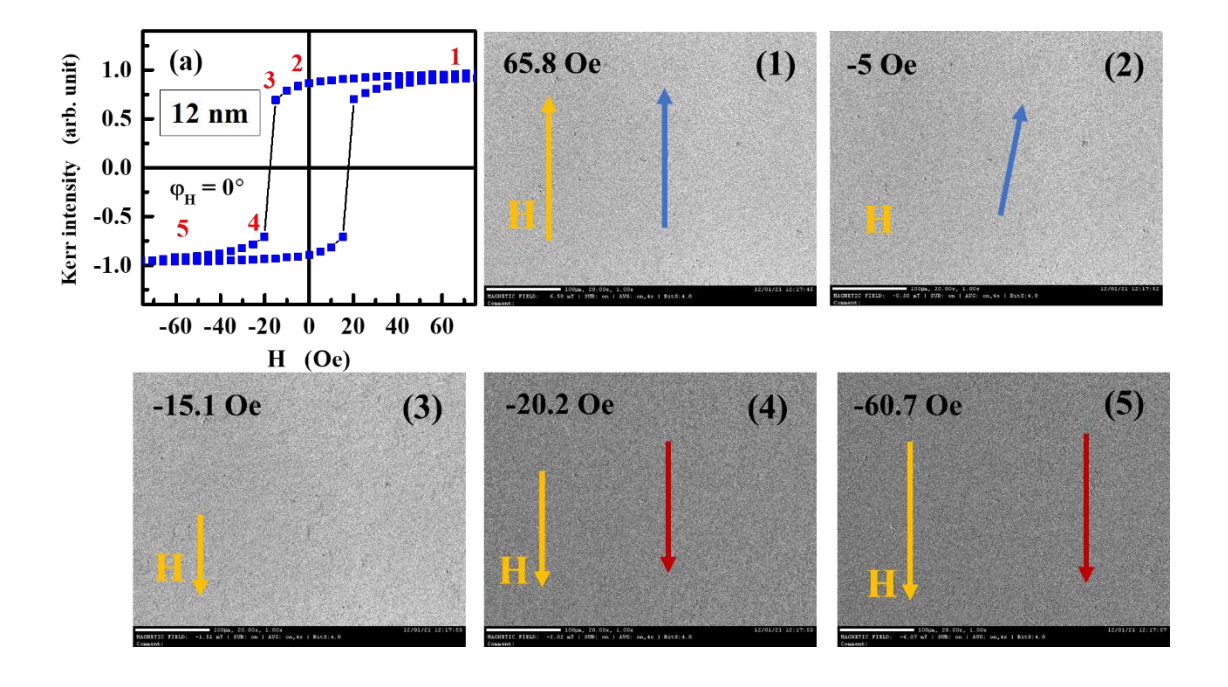
Table 6.2: The values of H_C , H_k , and the corresponding free-fitting parameters, derived from Equation (6.20) for the 12 nm, 25 nm, and 50 nm CFAS films, and from Equation (6.17) for the 75 nm film, are provided.

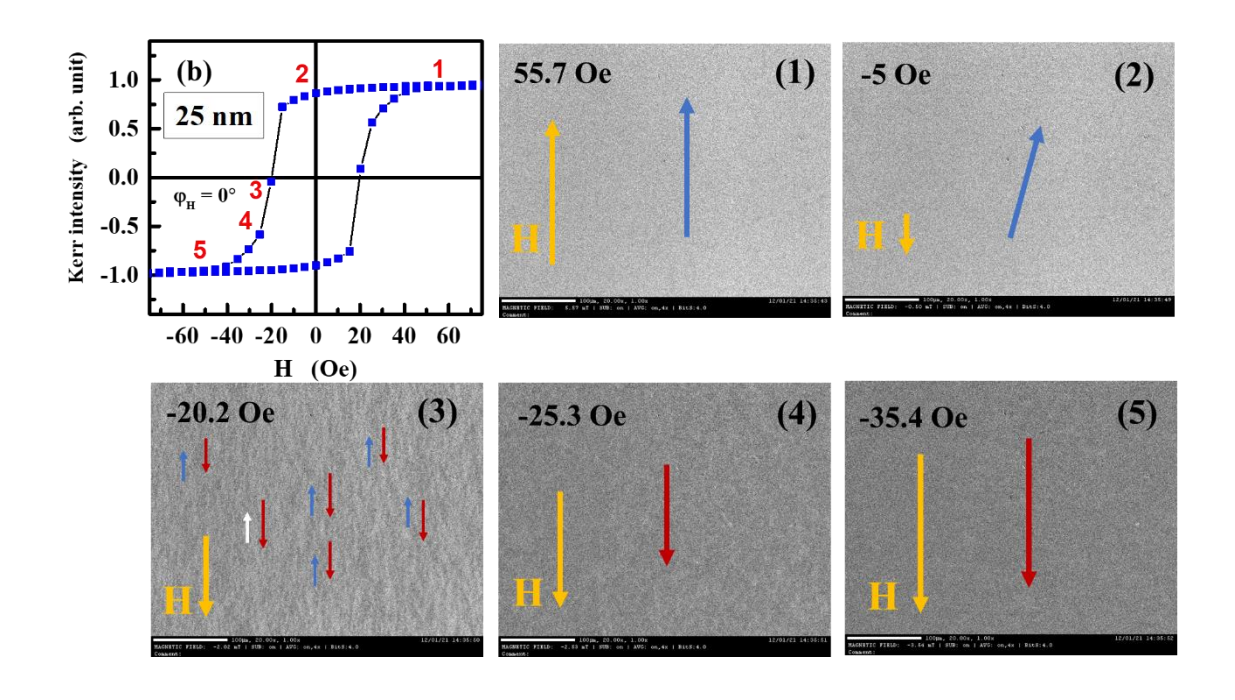
$H_{\mathcal{C}}$ (Oe)	$H_k(Oe)$	<i>y</i> ₁	y_2	$H_k^{ }(\mathrm{Oe})$
				from FMR
20	30	0.17(4)	0.016(4)	
20	30	0.72(6)	0.024(5)	7
9	20	1.8(2)		8
15	25	1.16586		5
	20 20 9	20 30 20 30 9 20	20 30 0.17(4) 20 30 0.72(6) 9 20 1.8(2)	20 30 0.17(4) 0.016(4) 20 30 0.72(6) 0.024(5) 9 20 1.8(2)

Similar to the TS series, Fig. 6.11, 6.12 and 6.13 present the domain images captured at different stages of the Kerr hysteresis loops at $\varphi_H = 0^\circ$, 50° and 90° for 12 nm, 25 nm and 75 nm CFAS thin films. The process for capturing domain images has been conducted in a manner consistent with the procedure outlined in the TS series. It is clear from the domain images presented in these figures that the mechanism governing the reversal of magnetization is contingent on φ_H , as explained below:

(i)
$$\varphi_H = 0^\circ$$

When the magnetic field is applied along the easy axis, $\varphi_H = 0^\circ$, The magnetization reversal in 12 nm, 25 nm and 75nm CFAS films are very rapid with a very small field change of ± 5 Oe being enough to reverse the domain. In these films, the reverse domain nucleates as H closes to H_C which grows by domain wall movement as H exceeds H_C . In the 12 nm and 75 nm films, only the saturated state of the domains is captured (bright and dark contrast). In the 25 nm film, the stage 3 on the hysteresis loop (very close to H_C) shows the existence of both the domains, (Fig. 6.11).





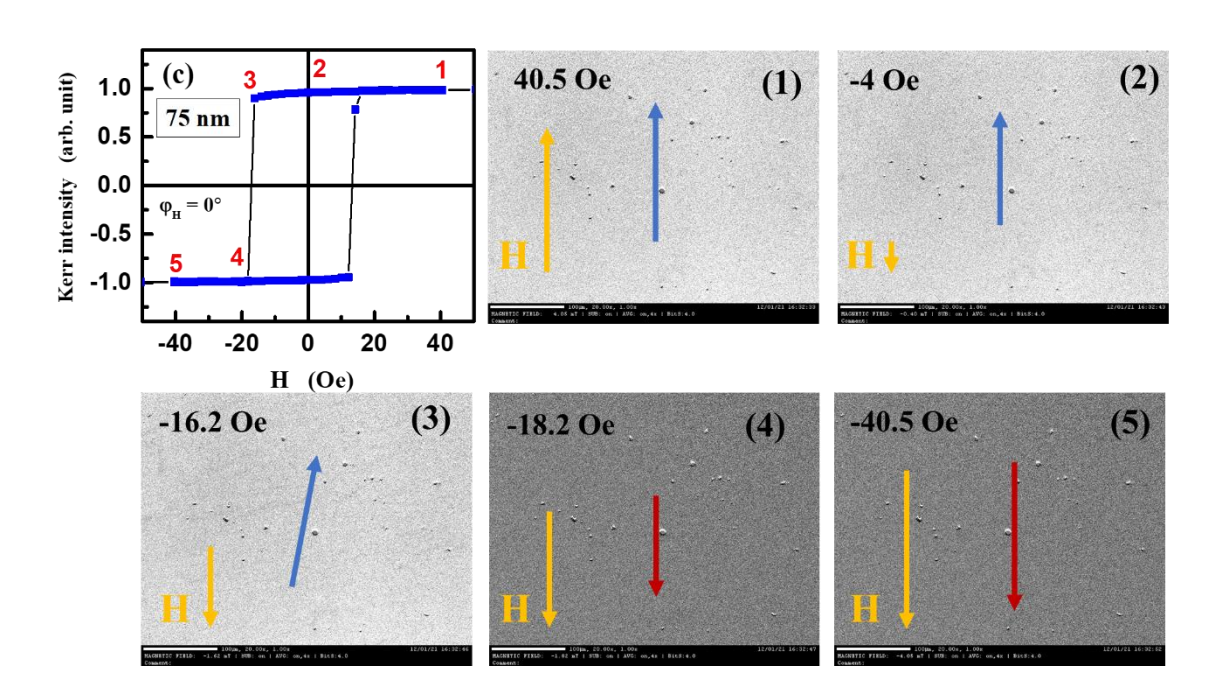
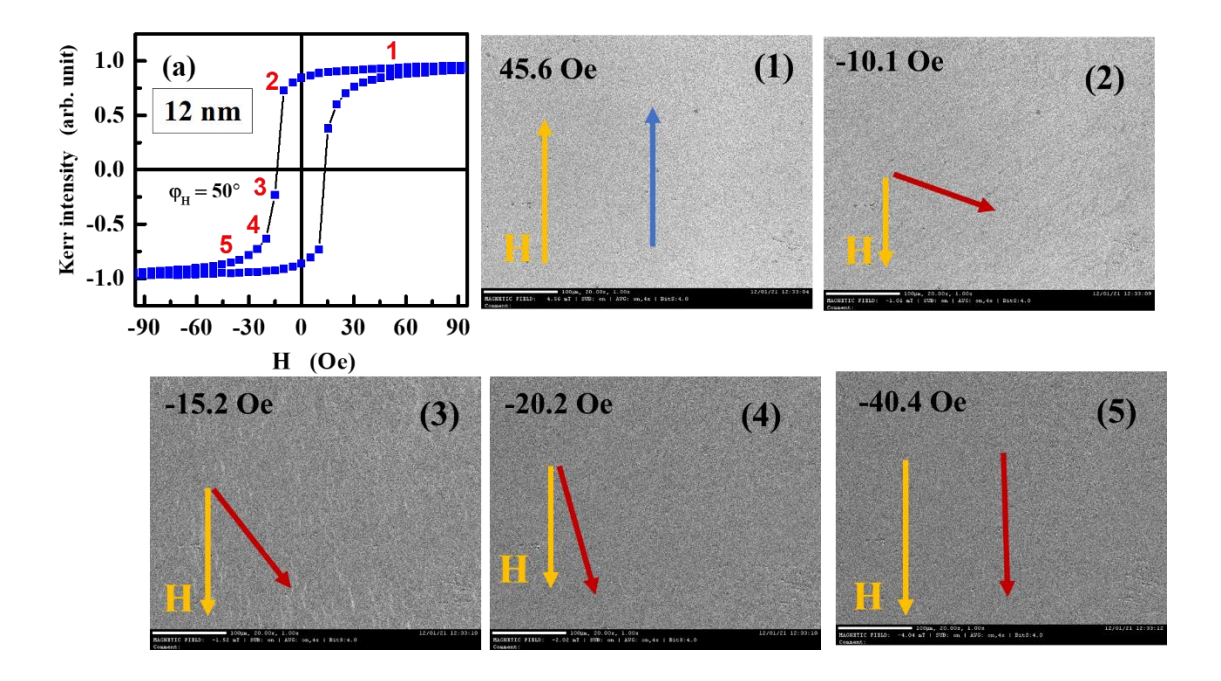
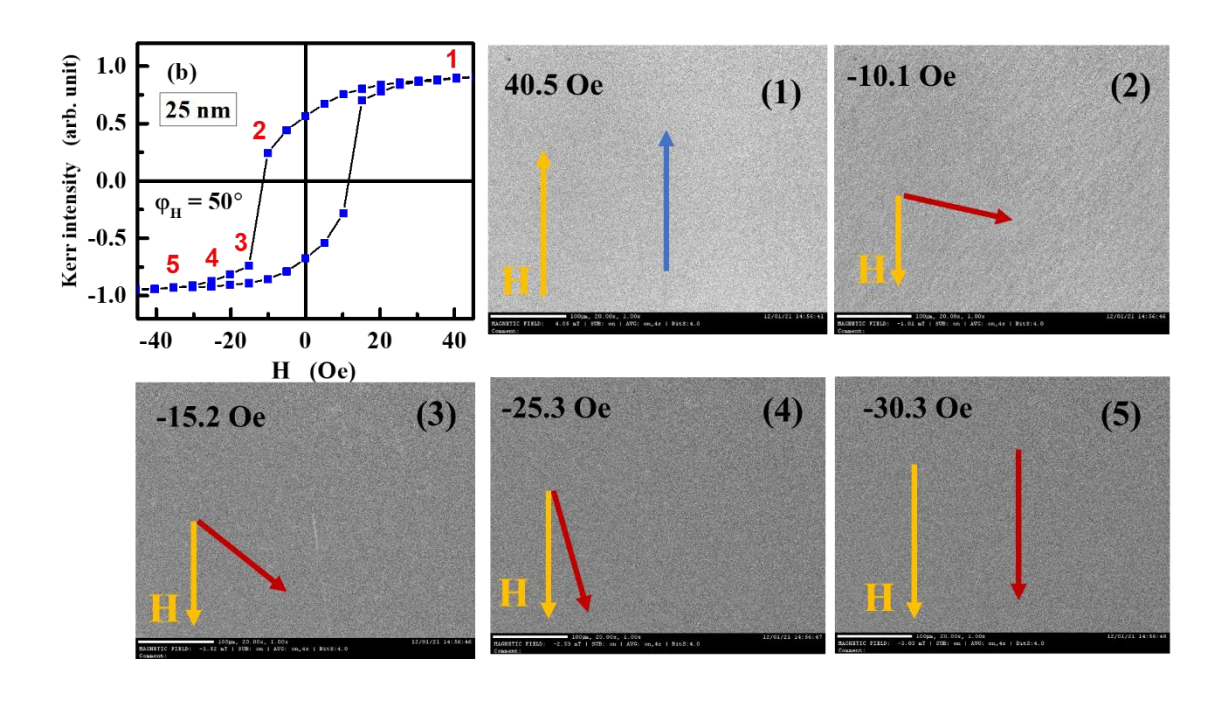


Fig. 6.11: Domain images taken at various points along the hysteresis curve for the (a) 12 nm (b) 25 nm and (c) 75 nm, CFAS film, captured with L-MOKE, at $\varphi_H = 0^{\circ}$.

(i)
$$\varphi_H = 50^\circ$$

In the intermediate direction $\varphi_H = 50^\circ$ ($\varphi_H = 45^\circ$ for 75 nm), the 12 nm and 25 nm films show coherent rotation. From a field variation of H = 10 Oe to 15 Oe (refer Fig. 6.12 (a) and (b)), a change in contrast is observed indicating that the domains rotation has occurred. Thus, complete saturation is obtained with increasing field in the reverse direction. In the 75 nm film, the magnetization reversal occurs with the coherent rotation up to H_c . Above H_c , reverse domains nucleate and grow as the field increases. This is clearly seen by the stripe domains [30, 31] at the state 3 of Fig. 6.12(c). As the field is further increased, the reverse domain grows and saturates.





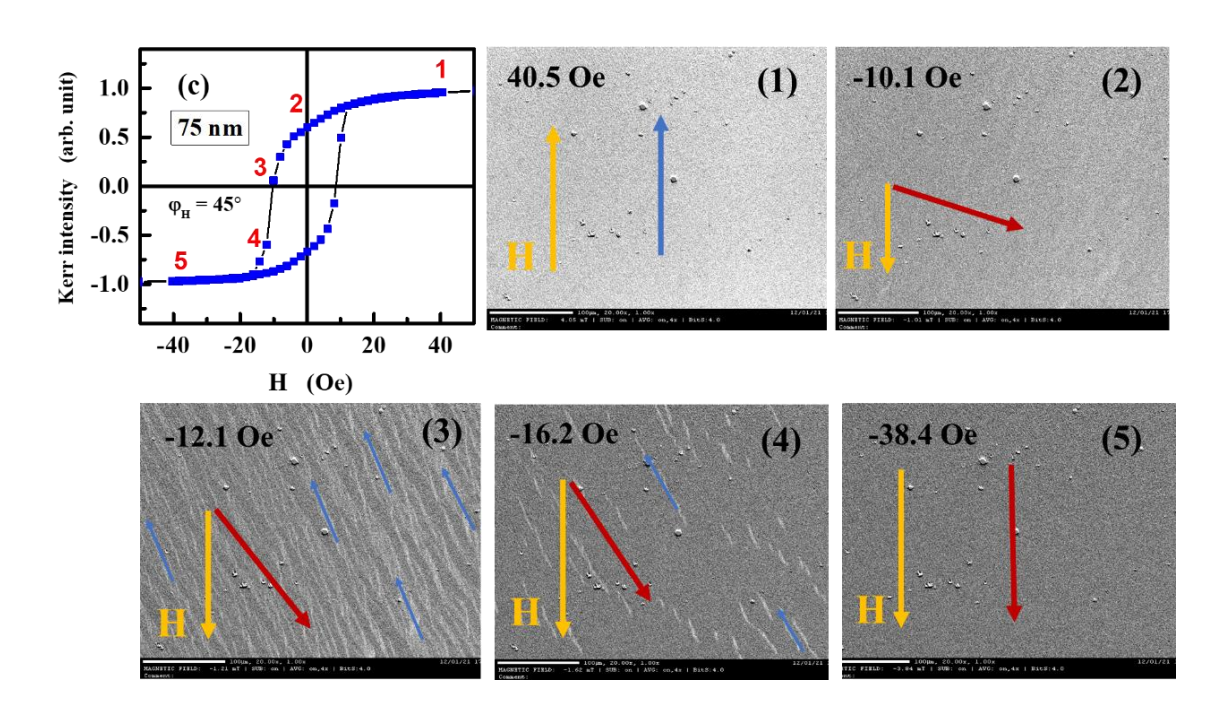
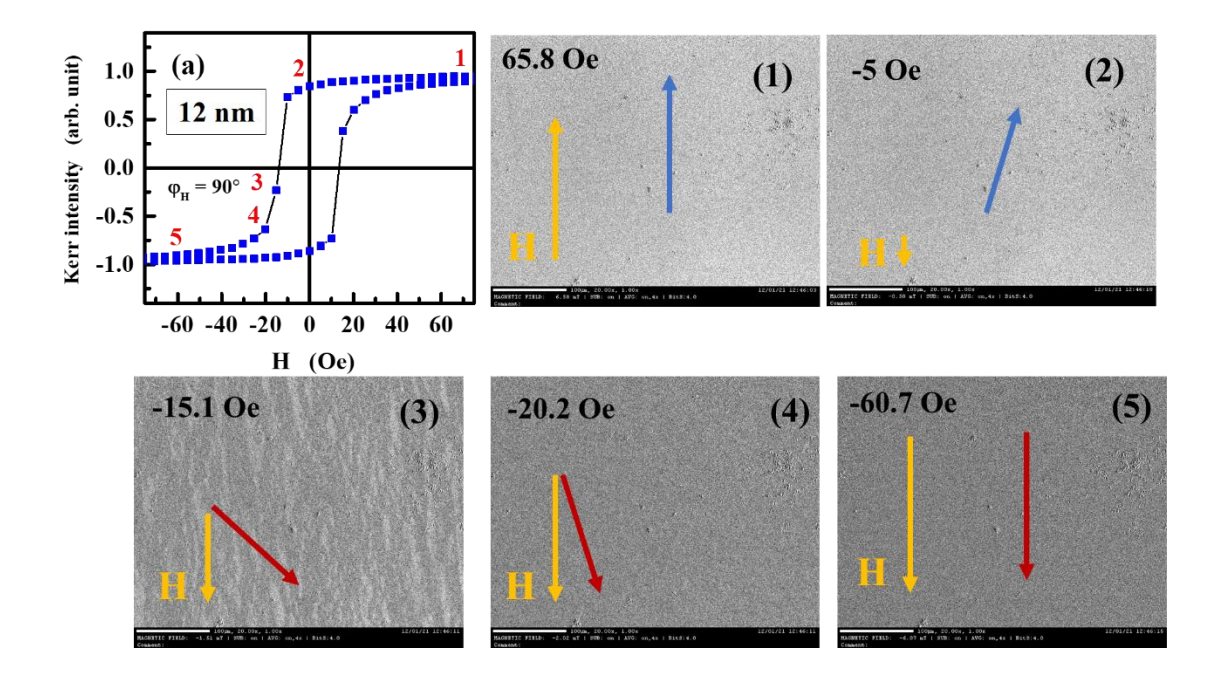
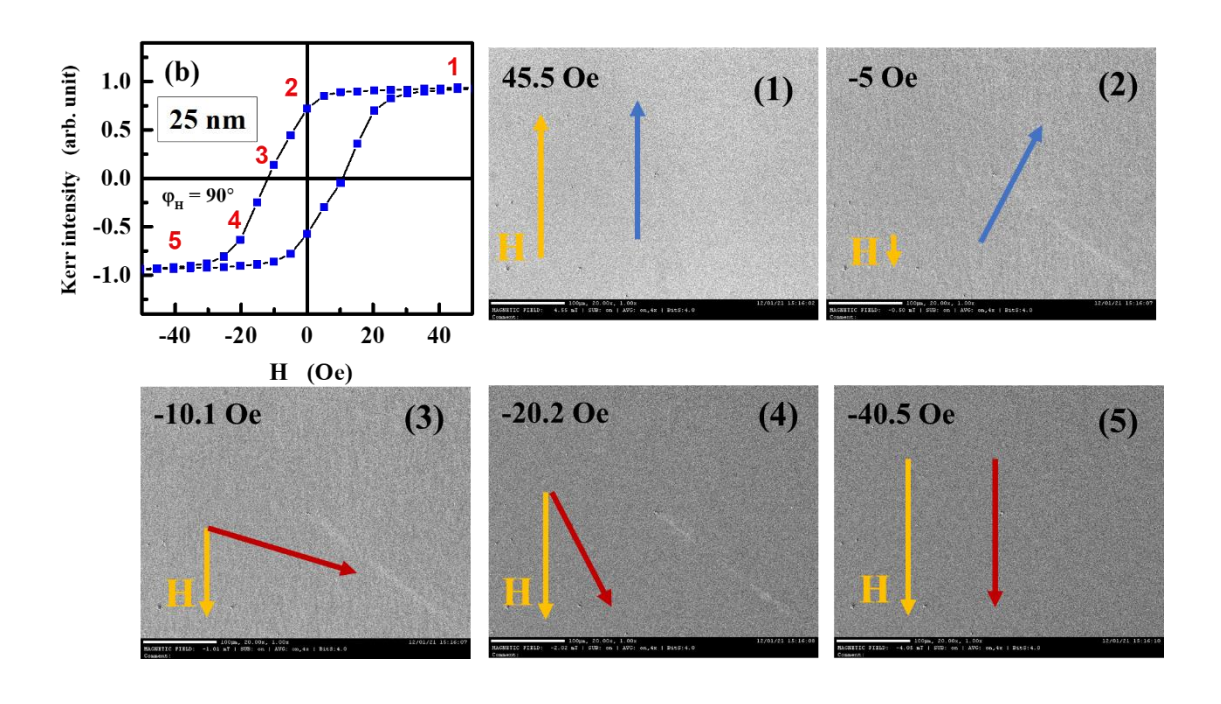


Fig. 6.12: Domain images taken at various points along the hysteresis curve for the (a) 12 nm (b) 25 nm and (c) 75 nm, CFAS film, captured with L-MOKE, at $\varphi_H = 45^{\circ}$.

(i)
$$\varphi_H = 90^\circ$$

When H is applied along the hard-axis of magnetization a very weak contrast is observed from the captured domain images. In this configuration, at high fields the external field hold the magnetization along the hard axis and as the field is decreased the magnetization vector prefer to return to the easy axis of magnetization, such that when the field is increased beyond H_C a complete reverse domain is observed. In the case of 75 nm film, the magnetization reversal is achieved by coherent rotation.





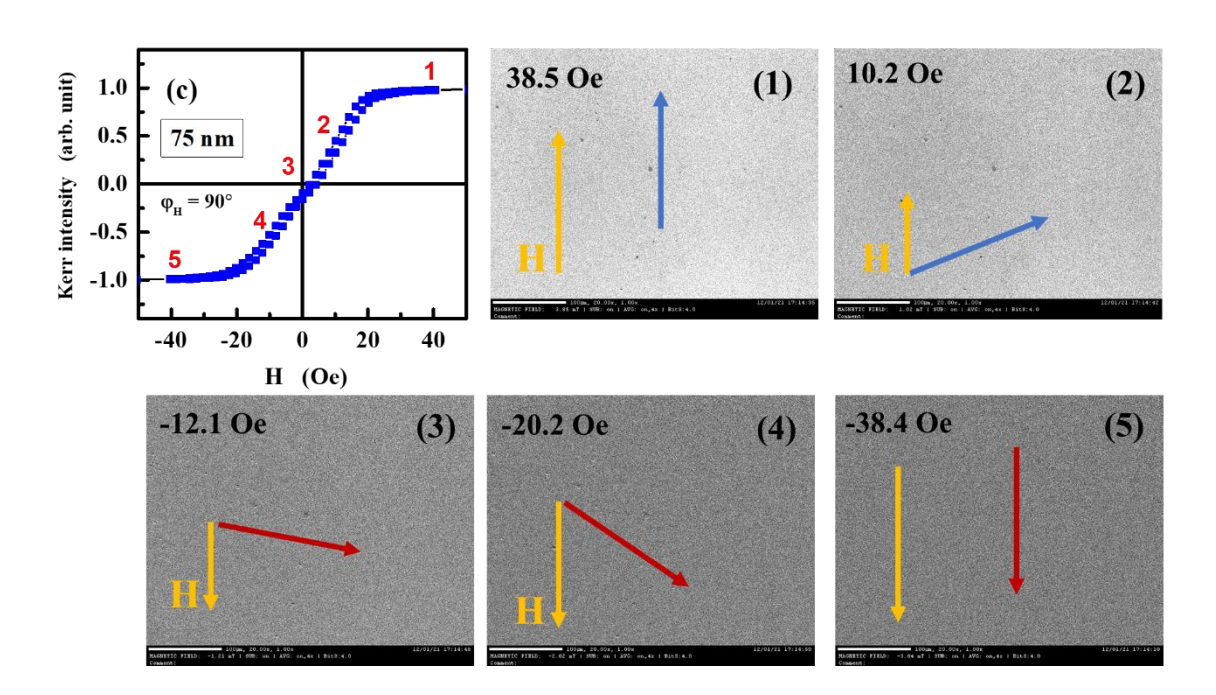


Fig. 6.13: Domain images taken at various points along the hysteresis curve for the (a) 12 nm (b) 25 nm and (c) 75 nm, CFAS film, captured with L-MOKE, at $\varphi_H = 90^{\circ}$.

6.4 Conclusion

The impact of anti-site atomic disorder and film thickness on magnetocrystalline anisotropy (MCA) and the magnetization reversal (MR) process has been explored in two distinct series of CFAS Heusler alloy thin films using longitudinal magneto-optical Kerr effect (MOKE) microscopy. The TS-series comprises CAFS films of a fixed thickness (50 nm) with varying degrees of atomic disorder, achieved by depositing them at different substrate temperatures (TS). On the other hand, the t-series consists of films with thickness (t) ranging from 12 nm to 75 nm, deposited at the optimum substrate temperature of 500 °C with B2 crystalline order.

- (i) Regardless of the TS, all the films show a dominant two-fold variation of $\frac{M_r}{M_S}$ and H_C which confirms in-plane uniaxial anisotropy.
- (ii) In the TS450 and TS550 CFAS films, the angular variation of H_c is well described by the modified two-phase model by considering two uniaxial anisotropies of different magnitude which are mutually perpendicular to each other. Such a description yields the strength of the two anisotropies, and it is observed that the second anisotropy is far less in magnitude compared with the primary anisotropy.
- (iii) In contrast, the angular variation of H_c in the TS350 and TS500 film is better described by the two-phase model. While for the RT film, both the SW as well as the two-phase model must be taken into account for the $H_c(\varphi_H)$ behavior.
- (iv) In the TS series, (a) when the H is applied along the easy axis ($\varphi_H = 0^\circ$), magnetization reversal occurs through the reverse domains nucleation and as H approaches H_c , the reverse domain grow by domain wall movement with increasing H. (b) When the magnetic field is applied at $\varphi_H = 45^\circ$, the magnetization reversal takes place through rotation plus growth giving rise to stripe domain and (c) When H is applied along the hard axis direction ($\varphi_H = 90^\circ$), a weak contrast between the dark and light regions is observed. When H is reversed, even a small magnitude ($\simeq 2$ Oe) is enough to nucleate the reverse domains which grows as a result of the 180° domain wall movement.
- (v) In the thickness series, a clear-cross over is seen for the $H_C(\varphi_H)$ variation which suggest that two UAs decreases with increasing thickness and a single UA is present above 50 nm thickness.

- (vi) Irrespective of the thickness, all the films show a dominant in-plane uniaxial anisotropy.
- (vii) In contrast to the 12 nm and 25 nm, the hysteresis loop at $\varphi_H = 90^\circ$ in the 50 nm and 75 nm film closes in accordance with the SW model.
- (viii) The magnetization reversal in the thickness series follows the similar process as the TS series.

References:

- 1. Allan H. Morrish, "The Physical Principles of Magnetism" John Wiley and Sons, Inc. Pg. 259 (1965)
- Mathias Getzlaff, "Fundamentals of magnetism". Springer Berlin Heidelberg New York, Pg. 89 – 117 (2008)
- 3. E. C. Berling and E. P. Wohlfarth, Philos. Trans. R. Soc. London Ser. A 240, 599 (1948).
- 4. E. C. Stoner and E. P. Wohlfarth, IEEE Trans. Magn. 27, 3475 (1991)
- 5. C. Tannous, J. Gieraltowski. Physica B **403**, 3563–3570 (2008)
- 6. T. M. L. Alves, C. G. Bezerra, A. D. C. Viegas, S. Nicolodi, M. A. Corr\u00eda, and F. Bohn, Journal of Applied Physics 117, 083901 (2015).
- 7. E. Kondorsky, J. Phys. USSR **2**, 161 (1940)
- 8. R. M. Grechishkin, S. S. Soshin, and S. E. Ilyashenko, in First International Workshop on Simulation of Magnetization Processes, (1995)
- 9. N. P. Suponev, R. M. Grechishkin, M. B. Lyakhova, and Y. E. Pushkar, J. Magn. Magn. Mater. **376**, 157-158 (1996)
- M. Mathews, E. P. Houwman, H. Boschker, G. Rijnders, and D. H. A. Blank, J. Appl. Phys. 107, 013904 (2010).
- 11. H. Boschker, J. Kautz, E. P. Houwman, G. Koster, D. H. A. Blank, and G. Rijnders, J. Appl. Phys. 108, 103906 (2010).
- 12. J. Ye, W. He, Q. Wu, H.-L. Liu, X.-Q. Zhang, Z.-Y. Chen, and Z.-H. Cheng, Sci. Rep. 3, 2148 (2013).
- 13. O. Idigoras, A. K. Suszka, P. Vavassori, P. Landeros, J. M. Porro, and A. Berger, Phys. Rev. B 84, 132403 (2011).
- 14. O. Idigoras, A. K. Suszka, P. Vavassori, B. Obry, B. Hillebrands, P. Landeros, and A. Berger, J. Appl. Phys. 115, 083912 (2014).
- V. Barwal, S. Husain, N. Behera, E. Goyat, and S. Chaudhary, J. Appl. Phys. 123, 053901 (2018).
- 16. L. Neel, R. Pauthenet, G. Rimet, and V. S. Giron, J. Appl. Phys. 31, S27 (1960).
- 17. Binoy Krishna Hazra, S. N. Kaul, S. Srinath, Zaineb Hussain, V. Raghavendra Reddy, and M. Manivel Raja. AIP Advances **10**, 065017 (2020). https://doi.org/10.1063/5.0002408

- 18. M. Belmeguenai, F. Zighem, T. Chauveau, D. Faurie, Y. Roussigné, S. M. Chérif, P. Moch, K. Westerholt, and P. Monod, J. Appl. Phys. **108**, 063926 (2010).
- 19. K. Gross, K. Westerholt, and H. Zabel, New J. Phys. 18, 033007 (2016).
- 20. M. Belmeguenai, H. Tuzcuoglu, M. Gabor, T. Petrisor, and C. Tiusan, J. Magn. Magn. Mater. **373**, 140 (2015)
- V. Barwal, S. Husain, N. Behera, E. Goyat, and S. Chaudhary, J. Appl. Phys. 123, 053901 (2018).
- M. Belmeguenai, H. Tuzcuoglu, M. S. Gabor, T. Petrisor, Jr., C. Tiusan, F. Zighem, S.
 M. Chérif, and P. Moch, J. Appl. Phys. 115, 043918 (2014)
- 23. S. Mallik, S. Mallick, and S. Bedanta, J. Magn. Magn. Mater. 428, 50 (2017).
- K. Umadevi, A. Talapatra, J. Arout Chelvane, M. Palit, J. Mohanty, and V. Jayalakshmi,
 J. Appl. Phys. 122, 065108 (2017).
- 25. Lanuakum A Longchar, Mainur Rahaman, Binoy Krishna Hazra, R. Rawat, M. Manivel Raja, S.N. Kaul and S. Srinath. Journal of Magnetism and Magnetic Materials **569**, 170439 (2023)
- 26. Lanuakum A. Longchar, Mainur Rahaman, Binoy Krishna Hazra, M. Manivel Raja, R. Rawat, S. N. Kaul and S. Srinath. AIP Advances **13**, 025106 (2023)
- 27. S. Qiao, S. Nie, J. Zhao, and X. Zhang, J. Appl. Phys. 117, 093904 (2015).
- 28. S. Qiao, S. Nie, J. Zhao, and X. Zhang, Appl. Phys. Lett. B **105**, 172406 (2014)
- 29. O. Chérif, Q. Shen, P. Schieffer, N. Tournerie, and B. Lepine, Phys. Rev. Lett. 90, 017205 (2003)
- 30. A. Hubert and R. Schafer, Magnetic Domains (Springer, New York, 1998)
- 31. J. McCord, R. Schäfer, R. Mattheis, and K.-U. Barholz, J. Appl. Phys. **93**, 5491 (2003).

Chapter 7

Conclusion and future scope

This chapter summarizes the research work and result presented in the thesis. Such a thorough investigation on Co₂FeAl_{0.5}Si _{0.5} thin films provides inside into the microscopic and fundamental understanding of the system. The chapter concludes with the future work and scope of the research

7.1 Summary

7.1.1 Effect of anti-site disorder on the structural, magnetic, electrical- and magneto-transport properties of Co₂FeAl_{0.5}Si_{0.5} Heusler alloy thin films.

For an in-depth study of the effect of anti-site disorder on structural, magnetic, electrical-and magneto-transport properties of Co₂FeAl_{0.5}Si_{0.5} (CFAS) Heusler alloy, 50 nm thick CFAS thin films with varying degree of site-disorder were prepared by depositing them on the Si(100) substrates with or without a 300 nm SiO₂ top layer at the substrate temperatures TS = 27 °C (RT), 350 °C, 450 °C, 500 °C and 550 °C, using high vacuum DC magnetron sputtering. The stoichiometry of the deposited films has been confirmed to be close to the required composition by employing EDS. Irrespective of deposition temperature, detection of the (222) diffraction peak in all the TS series films asserts the existence of B2 structure order with partial interchange of Fe and (Al, Si) atoms. Further, the percentage of relative B2 atomic order present in a given film is estimated by the integrated intensity ratio, $\frac{\binom{I^{(222)}}{I_{TS500}}}{\alpha}$, where $\alpha = \binom{\binom{I^{(222)}}{I_{TS500}}}{\binom{I^{(220)}}{I_{TS500}}}$, this confirms that among all the CFAS films, the TS500 film has the highest atomic site order (or equivalently, the least Y, Z anti-site disorder) within B2 structure.

An extensive quantitative analysis of the 'zero-field', $\rho(T, H = 0)$ and 'in-field', $\rho(T, H = 80 \text{ kOe})$, electrical resistivity data by taking into account the existing theoretical models for diffusive and ballistic transport mechanisms, helps to conclude that the electron-diffuson (e - d) scattering and weak localization (WL) mechanisms, responsible for *negative* temperature coefficient of resistivity (TCR) for $T < T_{min}$, compete with the *positive* TCR mechanisms, electron-

magnon (e-m) and electron-phonon (e-p) scattering, to produce the resistivity minimum at T_{min} . The *phonon-induced* non-spin-flip two-band $(s\uparrow\downarrow - d\uparrow\downarrow)$ scattering accounts for ρ_{e-p} , while the *magnon-induced* spin-flip s - d interband $(s^{\uparrow\downarrow} - d^{\downarrow\uparrow})$ transitions essentially determine ρ_{e-m} and the thermal renormalization of the spin-wave stiffness, $D_{sw}(T) = D_0(1 - D_2 T^2)$ with $D_2 \neq 0$, contributes significantly to $\rho_{e-m}(T)$.

The suppression of the WL effect and e-m scattering by external magnetic field results in negative magnetoresistance (MR). The 'zero-field' $\rho_{e-m}(T,H=0)$ data, when used in the expression given by the spin fluctuation model, permits an accurate determination of $\rho_{e-m}(T,H=80\ kOe)$ over the entire temperature range $5\ K \le T \le 300\ K$. This observation, in turn, implies that the WL contribution to MR is negligibly small. Another important conclusion is that, except the RT CFAS film, all the films show a negative AMR. Interestingly, large AMR % found in the TS450 and TS500 films with the highest B2 order is due to the scattering of the $s\uparrow$ electrons into the empty states in the $d\uparrow$ spin sub-band. This inference asserts that the TS450 and TS500 films are good candidates for half-metallicity.

Magnetization dynamics, magnetic anisotropy and Gilbert damping constant (α) in the CFAS films have been investigated by the ferromagnetic resonance (FMR) technique. H_r and ΔH were investigated over the frequency range 4 - 18 GHz using the broad-band CPW-FMR technique. The analysis of the broad-band FMR spectra shows that the TS500 film has the highest magnetization, $M_s \sim 1107$ G and lowest $\alpha \approx 1.31 \times 10^{-4}$. Additionally, a detailed analysis of the angular variations of resonance field (H_r) and FMR linewidth (ΔH) in both the in-plane (IP) and out-of-plane (OP) sample configurations, recorded at a fixed X- band frequency of 9.45 GHz by the cavity-based FMR reveals the following: (i) In the TS series, decrease in the disorder strength with increasing T_S is reflected as a systematic reduction in ΔH and H_r , (ii) Irrespective of the degree of disorder, the two-fold variation of H_r with the magnetic field angle (φ_H) establishes that the CFAS films have *in-plane* uniaxial anisotropy, (iii) Gilbert damping and angular spread in the crystalline misorientation are the dominant mechanisms responsible for the linewidth broadening in the OP case.

The hysteresis loops and domain images captured at different 'in-plane' magnetic field angles (φ_H) , by using longitudinal magneto-optical Kerr effect (L-MOKE) microscopy, reveals that for all the TS films, except for TS450, rectangular hysteresis loops are observed. Such loops are

characterized by the normalized squareness ratio $M_r/M_s \cong 1$ (where M_r is the remanent magnetization and M_s is the saturation magnetization). As the field angle increases from 0° , M_r/M_s decreases gradually and tends to 0 along the hard axis, i.e., $\varphi_H = 90^{\circ}$. This angular variation of the M_r/M_s shows a dominant two-fold variation which further confirms the existence of inplane uniaxial anisotropy in the CFAS films. H_c decreases with T_S due to the decrease in defects, magnetic inclusions, and local magnetic inhomogeneities. In the RT film, a combination of Stoner-Wohlfarth model and two-phase model describe the angular dependence of H_c whereas in the TS350 and TS500, two phase model alone describes the functional dependence of H_c on φ_H . In the TS450 and TS550, four-fold angular variation of H_c is observed (with four minimum and four maxima in $H_c(\varphi_H)$), in this case the modified two-phase model best describes the $H_c(\varphi_H)$. Following conclusions are drawn from the analysis of the domain images: (i) when the H is applied along the easy axis ($\varphi_H = 0^\circ$), magnetization reversal occurs through the reverse domains nucleation and as H approaches H_c , the reverse domain grow by domain wall movement with increasing H, (ii) at $\phi_H = 45^\circ$, the magnetization reversal takes place through rotation plus growth giving rise to stripe domain and (c) When H is applied along the hard axis direction ($\varphi_H = 90^\circ$), a weak contrast between the dark and light regions is observed. When H is reversed, even a small magnitude (≈ 2 Oe) is enough to nucleate the reverse domains which grows as a result of the 180° domain wall movement.

7.1.2 Effect of thickness on the structural, magnetic, electrical- and magneto-transport properties of Co₂FeAl_{0.5}Si_{0.5} Heusler alloy thin films

In the thickness series, the 12 nm, 25 nm and 50 nm films possess B2 structure order, while the film with the highest thickness, 75 nm, exhibits disordered A2 structure. The resistivity minimum at T_{min} , characteristic of disordered systems, results from the competition between negative TCR (ρ_{e-d} and ρ_{wl}) and positive TCR (ρ_{e-m} and ρ_{e-p}) contributions to resistivity. Observation of a resistivity minimum thus confirms the presence of disorder in the CFAS films. Irrespective of the film thickness, the resistivity upturn below $T < T_{min}$ is almost entirely accounted for by the -lnT and $-T^{3/2}$ temperature variations that characterize the e - d scattering and WL effect. The electron-magnon contribution, $\rho_{e-m}(T)$, is best estimated taking into account the thermal renormalization

of the spin-wave stiffness, i.e., $D_{sw}(T) = D_0(1 - D_2 T^2)$ with $D_2 \neq 0$. The electron-phonon contribution, $\rho_{e-p}(T)$, is best described by the Bloch-Wilson model.

From the broad-band FMR studies, the value of magnetization, obtained from the Kittel fit, increases with thickness, and has a maximum for the 50 nm film, $M_s \sim 1107$ G. The anisotropy is small for the 50 nm film but increases with decrease in thickness due to surface anisotropy at lower thicknesses. The in-plane resonance field as a function of 'in-plane' field angle (φ_H) shows two-fold symmetry which represents the dominant 'in-plane' uniaxial anisotropy for all the thicknesses. For all the films, Gilbert damping and inhomogeneous broadening due to crystallite misorientation give the dominant contributions to linewidth broadening. The Gilbert damping constant, α for 25 nm and 75 nm CFAS films is found to be 0.0057 and 0.016 respectively.

From the magnetization reversal studies using L-MOKE, angular dependence of M_r/M_s and H_c for the 12 nm and 25 nm films show four-fold variation, whereas for the 50 nm and 75 nm film, four-fold variation is observed, such a cross over suggest that two UAs decreases with increasing thickness and a single UA is present above 50 nm thickness. Thus, $H_c(\varphi_H)$ for 12 nm and 25 nm is described well by the modified two-phase model and for the 75 nm films the two-phase model becomes more relevant. Irrespective of the film thickness, the domain images for $\varphi_H = 0$ show the nucleation and subsequent growth of reverse domains by domain wall motion. At $\varphi_H = 45^\circ$, magnetization reversal occurs through ripple domains formation whereas for $\varphi_H = 90^\circ$, magnetization reversal mainly proceeds through domain rotation.

7.2 Future scope of the thesis work

- To study the effect of anti-site disorder on the spin polarization in these CFAS films, Point Contact Andreev Reflection (or PCAR) technique can be employed.
- Further investigation can be caried out to understand the underlying mechanisms responsible for the variation of (two-fold and four-fold) angular dependence of M_r/M_s and H_c .
- The study of interface effects between the CFAS films and the substrate can be carried out to further explore its effect on the physical properties.
- CFAS Heusler alloys with low Gilbert damping ($\alpha \approx 1.31 \times 10^{-4}$) makes it suitable for use in making electrodes for spin valves systems and magnetic tunnel junctions. Future research may focus on these materials for enhanced spin transport and device fabrications.

LIST OF PUBLICATIONS BASED ON THE RESEARCH WORK

- 1. **Lanuakum A Longchar**, Mainur Rahaman, Binoy Krishna Hazra, R. Rawat, M. Manivel Raja, S.N. Kaul, S. Srinath., "*Resistivity minima in disordered Co₂FeAl_{0.5}Si_{0.5} Heusler alloy thin films*". Journal of Magnetism and Magnetic Materials 569, 170439 (2023)
- 2. **Lanuakum A. Longchar**, Mainur Rahaman, Binoy Krishna Hazra, M. Manivel Raja, R. Rawat, S. N. Kaul and S. Srinath., "*Effect of film thickness on the electrical transport in Co*₂*FeAl*_{0.5}*Si*_{0.5} thin films". AIP Advances 13, 025106 (2023)

Papers in conference proceedings.

- 1. **Lanuakum A Longchar**, Mainur Rahaman, Lalita, G A Basheed, M. Manivel Raja, S. N. Kaul, and S. Srinath. "*Effect Of Film Thickness On The Structural and Magnetic Properties of Co₂FeAl_{0.5}Si_{0.5} Heusler Alloy Thin Film"* AIP conference proceedings (2023).
- Lanuakum A Longchar, Mainur Rahaman, M. Manivel Raja, V. Raghavendra Reddy, S. N. Kaul and S. Srinath, "Magnetization reversal and damping in Co₂FeAl_{0.5}Si_{0.5} quaternary Heusler alloy". Conference: 2023 IEEE International Magnetic Conference Short Papers (INTERMAG Short Papers)

Papers co-authored

- C.T. Lennon, Y. Shu, J. C. Brennan, D. K. Namburi, V. Varghese, D. T. Hemakumara, Lanuakum A Longchar, S. Srinath and R. H. Hadfield. "High-uniformity atomic layer deposition of superconducting niobium nitride thin films for quantum photonic integration" *Mater. Quantum. Technol.* 3, 045401(2023)
- Mainur Rahaman, Lanuakum A Longchar, Somesh Kumar Sahoo, Arabinda Haldar, M. Manivel Raja, S. N. Kaul, and S. Srinath., "Effect of site disorder on the resonant microwave absorption in Co₂Fe_{0.5}Ti_{0.5}Si Heusler alloy thin films", Journal of Magnetism and Magnetic Materials 559, 169519 (2022)
- 3. Manik Kuila, Archna Sagdeo, **Lanuakum A. Longchar**, R. J. Choudhary, S. Srinath and V. Raghavendra Reddy., "Robust perpendicular magnetic anisotropy in Ce

- substituted yttrium iron garnet epitaxial thin films", Journal of Applied Physics 131, 203901 (2022).
- 4. Mainur Rahaman, Lanuakum A Longchar, Rajeev Joshi, Rajeev Rawat, , M. Manivel Raja, S. N. Kaul, and S. Srinath. "Thermo-elastic Martensitic transformation in off-stoichiometric Co₂Fe_{0.5}Ti_{0.5}Si quaternary Heusler alloy thin films" Conference: 2023 IEEE International Magnetic Conference Short Papers (INTERMAG Short Papers)
- Mainur Rahaman, Lanuakum A Longchar, Pardeep, G A Basheed, M. Manivel Raja,
 N. Kaul, and S. Srinath "Broad-Band and X-Band Ferromagnetic Resonance Study
 on Co_{1.9}Fe_{0.58}Ti_{0.61}Si_{0.88} Quaternary Heusler Alloy Thin Film" AIP conference proceedings (2023).

Manuscripts under preparations:

- 1. "Gilbert damping and magnetization reversal of in-plane uniaxial Co₂FeAl_{0.5}Si_{0.5} (CFAS) Heusler alloy thin films."
 - Lanuakum A Longchar, Mainur Rahaman, V. Raghavendra Reddy, Lalita, G. A. Basheed, M. Manivel Raja, S. N. Kaul, and S. Srinath. (Submitted to ICMAGMA 2023)
- 2. "A comprehensive study of ferromagnetic resonance properties and magnetization reversal of Co₂FeAl_{0.5}Si_{0.5} Heuler alloy thin film."
 - Lanuakum A Longchar, Mainur Rahaman, Arabinda Haldar, Manik Kuila, V. Raghavendra Reddy, M. Manivel Raja, S. N. Kaul, and S. Srinath.
- 3. "Correlation between structural, static and dynamic magnetic properties in Co₂FeAl_{0.5}Si_{0.5} Heusler alloy thin films."
 - Lanuakum A Longchar, Mainur Rahaman, Pardeep, G. A. Basheed, M. Manivel Raja, Arabinda Haldar, S. N. Kaul, and S. Srinath.

Awards received.

- 1. Received 'Best Poster award' for presenting the work titled 'Magnetization reversal and Gilbert damping of in-plane uniaxial Co₂FeAl_{0.5}Si_{0.5} (CFAS) Heusler alloy thin films', at International Conference on Magnetic Materials and Applications (ICMAGMA 2023) held in Hyderabad.
- 2. Received 'Best Poster award' for presenting the work titled 'Effect of Film Thickness on The Structural and Magnetic Properties of Co₂FeAl_{0.5}Si_{0.5} Heusler Alloy Thin Film' at DAE-SSPS-2022, BITS, Mesra, Jharkhand.
- 3. Received 'Best Poster award' for presenting the work titled 'Correlation between structural, static and dynamic magnetic properties in Co₂FeAl_{0.5}Si_{0.5} Heulser alloy thin films' at 12th Indo-Japan Science and Technology conference (ICFAST 2022), Hyderabad.

Papers presented in conference.

- "Magnetization reversal and Gilbert damping of in-plane uniaxial Co₂FeAl_{0.5}Si_{0.5} (CFAS) Heusler alloy thin films." Lanuakum A Longchar, Mainur Rahaman, M. Manivel Raja, V. Raghavendra Reddy, Lalita, G. A. Basheed, S. N. Kaul and S. Srinath, ICMAGMA 2023, Hyderabad. (*Poster presentation*)
- 2. "Effect of disorder and thickness on the Structural, Magnetic and transport properties of Co₂FeAl_{0.5}Si_{0.5} Heusler alloy thin films." FIP 2023, University of Hyderabad. March (2023). (*Oral presentation*)
- 3. "Effect of thickness on the electrical- and magneto-transport in Co₂FeAl_{0.5}Si_{0.5} thin films." **Lanuakum A. Longchar**, Mainur Rahaman, Binoy Krishna Hazra, M. Manivel Raja, R. Rawat, S. N. Kaul and S. Srinath. *Magnetism and Magnetic Materials* 2022, *October* 31 to November 4, (2022), (Poster presentation)
- 4. "Effect Of Film Thickness on The Structural and Magnetic Properties of Co₂FeAl_{0.5}Si_{0.5} Heusler Alloy Thin Film." **Lanuakum A Longchar**, Mainur Rahaman, Lalita, G A Basheed, M. Manivel Raja, S. N. Kaul, and S. Srinath DAE-SSPS-2022, BITS, Mesra, Jharkhand, December 18 to 22, (2022), (*Poster presentation*)
- **5.** "Correlaton between structural, static and dynamic magnetic properties in Co₂FeAl_{0.5}Si_{0.5} Heulser alloy thin films." **Lanuakum A Longchar**, Mainur Rahaman, Manik Kuila, V.

- Raghavendra Reddy, M. Manivel Raja, Arabinda Haldar, S. N. Kaul, and S. Srinath. ICFAST 2022, University of Hyderabad. September 09 to 10, (2022). (*Poster presentation*)
- 6. "Magnetization reversal and damping in Co₂FeAl_{0.5}Si_{0.5} quaternary Heusler alloy." Lanuakum A Longchar, Mainur Rahaman, M. Manivel Raja, V. Raghavendra Reddy, S. N. Kaul and S. Srinath. INTERMAG 2023, Sendai, Japan. May 15 to 19, (2023). (Poster presentation)

Effect of anti-site disorder and film thickness on the structural, magnetic, electrical- and magneto-transport properties of Co2FeAl0.5Si0.5 Heusler alloy thin films

by Lanuakum A Longchar

Central University P.O.

HYDERABAD-500 046

Submission date: 29-Jan-2024 04:54PM (UTC+0530)

Submission ID: 2281118340

File name: 17PHPH18_LANUAKUM_A_LONGCHAR.pdf (12.29M)

Word count: 34754 Character count: 166582

Effect of anti-site disorder and film thickness on the structural, magnetic, electrical- and magneto-transport properties of Co2FeAl0.5Si0.5 Heusler alloy thin films

ORIGINALITY REPORT

29%

9%

289

1%

SIMILARITY INDEX

INTERNET SOURCES

PUBLICATIONS

STUDENT PAPERS

PRIMARY SOURCES

Lanuakum A Longchar, Mainur Rahaman, Binoy Krishna Hazra, R. Rawat, M. Manivel Raja, S.N. Kaul, S. Srinath. "Resistivity minima in disordered Co2FeAl0.5Si0.5 Heusler alloy thin films", Journal of Magnetism and Magnetic Materials, 2023

15%

Dr. S. Srinath
Professor
School of Physics

School of Physics
UNIVERSITY OF HYDERABAD
Central University P.O.
Hyderabad-500 046.

Publication

Lanuakum A. Longchar, Mainur Rahaman, Binoy Krishna Hazra, M. Manivel Raja, R. Rawat, S. N. Kaul, S. Srinath. "Effect of film thickness on the electrical transport in Co FeAl Si thin films ", AIP Advances, 2023

3%



Professor
School of Physics
UNIVERSITY OF HYDERABAD
Central University P.O.
Hyderabad-500 046.

pubs.aip.org

1%

iopscience.iop.org
Internet Source

1%

Binoy Krishna Hazra, S. N. Kaul, S. Srinath, Zaineb Hussain, V. Raghavendra Reddy, M.

1 %

Manivel Raja. " Magneto-optical Kerr microscopy investigation of magnetization reversal in Co FeSi Heusler alloy thin films ", AIP Advances, 2020

Publication

Simon Trudel. "Magnetic anisotropy, exchange and damping in cobalt-based full-Heusler compounds: an experimental review", Journal of Physics D Applied Physics, 05/19/2010

1 %

Publication

Mainur Rahaman, Lanuakum A Longchar, Somesh Kumar Sahoo, Arabinda Haldar, M. Manivel Raja, S.N. Kaul, S. Srinath. "Effect of site disorder on the resonant microwave absorption in Co2Fe0.5Ti0.5Si Heusler alloy thin films", Journal of Magnetism and Magnetic Materials, 2022

<1%

Publication

Springer Series in Materials Science, 2016.
Publication

<1%

etheses.whiterose.ac.uk

<1%

Lanuakum A Longchar, Mainur Rahaman, M. Manivel Raja, V. Raghavendra Reddy, S. N. Kaul, S. Srinath. " Magnetization reversal and Gilbert damping in Co FeAl Si (CFAS) quaternary Heusler alloy ", 2023 IEEE

Dr. S. Srinath
Professor
School of Physics
NIVERSITY OF HYDERABAD
Central University P.O.
Hyderabad-500 046.

International Magnetic Conference - Short Papers (INTERMAG Short Papers), 2023

Publication

Publication

11	baadalsg.inflibnet.ac.in Internet Source	<1%
12	Sergio M. Rezende. "Fundamentals of Magnonics", Springer Science and Business Media LLC, 2020 Publication	<1%
13	Lukas Wollmann, Ajaya K. Nayak, Stuart S.P. Parkin, Claudia Felser. "Heusler 4.0: Tunable Materials", Annual Review of Materials Research, 2017 Publication	<1%
14	www.csr.res.in Internet Source	<1%
15	www.researchgate.net Internet Source	<1%
16	www.niser.ac.in Internet Source	<1%
17	Frantz, J.A "Formation of a new phase of barium copper sulfur fluoride via sputtering", Materials Letters, 20080415 Publication	<1%
18	Nanoscale Magnetic Materials and Applications, 2009.	<1%

19	worldwidescience.org Internet Source	<1%
20	export.arxiv.org Internet Source	<1%
21	Binoy Krishna Hazra, M Manivel Raja, S Srinath. " Correlation between structural, magnetic and transport properties of Co FeSi thin films ", Journal of Physics D: Applied Physics, 2016 Publication	<1%
22	duepublico.uni-due.de Internet Source	<1%
23	Anita Semwal. "Magnetic properties of the weak itinerant-electron ferromagnet Ni ₇₅ Al ₂₅ : I. The effect of site disorder", Journal of Physics Condensed Matter, 12/01/2004 Publication	<1%
24	dspace.uohyd.ac.in Internet Source	<1%
25	Binoy Krishna Hazra, S N Kaul, S Srinath, M Manivel Raja. "Uniaxial anisotropy, intrinsic and extrinsic damping in Co FeSi Heusler alloy thin films ", Journal of Physics D: Applied Physics, 2019 Publication	<1%

26	F. J. Yang, Y. Sakuraba, S. Kokado, Y. Kota, A. Sakuma, K. Takanashi. "Anisotropic magnetoresistance in Co (Fe,Mn)Si Heusler epitaxial films: A fingerprint of half-metallicity ", Physical Review B, 2012 Publication	<1%
27	K SREEHARSHA. "Structure and Properties of Films", Principles of Vapor Deposition of Thin Films, 2005 Publication	<1%
28	Binoy Krishna Hazra, S. N. Kaul, S. Srinath, M. Manivel Raja, R. Rawat, Archana Lakhani. "Evidence for the absence of electron-electron Coulomb interaction quantum correction to the anomalous Hall effect in Heusler-alloy thin films ", Physical Review B, 2017 Publication	<1%
29	Advances in Superconductivity XII, 2000. Publication	<1%
30	P. V. Prakash Madduri, S. N. Kaul. "Magnon-induced interband spin-flip scattering contribution to resistivity and magnetoresistance in a nanocrystalline itinerant-electron ferromagnet: Effect of crystallite size", Physical Review B, 2017 Publication	<1%

Zainab Hussain, V. Raghavendra Reddy, Mukul Gupta, V. Srihari, K.K. Pandey. "Study of magnetic zigzag domain walls and magnetization reversal process in polycrystalline cobalt thin films: Effect of thickness and crystallographic texturing", Thin Solid Films, 2020

<1%

Publication

media.wiley.com
Internet Source

<1%

Handbook of Materials Modeling, 2005.

<1%

Mahathi Kuchibhotla, Abhishek Talapatra, Arabinda Haldar, Adekunle Olusola Adeyeye. "Field orientation dependent magnetization reversal and dynamics in sub-100-nm-wide Permalloy nanowires", Journal of Physics D: Applied Physics, 2022

< 1 %

Publication

Binoy Krishna Hazra, S.N. Kaul, S. Srinath, M. Manivel Raja, R. Rawat, Archana Lakhani. "Diffuson contribution to anomalous Hall effect in disordered Co2FeSi thin films", Journal of Magnetism and Magnetic Materials, 2019

<1%

Publication

Submitted to University of Sheffield Student Paper

Publication

oar.ptb.de

<1%

51	NanoScience and Technology, 2016. Publication	<1%
52	ir.amu.ac.in Internet Source	<1%
53	Jianlong Wang, Yanan Yin. "Chapter 6 Kinetic Models for Hydrogen Production", Springer Science and Business Media LLC, 2017 Publication	<1%
54	Liu, X., Y. Y. Zhou, E. Harley, L. E. McNeil, J. Wang, J. Qi, Y. Xu, A. Steigerwald, and N. Tolk. "", Ultrafast Phenomena in Semiconductors and Nanostructure Materials XIV, 2010. Publication	<1%
55	N. Patra, C.L. Prajapat, Rajnarayan De, K.D. Rao, P.D. Babu, A.K. Sinha, Siju John, H.C. Barshilia, S.N. Jha, D. Bhattacharyya. "Correlation of structural ordering with magnetic properties of pulsed laser deposited Co 2 FeGa Heusler alloy thin films", Journal of Alloys and Compounds, 2018 Publication	<1%
56	Satoshi Kokado, Masakiyo Tsunoda. " Theoretical Study on Anisotropic Magnetoresistance Effects of (15100) (15110)	<1%

Satoshi Kokado, Masakiyo Tsunoda. "
Theoretical Study on Anisotropic
Magnetoresistance Effects of // [100], // [110],
and // [001] for Ferromagnets with a Crystal
Field of Tetragonal Symmetry ", Journal of the
Physical Society of Japan, 2019





<1 % <1 %

www.rjlg.com
Internet Source 64

Exclude quotes On Exclude bibliography On Exclude matches

< 14 words



UNIVERSITY OF HYDERABAD HYDERABAD 500 046, INDIA

Dr. S. Srinath Professor School of Physics

29 January 2024 Hyderabad

Ref. Ph. D Thesis of Lanuakum A Longchar (17PHPH18)

Sub: Plagiarism check certificate

This is to certify that the thesis entitled, "Effect of anti-site disorder and film thickness on the structural, magnetic, electrical- and magneto-transport properties of Co₂FeAl_{0.5}Si_{0.5} Heusler alloy thin films", submitted by my student Lanuakum A Longchar (Regn No: 17PHPH18), has been screened by the Turnitin software at the Indira Gandhi memorial library (IGML)-University of Hyderabad. This software shows 29% similarity index out of which, 18 % (+ < 1%) (item no. 1, 2 and 10) came from the candidate's research articles (where he is the first author) directly related to this thesis.

From the detailed similarity index report, it is obvious that the remaining 11% of similarity index, is due to the similarity caused by the frequent use of the well- known standard terms such as temperature, magnetization, Stoner-Wohlfarth model magnetic field, magnetic anisotropy, spin waves, exchange interaction, magnetization reversal, resistivity, magnetoresistance, ferromagnetic resonance, linewidth, Heusler alloys, thin film thickness, to name a few. Use of such terms is common in the literature and it should be noted that the use of such standard terms cannot be avoided and as such cannot be considered as plagiarism. Therefore, the thesis may be considered to be free of plagiarism.

Professor S. Srinath

School of Physics University of Hyderabad

Hyderabad - 500 046. INDIA

Professor School of Physics UNIVERSITY OF HYDERABAD Central University P.O. Hyderabad-500 046.